Atmospheric Pitting Corrosion of Stainless Steel

by

Haval Bashar Mohammed Ali

A thesis submitted to the University of Birmingham for the degree of DOCTOR OF PHILOSOPHY

School of Metallurgy and Materials

College of Engineering and Physical Sciences

University of Birmingham

January 2016

Abstract

Atmospheric pitting corrosion of austenitic stainless steels 304L and 316L under droplets of $MgCl_2$ have been studied under conditions of relevance to long-term storage of nuclear waste containers using automated deposition of arrays of droplets.

The effect of microstructure on the morphology of atmospheric corrosion pits in 304L stainless steel plate was investigated. The presence of retained delta ferrite was found to influence the morphology of pits. Ferrite bands were preferentially attacked, and pits were found to have layered attack morphology dependent on the rolling direction and plane of the metal surface. Solution annealing of stainless steel resulted in ferrite reduction and formation of faceted pits.

Pits can grow with an initial shallow dish, which may propagate via “earring” or small satellite pits. The size and morphology were seen to vary with exposure humidity, chloride deposition density and distance from the droplet edge.

Pits propagated readily above chloride densities of ~10-4 μg/cm^2, depending on alloy and exposure time. Below this value much smaller pits were observed due to a discontinuous solution layer.

The formation of secondary spreading and micro-droplet formation was observed for $MgCl_2$ droplets on stainless steel when pits form close to or at the droplet edge. Small pits developed beneath these micro-droplets at lower humidities.

This work provides a basis to make recommendations for long-term storage

conditions of intermediate level nuclear waste (ILW) in order to minimise the risk of pitting corrosion.

Dedicated to

Peshmerga of Kurdistan, those who fight terrorism on behalf of the whole world and help to keep us safe …

Kurds everywhere as they wonder landless around the globe …

All the Kurdish martyrs who sacrificed their lives for the sake of a bit of Freedom …

Acknowledgments

I would like to show my gratitude for the Kurdistan Regional Government (KRG) for sponsoring me in the most intense economic crises it faces nowadays to do my PhD in Birmingham University which is one of the top universities in the UK.

I would like to express my gratitude and sincere thanks to my supervisor Professor Alison Davenport for her everlasting support, guidance, criticism and motivations during the period of my study. It was my great fortune to have her as my supervisor.

I would also like to especially thank my co-supervisor, Professor Moataz Attallah for his kindness and bright ideas, especially for the microstructure related work. And without his financial support, this PhD project would take longer to finish.

I would like to thank Professor Paul Bowen whose support has been very evident in helping me and my family.

I express my gratitude to Cem Örnek at the University of Manchester for the insightful discussions and help with EBSD measurements.

I also highly acknowledge the help from Steven and Angus for their priceless suggestions, comments and support.

I would like to thank and name individually all my colleagues in the corrosion group who have been there for sharing ideas and discussions: Majid, Ali, April, Weichen, Andrew, Fei, Rowena, Georgia, Sarah, Sophie and George.

Last but not the least; I would like to especially thank my wife Noor and my daughter Norjan for their endless support, love and patience along my study. Endless thanks to my lovely parents, brothers and sisters for their encouragement over a growing number of years.

Table of Contents

1 Introduction

Stainless steels are widely used Cr-rich Fe alloys developed to be resistant to corrosion. The high Cr content gives good resistance against general corrosion, but these alloys are often vulnerable to localised corrosion due to heterogeneities in the microstructure. Salt-rich aerosols can deposit on stainless steel surfaces, which can then draw in moisture during normal fluctuations in environmental humidity. This can create droplets of highly concentrated salt solutions on the steel surface, which can lead to atmospheric corrosion.

This corrosion is of particular interest to the nuclear industry, as intermediate level waste (ILW) is currently stored in stainless steel containers above ground with no immediate plans for final disposal. Aerosol deposition over decades can result in significant salt concentrations on the surface of waste containers. Although no significant corrosion damage has been seen to date, there is concern that this may lead to pitting corrosion, which could in turn develop into stress corrosion cracking, causing structural failure when moving the containers.

The initiation and propagation of pitting corrosion has been widely studied in full immersion conditions e.g. [1-3], but limited work has been done on atmospheric conditions. It is known, however, that the rate of atmospheric corrosion can be affected by variations in relative humidity (RH) [4-17], salt density [6, 15, 17-20], salt type [7, 15-17], droplet area [4, 21-23], temperature [15-17, 24, 25] and microstructure [24-29].

Atmospheric corrosion experiments can be simulated using several methods. Deposition of droplets of $MgCl_2$ solutions on stainless steel surfaces is a useful way to make a systematic study of atmospheric corrosion since $MgCl_2$ is a constituent of seawater and marine aerosols that has a low deliquescence point, so it remains in solution at low RH values where the solution is concentrated enough to cause pitting.

In this study, droplets of $MgCl_2$ solutions are deposited on sheets of 304L and 316L stainless steels to investigate the influence of different factors on the propagation and morphology of atmospheric corrosion pits. Key factors are the effect of residual ferrite on pit morphology, the critical chloride density below which pits do not propagate, and the critical relative humidity above which pits cannot develop. This information will provide underpinning knowledge to inform the operators of nuclear waste stores of safe conditions of operation.

2 Literature Review

2.1 Stainless steels

According to the microstructure, stainless steels are divided into four main groups: austenitic, ferritic, martensitic, and duplex which contain both austenite and ferrite. Stainless steels possess strong passivity due to their chromium content. However, they are susceptible to localized corrosion, such as pitting corrosion and intergranular corrosion in the existence of chloride or other aggressive ions [30-32]. Generally, stainless steels contain 11-30 wt.-% Cr, and ~1-25 wt.-% Ni, and other alloying elements such as Mn, Mo, N. The reason behind adding chromium Cr is to form an ultra-thin (nm thick) protective chromium oxide film (passive film) to protect the metal from corrosion [3], while adding Ni as an austenite stabiliser is to improve formability [31]. The addition of 2.0 - 3.0 wt.-% Mo improves the corrosion resistance of austenitic steels and imparts hot strength characteristics [33]. The low-carbon grades, 304L and 316L, are usually selected for the application of intermediate level nuclear waste containers in order to avoid intergranular attack and intergranular stress corrosion cracking [34]. Normally, austenitic stainless steels are processed in such way to obtain a primarily austenite microstructure. Based on the balance of ferrite-stabilising elements to austenite-stabilizing elements, the cast microstructure is either fully austenitic or a mixture of austenite and residual ferrite (Figure 2-1) [35]. The mechanism by which the residual delta ferrite forms will be described in the next section.

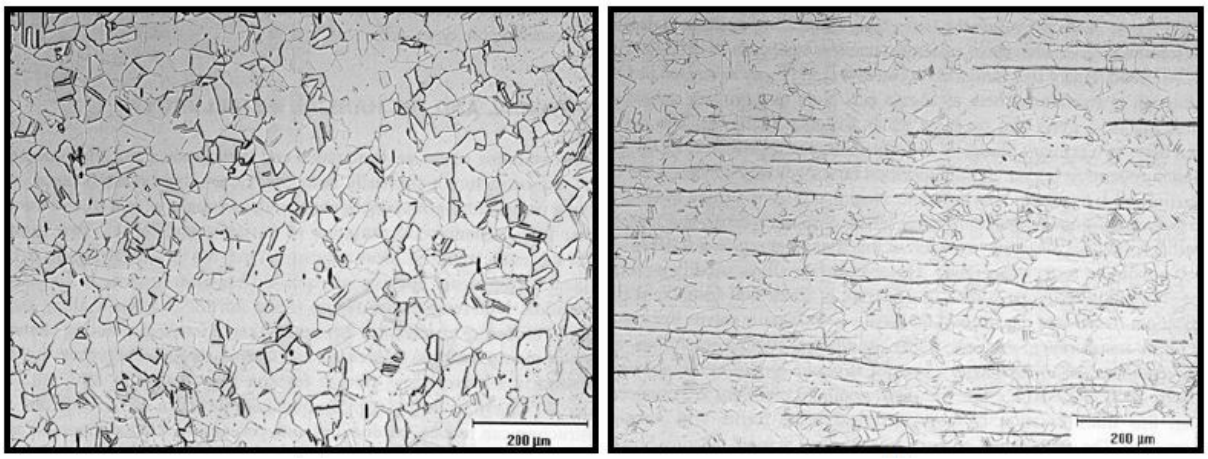

Figure 2-1 Microstructure of Type 304 stainless steel; fully austenitic (left) and mixture of austenite and residual delta ferrite stringers (right) [35].

2.2 Ferrite and martensite formation in stainless steels

In austenitic stainless steels, the formation of delta ferrite is described in terms of the solidification process [36-38]. They exhibit four solidification modes based on compositions and cooling rates; primary austenite, primary delta-ferrite, primary austenite followed by eutectic ferrite and primary delta-ferrite followed by austenite [37, 39-41]. Type 304L has a primary delta-ferrite phase, followed by a ferrite-austenite phase region exhibiting partial peritectic and eutectic reactions. A single austenite phase field exists at room temperature, as shown in (Figure 2-2). However, under more rapid solidification conditions, ferrite can be retained as a minor phase in the matrix of austenitic stainless steels [42] due to the segregation of ferrite stabilising elements, mainly chromium, during the solidification and thermo-mechanical processes such as cold rolling and hot rolling [35]. Retained ferrite usually present in relatively low fraction volume (2-5%).

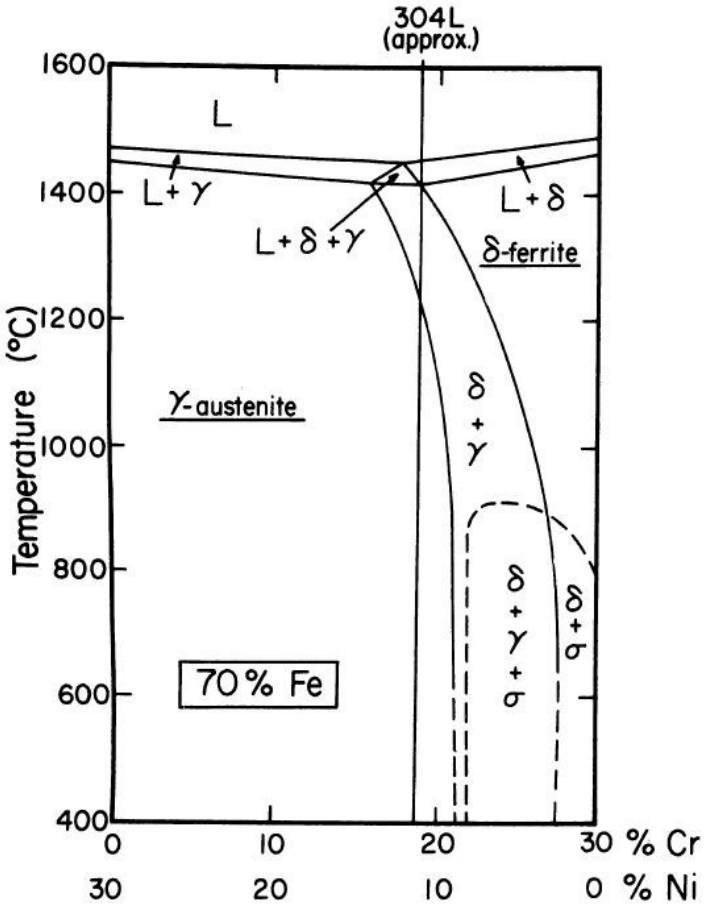

Figure 2-2 Fe-Cr-Ni equilibrium ternary diagram for constant-Fe section (70% Fe) [43].

Unstable austenitic stainless steels such us 304L and 316L stainless steels are also susceptible to martensitic transformation by plastic deformation process (cold work deformation) [44-46]. Two types of martensite may form; martensite ϵ (hcp, paramagnetic) and α′ (bcc, ferromagnetic). The latter is known as strain-induced martensite. The sequence of transformation is reported to be γ→ϵ→α′ by some authors [44, 46-48]. However, direct transformation γ→ α′ through dislocation reactions was also found to be possible [49]. Nucleation of strain-induced martensite (α′) occurs heterogeneously at intersections of martensite (ϵ) bands or unilaterally compressed regions such as twin or grain boundaries [44].

2.3 Formation of inclusions in steel

It is generally agreed that inclusion formation takes place during solidification of steel. Based on their chemistry, inclusions can be classified into two types: oxide inclusions (composed of multi-element oxide phases) and MnS inclusions (which usually have both oxide and MnS phases together). Figure 2-3 shows typical examples of these inclusions.

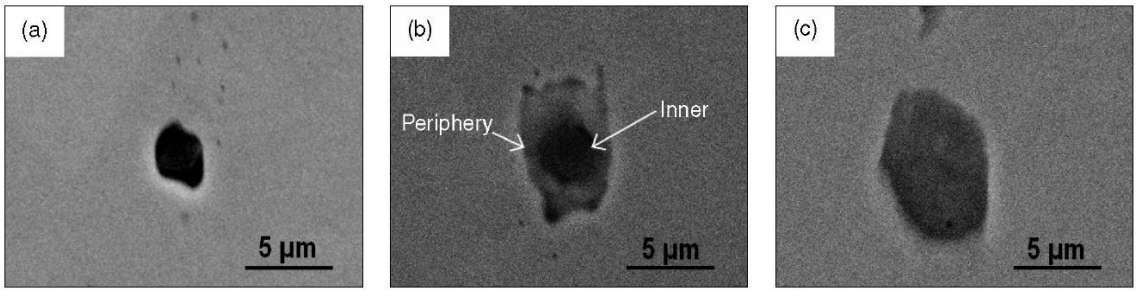

Figure 2-3 SEM images of different types of inclusions, (a) an oxide phase without MnS in clean 304 stainless steel; (b) an oxide phase surrounded by MnS in standard commercial 304 stainless steel; and (c) primarily MnS in standard 304 stainless steel [50].

MnS inclusions are difficult to avoid in the steel-making process. As an impurity, sulphur is added to the steel by ore and coke supplies to improve the machinability of steel [51]. However, sulphur is one of the most detrimental impurities remaining in the crude steel. If sulphur remains unalloyed after the bulk has solidified, hot shortness can take place during hot working processes (such as rolling) after casting. Considerable efforts have been directed towards removal of sulphur from the melt, particularly in the iron-making stage. Desulphurisation (sulphur removal) can be achieved through slag-metal reactions. This is commonly carried out by addition of CaO, which reacts with S

and forms CaS (which floats off as a buoyant slag) and O. Elements such as Mg, Al, Na and rare earth elements can also be used.

Desulphurisation does not remove all of the sulphur from the melt, and sufficient sulphur may still remain such that precipitation at grain boundaries may still lead to “hot shortening”. In order to further prevent hot shortening, Mn is added to the steel [52]. Added Mn to the steel can react with S to form MnS inclusions, which are generally not associated with grain boundaries.

Deng et al. [53] proposed a possible mechanism for the formation of multi-element oxide inclusions (Figure 2-4) based on results calculated using Factsage software that were consistent with experiment results. They proposed that during solidification, inclusions of high melting point, such as Al_2O_3 and CaS, can work as nucleation sites for MnS. TiOx, SiO_2, MnO, Al_2O_3, and sulphide inclusions, such as MnS, can precipitate during cooling of the melt. As the temperature decreases, MnS precipitates on inclusions either around the oxide core encasing it, or it precipitates in embedded form with the oxide inclusion. Once the MnS phase is formed, Mn in steel matrix will diffuse into the inclusion boundary, forming a Mn-depletion zone (MDZ) adjacent to the inclusion.

A further decrease in temperature leads to solidification of the remaining liquid to form inclusions such as TiOx+SiO_2 and (Mn-Si-Al)Ox.

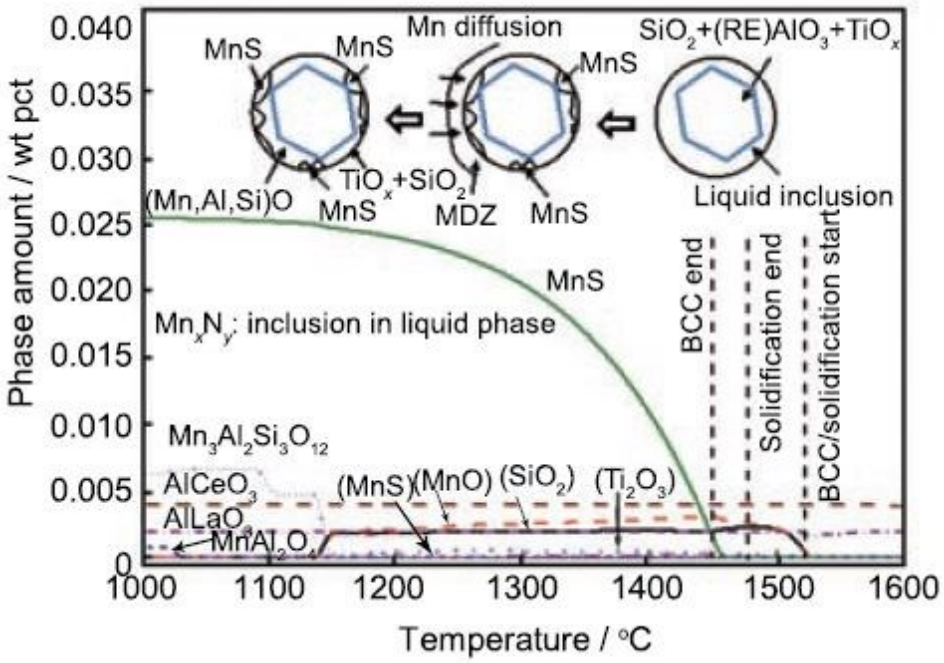

Figure 2-4 The mechanism of the evolution of complex inclusions during solidification [53].

Holappa et al. [54] and Lind [55] described a simplified system for inclusion formation based on the presence of four components: Al, Ca, O, and S. They derived ten key reactions governing the inclusion formation and transformation.

Calcium treatment is widely used to modify the shape, composition and size of the inclusions [54-56]. Figure 2-5 shows the change in inclusion morphology and composition after Ca-treatment.

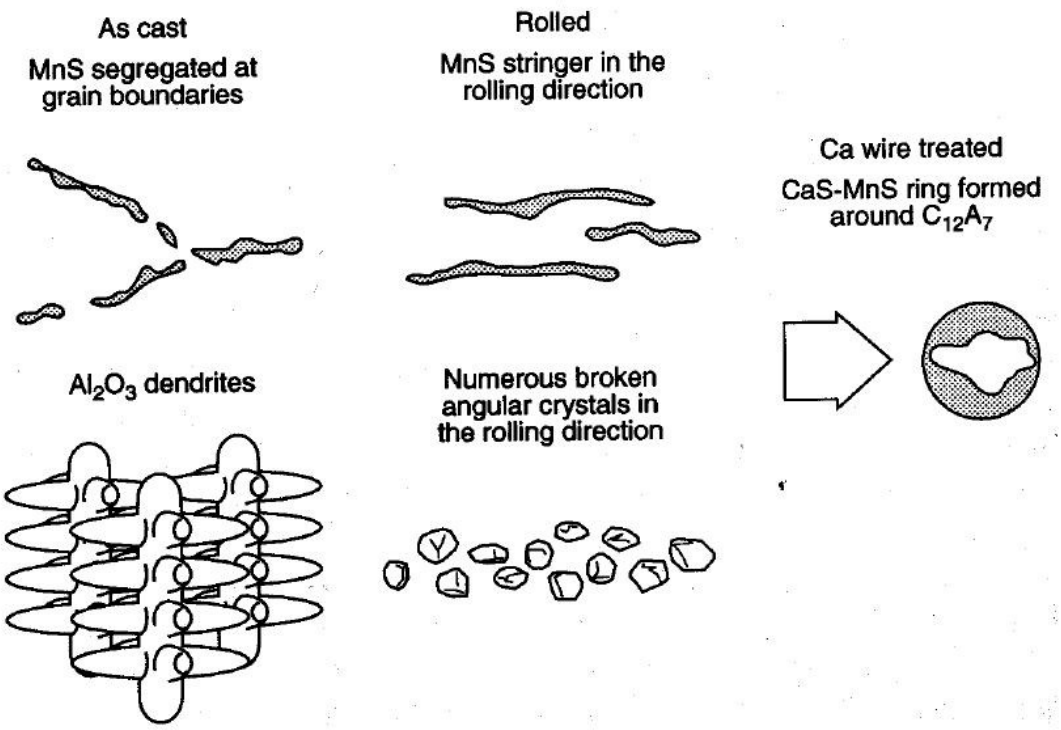

Figure 2-5 Schematic presentation of the development of inclusion shape after Ca- treatment of steel, figure reference is cited in reference [55].

Figure 2-6 schematically demonstrate the formation of inclusions in a non-treated with Ca steel (left) and in a Ca-treated steel (right).

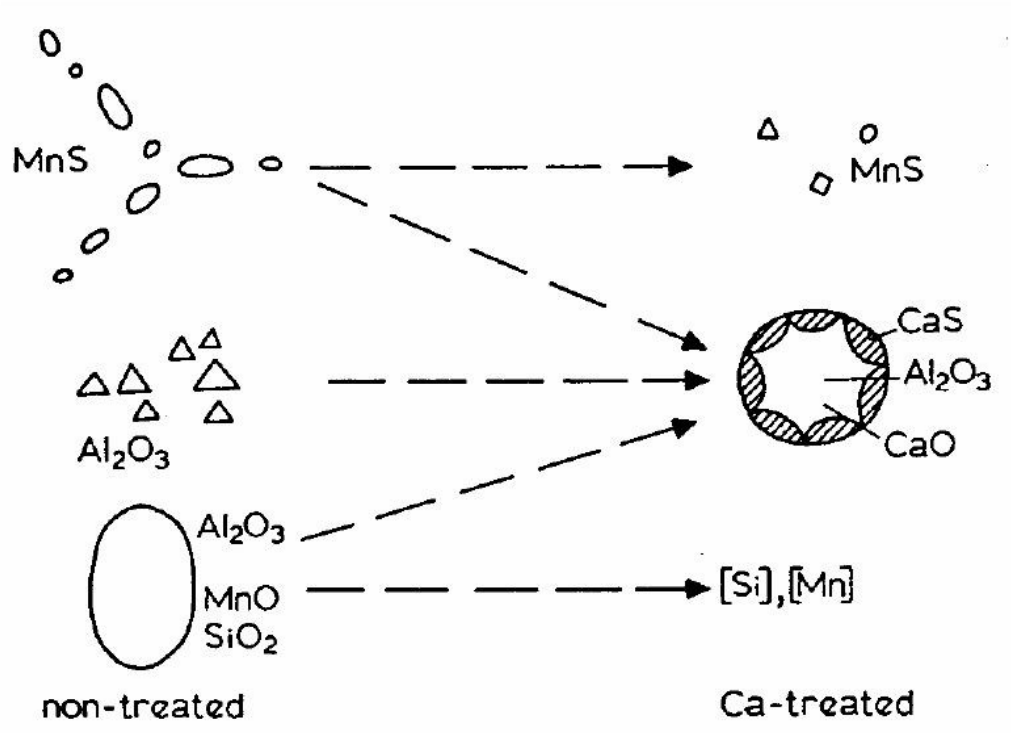

Figure 2-6 Schematic illustration of the effect of Ca-treatment on inclusions in steel, figure reference is cited in reference [55].

According to the morphology, as classified by Sims and Dahle [57], there are three specific types of sulphides which can be found in steels: (1) randomly dispersed globular sulphides (Type I), (2) elongated sulphides (Type II), and (3) angular sulphides (Type III).

2.4 Methods for delta ferrite determination in stainless steels

The δ-ferrite content can be determined either by predictive methods or experimental methods. The well-recognized predictive methods are Schaeffler diagram [58], DeLong diagram [59], and WRC-1992 diagram [60, 61], which require data of the chemical composition of the weld metal. Although these diagrams are primarily intended for use in welds, it has been reported that they can be used to estimate the ferrite content of a base metal, weld consumable or a weld metal and the microstructure of stainless steels [62, 63]. Experimental methods which require taking real measurements involve magnetic measurements (e.g. Magne-Gage magnetic balance, Fischer Feritscope equipment and Magnetometer with Sample Vibration (VSM)[64]), X-Ray Diffraction [45, 65]., Electrochemical determination, EDX [36] and quantitative metallographic determination. The scope, advantages and limitations of the predictive methods and currently used measurement techniques can be found in [63, 66].

2.5 Effect of solution treatment on microstructure

Solution annealing treatments were observed to be useful to eliminate and or reduce the presence of delta ferrite from austenitic stainless steels [36, 42, 67, 68]. Rho et al. [42] found that the amount of delta-ferrite (measured by ferritescope) in 304L stainless steel is decreased from 0.99% to 0.23% after the solution treatment conducted at 1050°C for about 25 minutes (Figure 2-7). It was also observed that, based on the selected annealing temperature and time, significant grain growth is usually associated with solution annealing process.

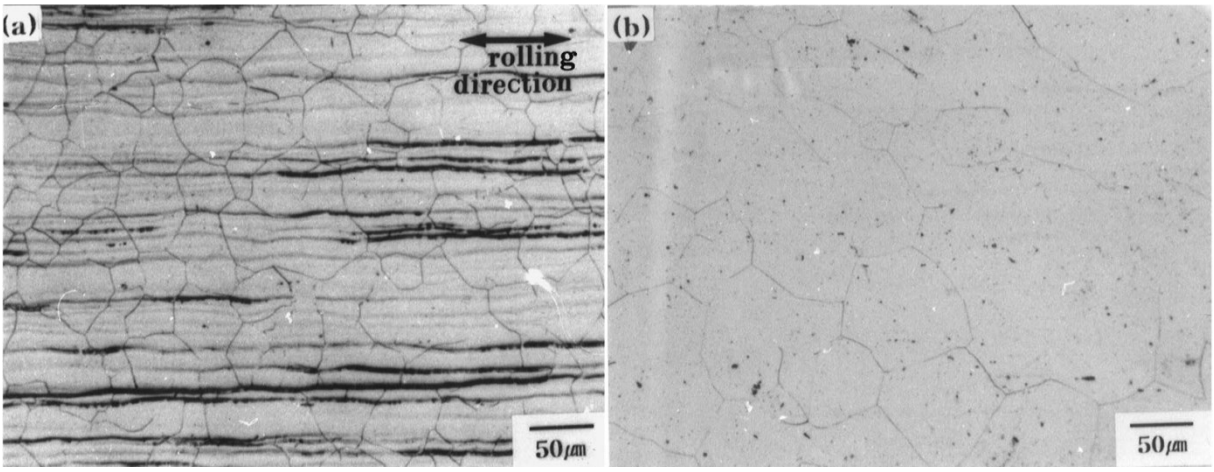

Figure 2-7 Optical micrographs of 304L stainless steel (a) as-received with narrow strips of delta ferrite in black parallel to the rolling direction; and (b) solution-treated at 1050 °C for 1 h then water quenched. The etchant solution was made from mixing of two solutions in equal amounts, solution one (methanol 100 ml, nitric acid 25 ml and hydrochloric acid 25 ml) and solution two (distilled water 100 ml and sodium pyrosulphate 1.5 g). The sample was immersed for 5–60 s at room temperature in the mixed etchant solution. The d-ferrite turns black [42].

The delta ferrite volume fraction was observed to decrease with increasing the exposure temperature [67, 68] and time [67]. Kim et al. [67] studied the dissolution kinetics of delta ferrite in 304 stainless steel samples and found that it is a function of annealing temperature and time. Figure 2-8 shows that the delta ferrite volume fraction decreases with increasing annealing temperature and time [67]. They claimed that a rapid dissolution was observed at the early stage of dissolution but came under diffusion control at the normal stage without reporting any data between 0 and 50 s. They attributed the rapid dissolution of delta ferrite to the large difference in Cr concentration between delta ferrite and austenite phases.

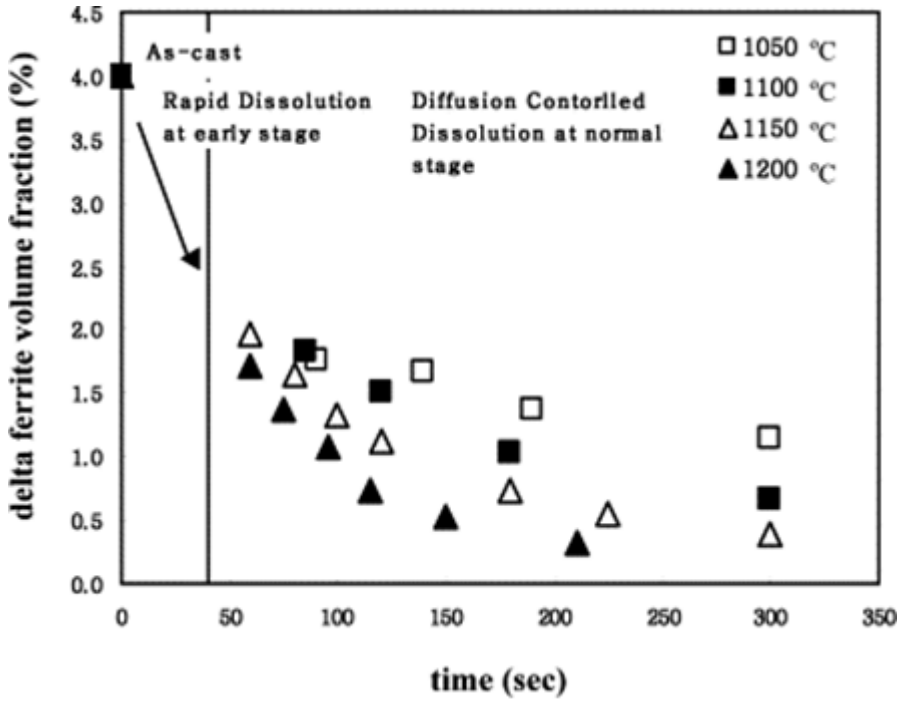

Figure 2-8 Change in delta ferrite fraction with annealing (dissolution) temperature and time for 304 stainless steel [67].

Toor [69], found that the corrosion rate decreased with increasing annealing temperature from 1030 °C/120 minutes to 1050 °C/30 minutes. This improvement in corrosion resistance was attributed to the dissolution of harmful inclusions and homogenization of the microstructure at 1050 °C.

2.6 Effects of the presence of delta ferrite on stainless steels

In general, austenitic stainless steels have good ductility and toughness and exhibit significant elongation during tensile loading. However, the presence of δ-ferrite in relatively low fraction volume (2-5%) in the microstructure of cast alloy can reduce the ductility and the toughness [35]. The presence of such small amount of ferrite is regarded as beneficial in fully austenitic stainless steels

because ferrite phase improves hot workability [70-73]. However, it has been reported that this retained delta ferrite has detrimental effects on pitting corrosion resistance for fully immersed stainless steels [74, 75]. These effects were explained in terms of; segregation of impurities such as sulphur and phosphorus along the austenite/ferrite interface [74, 76], the formation of Cr-depleted zone [76-78], the lower pitting resistance equivalent number (PREN) of austenite compared to ferrite phase [78-80], and low concentration of Cr and Mo in austenite phase [70]. In general, austenitic stainless steels were found not to be as readily embrittled by hydrogen as ferritic materials [25, 81, 82].

2.7 Preferential dissolution of ferrite and austenite

It has been reported that different electrochemical behaviours arise from the difference in the chemical composition of delta ferrite and austenite phases [83, 84]; the active, active-passive transition curve of the alloy shifts to more negative potentials due to the high chromium and low nickel contents [84].

Lo et al. [83] studied the influence of the H_2SO_4/HCl composition on the selective dissolution behaviour and found two distinct peaks in the active-to-passive transition region in the potentiodynamic polarization curves of 2205 duplex stainless steel. The higher anodic peak was associated with the preferential dissolution of austenite while that for ferrite at lower potential (Figure 2-9) [83].

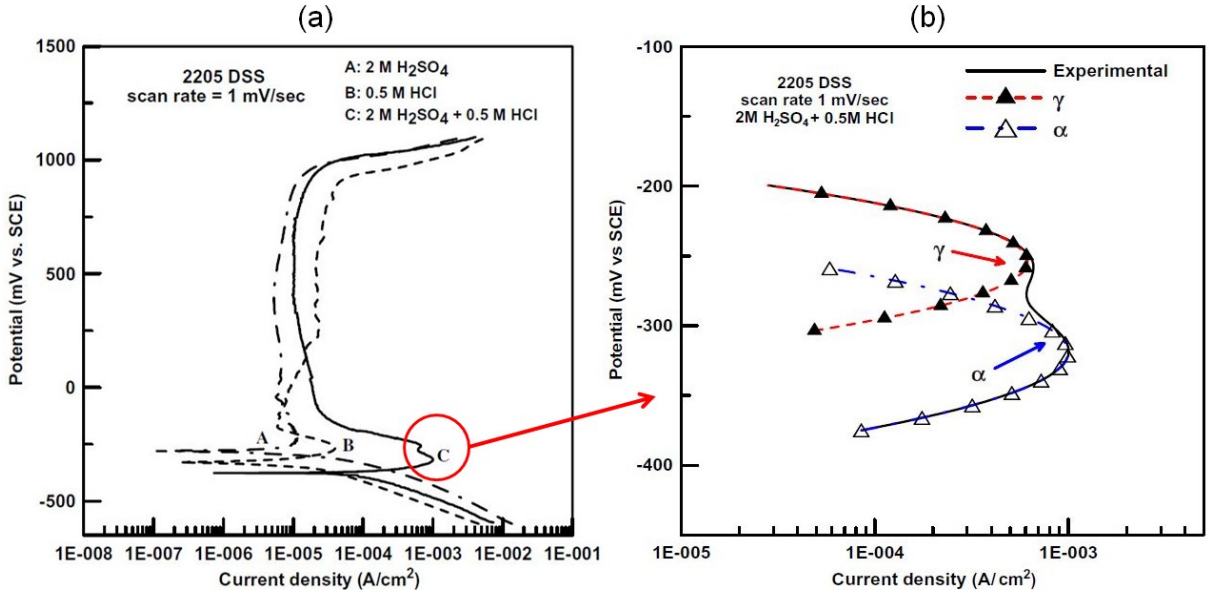

Figure 2-9 (a) Potentiodynamic polarization curves of 2205 duplex stainless steels (DSS) operated in the H_2SO_4/HCl solutions with different compositions at ambient temperature; (b) contributions of ferrite (α) and austenite (γ) phases on the anodic current density at active-to-passive potentials [83].

Recently, in an atmospheric corrosion study on as received grade 2205 duplex stainless steel, Örnek et al. [82] found that the formation of different failure morphologies is a function of location within the droplet containing a mixture of $FeCl_3$:$MgCl_2$ after exposure at 50°C and 30% RH for long term exposure (368 days); with attack of both phases at the anodic center but the austenite at the periphery of the droplet and the ferrite between the center and the droplet periphery. They attributed this to the local variations of electrochemical potentials beneath the droplet.

2.8 Pitting corrosion of stainless steels

Stainless steels are protected from corrosion by a naturally formed passive film on the surface. In the presence of chloride ions, however, stainless steels are susceptible to localised corrosion such us pitting corrosion which is one of the most destructive forms of corrosion [85-87]. For stainless steels, it is widely accepted that pits initiate at inclusions such us MnS inclusions. It is generally agreed that pitting is autocatalytic, self-generating process.

Figure 2-10 shows the electrochemical mechanism of pitting corrosion in steel in neutral chloride solution [88]. The mechanism can be described as follows: at the pit site (anodic dissolution reaction takes place), the metal will dissolve and produce metal ions, and then metal ions will react with the water to form an acidic environment within the pit (pH will decrease inside the pit) which will promote further growth of the pit. Consequently, oxygen will be depleted inside the pit. Chloride anions will diffuse into the pit to maintain the charge balance. The oxygen reduction reaction will take place outside the pit (cathodic area). The rust (corrosion product) will be precipitated. Usually, hydrogen bubbles well generate during pitting corrosion.

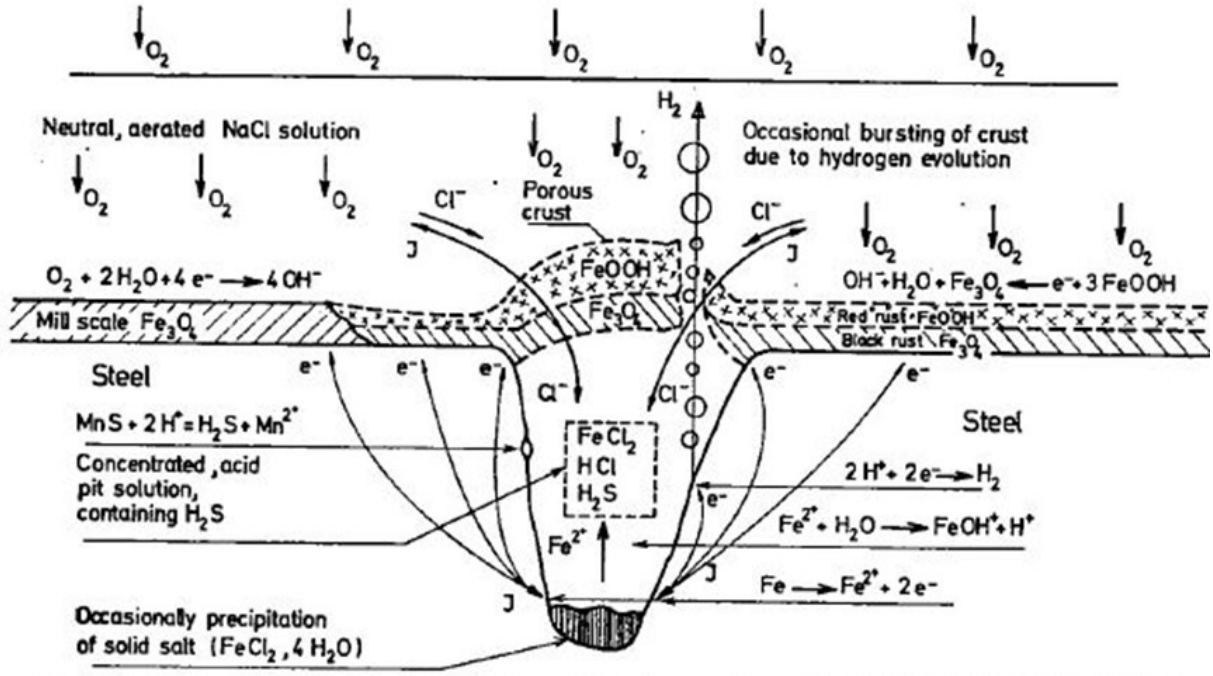

Figure 2-10 Schematic diagram of the electrochemical mechanism of pitting corrosion in steel in neutral chloride solution [88].

In the following sections, the pit initiation, propagation and pit morphology are discussed in detail.

2.8.1 Pit initiation

There are numerous theories of pit initiation on stainless steel concentrating on passive film breaking, penetration and adsorption [1]. However, it is widely accepted that pits initiate preferentially at inclusions, notably at MnS inclusions [1, 51, 88-90] in commercial stainless steels. It has also been observed that other types of inclusions such as multi-element (Cr, Mn, Al, Ti, V) oxides and mixtures of sulphides and oxides can cause pit initiation [50, 91-93]. It has been

reported that when both MnS and multi-element oxide inclusions exist together, pitting is generally not associated with the multi-element oxide inclusions but is related with MnS inclusions [92, 94, 95].

In addition to inclusion, other features for example delta ferrite, alpha prime and sigma phase may also enhance pitting corrosion [85]. Figure 2-11 schematically shows most of these features.

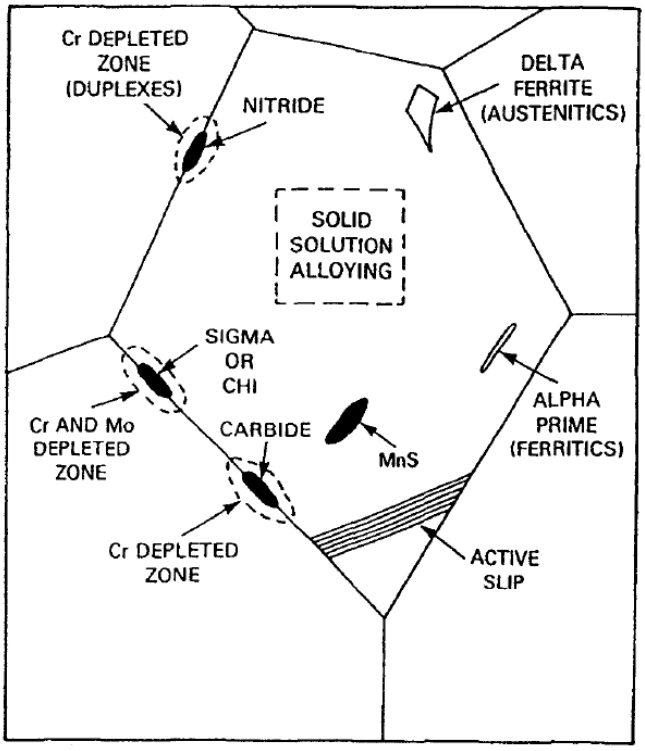

Figure 2-11 Schematic diagram of different metallurgical variables influencing the passivity of stainless steels [96].

Different researches have proposed different reactions for the dissolution of MnS inclusions [88, 89, 97-99]. Eklund [89] proposed that MnS inclusions can dissolve and led to the formation of aqueous sulphide (H_2S), sulphur (S) and sulphate (SO_4^{2-}). Castle and Ke also reported the formation of the elemental sulphure (S). The formation of elemental sulphur (S), sulphate (SO_4^{2-}) and sulphide (H_2S) has also been reported by Wranglen [88]. Both Lott [98] and

Web and Alkire [99-101] suggest that the MnS dissolution products can be thiosulphate ($S_2O_3^{2-}$) which has been reported to enhance Cl^- induced pitting corrosion for types 304 and 316L [102, 103].

Figure 2-12 illustrates schematically the initiation of pitting corrosion at the site of an MnS inclusion on stainless steel based on the observation of Castle and Ke [97]. They proposed the following reactions for MnS dissolution in neutral chloride solutions:

$$MnS + 3H_2O = Mn^{2+} + HSO_3^- + 5H^+ + 6e^- \qquad \text{Equation 2-1}$$

$$HSO_3^- + 5H^+ + 4e^- = S + 3H_2O \qquad \text{Equation 2-2}$$

A local acidic solution will form by the oxidation of MnS to HSO_3^-. Then Sulphur will precipitate by the reaction cathode at the cathode (Equation 2-2).

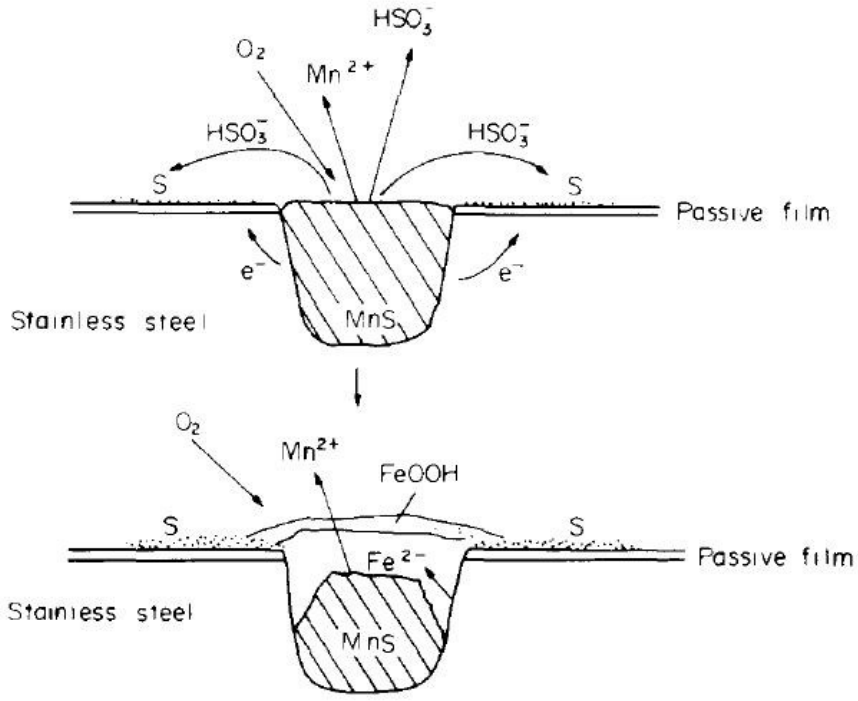

Figure 2-12 Schematic representation of pit initiation at an MnS inclusion site suggest by Castle and Ke [97].

It has been reported that initial attack on the metal close to the inclusion can take place due to the lower pH associated with inclusion dissolution process [88, 89]. It has also been reported that the formation of sulphur layer can prevent the passivation of the metal and decrease the strength of metal-metal bonds. Hence, increase the dissolution rate of metal [104, 105].

The geometrical shape [7, 18, 90, 99, 100, 106-108], size [51, 91-93, 109], composition [50, 90, 109-113] and distribution [50] of inclusions have been reported to significantly influence pit initiation (the onset of pitting) and growth on stainless steels. It has been proven that to cause stable pitting a critical size of inclusions is needed [92, 109]. Both the geometry and the orientation of inclusions were found to play a prevalent role in the pit initiation and further developments of pitting on stainless steels. Webb et al. [106] have studied the effect of MnS inclusion geometry and depth on pits and reported that narrow yet deep inclusions led to pits, but large yet shallow inclusions did not. The presence of extended needle-shaped inclusions parallel to the rolling direction [95] in commercial stainless steels was attributed to the rolling process during casting process.

2.8.2 Pit Growth (propagation)

Many researchers have investigated the growth of pits [2, 114-118]. It is generally accepted that inside a pit, a concentrated acidic chloride solution will develop that prevents the formation of the passive oxide film and allows continued dissolution.

As mentioned above, when pitting corrosion initiates, metal ions (M^{n+}) such as Fe^{2+} are generated by the dissolution of stainless steels (equation 2-3).

$$M \rightarrow M^{n+} + ne^{-} \qquad \text{Equation 2-3}$$

These metal ions (M^{n+}) increase the acidity inside the pit through the hydrolysis reaction (equation 2-4) which produces H^{+}.

$$M^{n+} + H_2O \rightleftharpoons MOH^{(n-1)+} + H^{+} \qquad \text{Equation 2-4}$$

To balance the electrical charge of positive metal ions inside the pit, negative Cl^{-} ions which are small and have high diffusivity, move into the pit [1, 88] as shown in Figure 2-10. Therefore the concentration of metal ions [M^{n+}] from dissolution of metal inside the pit controls the acidity inside the pit. When the concentration of metal ions increases, the acidity inside the pit increases and this favours dissolution over passivation, thus when the rate of metal ions production inside a pit is higher than the rate of metal ions escape from inside the pit, the pit will be stable [116, 118, 119].

After a while, the O_2 inside the pit will be consumed in cathodic reactions and there will be the shortage of O_2 inside of the pit. However, the area outside of the pit has relatively good access to O_2 compared to inside the pit, and the anodic reaction can continue inside the pit after the O_2 shortage while cathodic reactions continue outside the pit. Thus inside the pit will be a net anode and the outside of the pit will be a net cathode [119].

It has been reported that the rate of metal dissolution in a pit decreases linearly with the reciprocal of the pit depth. This indicates that the current density of the pit is self-regulated by migration or diffusion effects [120].

Isaacs et al. [121] reported from 1D artificial pit electrode studies that a resistive layer forms on the electrode interface. This layer self regulates its thickness as the potential is varied. They reported that because of the existence of this layer, the current is not dependent of potential, and showed that the diffusion rate of positive metal ions from the layer is the same as the moving rate of the metal ions through this layer to pit solution.

In order to study diffusion effects in artificial pits, Tester and Isaacs [122] used the Nernst-Einstein equation (Equation 2-5) for expressing the anodic current density *i* assuming that convection is not significant:

$$\frac{i}{nF} = -D\left[\frac{\partial C}{\partial x} + C\frac{nF}{RT}D\frac{\partial \Phi}{\partial x}\right] \qquad \text{Equation 2-5}$$

where Φ is the potential drop, *n* is the average valance of metal ions, F and R are Faraday and gas constant, respectively. C is the concentration of metal ions, D is the diffusion coefficient of dissolved metal ions, T is the absolute temperature, x is the pit depth.

When the potential drop (Φ) is insignificant and can be ignored, for diffusion-limited current density the above equation can be shown as:

$$i_{lim} = \frac{nFD\Delta C}{x} \qquad \text{Equation 2-6}$$

Where i_{lim} is the diffusion-limited current density, and ΔC is the metal ions concentration difference between the resistive layer and the pit mouth.

Ghahari et al. [123] have studied 2D pits growing at 0.005, 0.01, 0.1 and 1 M NaCl solutions under current and potential control using *in situ* synchrotron X-ray radiography. Their results revealed that the pit depth is under diffusion control and the pit width is under activation control [123].

2.8.3 Pit Morphology

Pitting corrosion can be seen in different forms such as narrow deep, wide shallow, hemispherical (elliptical), subsurface or undercutting, and microstructural orientation related pits as shown in Figure 2-13.

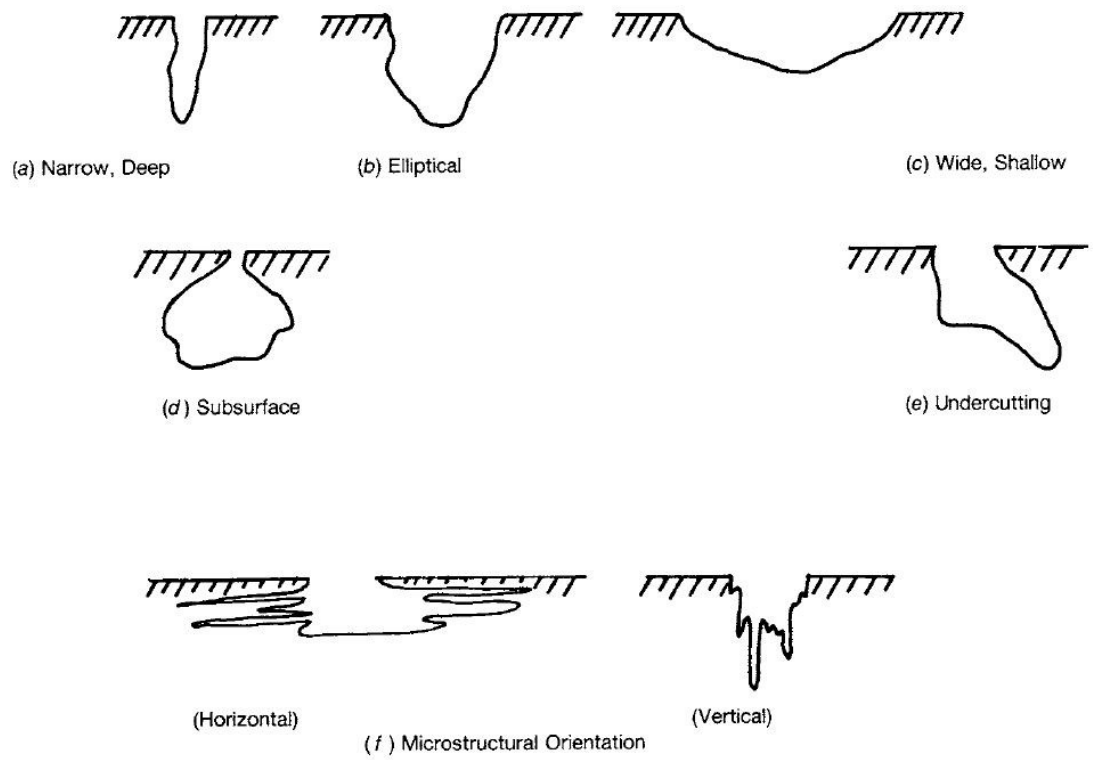

Figure 2-13 A schematic diagram of the various shapes of pits shown in cross-section [124].

The morphology of pits is a function of several parameters, such us metal structure, environment, and experimental conditions [110]. On both austenitic stainless steels and ferritic chromium steels, the formations of flat-walled pits were evident only at potentials near to pit nucleation potentials [110, 125, 126]. Schwenk [125] reported the formation of "*regularly etched pits, mostly hexagons and squares"* (Figure 2-14) on 18Cr-10Ni stainless steel in solutions containing Cl^- at low applied potentials (with low current density within pits). His analyses of the etch pits lead to the conclusion that the pit bounding planes belong to the type {111} having the lowest dissolution rate (the most closely packed crystal plane in the case of austenite). However, at higher applied potentials, both hemispherical and isotropic pits with polished or dull interiors have been evident to form. Schwenk also established that pits in their initial state are of hemispherical form covered with a thin and porous layer of metal. He found that the edges of the pits were almost, but not always, circular. Under hollowing and elongated areal pits were also reported by Schwenk.

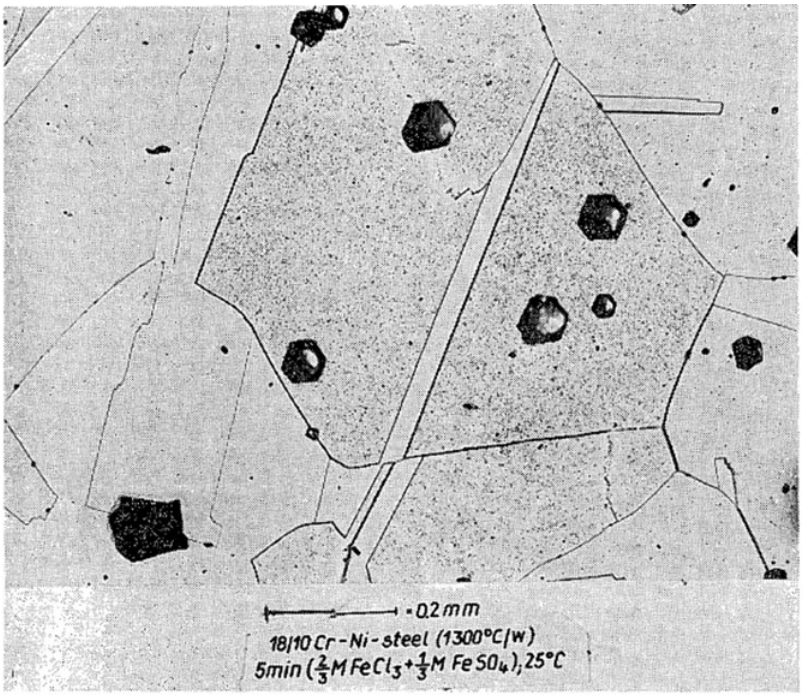

Figure 2-14 regularly etch pits morphology formed in 18Cr-10Ni solution annealed 1300 °C then water quenched steel surface [125].

Janik-Czachor and Szklarska-Smialowska [126] also reported anisotropic dissolution of the 16Cr-Fe alloy in solutions containing Cl^- ions near the pitting potential (also called as breakdown potential) resulting in formation of regular etch pits (polyhedrons flat walled pits) formed of most closely packed {110} and less closely packed {100} crystal planes.

Similar observations were also made by Pickering and Frankenthal [127, 128], they reported that pits are initially crystallographic in stainless steel and iron. However, they found a mixture of crystallographic etch and hemispherical pits at higher potentials (more noble). They observed two types of pits: (1) crystallographic pits not associated with inclusions and (2) covered pits which initiate at inclusions. The latter type was found to propagate radially underneath the metal surface away from the inclusion and finally penetrate the surface from underneath forming the lace-like structure and an often faceted interior.

2.9 Atmospheric corrosion of stainless steel

In marine environments marine aerosols, which consist of small particles (0.1-20 μm diameter range), can be produced by the bubbles that generate from ocean waves [129]. Such aerosols then are carried by coastal wind patterns and can be deposited on the metal surfaces. Later, these hygroscopic salt particles will absorb moisture from the environment when the relative humidity reaches a critical rate and form deliquescent salt droplets or thin electrolyte layers. When such droplets become aggressive enough because of change of temperature and RH they can greatly quicken the localised corrosion of metals [129]. Also, because of the presence of thin or discontinuous layers of solution, there can be easy access of oxygen to the surface. However, the chloride deposition rate can be influenced by the design and location therefore changes in chloride deposition rates are expected [130]. Besides, topography of land and the intensity and direction of predominant winds can play a vital role in variations of the composition of aerosols [131].

Although localised corrosion of stainless steel in fully immersed conditions has been widely studied, there remains insufficient information regarding atmospheric pitting corrosion of stainless steel [2].

2.10 Atmospheric pitting corrosion of stainless steel

Atmospheric pitting corrosion of stainless steel has been investigated by a number of authors under natural exposure conditions time [132, 133], under salt droplets [4-6, 15, 21, 22, 134-139], and under other conditions e.g. inkjet tests [22, 140].

There are several exposure factors which could affect the atmospheric pitting corrosion of stainless steels, for example microstructure, chloride deposition level and relative humidity etc. The effect of these factors will be explored in more detail in the following sections.

2.10.1 Pit initiation under atmospheric conditions

Some researchers have proposed mechanisms for the formation of atmospheric corrosion pits based on the laboratory experimental results under droplets containing chloride ions [4, 5, 21]. It is widely accepted that MnS inclusions are the most common sites for pit initiation in stainless steels under atmospheric conditions [4, 5]. Figure 2-15 shows a schematic diagram of pitting corrosion mechanism at a MnS inclusion under atmospheric conditions on stainless steel suggested by Tsutsumi et al. [4]. Hastuty et al. [5] have proposed a similar mechanism for Type 430 stainless steel under $MgCl_2$ droplets.

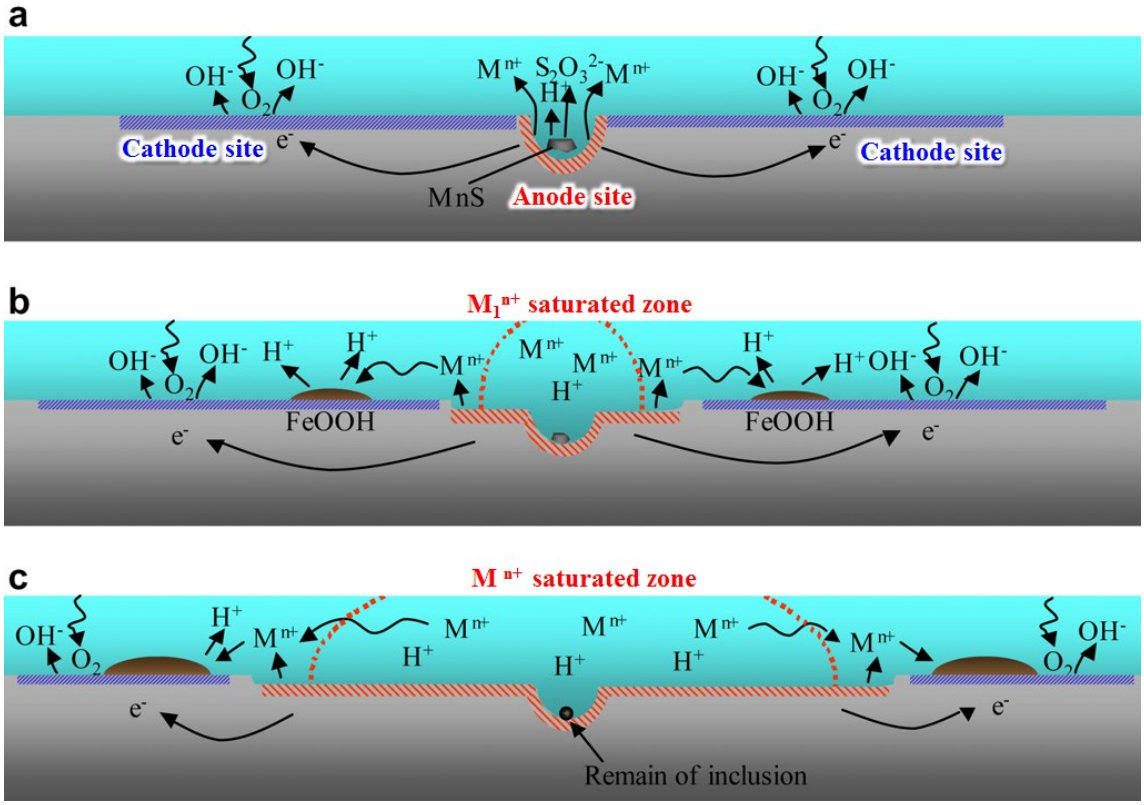

Figure 2-15 Schematic drawing of pit initiation and growth under atmospheric conditions [4].

The pit morphology under atmospheric conditions was investigated by several researchers [4, 6, 8, 18, 21]. Tsutsumi et al. [4] investigated the pitting corrosion of Type 304 stainless steel under droplets of $MgCl_2$ solution for a certain time in controlled relative humidity and at fixed temperature. They reported the formation of a shallow type pit with always at least one small hole (~10-30 μm diameter) in the centre of the corroded area (Figure 2-16), which proposed to be the remnant of a MnS inclusion dissolved out. Consistent with the work of Tsutsumi, Hastuty et al. [8] also reported the shallow type pit morphology using a similar method to characterise the atmospheric pitting corrosion of 430 stainless steel.

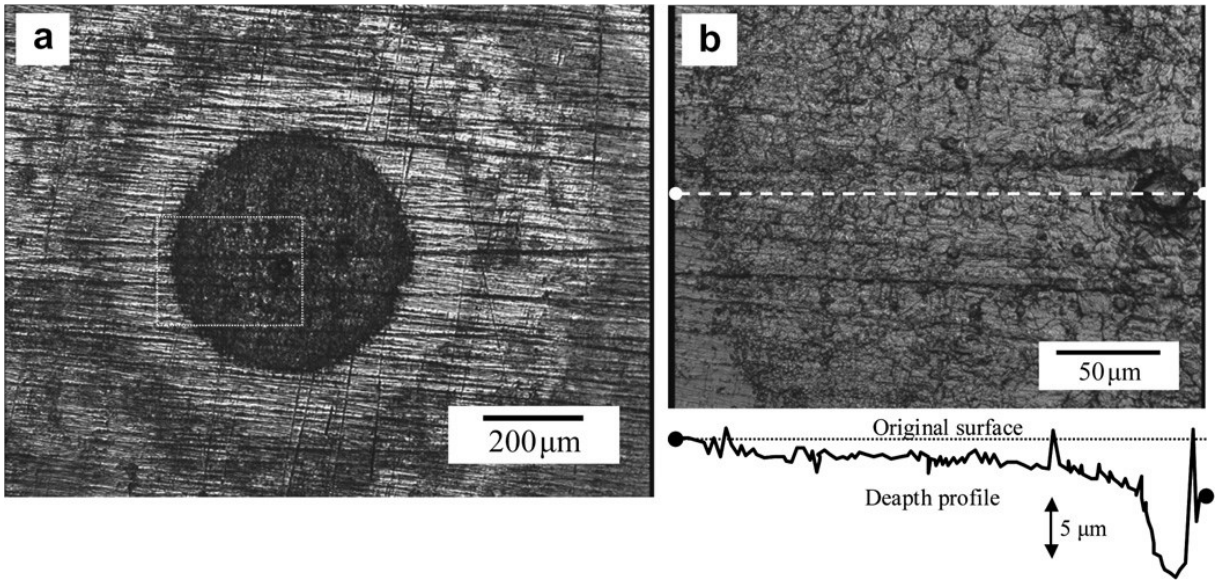

Figure 2-16 Laser-microphotograph and depth profile of pitting corrosion under a $MgCl_2$ droplet of 12 mm diameter 1.9 µm thickness exposed at 35% RH [4].

Maier and Frankel [21] also reported a shallow dish pit morphology while investigating the pitting corrosion of 304 stainless steel under electrolyte droplets of $MgCl_2$ using a Scanning Kelvin Probe (SKP). All of the above mentioned researchers proposed the formation of a shallow dish pit type with a small hole in the centre of the pit which assumed to be the initiation site. The shallow dish was found to propagate in the lateral direction at the early stage of initial attack. However, Maier and Frankel [21] further reported that after a certain time the pit stopped growing in the lateral direction but continued to propagate inside the shallow dish in a specific region leading formation of an “ear-shaped” pit as shown in Figure 2-17. The active region was considered to be the white dashed region of the pit as shown in Figure 2-17.

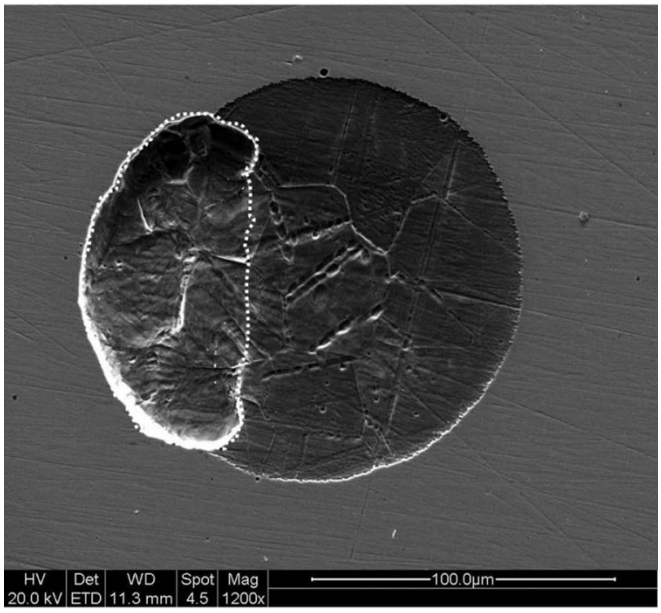

Figure 2-17 Ear-shaped pit formed on 304 stainless steel under MgCl2 droplet in atmospheric conditions[21].

Recently, Street et al. [6] observed a similar morphology under $MgCl_2$ droplet on 304L stainless steel. They named it as “spiral pit”. More details about this morphology and other morphologies obtained by Street will be given in Section 2.10.2.

Under atmospheric conditions, regularly etched pits were not observed on solution annealed 304L and 316L austenitic stainless steels.

2.10.2 Effect of RH

Among the exposure environmental factors, RH is very important because it determines the concentration of the solution droplets and/or electrolyte layers. As the RH is decreased, the chloride concentration in the solution droplet increases, increasing the probability of occurrence of pitting corrosion [4].

Figure 2-18 shows the relationship between the solution concentration (M) of $MgCl_2$ and (a) RH (%), (b) electrical conductivity ($mhom^{-1}$), and (c) self-diffusivity of Fe^{2+} ($m^2\ s^{-1}$) in $MgCl_2$ solutions at 30 °C, calculated by OLI Analyzer 9, shown in Street's work [6]. If RH is lower, droplet height is lower, solution concentration is higher, resistivity is high and the rate of diffusion of $[Fe^{2+}]$ is lower.

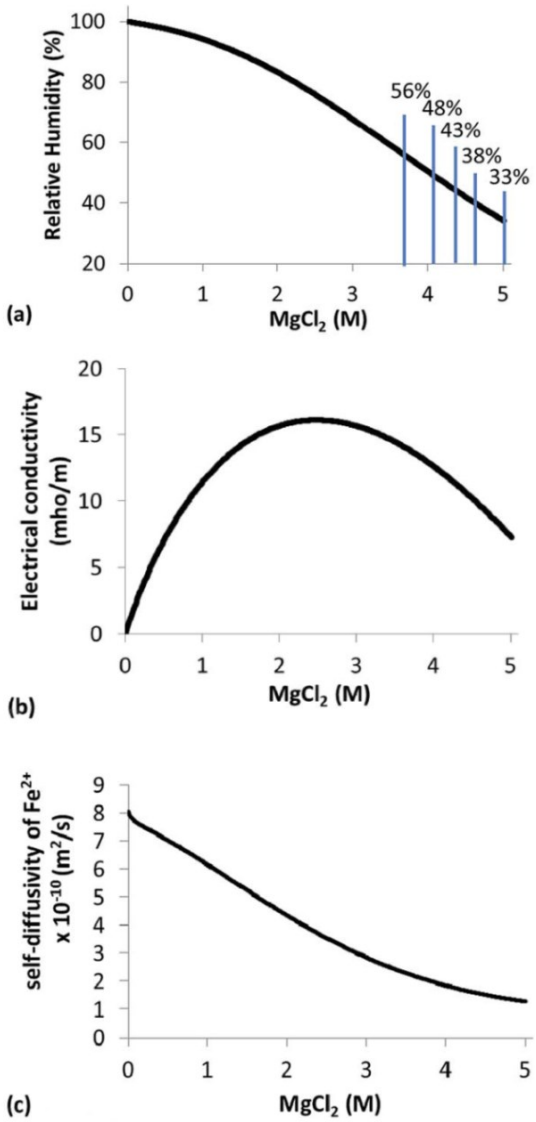

Figure 2-18 Relationship between the solution concentration (M) of $MgCl_2$ and (a) RH (%); (b) electrical conductivity ($mhom^{-1}$); and (c) self-diffusivity of Fe^{2+} ($m^2\ s^{-1}$) in $MgCl_2$ solutions at 30 °C. OLI Analyzer 9 used to calculate these parameters. Humidities investigated in Street's work are marked in (a) [6].

A number of studies were carried out to investigate the critical RH for pit initiation either by simply droplet deposition technique [4, 5] or by monitoring the potential or current [21, 141, 142].

Tsutsumi et al. [4] investigated the probability of pitting corrosion of 304 stainless steel beneath $MgCl_2$ droplets in lab and reported that the critical relative humidity for occurrence of pitting corrosion lies between 65% RH and 75% RH.

The critical RH for pit initiation was found to be related with the surface finish of the material. The finer the surface finish, the lower the critical RH. For a study of 304 stainless steel with surface finish of 1000 grit carried out by Tsutsumi et al. [141], the critical RH for pit initiation was found to be ~70% RH at 300 K. While, with a surface finish of 2000 grit for 304 stainless steel, Nishikata et al. [142] found that the critical chloride concentration for pit initiation was 7.5 M (corresponding to 55% RH) at 300 K using a similar experimental method used by Tsutsumi. In a recent work, by Nishikata's group [9], on 304 stainless steel with final polish surface (0.25 μm diamond suspension), the critical RH was found to be within the range of 47%-58% RH and the critical chloride concentration $[CL^-]_{pit}$ for onset of pitting of 304 stainless steel under $MgCl_2$ droplets was in the range of 7.1to 8.4 M at 298 K. The critical chloride concentration for onset of pitting has been reported by some other researchers [4, 9, 143, 144] . In a work by Matsumi et al. [143] an electrochemical method was used to record the corrosion potential beneath an electrolyte layer on 304 stainless steel. They reported that there is a threshold chloride concentration of ~6 M below which pits cannot initiate.

Cyclic RH fluctuation experiments were conducted by a number of researchers [7-14]. In such experiments, it is widely accepted that pits will repassivate during wetting stage (from low RH to high RH), while during the drying stage (from high RH to low RH) new pits can initiate and grow. Recently Nam et al. [9] have investigated pit initiation and repassivation of two types of stainless steels, austenitic (SS304) and ferritic (SS430) stainless steels during the wet-dry cycles beneath $MgCl_2$ droplets. They reported that at 298 K, for SS304, the RH_{pit} was obtained to be in the range of 58%–47% while that for SS430 was obtained to be in the range of 68%–48%. They also reported that both RH_{pit} and RH_{rep} vary with varying temperature. Significant increase in both of them was obtained as the temperature increased from 283 K to 313 K.

Chen et al. [10] reported that more meta-stable pitting occurred on the surface of mild steel samples in the wet cycles than that in the dry cycles. Also, the metastable pits were uniformly dispersed in wet cycles while locally distributed in dry cycles. Hastuty et al. [8] investigated the pitting corrosion of 430 stainless steel in drying process of chloride solution layer and concluded that pitting corrosion take place at higher chloride concentration as the drying rate increases.

Yadav et al. [11] investigated the corrosion behaviour of galvanized steel under wet–dry cyclic conditions at different drying periods using electrochemical impedance technique and reported that the corrosion is accelerated in the early stage of cycling but decreased after a number of cycles, returning to a similar rate as that found in the initial cycle.

RH was found to influence the pit morphology. Street et al. [6] have investigated the effect of RH on pit morphology and reported that at lower exposure RH values (33% and 38%) satellite pits can form (Figure 2-19(a, b)), while at higher RH values (38%- 48%), spiral pits can form (Figure 2-19(c-d)). Both these pit morphologies had a shallow dish region. Satellite pits were seen to be located toward the edge of the droplet while spiral pits were seen to be located toward the centre of the droplet. At 56% RH, However, pits were seen to have a circular morphology with no shallow dish region (Figure 2-19(f)). It was proposed that this variation in pit morphology is due to the difference in IR drop, solution diffusivity and conductivity. Street et al. [6] also reported that the diameter of the shallow dish region varies with the distance from the droplet edge, with larger diameters seen towards the centre of the droplet while smaller diameters seen towards the edge of the droplet (Figure 2-20). No significant variation in the average shallow dish diameters was observed at examined RH values (Figure 2-20).

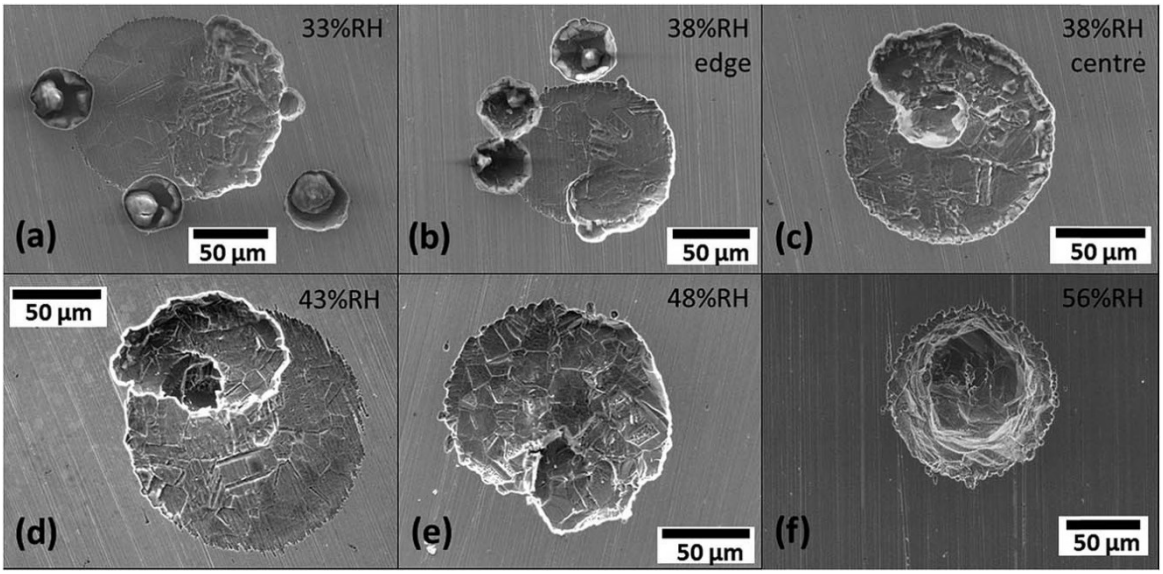

Figure 2-19 Typical examples of pit morphologies grown beneath $MgCl_2$ droplets with initial chloride deposition density (CDD) of 750 µg/cm^2 after exposure at constants RH values, shown in the figure, for 1 day at 30 ºC; (a) and (b) satellite pits; (b-d) spiral pits; (f) circular pit [6].

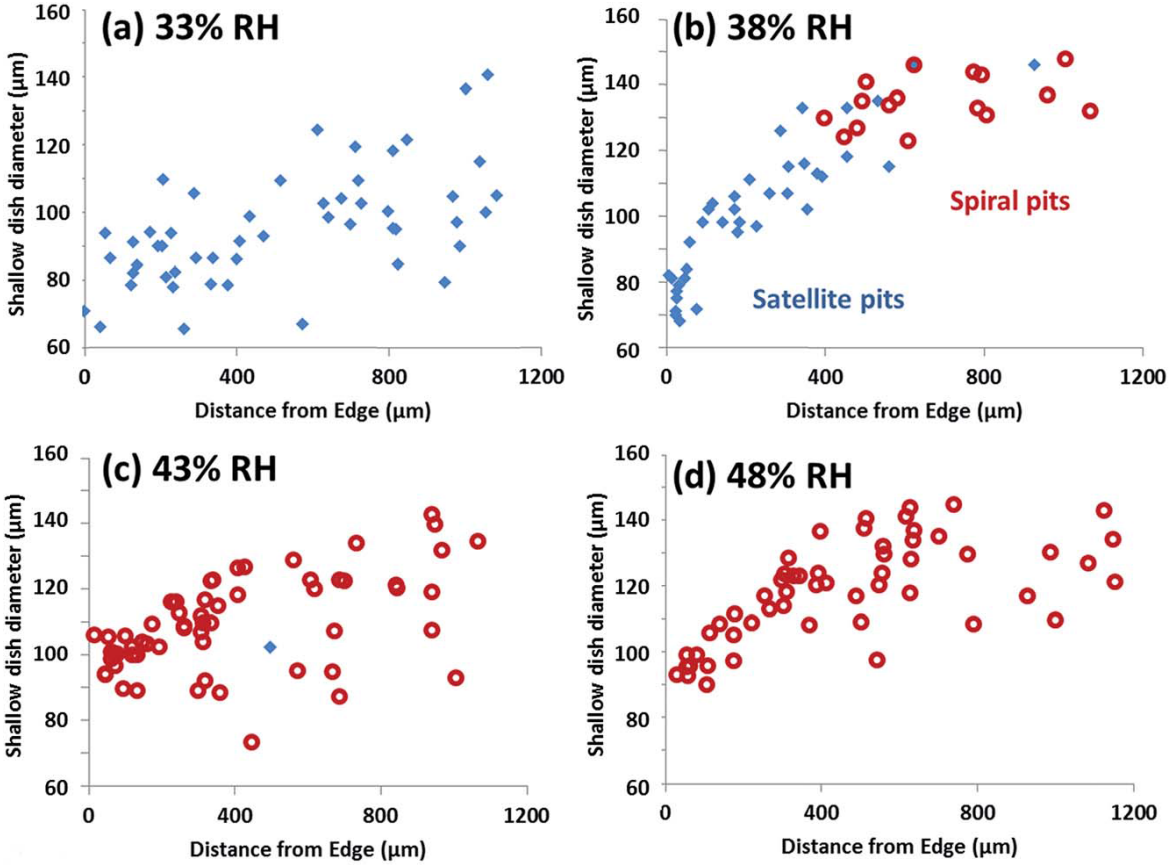

Figure 2-20 Shallow dish equivalent diameter versus the distance from the droplet edge for pits grown under $MgCl_2$ droplets with initial chloride deposition density of 750 µg/cm^2 on 304L stainless steel after 1 day of exposure at 30 °C [6].

2.10.3 Effect of Chloride Deposition Density (CDD)

For a fixed droplet area and at controlled exposure RH, any change in the salt deposition level will lead to a change in the height of the droplet because the salt concentration of the droplet is determined by the exposure RH. As a result of that both the diffusion rate and resistance of the droplet can be different.

It has been reported that the electrolyte layer morphology can be affected by the salt deposition density [18-20] under fixed exposure RH. Figure 2-21 are vertical sections of X-ray tomograms of $MgCl_2$ electrolyte layer morphologies as a function of CDD (indicated in Figure **2-21**) on 304 stainless steel pin samples after exposure at fixed RH (45%) and 21±1°C, shown in Mi's work [18]. She reported the formation of a non-uniform (discontinuous) electrolyte layer beneath $MgCl_2$ droplets of ≤100 μg/cm^2, while at higher deposition levels (400–4000 μg/cm^2), a uniform continuous layer was confirmed. The estimated solution height from Mi's X-ray microtomography experiments shows that the electrolyte layer height is increasing with increasing the salt deposition density at fixed RH and temperature (Figure 2-21).The estimated electrolyte height for 4000, 2000, 1000, and 400 μg/cm^2 was 260, 120, 60, and 25 μm respectively. For the lower depositing values (10, 20 and 100 μg/cm^2), the electrolyte layers were difficult to be measured because it was not clearly seen. For pitting corrosion to take place, Mi found that a lower chloride deposition density within the range of 10-20 μg/cm^2 is required for pit initiation.

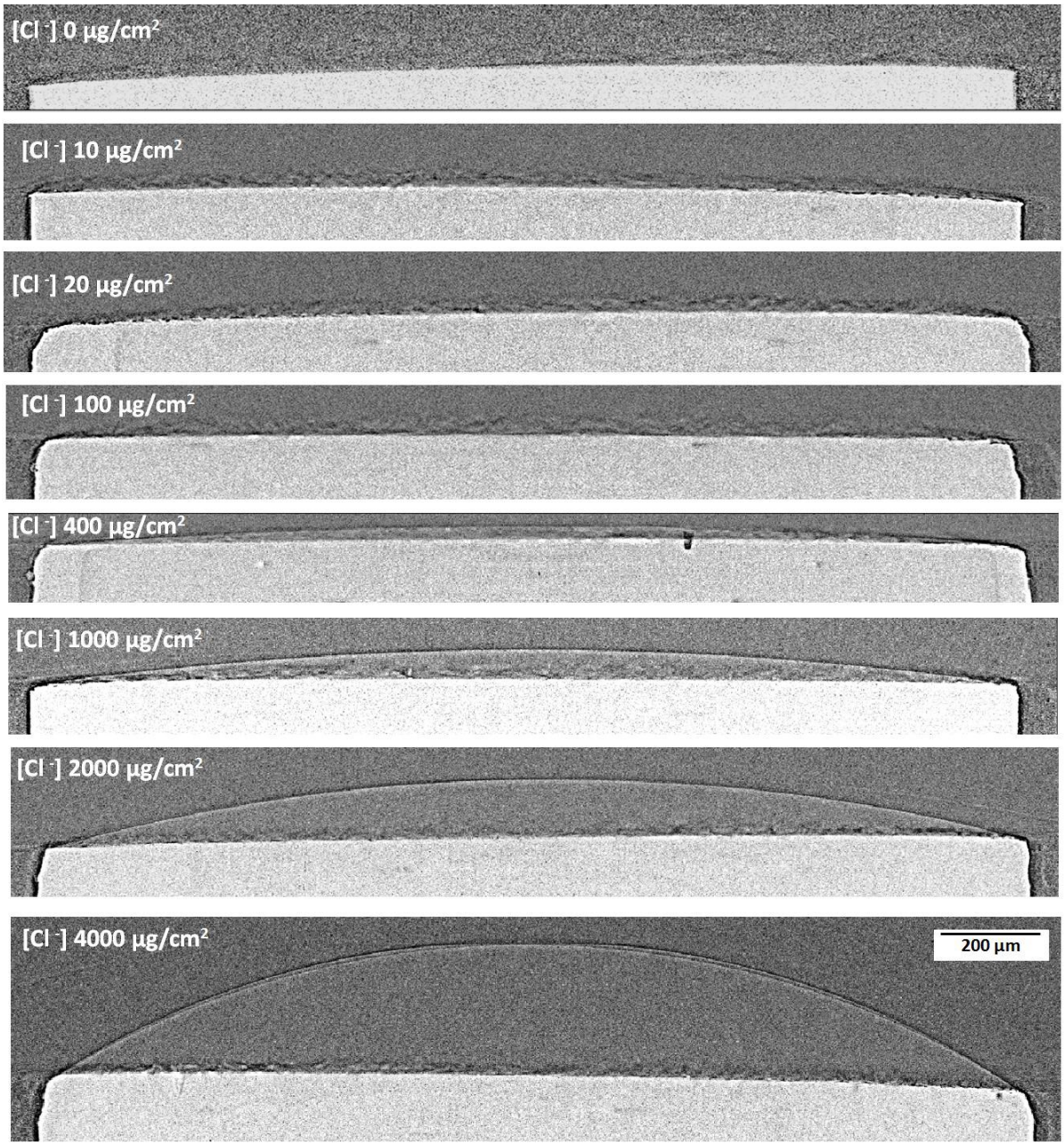

Figure 2-21 Vertical tomography sections of $MgCl_2$ salt solution morphologies as a function of CDD on 304 stainless steel (2 mm pins) at 21±1 °C and 45% RH [18].

Albores-Silva et al. [19] also reported that the continuity of the droplet was interrupted at lower CDD values. They have seen the formation of ring-like droplet morphology (Figure 2-22) under $MgCl_2$ solution with a CDD of 10 µg/cm^2 up to 50 µg/cm^2 on 316L stainless steel after exposure for 12 weeks. It was

proposed that the interruption of film continuity was due to the droplet shrinking while reaching equilibrium. Albores-Silva further reported that they observed superficial pitting within the range of 10-25 µg/cm^2 at 30 °C.

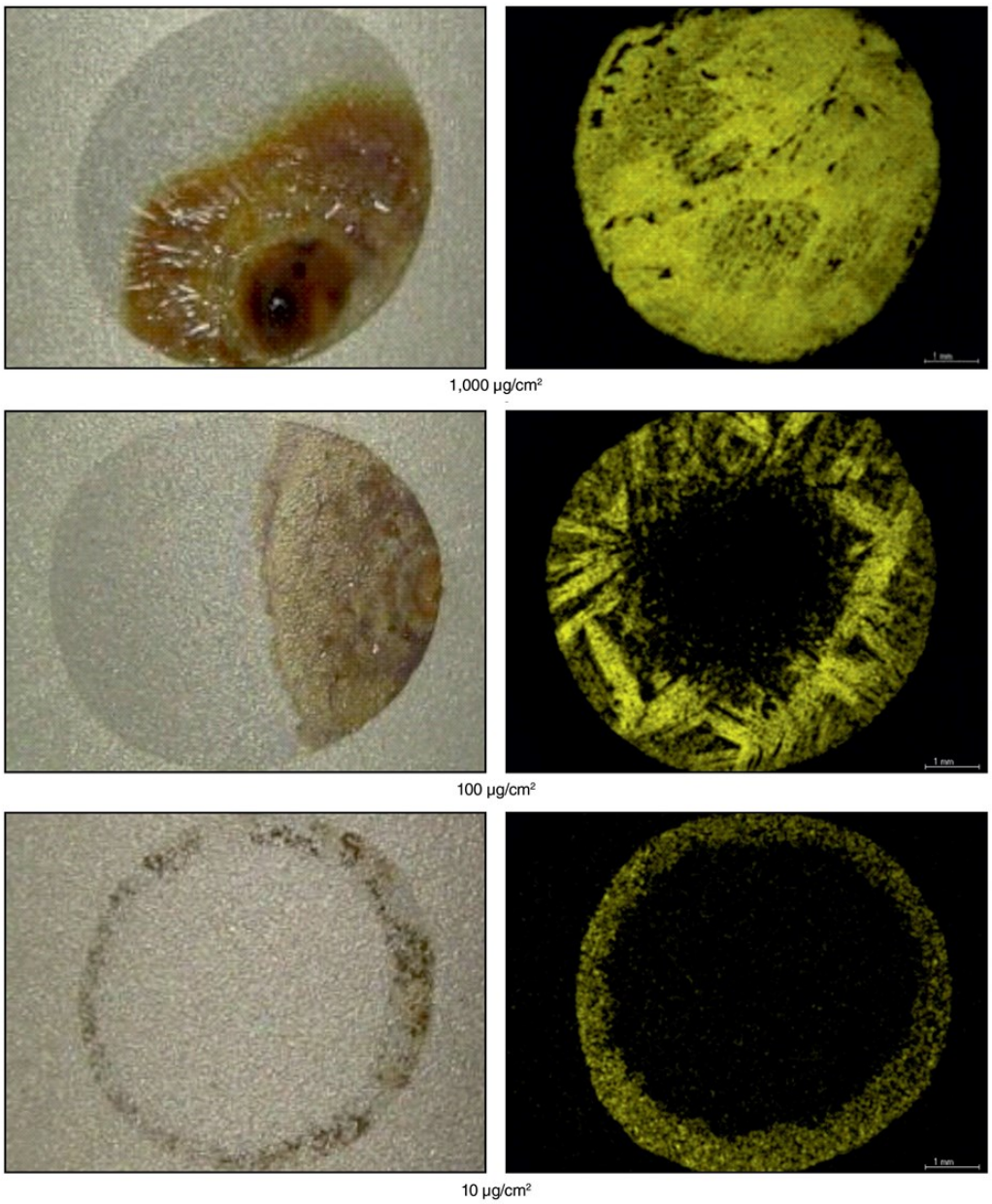

Figure 2-22 General appearance of $MgCl_2$ droplets with a CDD of 1000, 100, and 10 µg/cm^2 on 316L stainless steel following exposure for 12 weeks (left) and chlorine EDX elemental mapping after equilibrium was reached (right) [20].

The chloride threshold issue is very important as, in the presence of stresses, pits can develop atmospheric-induced chloride stress corrosion cracking (AISCC) [15, 19, 20, 145]. Albores-Silva et al. [19] and Padovani et al. [20] have reported that the lower threshold for the occurrence of AISCC is above 10 and 25 μg/cm^2 at 50 and 30 °C respectively at ~30% RH under $MgCl_2$ droplets on 316L stainless steel. Figure **2-23** shows the chloride deposition density and the temperature needed for the AISCC to take place under $MgCl_2$ droplets on 316L stainless steel at ~30% RH [20].

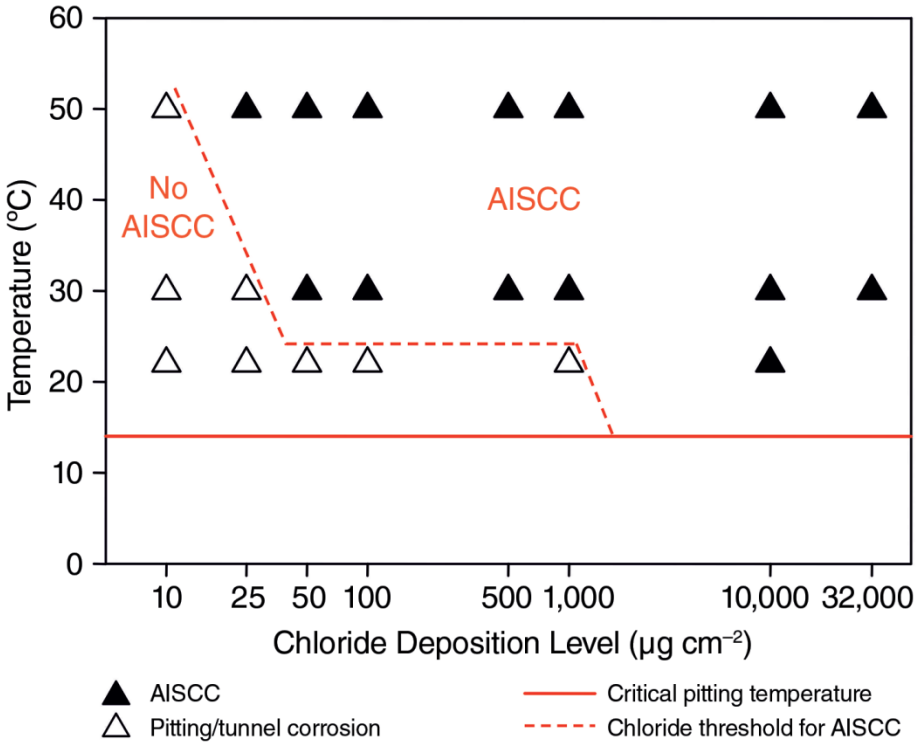

Figure 2-23 The influence of temperature and the chloride deposition density on the occurrence of AISCC on 316L stainless steel under MgCl2 droplets at ~30% RH. Tests carried out at 30 °C and 50 °C were exposed for 12 weeks while the exposure time for tests performed at room temperature (22 °C) was 52 weeks.

Padovani et al. [20] further reported that at higher RH (60% RH), there was need to higher chloride deposition densities for AISCC to take place at 50 °C,

while at 30 °C, AISCC was not seen up to very high CDD values (>10,000 μg/cm^2).

2.10.4 Effect of droplet Size

Maier and Frankel [21] reported that under small droplets, pits initiated more rapidly than under large ones in 33-34%RH due to faster evaporation rate and high increase in the chloride concentration of the droplet. A large droplet, however, can include more pitting initiation sites such as MnS inclusions. Therefore, Maier and Frankel found that the probability of occurrence of pitting corrosion was higher under a large droplet than under a small droplet at lower chloride concentrations (high RH). They attributed this to the presence of more susceptible defects within a large droplet than in a small droplet. Tsutsumi et al. [4] concluded that the probability of occurrence of pitting corrosion decreased with decreasing droplet diameter and thickness, which was attributed to the fact that the smaller exposed area can provide a less cathodic current. Similarly, Wang et al. [23] found that as the droplet size increases the susceptibility of stainless steel to localised corrosion increase as well. They suggested that the increase of cathodic area and the three-phase boundary could be the reason of this trend. Also, Mi et al. [22] found that the pit diameter increases with increasing droplet diameter under constant RH. They attributed this to the lower solution resistance for thicker droplets.

2.10.5 Effect of salt composition

Near coastal areas the atmospheric environments contain relatively high levels of chloride. However, in such environments NaCl (75% DRH) is the major chloride component while $MgCl_2$ is present in lower amounts. However, $MgCl_2$

has a lower deliquescence point (33% DRH) [130] so at relatively low relative humidity, droplets remain with a higher chloride concentration, and present conditions for electrochemical attack. Studies carried out so far about atmospheric corrosion of stainless steels have examined the influence of pure $MgCl_2$ [4, 5, 15, 21, 139, 146] pure NaCl [15, 23, 129, 146, 147] and artificial sea water [4, 5]. Just recently, however, Guo [7] investigate the effect of mixed salts droplets, containing of NaCl and $MgCl_2$, on localized corrosion behaviour of stainless steel. Therefore, there is need for more investigation to be carried out using mixed salts.

Prosek and his co-workers [15] studied the corrosion resistance of eight stainless steel grades, including type 304 and 316L, under manually deposited salt solutions of pure $MgCl_2$, $CaCl_2$, and NaCl as a function of temperature (20-50˚C) and RH (15-70%). They reported that both 304 and 316L were prone to pitting in the presence of $MgCl_2$ and $CaCl_2$ at 20˚C and higher and at relative humidity of 30% and 50% while at low ~15% RH and 30˚C they were susceptible to SCC. However, no pits where observed under pure NaCl at 40˚C and at 30, 50, or 70% RH.

Tsutsumi et al. [144] monitored the occurrence of pitting corrosion of stainless steels samples in both marine and rural atmospheric environments and concluded that pitting corrosion on 304 stainless steel only occur under a relative humidity range from 35% to 75% in marine environments. In a later study by Tsutsumi et al. [4], they studied the probability for pitting corrosion to occur on 304 stainless steel under $MgCl_2$ droplets in lab and reported that the critical relative humidity for occurrence of pitting corrosion lies between 55% RH

and 75% RH corresponding to (8.5 M) and (4.9 M) chloride solution respectively. This range is in agreement with exposure experiments carried out in marine aerosol conditions [144].

2.10.6 Effect of microstructure

As mentioned previously, the presence of small amount of retained delta ferrite in austenitic stainless steels can significantly influence pitting corrosion. In a recent work published by Davenport et al. [26] on 304L stainless steel plate, the morphology of atmospheric corrosion pits was found to be influenced by the presence of retained delta ferrite, with the formation of circular layered pit morphology on top surface of the plate and horizontal stripes on the end grain and side grain of the plate. This layered morphology was attributed to the preferential attack of ferrite phase.

In addition to residual delta ferrite, it is well agreed that pits in stainless steels often initiate at inclusions under atmospheric conditions [4-6, 21]. It has been reported that elongated inclusions play an important role in pit initiation and propagation in austenitic stainless steels [7, 18]. Figure 2-24, from Mi's work, shows the growth of a pit with time on 304 stainless steel beneath a $MgCl_2$ droplet. After 3 hours of exposure at constant RH and temperature, there is no sign of pits, however, only a pre-existing defect parallel to the rolling direction. After 17 hours, a pit was found at the site of the defect. The pit was found to grow both radially and vertically with time. It was proposed that the propagation of the pit down bottom was due to the pre-existing defect (probably a narrow cavity formed during fabrication of material or an elongated inclusion).

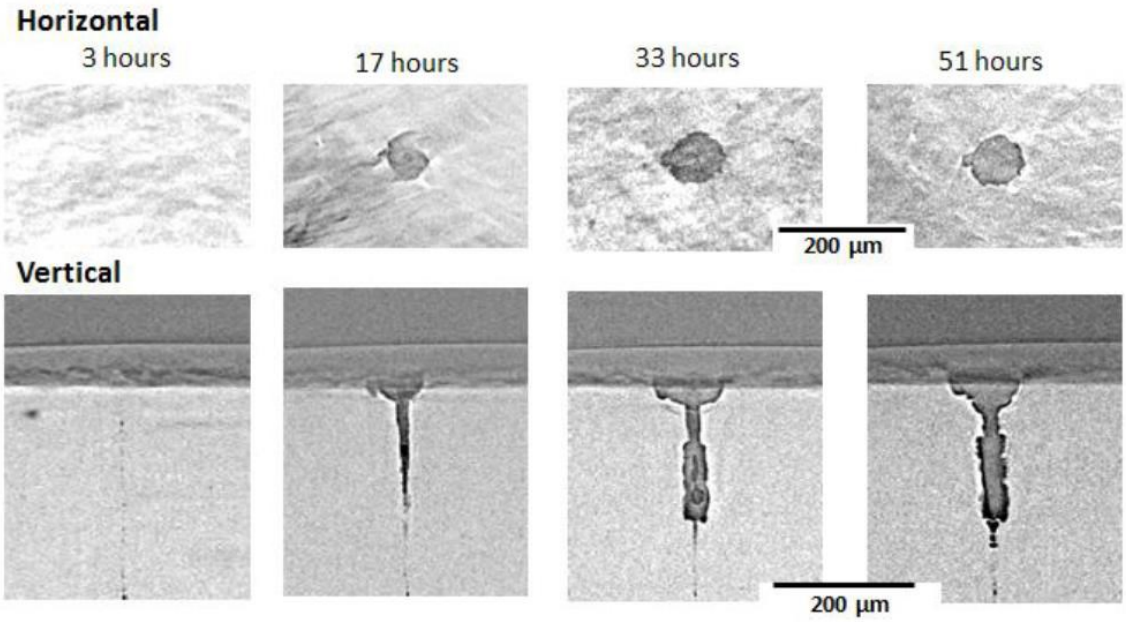

Figure 2-24 Time-dependent pit growth imaged with X-ray microtomography of a pit on 304 stainless steel pin (2 mm diameter) beneath a droplet of $MgCl_2$ of CDD ~1000 µg/cm^2 after exposure at 45% RH and 21±1 °C; top images are horizontal sections and bottom images are vertical sections [18].

Similarly, Guo [7] found an elongated deep fissure growing together with the pit (Figure 2-25) on a 304L stainless steel pin sample machined parallel to the rolling direction while studying the effect of wet-dry cycling on pitting corrosion under $MgCl_2$ droplets using X-ray microtomography technique. It was proposed that the deep fissure attack was because of the presence of elongated inclusions or ferrite bands in the alloy. It is important to bear in mind that the plate used in Guo's work and the current work is from the same supplier.

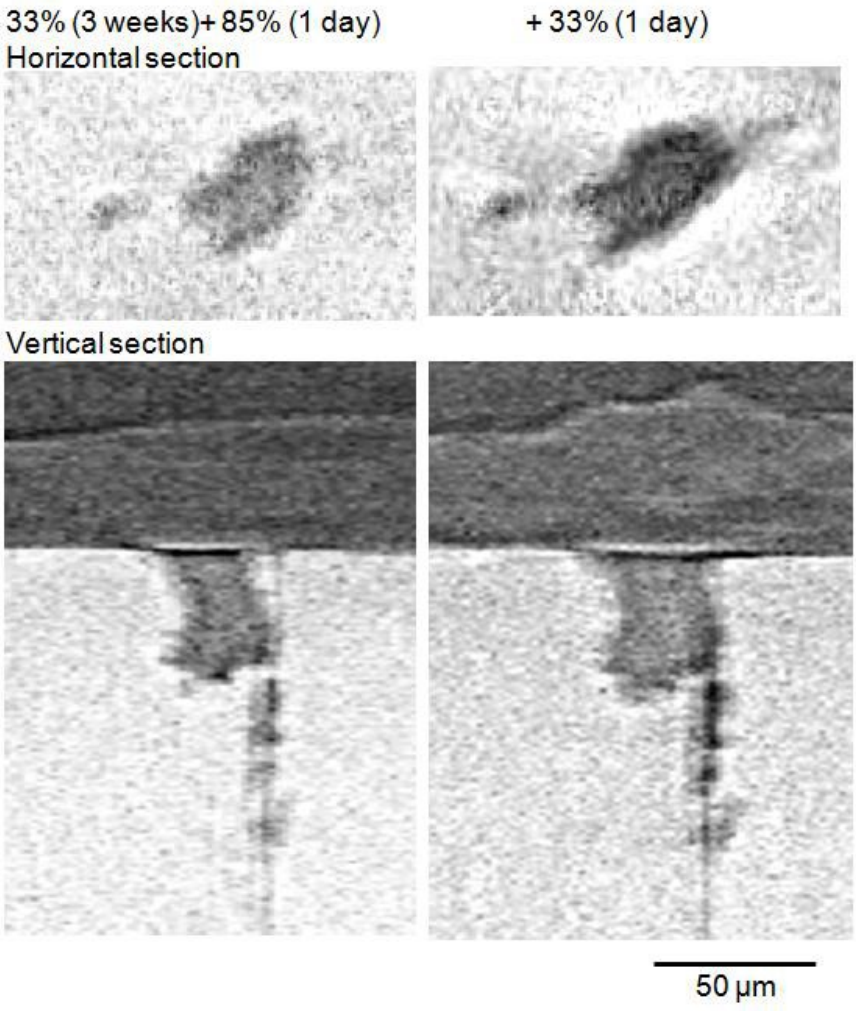

Figure 2-25 Horizontal and vertical sections of a tomogram of a 304L stainless steel pin sample beneath an $MgCl_2$ droplet (CDD ~1000 µg/cm^2) after wet-dry cycling exposure at 21±1 ºC. Cyclic exposure conditions are indicated in the figure [7].

2.11 Methods of deposition of salts for lab-based atmospheric corrosion experiments

In the literature, both indoor and outdoor exposure tests were carried out to study atmospheric pitting corrosion. In outdoor experiments, samples usually can be placed at specialized positions to be exposed to marine environments for a period of time [132, 133]. Aerosols salt particles present in the

environment can deposit on the sample surfaces and then leads to atmospheric pitting corrosion. However, in indoor lab experiments a controlled amount of concentrated solution of salts in shape of droplets [4-6, 15, 21, 22, 134-139] or salts particles [129, 148-152] can be deposited on the metal surfaces for investigations. Therefore, such experiments are more common in the literature.

2.11.1 Deposition of Salt Droplets

Droplets of aqueous salt solution can be deposited on samples by several methods:

(1) The use of a micropipette or a fine tube to deposit a controlled volume of salt solution of a known concentration to the metal surface. This method is the most common one in lab based experiments [4, 5, 18, 21, 136-138].

(2) Spraying of salt solutions on samples in a shielded environment. In this method the particle size, the distribution and the mass of salt can be controlled by controlling the spray nozzle dimensions, the spraying time, and the settling time (the time to keep the samples in the shielded environment after spraying) [153].

(3) Inkjet printing technique can be used to deposit patterns of salt solutions prior to atmospheric corrosion tests [22, 140].

(4) Recently a Multiprobe II liquid handling technique is used to deposit arrays of droplets on sample surfaces [6]. It uses a peristaltic pump to drive a high-precision hydraulic system for deposition of arrays of solutions down to 0.5 µl, particularly for applications in biosciences.

In the present study, it is shown that Multiprobe II liquid handling system can be used to deposit well-defined salt solution droplets of different size and concentrations on sample surfaces, allowing more systematic investigations of the influences of salt density and droplet diameter on atmospheric pitting corrosion.

2.11.2 Deposition of Salt Particles

Salt particles can be deposited on metal surfaces by several methods, such us using a probe for selecting salt particles with a chosen size then putting them on metal surfaces [148]; Dissolving the salt in ethanol then depositing drops of that solution on the sample surface and keeping them to dry out forming clusters of salt particles [150, 151, 154]; exposing the sample to a salt fog produced by an ultrasonic humidifier [129]. In the above methods the sample is kept in a humid environment in order to allow the salt crystals to deliquesce and form droplets.

In addition to droplet deposition methods, in the literature, a variety of electro-chemical techniques were also used to study atmospheric pitting corrosion in laboratory conditions such as Kelvin Probe (KP) [21, 155-159], Scanning Kelvin Probe Force Microscopy (SKPFM) e.g.[27, 28, 82], coplanar-electrode methods [13, 14, 141, 142, 146, 160, 161], Electrochemical Impedance Spectroscopy (EIS) measurements [13, 161].

2.12 Overview of conditions within intermediate level nuclear waste container stores

Figure 2-26 shows the air temperature and RH monitored in waste stores of intermediate level waste containers during two years. According to the atmospheric conditions, the RH was found to fluctuate between 30% and 90%, while the temperature changes between 0 and 50 °C [162] over a two year period.

Figure 2-27 is a collection of micrographs showing the appearance of different surfaces of prototype 304L stainless steel container after exposure to an inland, indoor atmosphere (Culham/Harwell warehouses) for ~10 years [163]. A higher degree of corrosion was observed on the container base (including welds) than on the other surfaces (centre images). However, very small pits observed on horizontal ledges of the container (right hand images) but extensive rusting was observed on areas of embedded iron or carbon steel (left hand images) [163].

Swab samples collected from different locations at the storages showed the presence of a variety of cations (e.g. calcium, potassium, and sodium) and anions (e.g. chloride, nitrate, and sulphate) [163]. The concentrations of such ions deposited onto the container surfaces were found to be a function of the surface orientation. For example, small amount of chloride ion was found on vertical and overhanging surfaces but a greatest amount of such ion was found on horizontal surfaces [162, 163].

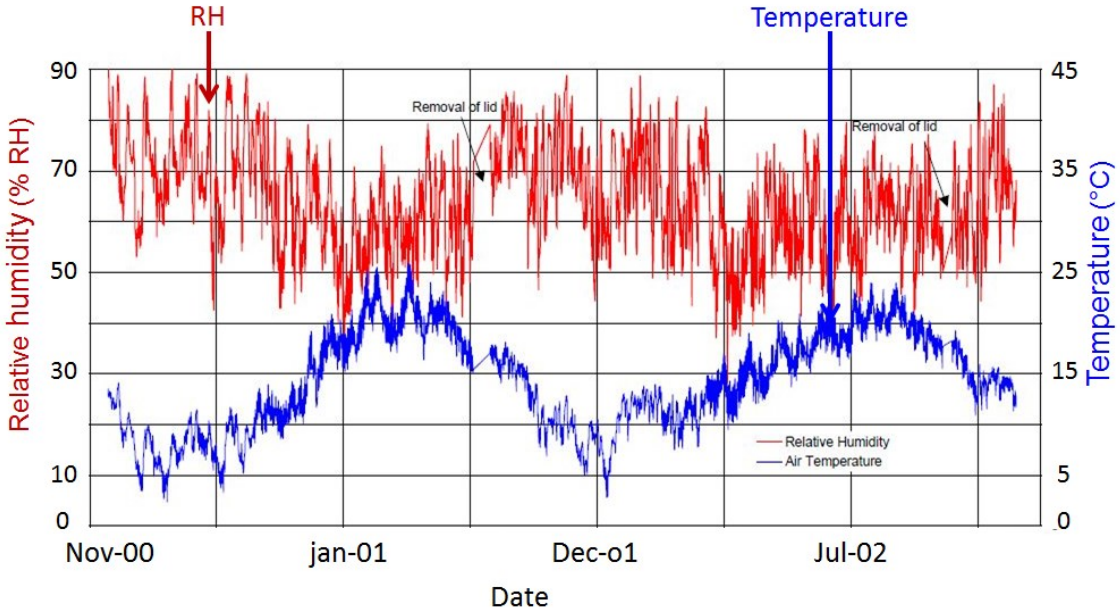

Figure 2-26 The external air RH and temperature observed in the 4 meter box program for two years (from Nov. 2000 to Nov. 2002) [162].

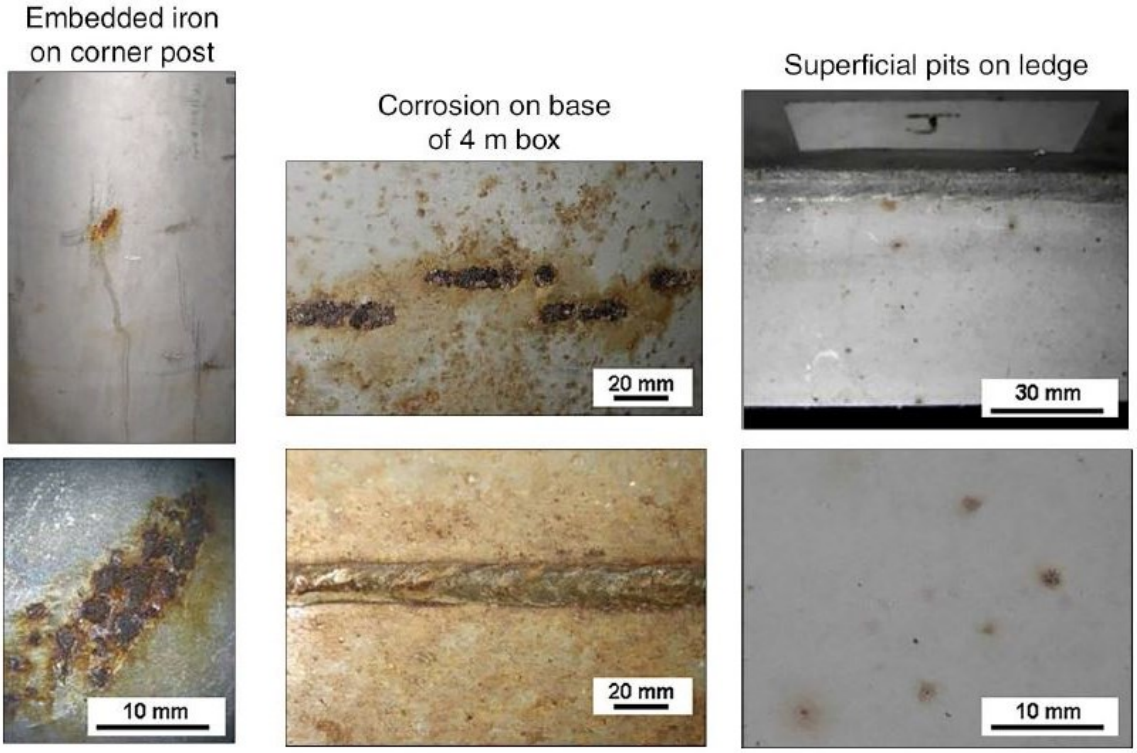

Figure 2-27 Condition of 304L prototype container after ~10 years of storage within an inland warehouse in Culham, UK. (left) region of embedded iron; (centre) bottom of container, which was exposed to road-salts during transport (CDD of some measurements >100 µg/cm^2); (right) horizontal ledge (CDD ~10 µg/cm^2)[163].

2.13 Secondary spreading and micro-droplet formation

One phenomenon of interest which can take place during the course of atmospheric corrosion is the secondary spreading and micro-droplets formation. Secondary spreading can be defined as the formation of an ultra-thin layer of moisture or concentrated region of micro-droplets around the edge of the primary droplet [164]. Micro-droplets are a precursor to the formation of secondary spreading region [164]. With time, the gradual merging of micro-droplets results in the formation of secondary spreading region. The phenomenon of micro-droplet formation is linked firmly to the atmospheric corrosion process [156, 165]. The secondary spreading and micro-droplet phenomena have been investigated for several materials including stainless steel and under different salts solutions including $MgCl_2$ by many researchers [136, 151, 156, 165, 166].

It has been reported that the main driving force for the formation of micro-droplets is the corrosion current established by the potential gradient between the centre of the main-droplet and its periphery [129, 151, 156]. Development of potential difference is probably because of the tendency of droplets to form an anodic region within the droplet and a cathodic region at the edge. The cathodic reaction takes place at the edge of the droplet due to differential aeration, with easy access of oxygen at edge compared to the droplet centre. Oxygen reduction reactions result in increase in pH due to generation of OH^-. The increase in negative charge draws in cations present in solution in order to preserve charge balance. The mechanism of micro-droplets formation has been

established for stainless steel [136, 156] and for aluminium [167, 168] under NaCl droplets.

According to both Zhang et al. [151] and Tsuru et al. [136], there are three steps for the formation of secondary spreading: firstly the formation of a thin “invisible” electrolyte layer that contains clusters of water molecules on active sites such as surface defects and protuberant sites. Secondly, such water clusters work as the reaction sites for the cathodic oxygen reduction reaction. Finally, migration of cations from the main droplet into peripheral region leads to the formation of micro-droplets. Figure 2-28 schematically shows these stages for a case of a main droplet of NaCl on a carbon steel sample [136, 151].

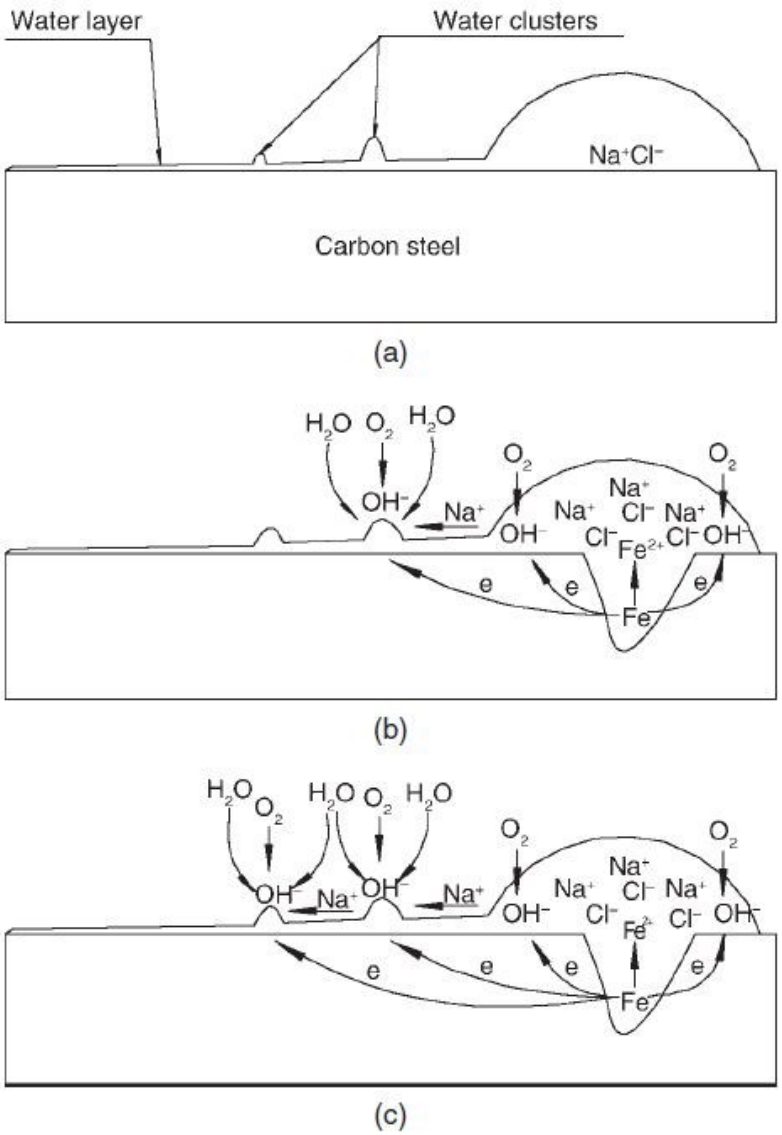

Figure 2-28 The mechanism of micro-droplets formation proposed by Zhang et al. [151]. The formation of micro-droplets was considered to take place in the following three main stages: (a) formation of a thin water film with clusters of water molecules; (b) synergistic action of the oxygen reduction and the water molecule adsorption; and (c) migration of cations and formation of micro-droplets.

There are various variables that influence formation of micro-droplets, such as oxygen, RH, different combinations of salts and alloys, cathodic polarization [136, 151, 156, 164-166, 169]. The effects of these variables showed that the formation of microdroplets is very linked to the atmospheric corrosion process.

In a study of AA2024 under NaCl droplets, du Plessis [164] observed extensive formation of micro–droplets and secondary spreading at 85% and 90%, while little spreading at 75% but no spreading for RHs lower than 75%. Tsuru et al. [136] reported that the secondary spreading area is greater at 90% RH than that at 65% RH beneath droplets of NaCl solutions deposited on carbon steel.

Both Tsuru et al. [136] and Zhang et al. [151] reported that secondary spreading and microdroplet formation cannot develop under $MgCl_2$ droplets on stainless steel. They suggested that the secondary separating might be blocked by the formation of relatively insoluble magnesium hydroxides $Mg(OH)_2$ at the edge of the main droplet.

For aluminium alloys, it has been shown that when a pit is formed at the edge of the main droplet, secondary spreading can take place close to the pit [166-168]. Morton and Frankel [167] studied the corrosion behaviour of AA7075-T6 under chloride droplets and compared it to that in bulk solutions. Figure 2-29 shows the corrosion of AA7075-T6 under a droplet with 0.03 mM Ce^{3+} ions in a 3.5 wt% NaCl solution after exposure for 20 hours at an equilibrium humidity of 85%. A secondary droplet can be seen at the left of the main droplet (Figure 2-29(b)). The SKP line-scan shows that the advancing edge of the secondary droplet was at highest potential relative to both the secondary droplet and the

remaining area of the main droplet, indicating this site and a wide area surrounding it acted as a cathodic region to support the attack. The area under the secondary droplet was at a lower potential relative to the entire main droplet, indicating the site of the “anodic half reaction” [167]. The area of the secondary droplet, marked as “1” in Figure 2-29, was covered with large amounts of corrosion products. A region of “elevated potential” relative to both the secondary droplet and the remaining area of the initial droplet was found between the secondary droplet and the arc of discoloration. The potential decreases as scan goes away from the secondary droplet to the main droplet, until reaching an “intermediate potential” far away from the secondary droplet [167].

Li et al. [168], found that secondary droplets formed close to a pit at the edge of the $MgCl_2$ solution droplets on Al–Mg–Si alloy exposed at 33% and 75% controlled relative humidity (RH) are associated with filiform-like attack. However, there have been no reports to date showing secondary droplets on stainless steels under $MgCl_2$ solution droplets.

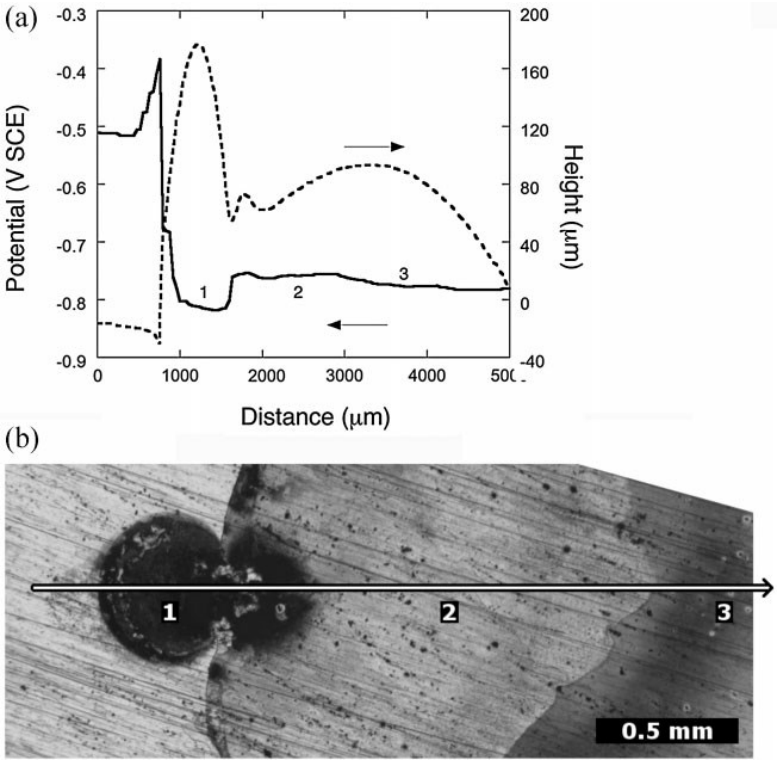

Figure 2-29 (a) Scanning Kelvin probe (SKP) line-scan profiles for potential and height of a droplet test with 0.03 mM cerous ions and 3.5 wt% NaCl after 20 hours of exposure at 85% RH by the use of open beakers of saturated KCl. (b) optical image of the droplet upon completion of the test. The arrow indicates the direction and location of the SKP line-scan. Corresponding sites (1, 2, and 3) are labelled numerically.

It has been reported that the secondary spreading area increases with increasing exposure time and their growth take place at the early stages of the exposure very rapidly with time [136, 156, 164, 166-168].

The shape of secondary spreading covering area was observed to be influenced by the superficial grinding marks. Both Bian et al. [166] and Zhang et al. [165] reported that the covering area of micro-droplets developed outwards in a semi-circle or oval shape. They linked this with the direction of the polishing marks.

2.14 Synchrotron X-ray Techniques

2.14.1 Principles of X-ray Tomography

Figure 2-30 shows the structure of a common synchrotron facility which generally consists of four main components: injection system (The electron gun and linear accelerator “linac”), the booster synchrotron ring, the storage ring and the beamlines [170]. The electron gun produces the electrons which then are accelerated up to very high speeds through three series of accelerators. First the electrons accelerate by a linear accelerator before entering into the booster ring. Electrons are accelerated again in the straight sections of the booster ring and then bent around the curved sections via bending magnets (electrons travel at nearly the speed of light at this stage). Thereafter, the electrons are released into the storage ring (to be accelerated for the third time) which is actually a polygon with bending magnets at the corners. Insertion devices found in third generation synchrotrons, allow electrons to be “wiggled” across of magnets with alternating poles. This causes electrons to change direction, giving of energy in the form of X-rays. Finally, the X-rays enter the beamline, where they are collimated and refined. The two types of X-ray source used for tomography are laboratory micro-focus X-ray tubes and synchrotron radiation [170-173]. Time dependent *in situ* experiments can be conducted using synchrotron radiation facilities because of the significantly high flux (resulting in a shorter acquisition time for the experiments) compared to laboratory micro-focus X-ray tubes.

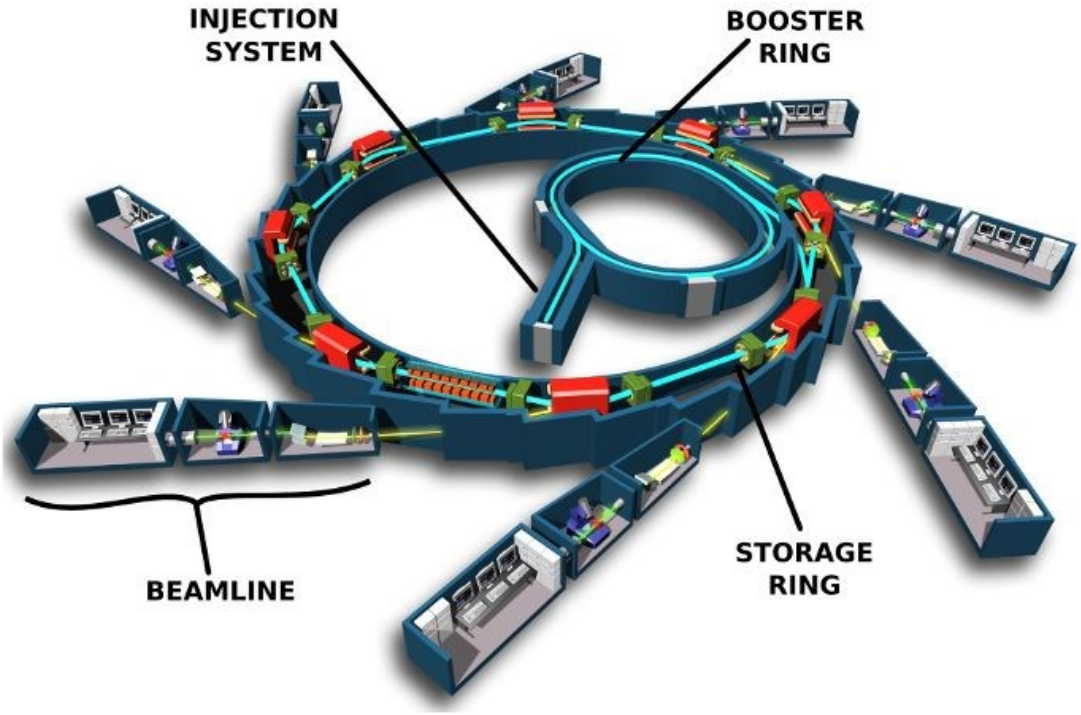

Figure 2-30 Schematic diagram of a synchrotron X-ray facility [174].

Figure 2-31 shows the setup of in situ synchrotron X-ray tomography. A series of radiographs is collected as the sample is rotated through 180°, and these are then reconstructed to give a 3D tomogram. For each radiograph, the intensity of the monochromatic X-ray beam is attenuated by absorption in the sample according to the electron density, which in turn is relates to mass density.

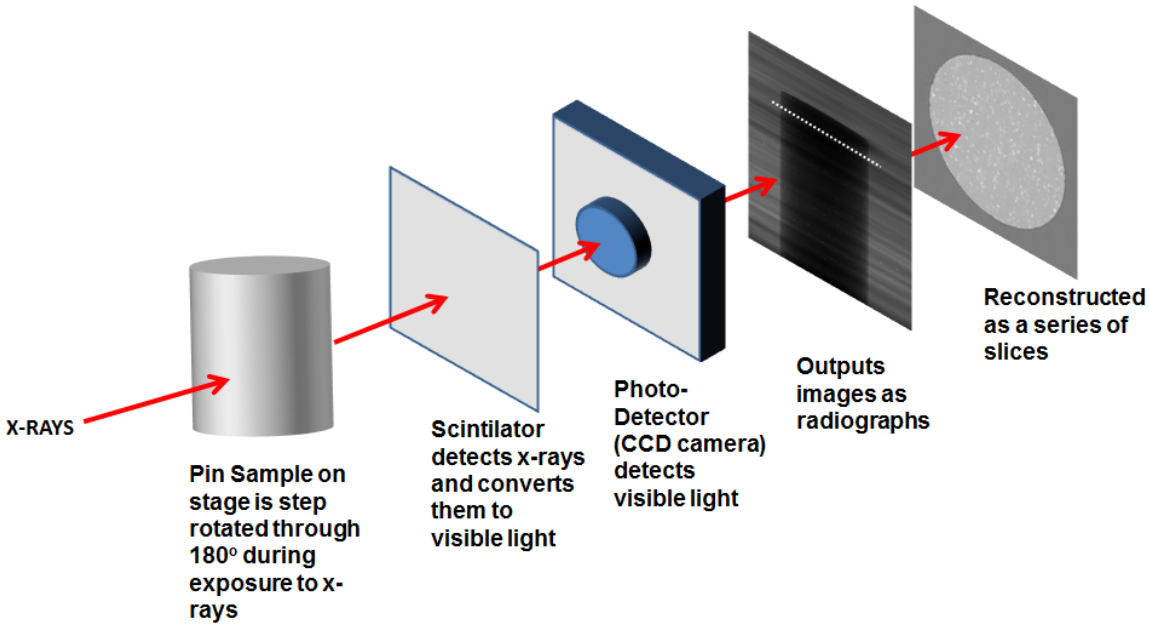

Figure 2-31 Schematic diagram illustrating data collection of a synchrotron X-ray microtomography experiments [164].

2.14.2 Use of X-ray Tomography in Corrosion Research

Synchrotron X-ray microtomography has been used to study the localised corrosion such us pitting corrosion and intergranular stress corrosion cracking on austenitic stainless steel [7, 18, 107, 175-177], aluminium [164, 178-180], magnesium [181] alloys. Synchrotron X-ray microtomography is a promising method to evaluate pitting corrosion in wet environment because it is a non-destructive technique for 3D analysis of microstructure and the resolution is on the micro-meter length scale [123, 175, 178-181]. For atmospheric corrosion studies on austenitic stainless steel, Ghahari [107, 175] investigated pitting corrosion using a capillary cell with electrochemical control on 304 stainless steel pin. Mi [18] studied the effect of chloride deposition density and time dependent pit growth on SS304 pin samples under $MgCl_2$ droplets. Guo [7]

performed *in situ* X-ray microtomographic tests to study the influence of RH fluctuations and the effect of mixed salts on SS304 stainless steel pins. She also monitored the pit growth with time on such samples. More recently, Burnett et al. [177] introduced the concept of “correlative tomography” which involve using multiple techniques together to study the same three dimensional (3D) region of interest which was hidden beneath the sample surface. In their work, they investigated the interaction between different forms of localised corrosion mechanisms, namely intergranular corrosion and pitting corrosion in the NaCl solution in austenitic stainless steel sample with solution annealed condition. They reported that intergranular corrosion can nucleate within a pit.

The effect of beam damage, however, has been reported by a number of researchers [7, 18, 182, 183]. Both Mi and Guo have reported that a greater number of pits were observed in tomography tests than that formed in lab-based tests.

2.15 Summary

Austenitic stainless steels are susceptible to atmospheric pitting corrosion due to deliquescence of salt particles on their surface. This is a concern in the long-term storage of nuclear waste in stainless steel containers. Although the mechanism of localised corrosion of stainless steel under full immersion conditions is extensively investigated, there has been relatively little work published on pitting corrosion of stainless steel under atmospheric conditions. Studies of atmospheric pitting corrosion of austenitic stainless steels carried out

so far have not been focusing on the effect of microstructure, especially the effect retained delta ferrite. Besides, none of the previous investigations have studied such effect on the three plate orientations. Therefore there was need to investigate the effect of delta ferrite on pit propagation on all plate planes. Lab-based experiments carried out to study such effect cannot show the undercut attack in 3D. Therefore, synchrotron X-ray microtomography was used for this purpose.

Since in realistic conditions the deposited salt particles (which can form different droplet sizes) may vary, it is essential to study a wide range of droplet diameters. Besides, as the final chloride concentration of the solution is governed by the exposure relative humidity. It is important to study a wide range of RH values and chloride concentrations to achieve a better understanding of the pitting behaviour under these conditions.

The phenomenon of secondary spreading and micro-droplets formation has already been investigated and reported by many researchers for several materials under different salts. However, the formation of micro-droplet on stainless steel under $MgCl_2$ droplets was not reported previously. In the present work, such micro-droplets were observed and briefly investigated using time-lapse imaging.

Robotic deposition technique is determined to be a suitable method to deposit arrays of droplets on stainless steel to study atmospheric corrosion.

3 Experimental Method

3.1 Materials

Austenitic stainless steel sheet of grades 304L and 316L was obtained from Aperam-France and Acerinox, respectively. The thickness of the 304L and 316L sheets was 3 mm and 6 mm, respectively. The alloys were cold-rolled, solution treated at 1040-1100 ºC followed by forced air cooling by the manufacturer and denoted as “as-received”. Table 3-1 shows the foundry specification of composition of the both materials as taken from the mill certificates (Appendix 1).

Table 3-1 Foundry specification of composition of the both alloys used in this study.

Element (wt%) / Material	Cr	Ni	Mn	S	Mo	C	Si	N	P	Fe
304L	18-19.5	8-10.5	2	0.015	-	0.03	0.75	0.1	0.045	Bal.
316L	16.5-18.5	10-13	2	0.015	2-2.5	0.03	1	0.11	0.045	Bal.

3.2 Solution annealing treatment

A solution annealing treatment was carried out for 304L stainless steel samples sealed in a silica glass tube that had been evacuated and backfilled with Ar gas. The samples were annealed for 1 hour at 1050±5 °C and water quenched.

3.3 Sample preparation for lab-based droplet experiments

304L sheet was cut using a Buehler Isomet 4000 SiC blade into 20-25 mm squares and mounted in bakelite. Pieces of plate were orientated to expose LT plane (top surface) and LS plane (side grain) and ST plane (end grain) surfaces (Figure **3-1**). For studies of effect of RH, droplet diameter, and CDD, samples were cut in larger sections. The 304L plate was cut into 25 mm x 70 mm samples and 316L plate was cut into 25 mm x 60 mm samples. The top surface of the plate was then ground using 800 grit SiC paper and then ultrasonically cleaned in deionised (DI) water (18 MΩ cm) for 10-15 minutes. An empty squeeze plastic bottle was used to blow air on samples to dry them. The samples were then kept in a covered container in ambient conditions for 24 hours to allow the passive film to thicken.

3.4 Sample preparation for synchrotron experiments

For synchrotron experiments, 2 mm pins were machined from the middle of the plate with their axis parallel to the rolling direction (Figure 3-1). Then pin samples were ground to 800 grit using SiC papers, washed with deionised (DI) water and methanol afterwards.

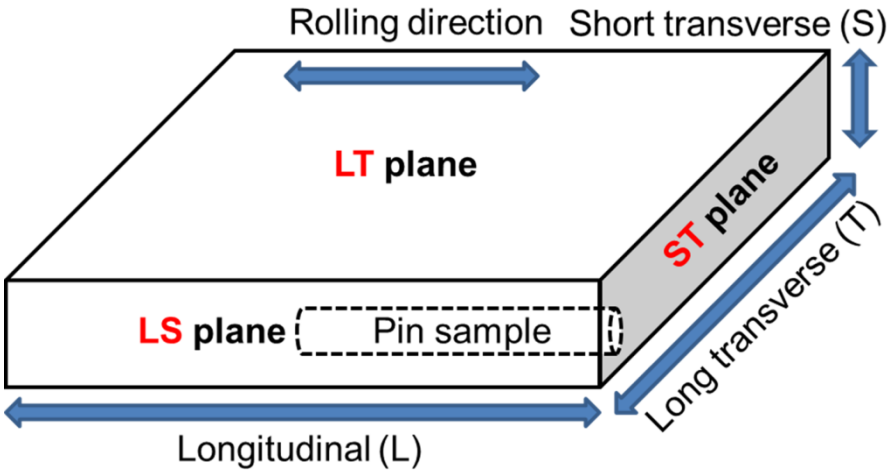

Figure 3-1 Plate planes and the orientation of machined pin samples with respect to the plate.

3.5 Microstructural characterisation

304L samples were ground and polished to a mirror finish using oxide polishing suspensions (OPS) (Struers) and etched with Kalling's 2 reagent (5 g $CuCl_2$, 100 ml HCl, 100 ml ethanol) for 5 s at lab temperature (~22 °C). SEM JEOL 6060, Phillips XL-30, and JEOL 7000 machines were used for pit and material characterisation. These machines were equipped with energy dispersive X-ray (EDX) systems and INCA analysis software for elemental analysis. EDX measurements were carried out using an accelerating voltage of 20.0 keV at 10 mm working distance. SEM micrographs were also taken at this working distance.

3.6 Ferrite detection and measurements

3.6.1 XRD

X-ray diffraction analysis was carried out on a Bruker D8- Advanced diffractometer using monochromatic CuKα radiation (λ = 1.54056 Å) with an

accelerating voltage of 40 kV and current 40 mA, angular range 20°-100°, to detect the presence of delta ferrite on the LT plane (top surface) of the base alloy of 304L stainless steel.

3.6.2 Vibrating Sample Magnetometer (VSM)

A Lakeshore Vibrating Sample Magnetometer (VSM) shown in Figure 3-2 was used to detect the presence of delta ferrite in the as-received and solution annealed 304L stainless steel alloy by measuring the magnetic hysteresis loop. Before the measurements, the VSM was calibrated with a standard sample of known saturation magnetization (a sphere of pure Ni). Each stainless steel sample was a ~3 mm cubes (~0.19 g) that was attached to the end of the sample rod that was fixed to vibrating unit.

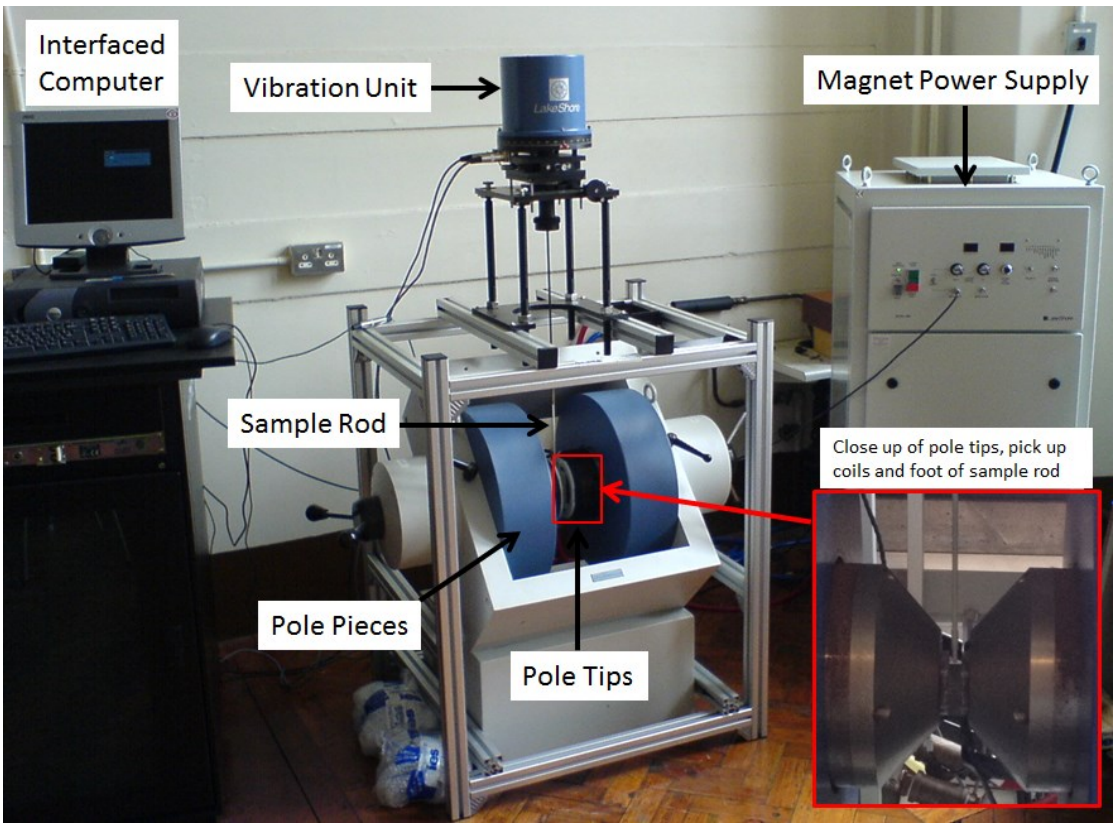

Figure 3-2 Lakeshore vibrating sample magnetometer and close up of pick up coils.

3.6.3 Electron backscatter diffraction (EBSD)

Samples for EBSD measurements were mounted in Bakelite and polished through successive grades of SiC paper to 4000 grit using the minimum polishing time at each grade. They were then successively polished using diamond suspensions: Diapro Dac3 (3 µm), DP-suspension A (1 µm) and colloidal silica suspension (0.25 µm) for 5 minutes each. EBSD was used to quantify crystallographic phases and grain sizes using an FEI Quanta 650 SEM connected with a Nordlys EBSD detector from Oxford Instruments with AZtec Version 2.2 acquisition software. An area of 150 x 131 μm^2 was scanned with an acquisition step size of 0.2 µm and with an accelerating voltage of 20 kV. The indexing rate was typically close to 99%. Data post processing was carried out with Oxford Instruments HKL Channel 5 software. The phase database used in this study (Table 3-2) was included in AZtec software. For successful phase identification at least eight Kikuchi bands were selected.

Table 3-2 Ferrite and austenite crystallographic geometry parameters for EBSD phase identification given by HKL database.

Phase	*a* (Å)	*b* (Å)	*c* (Å)	Alpha (α)	Beta (β)	Gamma (γ)	Space Group
Ferrite Iron bcc (old)	2.87	2.87	2.87	90°	90°	90°	229
Austenite Iron fcc	3.66	3.66	3.66	90°	90°	90°	225

The grain size distribution was determined by the mean linear intercept method using 50 lines in vertical and horizontal directions (excluding twin grain boundaries). The average grain size was found to be 9±6 µm (Figure 3-3).

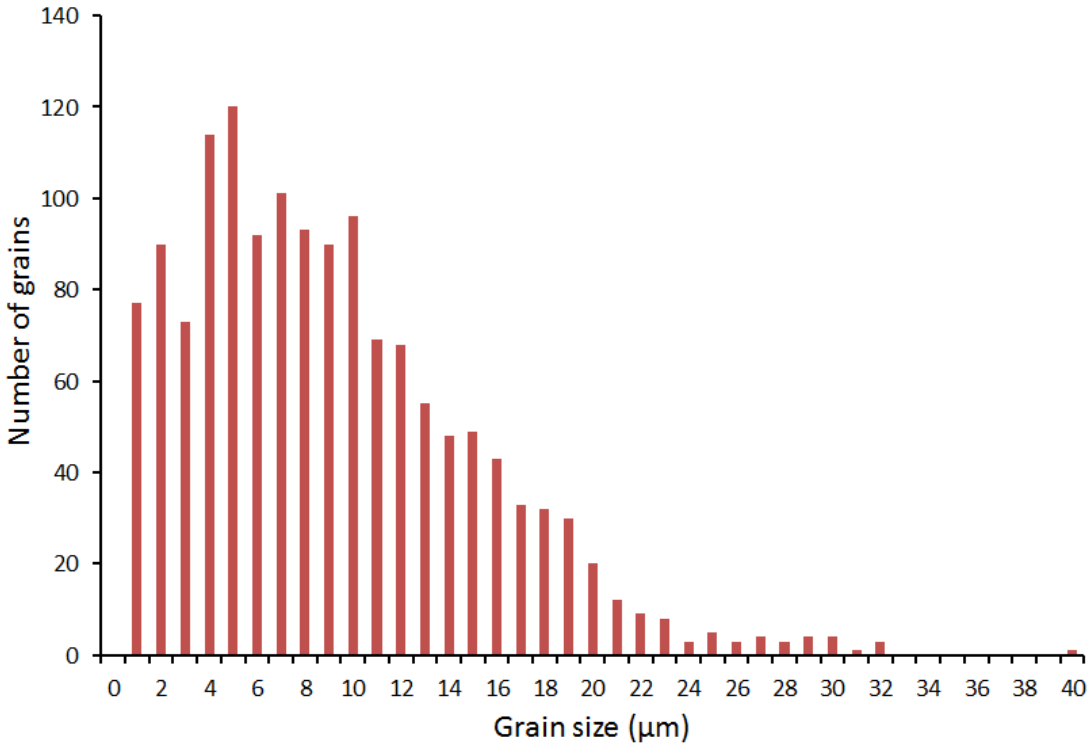

Figure 3-3 The grain size distribution determined by the mean linear intercept method as the mean of vertical and horizontal directions (Excluding twin grain boundaries) for 316L stainless steel sample (LT plane).

3.6.4 Predictive diagrams

A free online tool (MIG WELD GmbH International) [184] was used to predict the ferrite content using a Schaeffler diagram, a DeLong diagram, and a WRC-1992 diagram. These diagrams depend on the chemical composition of the alloy. By entering the cast analysis (Appendix 1) and minimum and maximum alloy specification, the Cr-equivalent (Cr_{eq}) and the Ni-equivalent (Ni_{eq}) were calculated and shown in a diagram. Each diagram has its own Cr_{eq} and Ni_{eq} equations.

3.7 Atmospheric Corrosion Tests

A summary of the atmospheric corrosion tests and conditions investigated in this study is shown in Table 3-3. Tests were performed to investigate the effect of microstructure, relative humidity (RH), chloride deposition density (CDD) and droplet diameter on pitting corrosion behaviour. Tests were performed by depositing water droplets containing $MgCl_2$ onto the surface of each specimen used. All corrosion tests were performed on specimens with 800-grit surface finish. The exposure time was from 1 day to 6 weeks. Further detailed test conditions can be taken from Table 3-3.

Information about salt solutions, droplet deposition methods, control of relative humidity and temperature, time-lapse and synchrotron microtomography corrosion tests are given in the following sections.

Table 3-3 Atmospheric corrosion test conditions.

Type of material	Heat treatment condition	Surface condition	Process orientation	Electrolyte used	Surface Cl^- coverage [µg/cm²]	RH [%]	Temp. [°C]	Time	Investigation, effect of:
304L sheet, 3 mm thickness, Supplier Aperam-France	As-received	800 grit	LT, LS, ST	$MgCl_2$	1000	33, 43, and 56	30	1 Week and 6 Weeks	Microstructure
			ST	$MgCl_2$	1000	33, 43, and 56	21	32 hours	Microstructure using tomography
			LT	$MgCl_2$	1000	33, 43, and 56	30	1 day and 1 week	RH
			LT	$MgCl_2$	0.1 - 10000	43	30	1 day and 1 week	CDD
			LT	$MgCl_2$	1000	43	30	1 week	Droplet diameter
	Solution annealed	800 grit	LT, LS	$MgCl_2$	1000	43	30	1 week	Microstructure
316L sheet, 6 mm thickness, Supplier Acerinox-Spain	As-received	800 grit	LT	$MgCl_2$	1000	33, 43, and 56	30	1 day and 1 week	RH
			LT	$MgCl_2$	0.5 - 10000	43	30	1 day	CDD
			LT	$MgCl_2$	1000	43	30	1 week	Droplet diameter

After exposure, the samples were photographed and droplets were individually photographed and then the samples were rinsed with deionised water. The corrosion products were removed by immersing the samples in dilute nitric acid (2.9 M HNO_3) for 1 hour at lab temperature. The diluted HNO_3 was made by mixing 200 ml HNO_3 (65%, Sigma-Aldrich) with DI water to obtain a 1000 ml solution.

3.7.1 Salt solutions

Solutions for atmospheric corrosion tests were made up from $MgCl_2.6H_2O$ (Fisher Scientific) and de-ionised water (18 MΩ cm).

3.7.2 Droplet deposition methods

Droplets were deposited manually from a Eppendrof Research plus micropipette with ±0.03 µl error in volume. The typical time of deposition of 10 droplets was within 2 minutes. Figure 3-4 shows a schematic of droplets deposited onto three plate planes. Droplets were also deposited by a MultiPROBE II Ex robotic liquid handling system (Figure 3-5) which automatically mixed the solutions prior to deposition.

Note that the droplets were deposited at ambient RH and Temperature, which ranged from (44±6%, 25±1 °C) in the summer to (35±5%, 22±0.7 °C) in the winter. The full array of 70 droplets was deposited within 8 -10 minutes.

The amount of chloride deposited was known from the volume and concentration of the droplet, the average area of as-deposited droplets was determined using FIJI/ImageJ image processing software [185]. For tests which required deposition of different CDD values. Solutions were automatically mixed

via serial dilution with DI water of a stock magnesium chloride solution. The system was programed to wash the pipette tip after each deposition set.

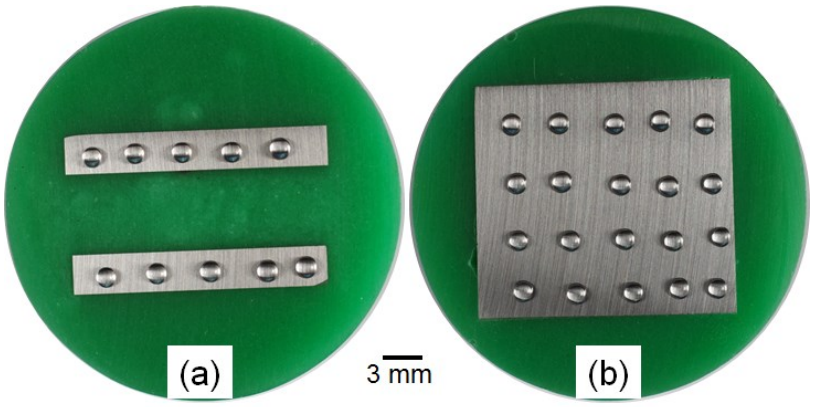

Figure 3-4 Micropipette salt solution deposition on 304L stainless steel (a) LS and ST plane; (b) LT plane.

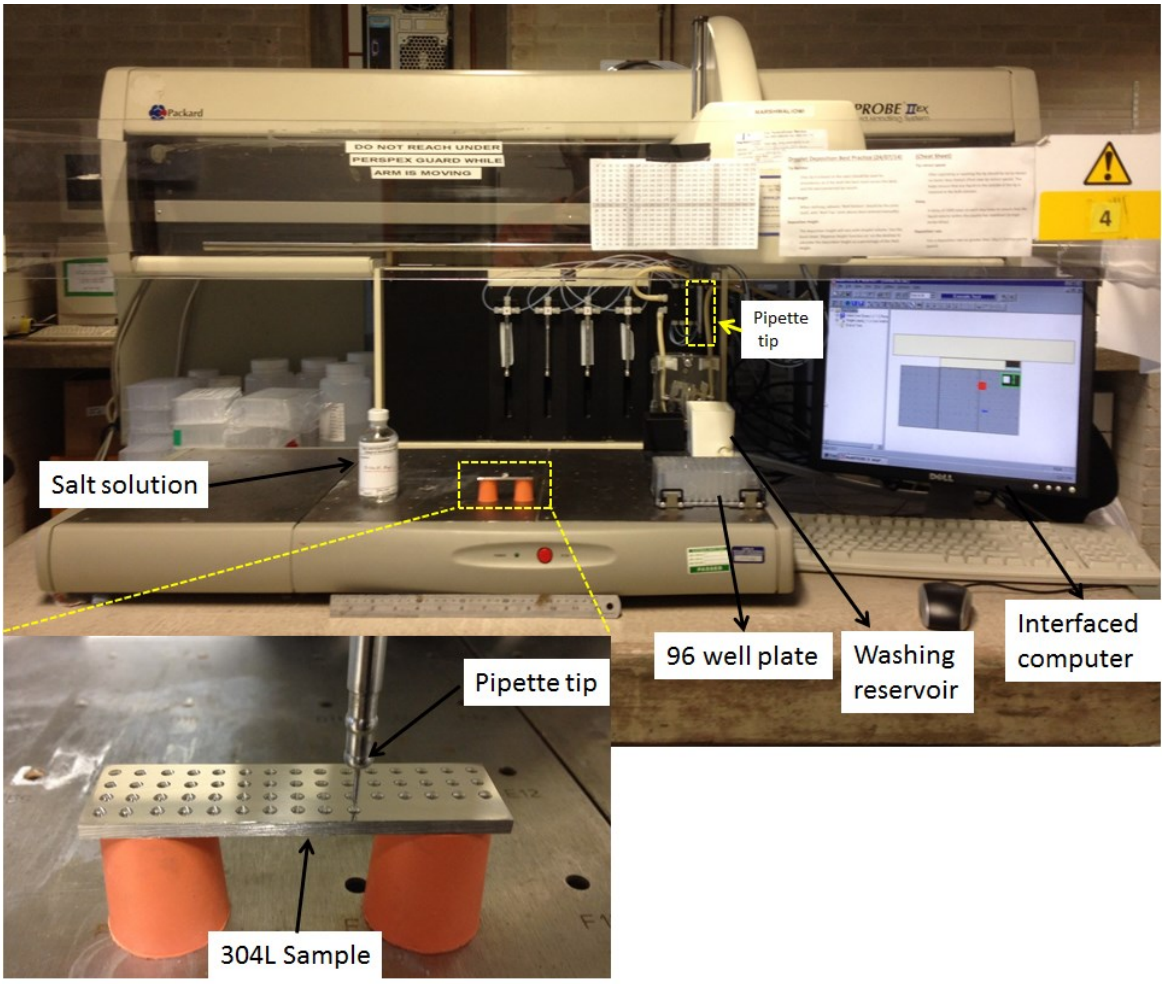

Figure 3-5 MultiPROBE II Ex robotic liquid handling system.

3.7.3 Controlling of relative humidity and temperature

The relative humidity of tests carried out in desiccators was maintained by using saturated salt solutions according to ASTM E104-02 [186] as shown in Table 3-4. The desiccators were then placed in a temperature controlled chamber HT135 (TAS Ltd) at 30±1 °C.

Other tests were conducted in an ECO135 atmospheric chamber (TAS Ltd) at 30±1 °C and at a fixed humidity between 35-75% RH.

In all experiments, RH and temperature was monitored using RH/TEMP data loggers (EL-USB-2-LCD, Lascar Electronics) was kept inside to verify the environment RH and temperature. Typical examples of the monitored RH and temperature for the experiments carried out in desiccators (RH was controlled by the saturated salts) and the controlled atmospheric chamber are shown in Appendix 2.

Table 3-4 Saturated salts used for RH control according to ASTM E104-02 [186].

RH (%)	Salt Type	Effective Temperature Range(°)
33	$MgCl_2.6H_2O$	5 – 80
43	K_2CO_3	5 – 30
56	NaBr	5 – 80
70	KI	5 – 80
75	NaCl	5 – 80

3.7.4 Time-lapse tests

A Leica DMLM optical microscope equipped with Micro-Manager version 1.4.22 software was used to carry out time-lapse tests. Two time-lapse tests were carried out in this work. One was used to monitor the pit growth, while the other was used to monitor the formation of micro-droplets and secondary spreading. Both were conducted in ambient laboratory conditions. Replicate tests were performed when test conditions were not sustained, such as out of focus of images during the time-lapse.

3.7.5 Synchrotron microtomography corrosion tests

2 mm pin stainless steel samples were used for in situ X-ray microtomography tests, with the top surface ground to 800 grit, and then washed with DI water and methanol. ~1.1 µL droplets of 0.4 M $MgCl_2$ were deposited on the end of pins. Figure 3-6 shows a schematic illustration of the design of the cell used for this type of tests. The design of the sample cell was set up by covering the base side of the 2 mm pin stainless steel sample with a short section of silicon tube of 2 mm internal diameter, then wrapped with some parafilm for better sealing. Then a longer silicon tube section of 4 mm inner diameter was used to cover the cell. The humidity inside the sample cell was controlled by inserting a piece of filter paper soaked with a saturated salt solution (mentioned in Section 1-8) into the silicone tube. Then an aluminium cap was used to seal the cell. An extra seal with Parafilm was performed to the top of the sample cell for effective sealing. The experiments were conducted at 21±1°C.

The tests were performed at Beamline I12 at Diamond Light Source. The energy of the beam and the pixel size were 70 keV and ~1.8 µm, respectively. During a 180° rotation for each sample, 1800 projections were collected. An algorithm (filtered back projection) was used to reconstruct the projections. The exposure time was typically 1 s per projection and for each sample the full scan takes 40–45 min. In order to make 3D rendered images, Avizo software was used [26].

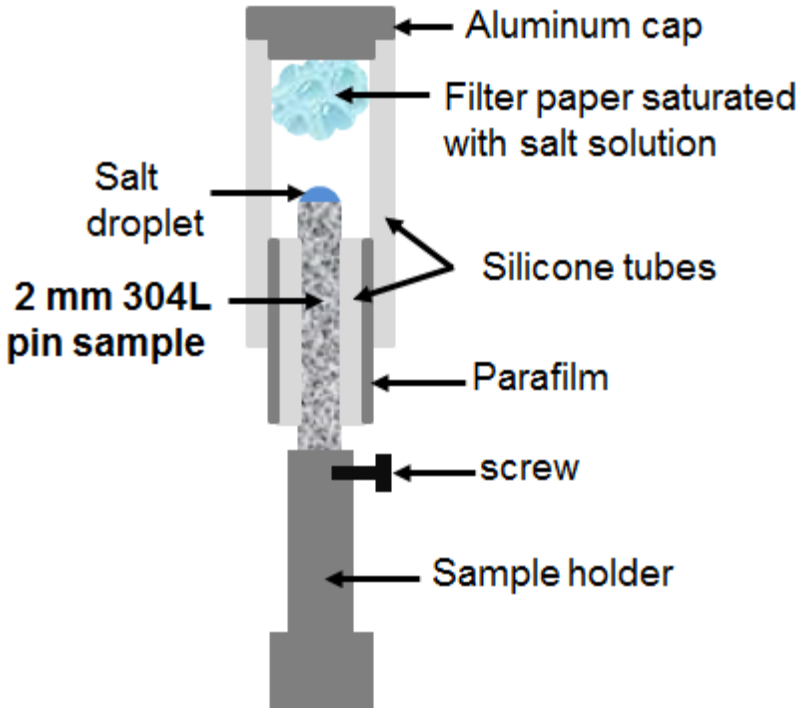

Figure 3-6 Schematic diagram of cell used for in situ X-ray tomography experiments using 2 mm diameter 304L stainless steel pin.

3.8 Measurements

3.8.1 Distance from the shallow dish and/or pit centre to the droplet edge

The distance from approximately the centre of the shallow dish region to the nearest edge of droplet was determined by drawing a straight line using "straight line" tool in FIJI/ImageJ software [185] (Figure 3-7). For pits where no shallow dish region was present, a line was drawn from the centre of the pit to the nearest droplet edge. The uncertainty in such manual measurement was typically ±5 μm. In general terms the errors were determined from the standard deviations of 5 measurements.

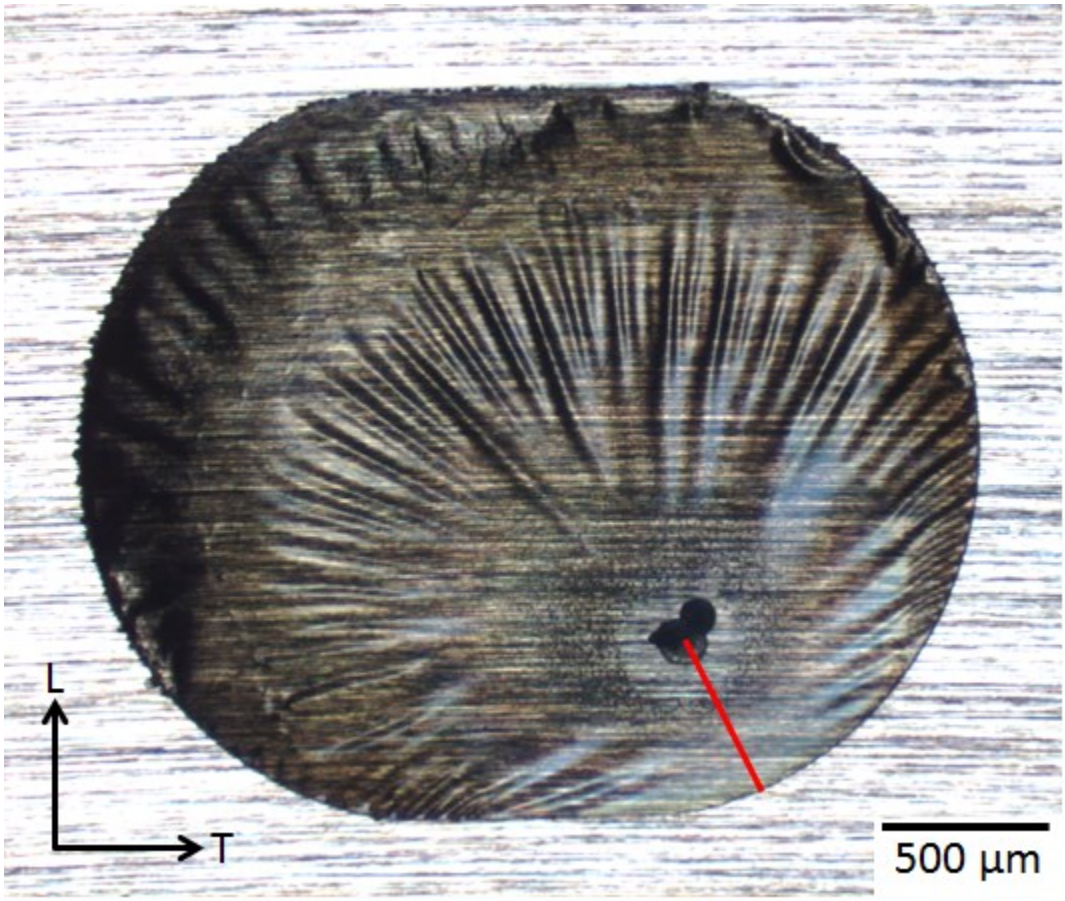

Figure 3-7 Measurement of the distance from the shallow dish region observed during pitting. Pit was grown under $MgCl_2$ droplet (~2.5 mm equivalent diameter with ~1000 µg/cm^2 CDD at deposition) on 304L stainless steel surface (LT plane) after 1 week exposure at 33% RH and 30 °C.

3.8.2 Measurement of shallow dish region, active region and total pit diameter

A Leica DMLM optical microscope equipped with a Leica DFC 420 digital camera of maximum 5 mega pixel resolutions was used for optical microscopy. For pits that showed a “shallow dish region”, the diameter of the shallow region was determined, by considering that the shallow dish region was circular, by drawing an circle (using the “oval” tool in FIJI/ImageJ software) around the remaining dish region after pitting corrosion test (Figure 3-8). The area of the

drawn circle was measured directly from FIJI/ImageJ software. The equivalent diameter of the circle was obtained from the area of the circle using the (Equation 3-2). The uncertainty in the area of the shallow dish measurement was ±64 μm^2. Consequently, the uncertainty in the equivalent diameter of the shallow dish was ±0.4 μm. The standard deviations are from 5 measurements.

$$d = \sqrt{\frac{4A}{\pi}} \qquad \text{Equation 3-2}$$

Where d is the diameter and A is the shallow dish area measured.

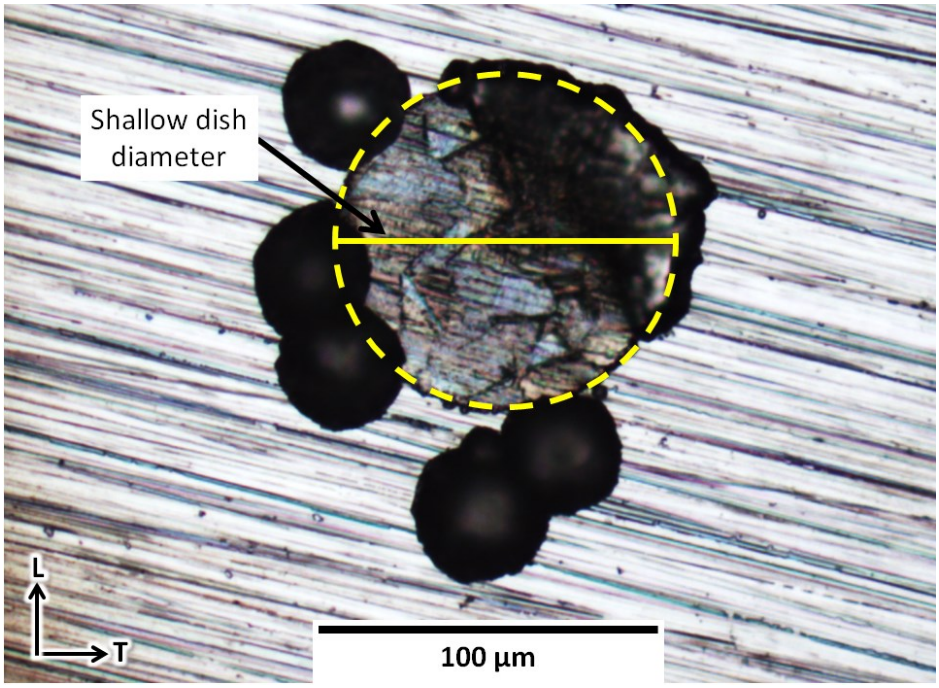

Figure 3-8 Measurement of the shallow dish region observed during pitting. The pit was grown under $MgCl_2$ droplet (~2.5 mm diameter with ~1000 μg/cm^2 CDD at deposition) on 304L stainless steel surface (LT plane) after 1 day exposure at 33% RH and 30 °C.

Pits that did not show a shallow dish region and had only circular morphology (e.g. at ≥ 56% RH for 304L and ≥ 48% RH for 316L), the pit mouth area (total pit area) was selected and measured using the semi-automatic “wand” tool combined with the “Freehand selections” tool in FIJI/ImageJ software. Then the equivalent pit diameter was obtained from (Equation 3-2) based on the assumption that the selected region was circular.

Figure 3-9 shows the methodology for selecting the active region and the total pit area. The active area is defined as the deep region of the pit outlined in red. The total pit area is defined as the area as outlined in yellow. The equivalent diameters of these measurements were calculated by considering the selected area as a circle. The uncertainty in the active area and the total pit area measurements was ±300 μm^2 and ±15 μm^2 respectively. Consequently, the uncertainty in the equivalent diameter of the active region of pit and the total pit area was ±2.1 μm and ±0.1 μm respectively. The standard deviations are from 5 measurements.

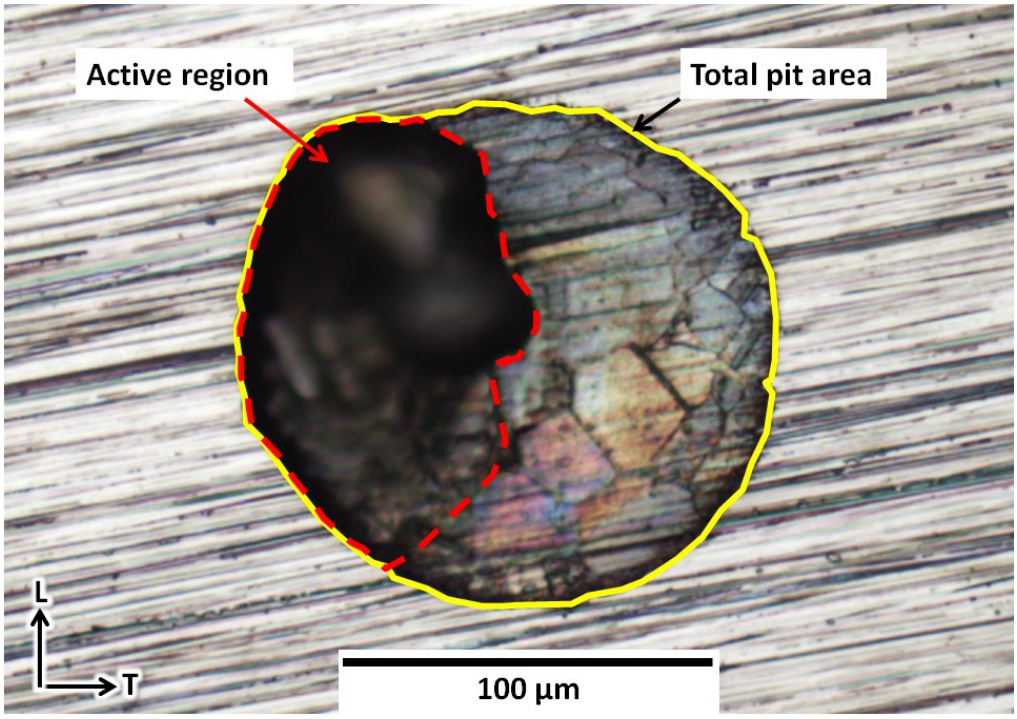

Figure 3-9 Technique used for measuring the active region and the total pit area. The pit was grown under a $MgCl_2$ droplet (~2.5 mm diameter with ~1000 µg/cm^2 CDD at deposition) on 304L stainless steel (LT plane) after 1 day exposure at 43% RH and 30 °C.

3.8.3 Pit depth measurements

A Leica DMLM optical microscope with fine focus resolution of 1 µm was used to characterize the pit size for lab-based experiments. The pits depth was measured using the fine focus method [124], where the pit depth was estimated as the difference between optical focus on the surface of sample and the optical focus on the base of the pit (the lowest observable point). The uncertainty in pit depth measurements was found to be ±2 µm (based on 5 measurements). The maximum depth within a pit was considered to be the pit depth.

4 Effect of microstructure on the morphology of atmospheric corrosion pits in 304L stainless steel

4.1 Introduction

It is widely accepted that small quantities of residual ferrite can be found in “fully austenitic” stainless steels such as 304L and 316L [36, 42, 68, 70, 187, 188]. However, its effect on pitting corrosion has not been studied under atmospheric conditions. From studies of duplex stainless steel, it is known that ferrite is attacked in preference to austenite under atmospheric corrosion conditions [24].

In this work, the effect of residual ferrite on atmospheric pitting corrosion of 304L is investigated on three plate orientations. In addition, the effect of solution annealing is also outlined. Both MnS and mixed oxide inclusions were characterised.

4.2 Results

4.2.1 Microstructure

The ST plane of the 304 stainless steel plate has a microstructure that is predominantly composed of equiaxed grains (Figure 4-1(a)), which have been confirmed by electron back-scatter diffraction (EBSD) to be austenite (Figure 4-1(b)). Bands can be seen parallel to the surface of the plate (in the plane of the rolling direction). In the EBSD map (Figure 4-1(b)), it can be seen that these elongated features are red, indicating that they are ferritic (point 1). However, there are other regions that appear to have a ferritic structure that are not

parallel to the plate surface, such as point (2 and 3) in Figure 4-1(b). These regions are not obviously distinct on the SEM image, and might possibly be deformation-induced martensite. The total area fraction of ferrite and martensite phases determined by EBSD makes up ~6% of the steel.

The presence of ferritic phases in the microstructure was confirmed by X-ray diffraction (XRD) (Figure 4-2). There are strong austenite peaks and one smaller peak that correlates with the ferrite (110) peak. The presence of ferrite was also confirmed by vibrating sample magnetometer (VSM) measurements. Figure 4-3 shows the hysteresis loops, magnetisation as a function of applied magnetic field, for 304L samples before and after solution annealing. It was found that the alloy behaves in a soft magnetic manner in the presence of a magnetic field, consistent with the presence of the ferrite phase. After solution annealing, however, it is evident that there is a significant reduction in the magnetisation, which indicates that the ferrite content is lower.

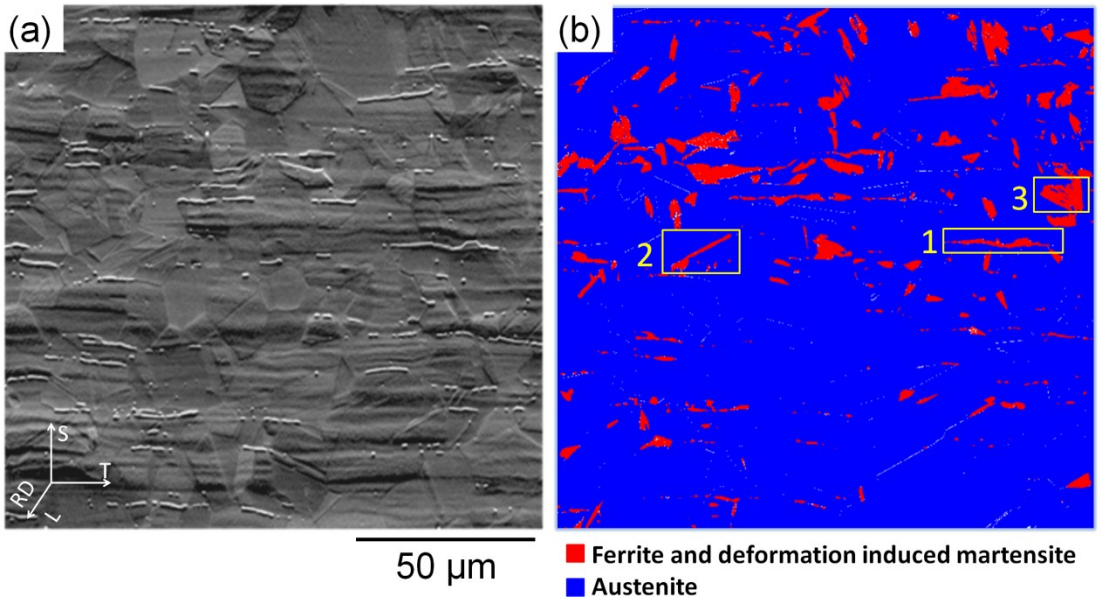

Figure 4-1 304L stainless steel, ST plane, rolling direction normal to the page (a) SEM image showing the microstructure; (b) EBSD of ST plane.

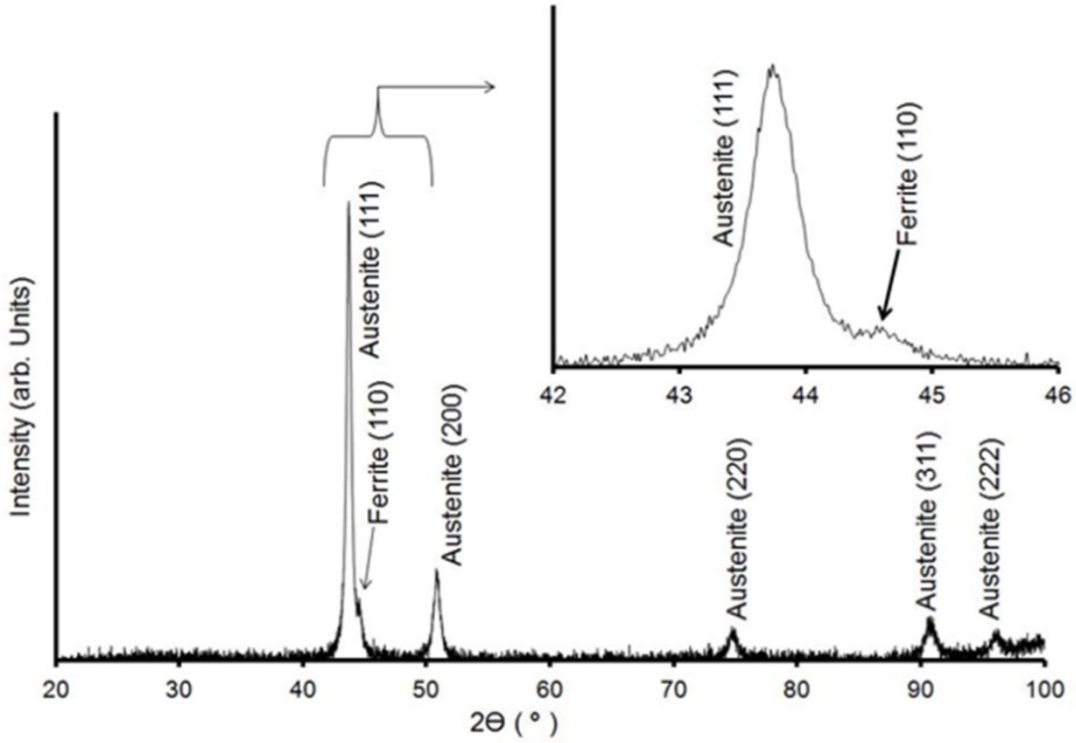

Figure 4-2 XRD pattern of LT plane of 304L stainless steel

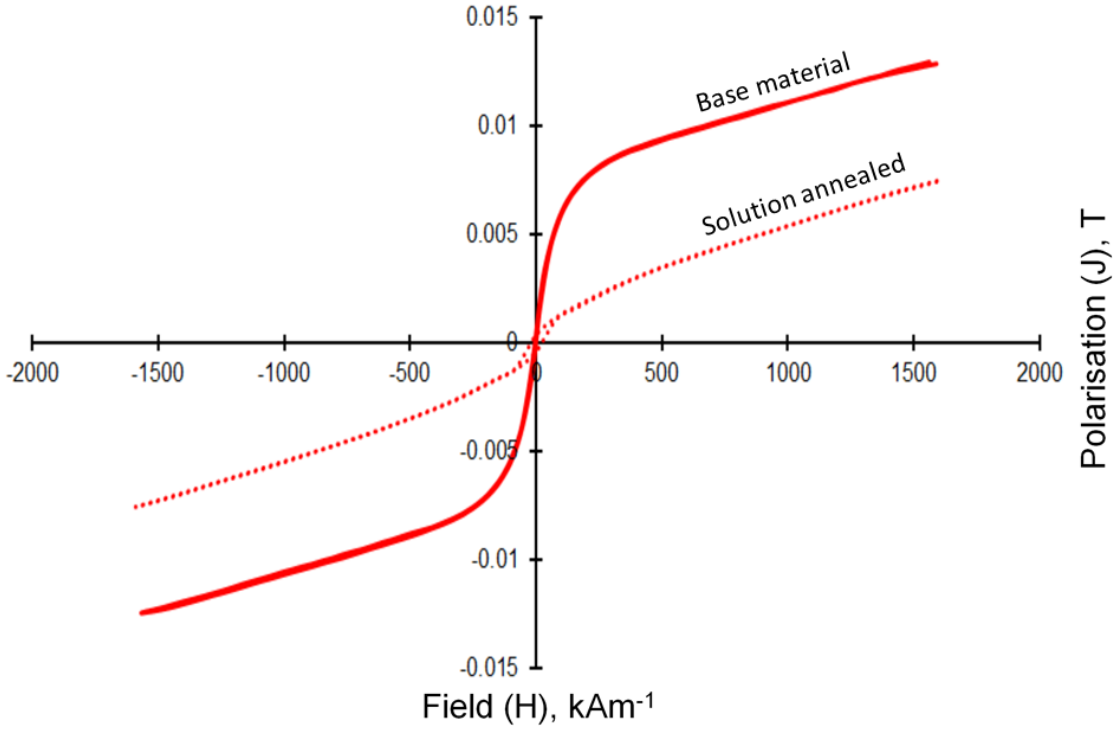

Figure 4-3 Hysteresis loops of 304L stainless steel obtained by VSM: base material shown in solid red and solution annealed shown in dashed red.

A Schaeffler diagram (Figure 4-4), a DeLong diagram (Figure 4-5), and a WRC-1992 diagram (Figure 4-6) were used to predict the ferrite content [184]. The predicted volume fraction of ferrite content was 12%, 6.2% and 8% from the Schaeffler diagram, DeLong diagram and WRC-1992, respectively. The methodology for obtaining these diagrams is described in Section 3.6.4.

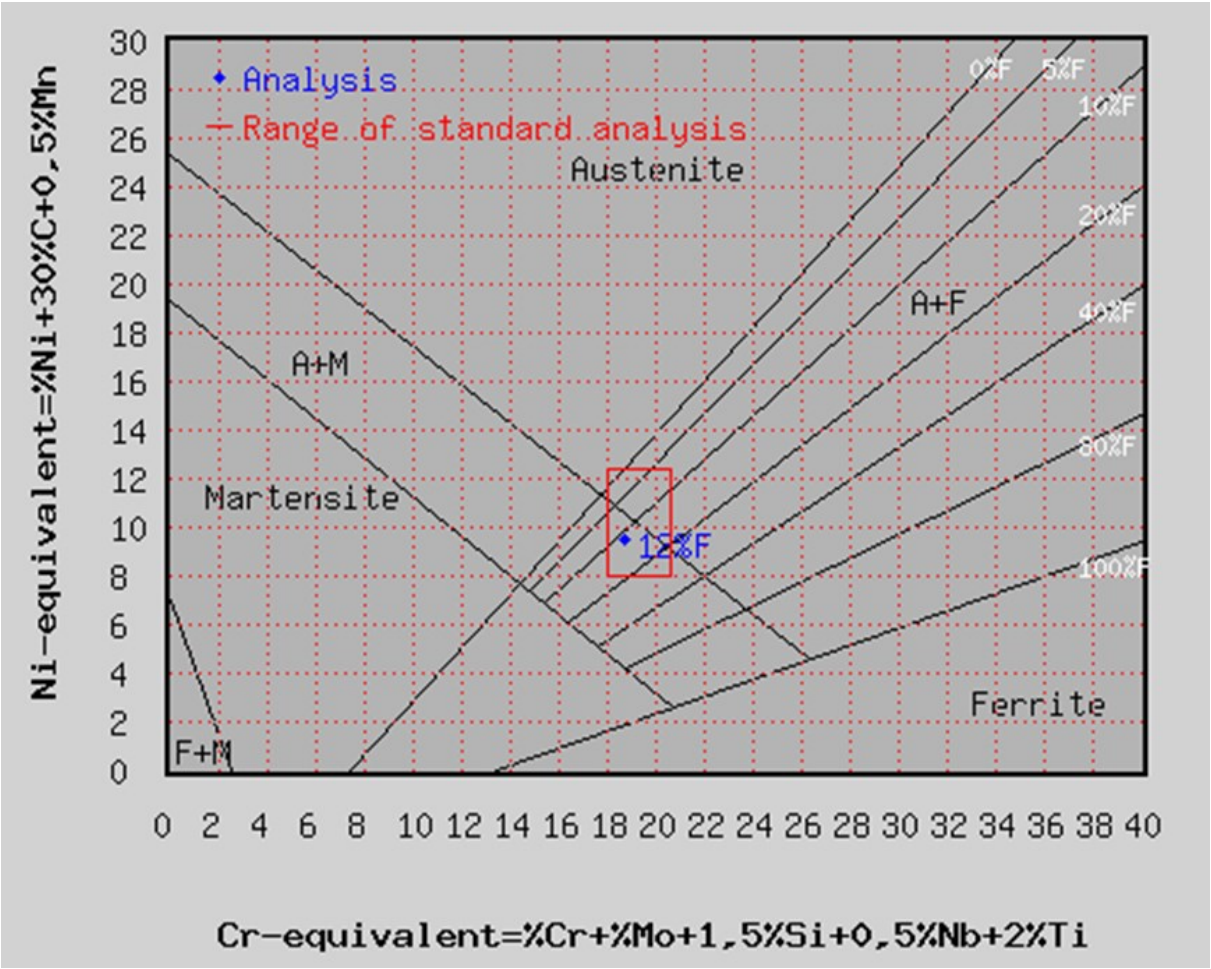

Figure 4-4 Schaeffler diagram showing the predicted prevalence of austenite (A), ferrite (F) and martensite (M); the blue point represents the theoretical ferrite content of the 304L alloy used in this work using the procedure described in Section 3.6.4; the red box outlines the range of standard analysis based on composition range.

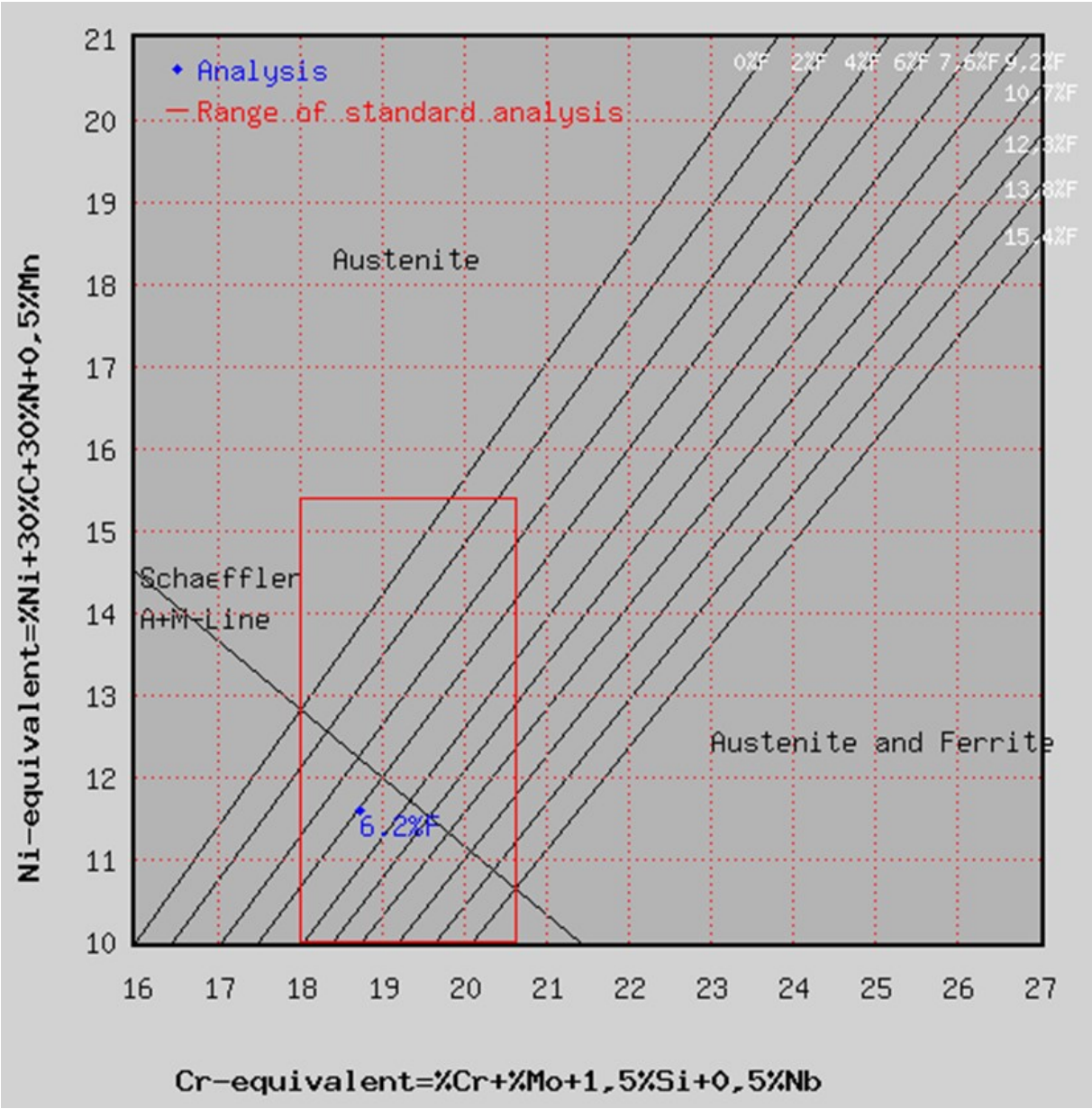

Figure 4-5 DeLong diagram showing the predicted prevalence of austenite (A), ferrite (F) and martensite (M) as a function of composition; the blue point represents the analysis of ferrite content of the 304L alloy used in this work using the procedure described in Section 3.6.4, the red box outlines the range of standard analysis .

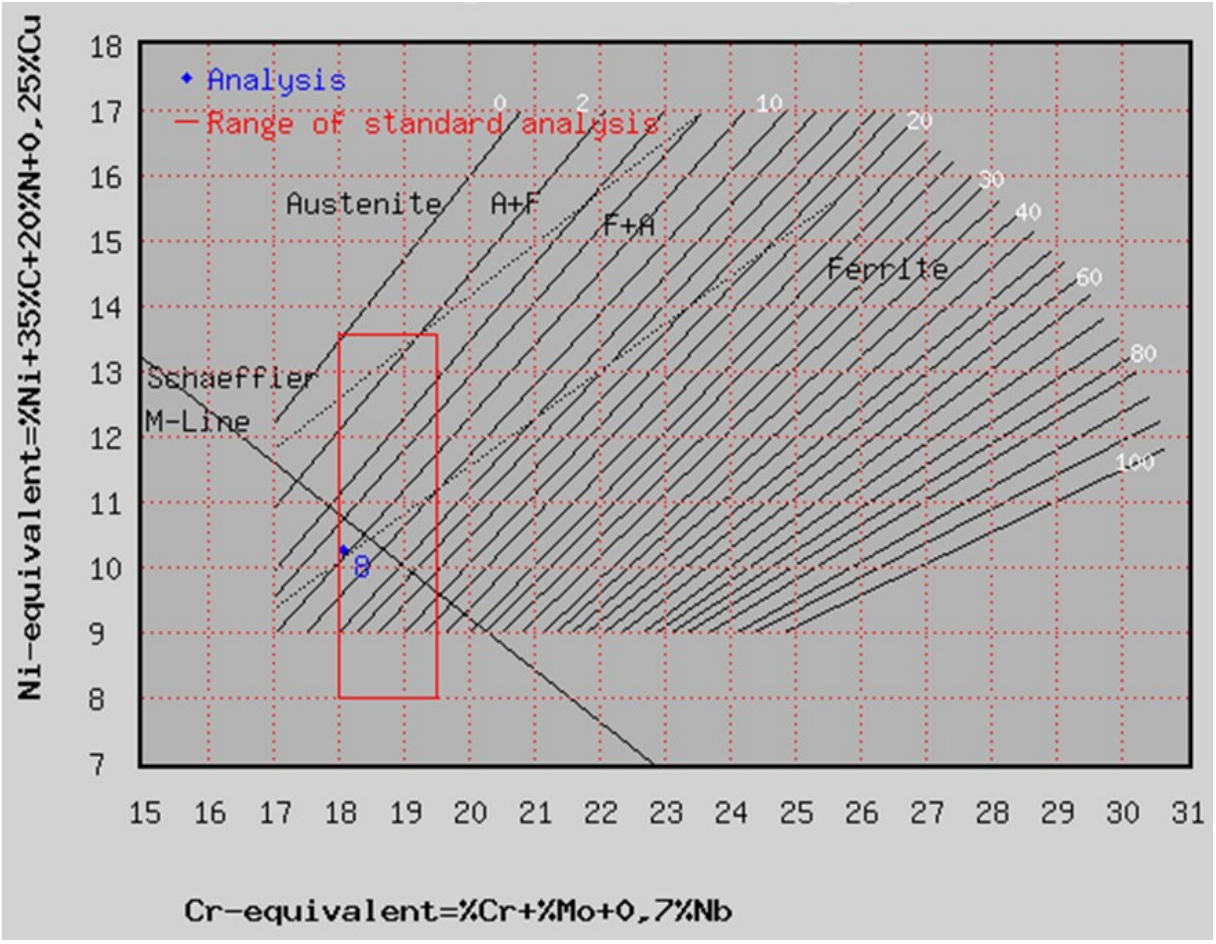

Figure 4-6 WRC-1992 diagram shows the predicted prevalence of austenite (A), ferrite (F) and martensite (M) as a function of alloy composition; the blue point represents the analysis of ferrite content of the 304L alloy used in this work using the procedure described in Section 3.6.4, the red box outlines the range of standard analysis.

Figure 4-7 shows SEM images of the three plate orientations (LT, LS and ST) of 304L stainless steel after 5 s etching with Kalling's 2 reagent following polishing. The bands along the rolling direction were preferentially dissolved. These bands correlate with ferrite bands, as observed in Figure 4-1. Wider bands were revealed on the LT plane (Figure 4-7(a)). Coarse equiaxed austenite grains were observed in all plate orientations.

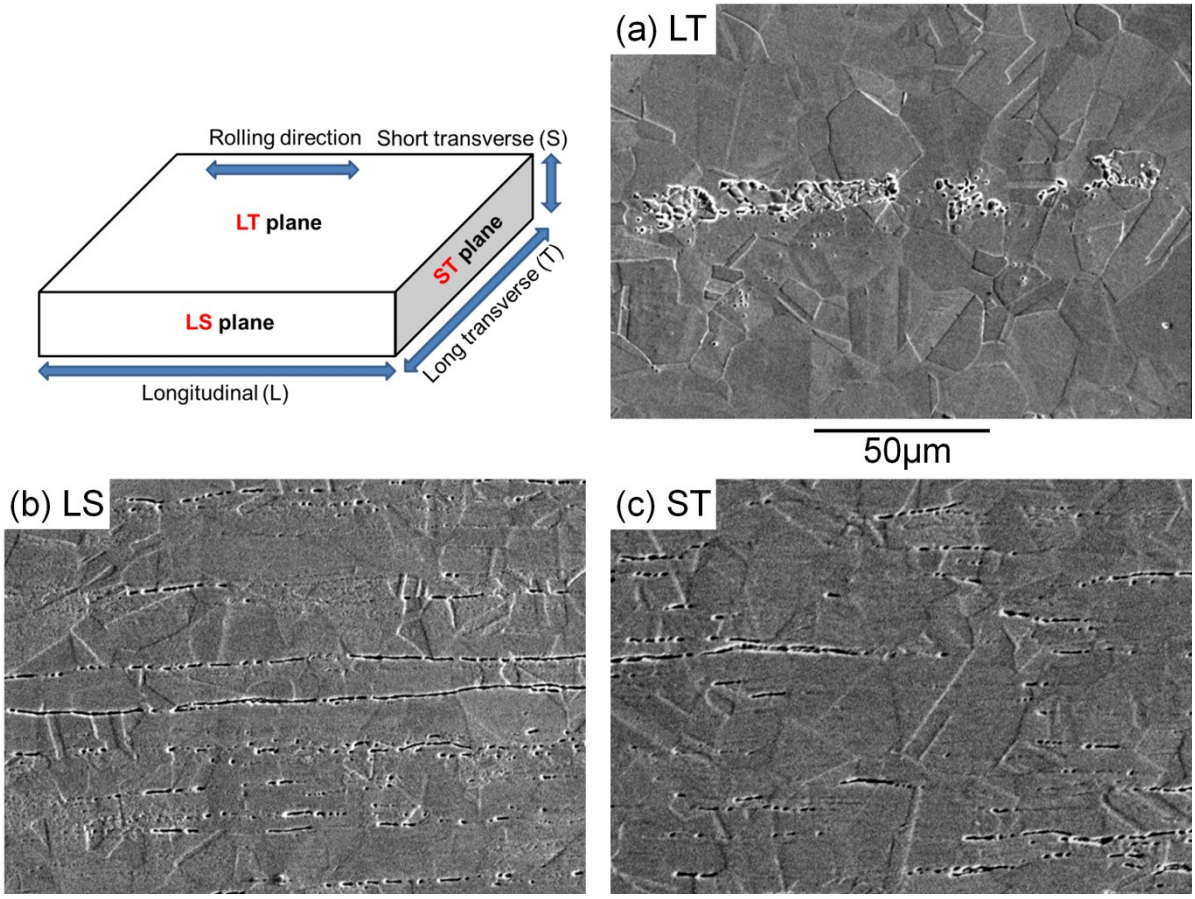

Figure 4-7 SEM images of the microstructure of the LT, LS and ST planes of 304L stainless steel plate after 5 s etching with Kalling's 2 reagent.

4.2.2 Effect of three plate orientations on pit morphology

The effect of plate orientation on pit morphology was investigated for 304L stainless steel. Two sets of specimens were tested; one set was exposed for 1 week while the other one exposed for 6 weeks. The exposure RH was 33, 43, or 56% for both sets. Droplets of $MgCl_2$ (~2 mm equivalent diameter, ~1000 μg/cm^2 CDD) were deposited manually onto the three plate planes (LT, LS, and ST) using a micropipette. At least 10 droplets were deposited on the LS and ST planes while 12-20 droplets were deposited on LT plane (see Figure

3-4). Summary of the results of the pitting behaviour of these tests is given in Table 4-3.

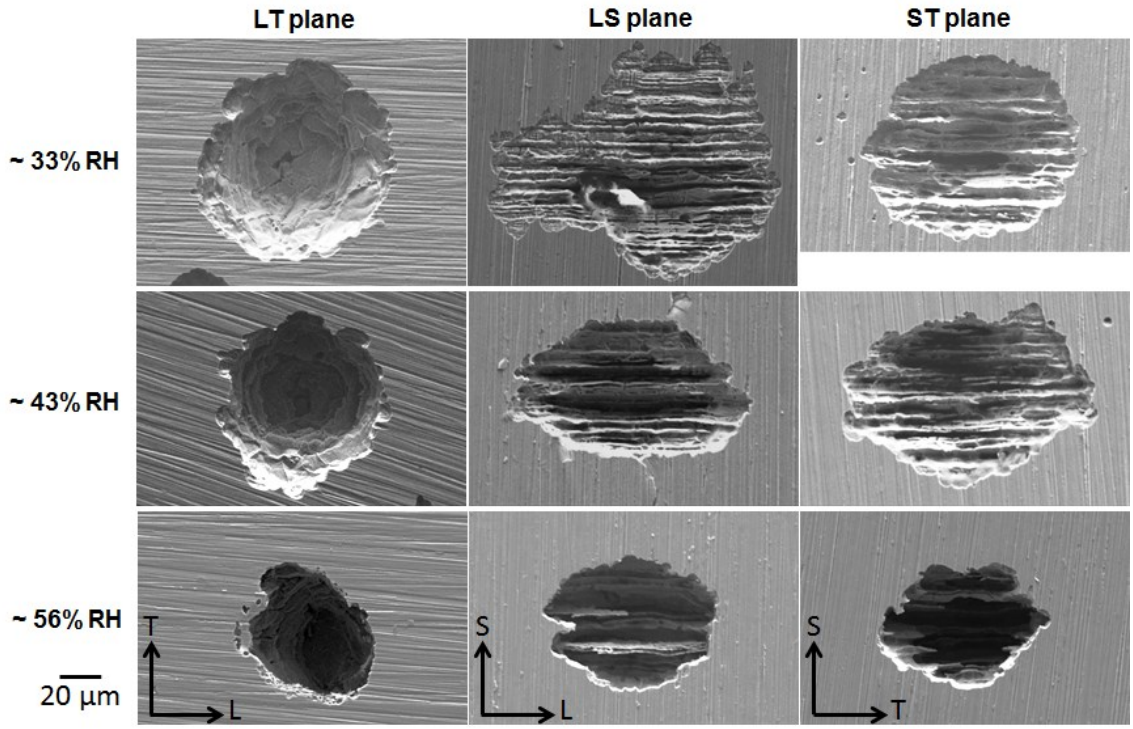

Figure 4-8 SEM images of pits grown on 304L stainless steel plate (LT, LS, and ST planes) under droplets of $MgCl_2$ (chloride deposition density, CDD, of ~1000 µg/cm^2), 30 °C, after 1 week of exposure at 33±2% ,43±2%, 56±2% RH. The corrosion products were removed by immersing the samples in dilute nitric acid (2.9 M HNO_3) for 1 hour at room temperature.

Figure 4-8 shows the SEM images of pit morphologies on the three plate orientations at 33±2%, 43±2%, and 56±2% RH. The LT plane (top surface of the plate) shows layered attack morphology. Both LS and ST planes show a striped morphology of elongated strands of undissolved metal parallel to the rolling direction. This was consistent at all exposure RHs. However, the effect of RH on pitting is not considered in this chapter.

Figure 4-9(a) shows a droplet of $MgCl_2$ solution on the LS plane that has been corroding for 6 weeks. Figure 4-9(b) shows the surface following removal of the droplet and washing in deionised water. The primary pit is elongated in the rolling direction. Figure 4-9(c) shows the sample after sectioning through the pit along the line indicated in Figure 4-9(b), and Figure 4-9(d) shows an SEM image of the sectioned sample following cleaning in dilute nitric acid at room temperature for 1 hour and polishing with OPS. The section on the left side (ST), shows narrow fissures of attack deep into the surface, and the pit surface on the right side (LS) shows bands of attack in the pit surface. Figure 4-9(e) shows an SEM image of the fissures in the ST plane, and (Figure 4-9(f)) shows a higher resolution image of the tip of a fissure. The tip of the lower fissure is located in a band of narrow grains that was confirmed by EDX mapping (Figure 4-9(g)) to be delta ferrite, as it shows higher levels of Cr and lower levels of Ni than the adjacent austenite grains. Table 4-1 shows the chemical compositions of ferrite and austenite phases obtained by EDX analysis. The average elemental composition of both phases were measured for Fe, Cr, Ni, Si, Mn and S content in weight percent. 5 point scans were measured over the centre of the ferrite band at different regions, and a similar number of scans were measured over an austenite region. The average chromium and nickel content of ferrite phase was 24±1% and 4±0.5% respectively, while that for austenite phase was 19%±0.5 and 8±0.4% respectively.

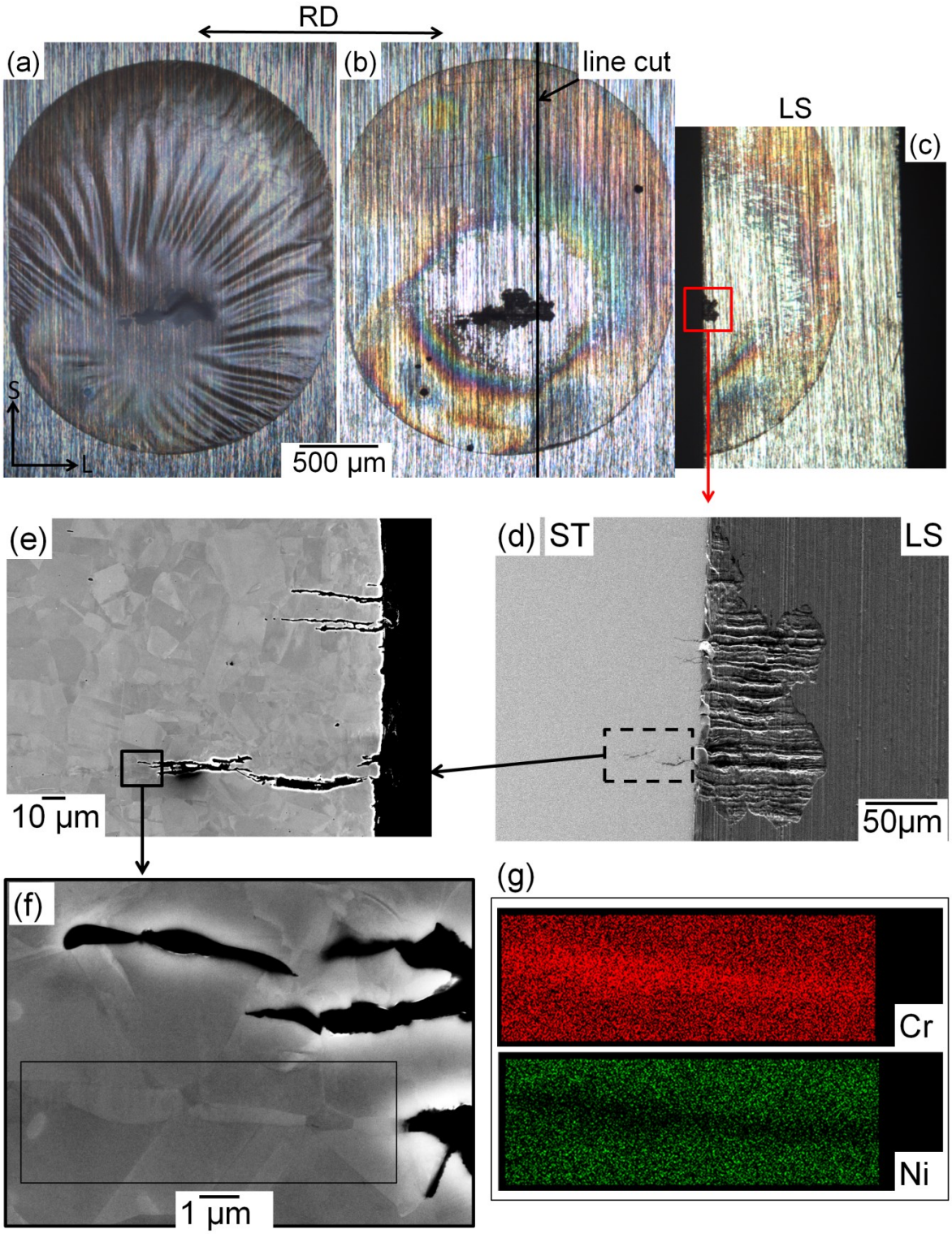

Figure 4-9 304L plate (LS) with a droplet of $MgCl_2$ (CDD ~1000 µg/cm^2); (a) after 6 weeks at 33±2% RH, 30 °C; (b) washed with DI water (c) section of pit; (d) SEM of sectioned sample, tilted (45°), showing both end grain (ST) and side grain (LS) sides of the pit; (e) polished with OPS end grain side (ST); (f) magnified part of (e); (g) EDX maps of region outlined in (f). The rolling direction (RD) is indicated.

Table 4-1 The average elemental composition with standard deviation of ferrite and austenite phases in weight percent (wt.-%) for 304L stainless steel, ST plane.

Weight %	Cr	Ni	Mn	S	Si	Fe
Ferrite phase	24±1.0	4±0.5	1.5±0.17	0.2±0.01	0.6±0.04	balance
Austenite phase	19±0.5	8±0.4	1.7±0.10	0.1±0.05	0.5±0.04	balance

Figure 4-10(a) shows a droplet of $MgCl_2$ solution on 304L stainless steel (LS plane) that has been corroding for 6 weeks at 30 °C and 33±2% RH. A single pitting site had developed at the edge of the droplet (Figure 4-10(a)). After being washed (Figure 4-10(b)), the pit was lightly polished to a mirror finish (Figure 4-10(c)) to allow the microstructure to be resolved (Figure 4-10(d)). Propagation along the pit surface was seen to follow narrow grains (Figure 4-10(e)) that were higher in Cr and lower in Ni than the adjacent austenite (Figure 4-10(f)), confirming that they are ferritic.

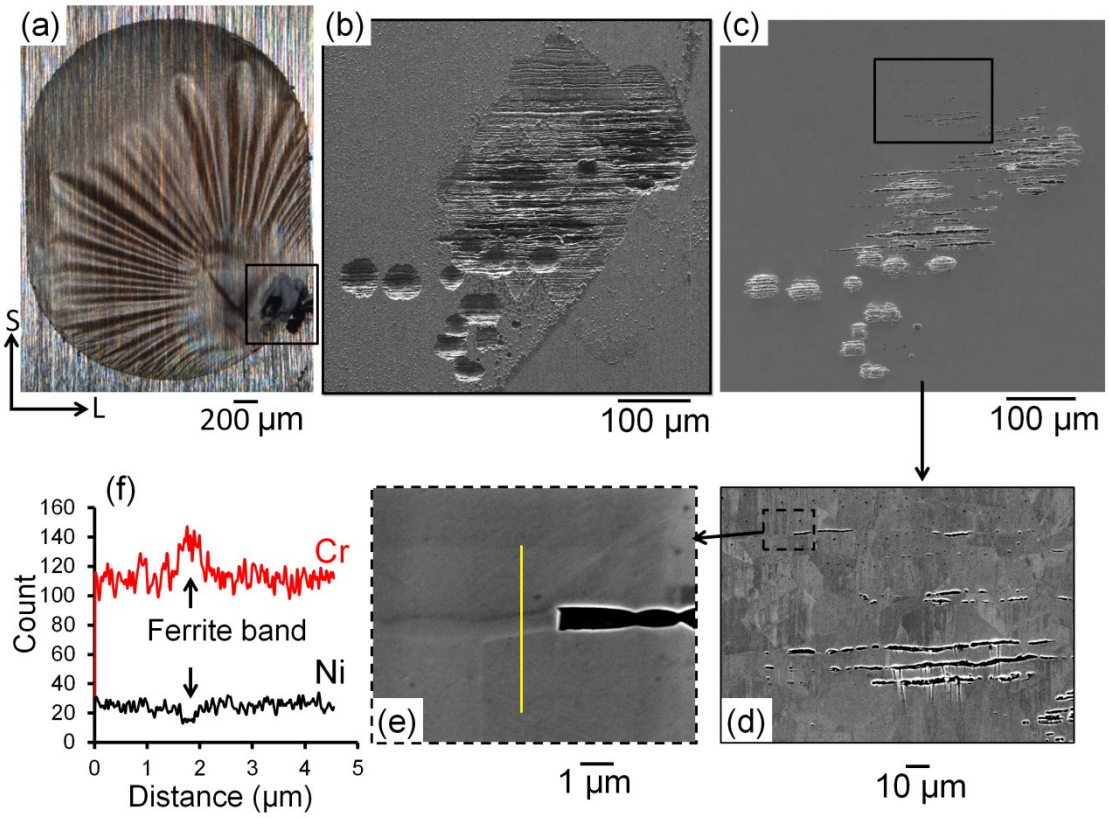

Figure 4-10 (a) a 304L stainless steel plate, LS plane, with a droplet of $MgCl_2$ on its surface (CDD ~1000 µg/cm^2) after 6 weeks of exposure at 33±2% RH and 30 °C; (b) SEM image of pit following gentle washing with deionised water; (c) following gentle polishing with OPS; (d) magnified region of (c); (e) magnified region of (d); and (f) EDX line scan through the ferrite band shown in (e).

An SEM image of a pit grown for 1 week at 56±2% RH at 30 °C on the LT plane is shown (Figure 4-11). The layered attack is clear from the surface (Figure 4-11(a)), with corrosion not only propagating down into the plate but also parallel to the rolling direction. After focused ion beam (FIB) milling adjacent to the pit mouth (Figure 4-11(b)), it is clear that dissolution parallel to the rolling direction occurs under the metal surface in a planar morphology consistent with attack on the ferrite bands. The walls of the pit also show this preferential attack.

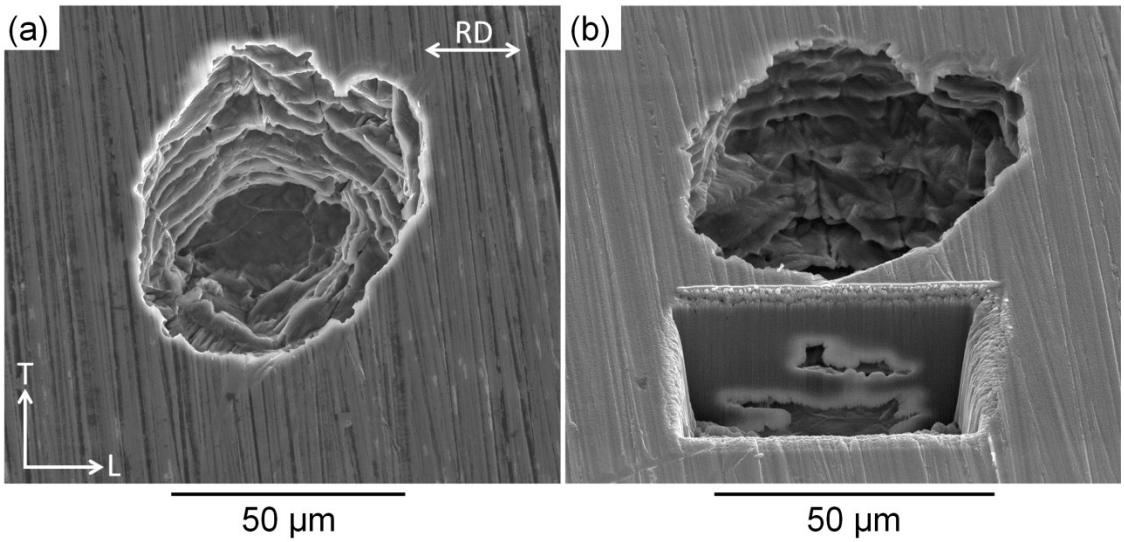

Figure 4-11 (a) SEM image of a pit grown on 304L stainless steel plate, LT plane, with a droplet of $MgCl_2$ (CDD ~1000 µg/cm^2), after 1 week of exposure at 30 °C, 56±2% RH; (b) after FIB milling, sample tilted at 52°.

4.2.3 Tomography results

In-situ X-ray tomography of a 304L pin (2 mm diameter) corroding at 59% RH after 32 hours is shown in Figure 4-12(a). Segmentation of the pit surface (shown in red) again shows propagation of the pit along the rolling direction (Figure 4-12(b and c). An SEM image of the pit surface after 79 hours (Figure 4-12(d) shows that the grinding direction on the surface of the pin is perpendicular to the microstructure.

In total, six tomography pin samples were examined, two samples at each exposure RH (33, 43, and 56% RH). It should be noted that there were always multiple pits per droplet ‘’sample’’ (a greater number of pits per droplet compared with lab-based tests). This was attributed to the effect of beam damage, which has been reported previously [7, 18, 182, 183, 189].

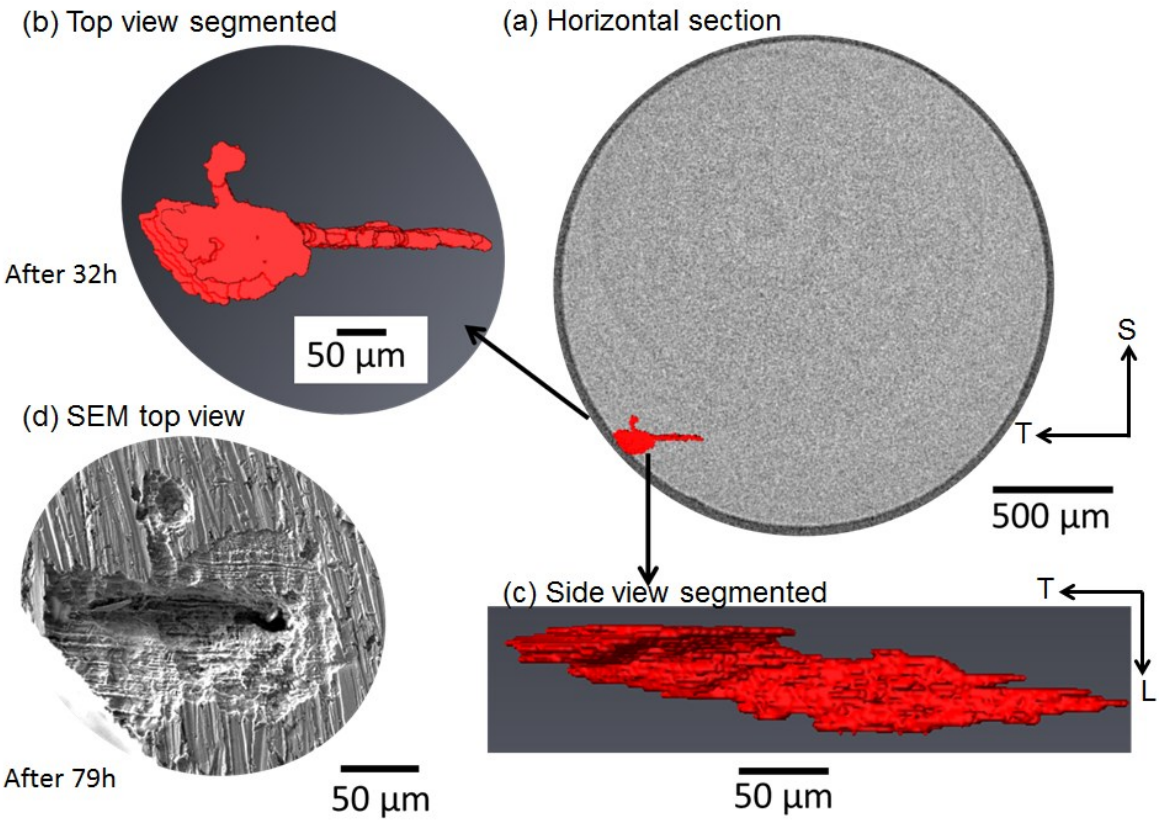

Figure 4-12 In situ X-ray tomogram of a stainless steel pin, ST plane, exposed to an $MgCl_2$ droplet (CDD ~1000 µg/cm^2) at 21±1°C and 59% RH for 32 hours; (a) horizontal section of the tomogram with the surface of the pit shown in red (segmentation using Avizo); (b) top and (c) side 3D view of the pit; (d) SEM image after 79 hours.

4.2.4 Effect of elongated inclusions on pit morphology

In Figure 4-13(a) (LS plane), an elongated inclusion can be seen along the ferrite bands parallel to the rolling direction of 304L base material. Figure 4-13(b) shows an elongated pit on the same plane formed under a droplet of $MgCl_2$ (chloride deposition density of 1000 µg/cm^2), after 1 week of exposure at 33±2% RH and 30 °C. Such elongated pits were also observed at 43±2% and 56±2% RH (see Table 4-3). The inclusions on three plate planes were

characterised with EDX for the alloy used for these experiments, and found to be either MnS or mixed oxides. SEM and EDX maps of MnS and a mixed oxides inclusion are shown in Figure 4-14 and Figure 4-15, respectively. EDX analysis was carried out to determine the chemical composition of these inclusions, a typical example of each type and the chemical composition of the base metal is given in Table 4-2.

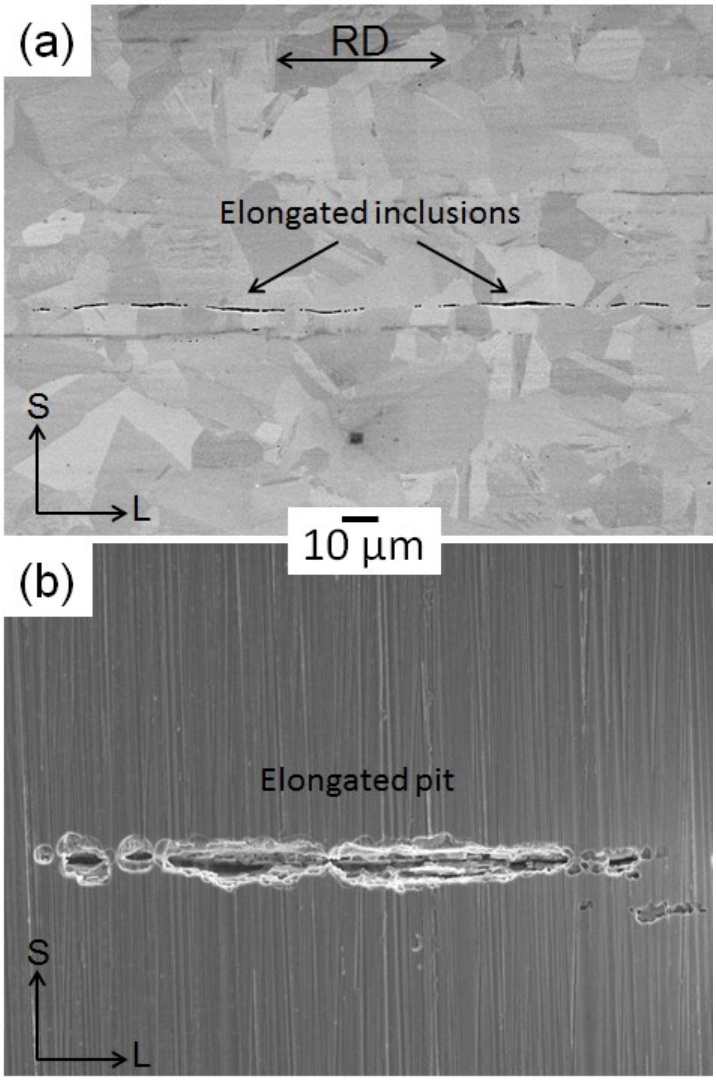

Figure 4-13 (a) 304L base material, LS plane; (b) an elongated pit on LS plane formed under a droplet of $MgCl_2$ (chloride deposition density ~1000 µg/cm^2), after 1 week of exposure at 33±2% RH and 30 °C. Following removal of corrosion products by immersing the sample in dilute nitric acid (2.9 M HNO_3) for 1 hour at room temperature.

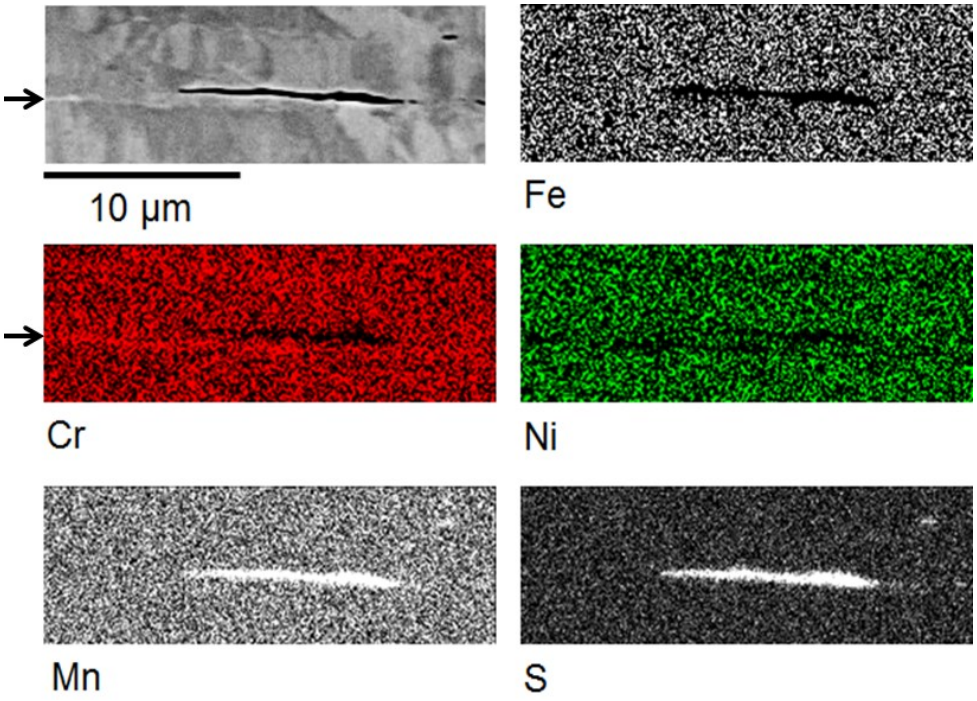

Figure 4-14 SEM and EDX maps of an MnS inclusion on a mirror polished 304L stainless steel sample (LS plane); the arrows indicate the location of a ferrite band.

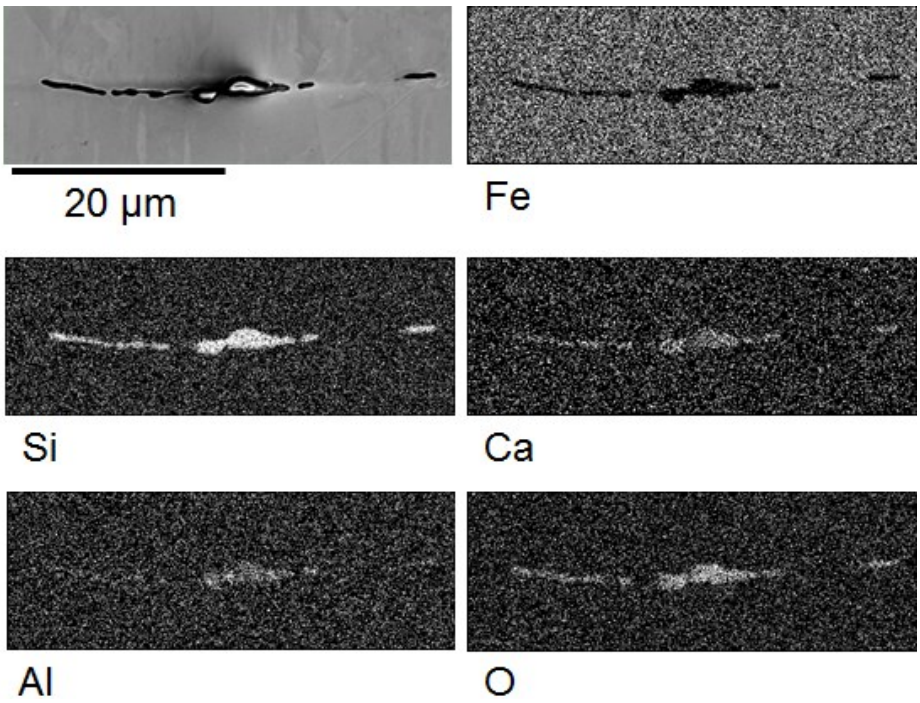

Figure 4-15 SEM and EDX maps of a mixed oxide inclusion on a mirror polished 304L stainless steel sample (LS plane).

Table 4-2 The chemical composition of typical MnS and mixed oxide inclusion observed in 304L stainless steel detected with EDX.

Weight %	O	Mg	Al	Si	S	Ca	Ti	Cr	Ni	Mn	Fe
MnS-containing	0	0	0	0.2	8.3	0	0	16.3	5.0	19.4	balance
mixed oxides	18.7	4.7	4.3	11.9	0.1	11.5	0.9	10.7	2.8	2.00	balance
Base metal	0	0	0	0.6	0.1	0	0	18.6	8.2	1.9	balance

4.2.5 Effect of solution annealing on the microstructure and pit morphology

The 304L plate was solution treated at 1050 °C for 1 hour before quenching in water. Figure 4-16 and Figure 4-17 shows the microstructure of 304L stainless steel (LS plane) that has been etched with Kalling's 2 reagent for 5 s. It can be seen that there is no preferential attack of ferrite bands, suggesting that the ferrite has transformed to austenite. It can also be seen that only certain grains have been attacked. Furthermore, Figure 4-17(b) shows that the annealing twin is free from the attack. It suggests that the attack is related to the crystallographic orientation.

Figure 4-18(a) shows a pit from an atmospheric corrosion test on the LT plane (top surface) of the plate without heat treatment, and Figure 4-18(b) shows a pit on the plate after heat treatment. Figure 4-18(a) shows the layered morphology usually seen for the plate resulting from attack on the ferrite phase (see e.g. Figure 4-11). In contrast, Figure 4-18(b) shows a pit on the solution-treated plate, which shows faceted crystallographic attack with no sign of layers. The difference in pit morphology is even more striking on the LS plane (Figure 4-19). The layered attack is seen for the as-received plate, whereas crystallographic

facets are again seen following heat treatment. This suggests that the heat treatment has greatly decreased the amount of residual ferrite in the plate. This has been confirmed by VSM (Figure 4-3).

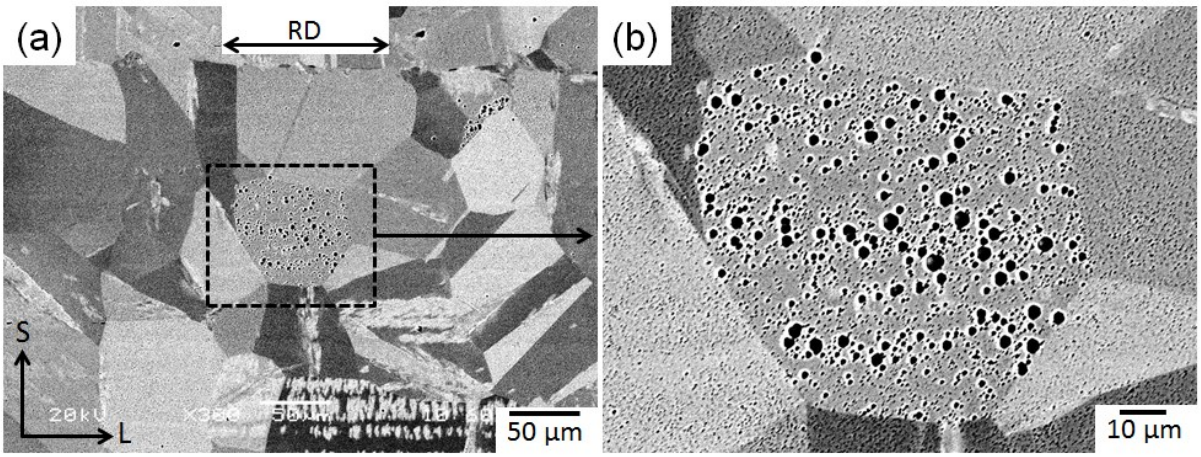

Figure 4-16 (a) Microstructure of the solution annealed 304L stainless steel plate (LS plane) after 5 s etching with Kalling's 2; (b) single grain with preferential attack.

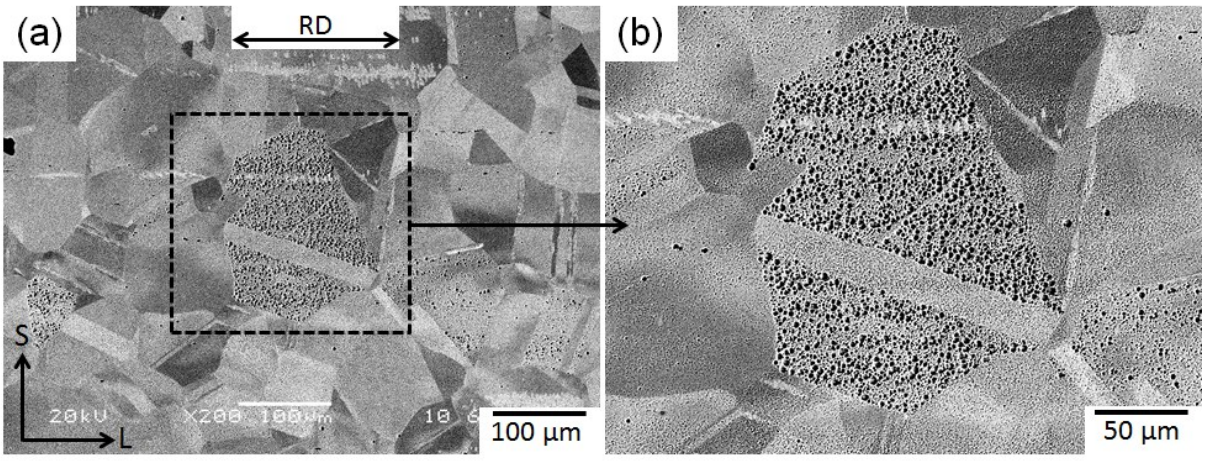

Figure 4-17 (a) Microstructure of the solution annealed 304L stainless steel plate (LS plane) after 5 s etching with Kalling's 2; (b) A grain with preferential attack with annealing twin unattacked.

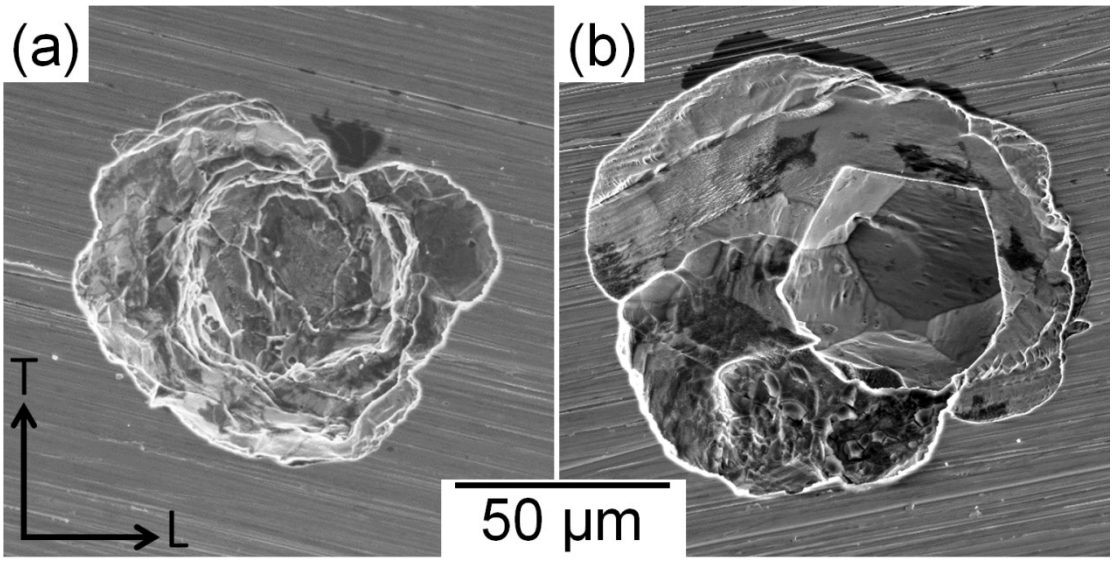

Figure 4-18 SEM images of pits on 304L stainless steel plate (LT plane); (a) base material; (b) solution annealed at 1050 °C for 1 hour followed by water quenching. Pits grown on 304L stainless steel plate under droplets of $MgCl_2$ with a chloride deposition density of ~1000 µg/cm^2, for 1 week at 43±2% RH and 30 °C.

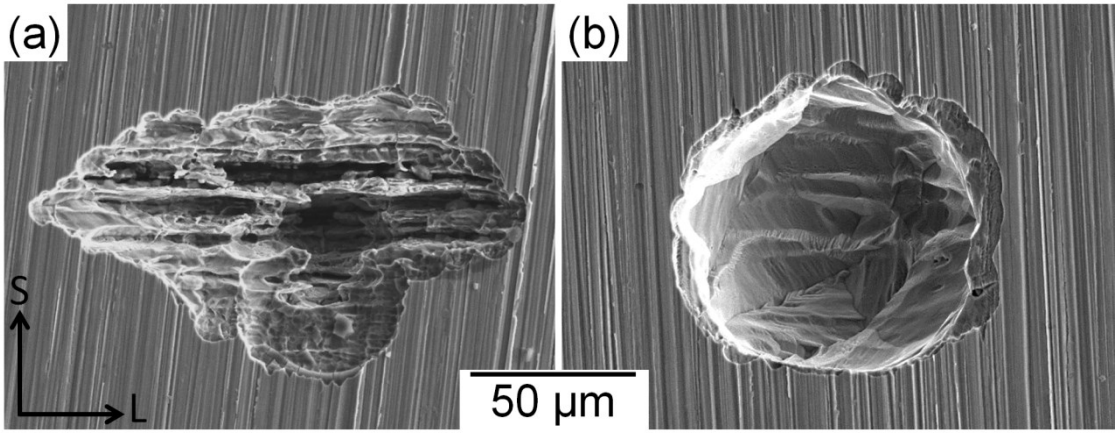

Figure 4-19 SEM images of pits on 304L stainless steel plate (LS plane); (a) as received; (b) solution annealed at 1050 °C for 1 hour followed by water quenching. Pits grown on 304L stainless steel plate under droplets of $MgCl_2$ with a chloride deposition density of ~1000 µg/cm^2, for 1 week at 43±2% RH and 30 °C.

Table 4-3 summarises the results of the corrosion tests carried out in this section on the different plate orientations of 304L stainless steel. The pit morphologies and the number of droplets pitted at each exposure RH and time are presented. It can be seen that the faceted pit morphology (marked with red) was associated with the solution annealed material. A layered pit morphology (marked with blue) was found on the LT plane of the steel while a striped pit morphology was observed on the LS and ST planes. Elongated pits (marked with violet) were usually observed on both LS and ST planes but more often on LS plane. Details of the test conditions can be taken from Table 4-3. The ratio x/y in the table represents the number of droplets with pits/total number of droplets investigated. In total, 274 droplets were investigated in this section, 261 of them were pitted.

Table 4-3 Summary of the results of pitting behaviour on the three plate orientations of 304L stainless steel under $MgCl_2$ droplets (~2 mm equivalent diameter, ~1000 μg/cm^2 CDD at deposition) at different exposure time and RH.

Exposure time	RH (%)	Orientation	Material condition	Number of droplets pitted	Pit morphology
1 week	33%	LT	As-received	14/16	Layered
		LS	As-received	11/12	9 Striped 2 Elongated
		ST	As-received	12/12	10 Striped 2 Elongated
	43%	LT	As-received	26/30	Layered
			Solution annealed	20/20	Facet pits
		LS	As-received	12/12	6 Striped 6 Elongated
			Solution annealed	9/14	Facet pits
		ST	As-received	12/12	Striped
	56%	LT	As-received	16/16	Layered
		LS	As-received	12/12	Striped
		ST	As-received	12/12	Striped
6 weeks	33%	LT	As-received	12/12	Layered
		LS	As-received	10/10	5 Striped 5 Elongated
		ST	As-received	10/10	Striped
	43%	LT	As-received	12/12	Layered
		LS	As-received	11/11	9 Striped 2 Elongated
		ST	As-received	11/11	Striped
	56%	LT	As-received	12/12	Layered
		LS	As-received	11/12	7 Striped 4 Elongated
		ST	As-received	10/10	Striped
32 hours Tomography pin samples	33%	ST (pin)	As-received	2/2	Striped
	43%	ST (pin)	As-received	2/2	Striped
	56%	ST (pin)	As-received	2/2	Striped

4.3 Discussion

4.3.1 Pit initiation sites in stainless steels and the dependence of pit shape on inclusion shape

In the 304L plate used in the current work, extended inclusions (10-20 μm in length) of both MnS and mixed oxides (Figure 4-14 and Figure 4-15, respectively) were observed parallel to the rolling direction. Highly elongated pits (~150 μm in length) (Figure 4-13(b)) developed under $MgCl_2$ droplets of chloride deposition density ~1000 μg/cm^2 at 33±2% RH. It is likely that these inclusions are the initiation sites for these very long pits.

Pit initiation in austenitic stainless steels under full immersion conditions is usually associated with inclusions such us MnS as described in Section 2.8.1. In atmospheric corrosion studies, researchers also usually attribute pit initiation to MnS inclusions [4-6, 18, 21]. Li and Hihara [129], however, found evidence that slag based inclusions under relatively large NaCl droplets can initiate pitting.

Commercial stainless steels are usually subjected to hot-rolling or cold-rolling during the casting process before component-making. During such processes, inclusions e.g. MnS can be deformed to extended needle-shaped inclusions parallel to the rolling direction [95]. The alloy used in the current work is cold rolled. Therefore, it is reasonable to expect the formation of elongated inclusions (Figure 4-13(a)).

Some authors have reported the initiation and growth of pits along the extended needle shaped inclusions [7, 18, 95, 107, 190]. Mi [18] investigated pitting

corrosion on the end of a SS304 rod under $MgCl_2$ droplets using X-ray microtomography technique and found that a deep pit can develop with time along a pre-existing defect, probably a MnS inclusion. Chiba et al. [190] investigated real-time observation of pit initiation at MnS inclusion in type 304 stainless steel in NaCl solutions and found that a pit can grow deeply into the steel matrix beneath the inclusion resulting in the formation of a large occluded cavity.

The rod used in Chiba et al.'s work was cut into coupons parallel to the rolling direction (i.e. inclusions will be parallel to the rolling direction). The pre-existing defect (probably a MnS inclusion) observed in Mi's work was also parallel to the rolling direction. The elongated pit morphology shown in Figure 4-13(b) was observed on the side grain of the plate (elongated inclusions will be parallel to the rolling direction and perpendicular to the grain of the plate). Therefore, it is reasonable to suggest that the formation of elongated pits can be attributed to the presence of elongated inclusions.

It has been reported that pit initiation can take place at the delta ferrite (δ)/austenite (γ) interface in stainless steel alloys [43, 74, 77]. Tomashov et al. [77] suggested that the susceptibility of the delta ferrite/austenite interface in 18Cr-14Ni stainless steel is because of the chromium depletion (which occurs during non-equilibrium solidification) assuming that a more imperfect protective oxide film would form over the interface, resulting in a more susceptible portion of the surface for pit initiation. Manning et al. [43, 74], however, disproved the presence of chromium depletion region using Scanning Transmission Electron Microscopy (STEM) on Type 304L stainless steel. They suggested that

segregation of impurities such as sulphur and/or phosphorus to the boundary increases the dissolution tendency of protective film over the δ/γ interface. In addition, S might tend to inhibit the repassivation kinetics at the δ/γ interface.

In the present study, it can be seen that elongated inclusions (MnS and mixed oxide inclusions) were found to be aligned with the residual delta ferrite stringers (Figure 4-13a and figure 4-14), which might had a direct role in pit initiation and propagation.

4.3.2 Observation of ferrite and martensite in austenitic stainless steels

Delta ferrite δ (bcc, ferromagnetic), martensite ϵ (hcp, paramagnetic) and strain-induced martensite α′ (bcc, ferromagnetic) can be seen in metastable steels e.g. 304L and 316L [35, 36, 42, 44, 67, 68, 70, 187, 191-194].

In fully austenitic stainless steels, the presence of residual delta ferrite (2-5%) as a secondary phase has been confirmed by a number of researchers [42, 67, 68, 70]. The formation of delta ferrite in austenitic stainless steels has been described in terms of the solidification process (Section 2.2). However, during non-equilibrium solidification processes delta ferrite is retained as a secondary phase in a matrix of austenite [36, 70, 187].

Ferrite stringers can form as a result of the segregation of ferrite stabilising elements (particularly chromium) during solidification and thermo-mechanical processes such as cold rolling and hot rolling. Consequently, ferrite stringers are usually aligned along the rolling direction [35, 191]. The alloy used in this work was cold-rolled and solution treated at 1040-1100 °C followed by forced air

cooling. Therefore, it is reasonable to expect the formation of residual delta ferrite in the form of stringers (bands).

In austenitic stainless steels, the cold working process can lead to the formation of strain (deformation) induced martensite α' (bcc) [192]. It has been reported that deformation-induced martensite preferentially nucleates at twin boundaries and grain boundaries [44, 193]. In this work, the occurrence of non-austenitic phase along the twin boundaries (Figure 4-1(b region 2)) and as equiaxed grains (Figure 4-1(b region 3)), which are not orientated along the rolling direction, suggest the possible formation of stress-induced martensite. This has been observed previously in similar alloys [194]. The trace presence of this strain-induced martensite is most likely caused by surface grinding and cold working [194].

The amount of ferrite predicted from the 304L alloy used in this research is estimated via predictive methods; the Schaeffler diagram (Figure 4-4), DeLong diagram (Figure 4-5), WRC diagram suggested 12%, 6.2% and 8% respectively. However, these diagrams are limited in their accuracy by specific considerations in the formation of retained ferrite. These diagrams depend on accurate measurements of the chemical composition of the alloy [66]. Moreover, these diagrams do not consider the effect of the cooling rate upon solidification of the residual delta ferrite. The Schaeffler diagram has not been verified as accurate for 304L but is known to be valid for a wide range of other austenitic stainless steels [63].

EBSD was used to quantify the presence of ferrite experimentally. In this technique, it is not possible to distinguish between delta ferrite (bcc) and strain-induced martensite α′ (bcc) so their volumes are combined. The volume fraction of the combined ferrite-martensite phases obtained using EBSD (~6%) correlates with the amount obtained from DeLong diagram within a reasonable error for techniques used.

XRD can be used to detect and quantify delta ferrite and both martensite phases. However, XRD has limitations in use that include a minimum volume needed to achieve sufficient signal (quoted as 5% vol [45, 65]). XRD is also sensitive to orientation effects [195]. The small peak of delta ferrite observed in XRD results (Figure 4-2) shows at least 5% volume of delta ferrite.

It has been reported that VSM can be successfully used to determine the amount of residual ferrite in stainless steel alloys [64], as well as stress induced martensite [45, 192]. However, the accuracy of VSM method depends on the presence of nonmagnetic phases and the availability of standard samples. Moreover, if more than one ferromagnetic phase is present in the sample the result obtained will be the combination of both phases. Another limitation is making identical (in weight) samples for comparisons. In addition, in this work, due to system limitations it was not possible to completely saturate the samples (i.e. it was not possible to reach the linear parts of magnetisation) to obtain the saturation magnetisation (which is proportional to the volume percent of the ferromagnetic phase and can be obtained from intercepting the linear parts of magnetisation curves back to the zero applied field). Hence, the amount of residual ferrite was not quantified. However, Figure 4-3 shows that there is a

decrease in magnetisation after annealing which suggests a decrease in ferrite content.

Since strain- induced martensite α′ (bcc), and residual delta ferrite (bcc) are very similar in 304L stainless steel, certainly in terms of XRD and magnetic measurements, it is not be possible to distinguish between them. The only way to separate them is to identify the regions of ferrite/martensite from metallography, then do EDX in the SEM. If there are regions of delta ferrite they should have lower Ni content (significantly different) than austenite and strain induced martensite. An EDX map (Figure 4-9) and line scan (Figure 4-10) across the elongated micro grains successfully showed Cr-enriched and Ni-depleted regions, indicating the presence of ferrite.

4.3.3 Effect of ferrite on pit morphology

Figure 4-8 show that the morphology of corrosion pits was affected by the orientation of residual delta ferrite in the plate. Layered attack morphology was observed on LT plane, which appears as circular layers on the top surface of the plate. A striped morphology, however, was observed on both LS and ST planes, which appears as horizontal sheets parallel to the rolling direction. In all cases, the ferrite was preferentially attacked, as can be seen, for example, in figures 4.9(f) and 4.10(e).

As mentioned previously, pits generally initiate at inclusions, most commonly MnS inclusions, for stainless steel. However, pit initiation can also take place at the delta ferrite (δ)/austenite (γ) interface in Type 304L [43, 74] and 18Cr-14Ni stainless steels [77]. In this work, it seems the growth of atmospheric corrosion

pits takes place preferentially in the residual delta ferrite. The sheets of undissolved austenite inside the pit might act as a barrier for diffusion of ions therefore the attack could appear to be more crevice corrosion attack.

In terms of pitting theory, there will be slight differences in the continued corrosion on LT and the LS/ST planes, caused by the preferential dissolution of delta ferrite inside the pit. To propagate, pits require the diffusion of metal ions away from the corroding surface to be less than the generation of metal ions [118]. In a relatively broad pitting surface, such as on the LT plane, the required area requiring a sufficiently high current density to maintain a salt layer is much higher than that inside the crevices of a LS/ST plane pit. As such, the cathodic current needed to be drawn on the LT plane is higher. This would cause these pits to be less stable in boundary conditions, such as concentration dilution in higher RH. Pits on the LS/ST planes would require much less total cathodic current to be drawn to keep the pit alive as only the narrow region in between the remaining austenite ridges would need to remain active which has a significantly lower surface area.

Figure 4-9 and Figure 4-10 clearly show that ferrite bands have been preferentially attacked on both the LS and ST planes, giving a layered morphology to the pit. Pitting on the LT plane (top surface of the plate) showed a circular layered structure. FIB milling next to a pit on the LT plane showed that attack undercut the surface and propagated along the ferrite bands (Figure 4-11). From the tomography results (Figure 4-12), it is evident that attack on the ST plane after 32 hours also shows propagation parallel to the plate surface and thus parallel to the ferrite bands. This is confirmed by SEM after the

experiment. Overall, the orientation of residual ferrite in the plate strongly influenced the morphology of atmospheric pits.

Prosek et al. [15, 16] studied the corrosion resistance of eight stainless steel grades, including type 304 and 316L austenitic stainless steels, under salt solutions of pure $MgCl_2$, $CaCl_2$, and NaCl as a function of temperature (20-50˚C) and RH (15-70%). They reported that, for duplex stainless steels exposed to different conditions, the corroded phase was ferrite, which contained more Cr (identified by the use of Energy Dispersive X-ray (EDX) analysis. However, they didn't give information about austenitic stainless steels type 304 and 316L.

In duplex stainless steels under chloride deposits in atmospheric conditions, it is often observed that one phase, either ferrite or austenite, corrodes preferentially [15, 16, 24, 25, 27-29]. This depends on the exposure conditions and material composition. Lothongkum et al. [196] reported that the phase sensitivity to localised corrosion in aerated NaCl solution is a function of the concentration of nitrogen (N), which is one of the strongest austenite stabilizers, in highly alloyed duplex stainless steels. They found that the corroded phase in the tested stainless steels with nitrogen alloying was ferrite while those without nitrogen alloying were austenite. They attributed this to the higher dissolved nitrogen in austenite phase than in ferrite phase which might increase the pitting resistance equivalent number (PRE) of austenite to be higher than that of ferrite (although ferrite had a higher chromium content than austenite).

Based on this work and the results of the energy dispersive X-ray (EDX) analysis (Figure 4-8, 9, 10), it can be seen that the ferritic phase was preferentially attacked in all exposure conditions to which the 304L stainless

steel was exposed. Based on the cast analysis given in mill certificate (see Appendix 1), the 304L stainless steel had 0.072 wt. % nitrogen, therefore it is possible nitrogen had the similar effect shown in Lothongkum's work [196]. It was not possible to detect the nitrogen content of either phase using the EDX analysis. Therefore, the pitting resistance equivalent number (PREN) of ferrite and austenite were not obtained. The PREN of the phases is a function of the concentrations of alloying elements present in the phase therefore it can vary significantly if there are any differences in phase's compositions [197].
Örnek et al. [24] studied atmospherically-induced corrosion (AIC) of two grades of duplex stainless steels, 2205 and 2507, under $MgCl_2$ salt deposits exposed to 80 °C and 40% RH for 7 days. They found that ferrite is more susceptible to corrosion than austenite in the as-received microstructures of both grades. They also found that heat treatment (at 750 °C for 3 hours followed by water quenching) led to selective attack of ferrite and ferrite/austenite interfaces in Grade 2205, while in Grade 2507, mainly primary and secondary austenite was attacked.

Donohoe et al. [75] found up to 2% ferrite in an austenitic stainless steel and observed a striped morphology during pitting corrosion of austenitic stainless steel under full immersion condition and attributed it to preferential attack of austenite, leaving ferrite unattacked.

The active-passive transition behaviour between austenite and ferrite occurs in a narrow range of potentials (Figure 2-9), with the active peak for ferrite being slightly lower in potential for that of austenite [83], so it is possible that small changes in potential can change the active phase under particular conditions. It

should be noted that Donohoe et al. [75] were conducting experiments in full immersion conditions instead of the atmospheric conditions in the current work, so a shift in local potential can lead to the preferential dissolution of ferrite instead of austenite in this study.

More recently, Örnek et al. [82] found that corrosion attack of ferrite and austenite is a function of location within the droplet on grade 2205 duplex stainless steel under droplets containing a mixture of $FeCl_3$:$MgCl_2$ after exposure to 50°C and 30% RH for approximately one year. At the centre of the droplet, both phases were found to be attacked while at the rim of the droplet, austenite was found to be attacked. In between of these two regions, ferrite was found to be attacked. They discussed this observation in light of possible local variations of electrochemical potentials under the droplet. In this work, however, the preferential attack of ferrite was not a function of pit location within the droplet, for example in Figure 4-9 the pit is near the centre of the droplet and in Figure 4-10 the pit is at the edge of the droplet. This difference in results might be due to the different material and experiment conditions such as salt solution (mixture of $FeCl_3$:$MgCl_2$) used in Örnek's study [82].

4.3.4 Effect of annealing on the ferrite content of 304L stainless steel

A number of researchers have reported that solution annealing treatments are successful in reducing or eliminating retained ferrite in austenitic stainless steels [36, 42, 67, 68]. This is consistent with the results obtained in the present work. The preferential attack of ferrite bands seen in Figure 4-7(b) was not observed after the solution annealing treatment (Figure 4-16 and Figure 4-17). Although the volume fraction of ferrite was not quantified after solution annealing, VSM

results (Figure 4-3), also indicate a significant reduction in ferrite content in this work.

4.3.5 Effect of annealing on pit morphology

To my knowledge, this is the first study to examine the effect of solution annealing on pit morphology on different plate orientations of austenitic stainless steel in atmospheric condition environments. Figure 4-18 and Figure 4-19 shows that following solution annealing of the stainless steel at 1050 °C for 1 hour, the layered morphology ordinarily present in these pits is no longer observed. Instead a faceted pit has formed. This implies that solution annealing resulted in different pit morphology.

In full immersion condition, faceted pits have been previously reported on both austenitic stainless steels and ferritic chromium steels [110, 125, 126]. Schwenk [125] found regularly etched pits, mostly hexagons and squares (Figure 2-14), on 18Cr-10Ni stainless steel surface (which has been solution annealed at 1300 °C, duration not given, followed by water quenching) in solutions containing Cl^- at low applied potentials. Based on the examination of the etch pits Schwenk [125] reported that pit bounding planes belong to the type {111}, having the lowest dissolution rate (the most closely packed crystal plane in the case of austenite).

In this study, it was not possible to confirm the crystallographic orientation of the pit facets. Based on Schwenk's observation, however, It is possible that the planes of the flat-walled pit to be belong to the {111} close-packed crystal planes of austenite. Further research is required to confirm this.

4.4 Conclusion

The effect of microstructure on atmospheric pitting corrosion of 304L stainless steel under $MgCl_2$ salt droplets at 30 °C has been investigated.

1. Atmospheric pitting corrosion of 304L austenitic stainless steel is strongly affected by the presence of residual delta ferrite. Ferrite bands were preferentially attacked on both LS and ST planes and corrosion continued to propagate down the ferrite bands. On the LT plane, pits propagated downwards into the steel, but also parallel to the rolling direction along the ferrite bands. This has been shown using FIB.

2. Solution annealing of stainless steel to remove the residual ferrite leads to equiaxed etched faceted pits. The facets may be {111} planes. Such planes are most densely packed for the austenite.

3. Pits can take on an elongated shape. This is attributed to the presence of elongated MnS and mixed oxide inclusions banded along the rolling direction.

5 Effect of relative humidity on atmospheric pitting corrosion of Type 304L and 316L austenitic stainless steels

5.1 Introduction

The atmospheric pitting corrosion of stainless steel under Cl^- rich droplets is known to be influenced by the relative humidity (Section 2.10.2). The concentration of the solutions that form on the metal surface depends on the relative humidity to which the deposits are exposed [6, 141].

Pit morphologies have been found to be affected by relative humidity [6] and microstructure [18, 26]. It is important to obtain large data sets in order to draw convincing conclusions of the most significant factors affecting atmospheric pitting corrosion of commercial alloys. In this study and some recently published studies [6, 134, 135, 198], large data sets were obtained.

The work presented in this chapter will explore the effect of relative humidity on the pit morphology of atmospheric pitting corrosion of 304L and 316L austenitic stainless steels. The effect of pit position as well as the exposure time on the pit size is also investigated. The formation of micro-droplets surrounding pits formed at or close to the droplet edge will be described in Section 6.4.4.

The plates were used “as received” (see Appendix 1) and did not go through any additional solution treatments.

5.2 Results

5.2.1 Time-dependence of growth of pits

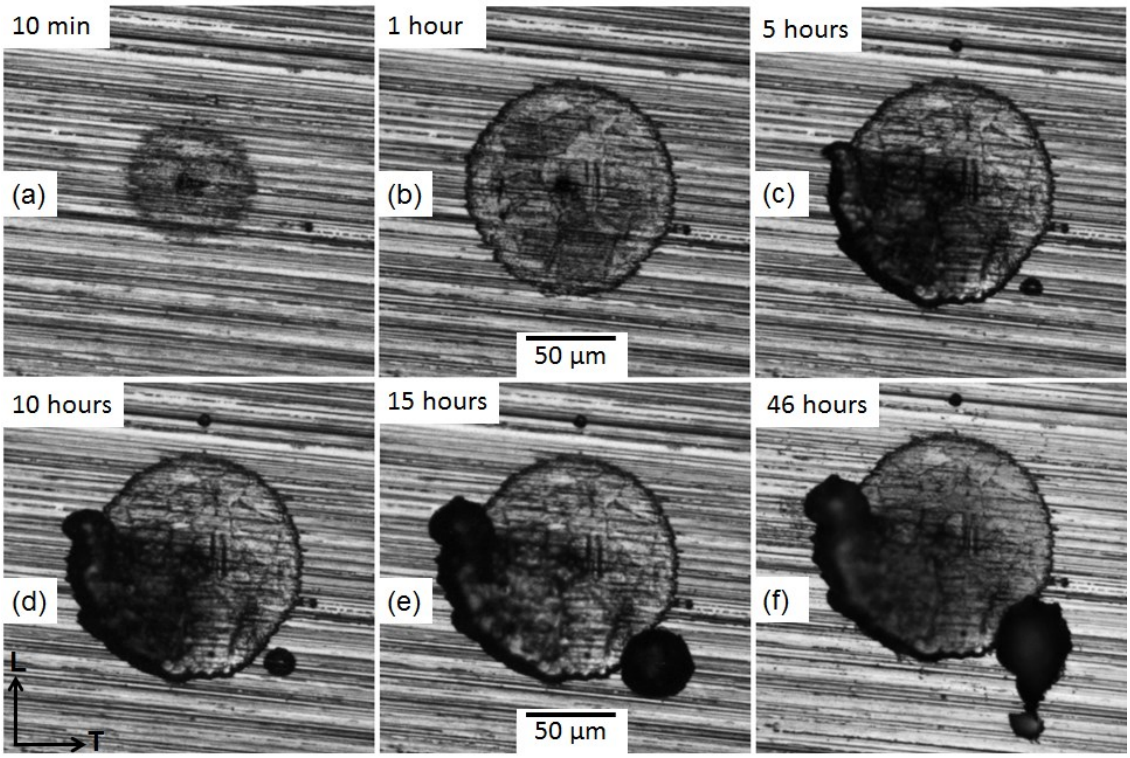

Figure 5-1 Time sequence of optical images of a pit grown under a $MgCl_2$ droplet (~1000 µg/cm^2 CDD) on 304L stainless steel (LT plane) in ambient conditions (RH 37±3%, temperature 24±2 °C).

Figure 5-1 shows a sequence of micrographs of a pit growing in a droplet of ~1000 µg/cm^2 CDD $MgCl_2$ in ambient conditions (RH 37±3, temp 24±2 °C) on 304L. 10 minutes after droplet deposition, shallow dish-like attack is observed with a deeper hole in the centre (Figure 5-1(a)). The shallow attack continues to grow radially for another hour (Figure 5-1(b)), with the shallow dish region showing crystallographic attack of the underlying microstructure, but is still shallow enough to show work-hardening effects from grinding. The shallow dish region stops growing radially after 1 hour. Instead, both “ear-shaped” attack [21] into one edge of the shallow dish and localised “satellite” pitting [6] outside the

dish begin simultaneously (Figure 5-1(c)). Both ear-shaped attack, which produces an “earing” morphology (Street et al. [6] call them “spiral” pits), and satellite attack continue to grow at the same time (Figure 5-1(d) and (e)). After 15 hours, the earing attack has ceased to operate and the earing morphology does not change with continued pitting (Figure 5-1(f)). However, the satellite attack does continue to grow until the end of the experiment at 46 hours.

The shallow dish diameter was measured by using the FIJI/ImageJ software, the procedure was detailed in Section 3.8.2. No significant change was observed in the shallow dish diameter after the first hour of exposure. After 1 hour (Figure 5-1(b)), the shallow dish diameter was found to be about 117 μm. After 46 hours (Figure 5-1(f)) it was found to be 120 μm. This is consistent with the results observed by Street et al. [6], who carried out the time-lapse measurements on the same material and plane at RH of 33% with a CDD of ~750 μg/cm^2) . They reported that the shallow dish diameter had stopped increasing after 2 hours of exposure, but further etching was seen. Street carried out the. They also observed that the diameter of the shallow dishes increased as the distance from the droplet edge increased [6].

A large number of shallow dishes were measured in this study at different RH values and at 1 day or 1 week of exposure (See Table 5-4) on both 304L and 316L. This will be shown in the following sections.

5.2.2 Pit covers

Figure 5-2(a) shows satellite pitting attack found on 304L after 1 day at 35% RH under a $MgCl_2$ droplet with a CDD of ~1000 μg/cm^2. The shallow dish is surrounded by several satellite pits at different distances (Figure 5-2 b and c). Each of these pits was found to have a cover as shown in the SEM image (Figure 5-2(c)). The cover was found to have grinding marks that matched with those on the metal surface Figure 5-2(d). Three pit covers were analysed with EDX and found to be enriched in Cr, Mn, S, O and Cl. Table 5-1 shows the chemical compositions of typical pit covers formed on 304L and 316L. Similar pit covers were also found on pits after 1 week exposure at 45% RH.

In tomography experiments, pits were also observed to have covers. From the vertical section in Figure 5-3, it can be seen that there is a bright line just above the pit, consistent with the presence of a high density cover. The pit was observed on 304L pin sample under $MgCl_2$ droplet of CDD ~1000 μg/cm^2 after exposure at 45% RH for 31 hours at 21±1 ºC.

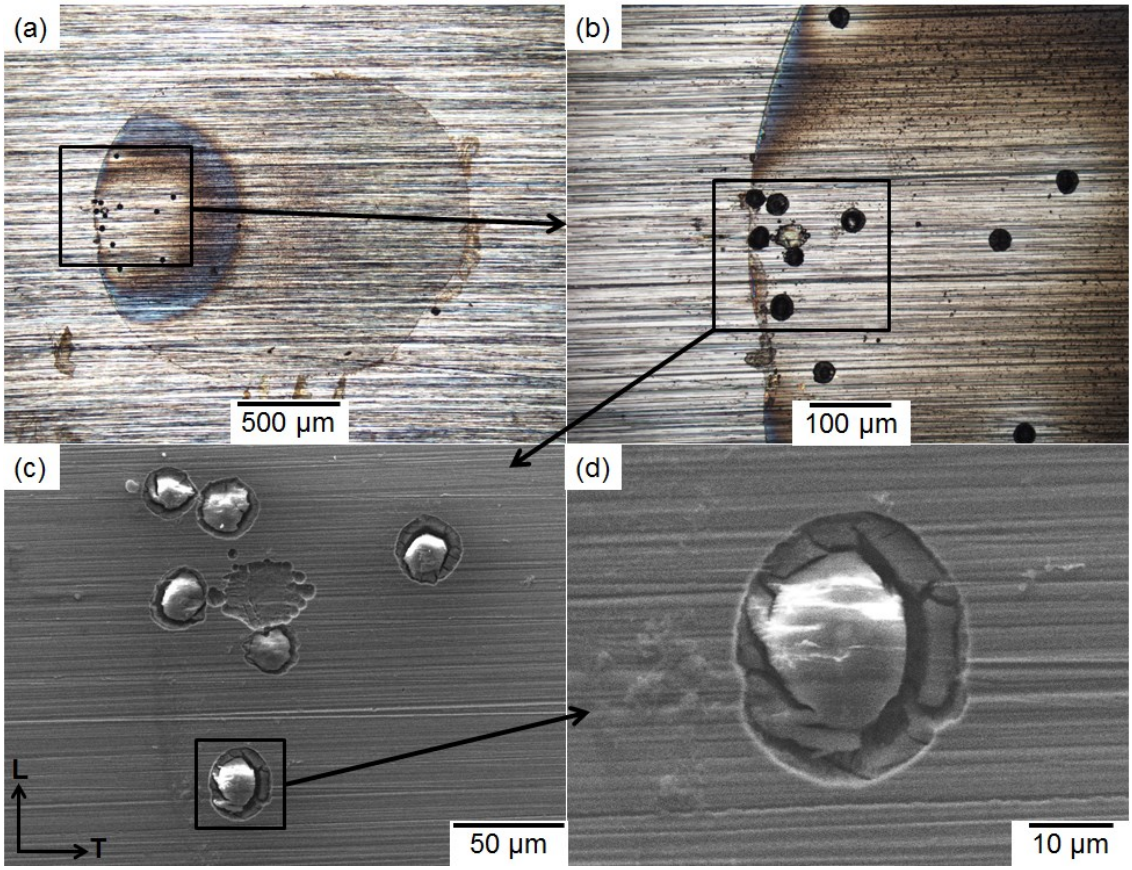

Figure 5-2 Satellite pitting attack found under a droplet of $MgCl_2$ of CDD ~1000 µg/cm^2 on 304L stainless steel (LT plane) after 1 day exposure at 35% RH and 30 °C; (a) after washing with DI water; (b) magnified section of (a); (c) SEM image of selected region of (b) showing the shallow dish region and the satellite pits with caps; and (d) magnified image of a satellite pit showing the pit cover.

Table 5-1 typical EDX analysis of pit typical covers observed on 304L and 316L after 1 day exposure at 35% RH and 30 °C.

	Weight %	Cr	Ni	Mn	S	Si	O	Cl	Fe
304L	Pit cover	60.0	0	4.6	3.3	0	13.6	15.6	3.8
316L	Pit cover	60.1	1.9	0	6.7	0.7	13.1	9.9	7.5

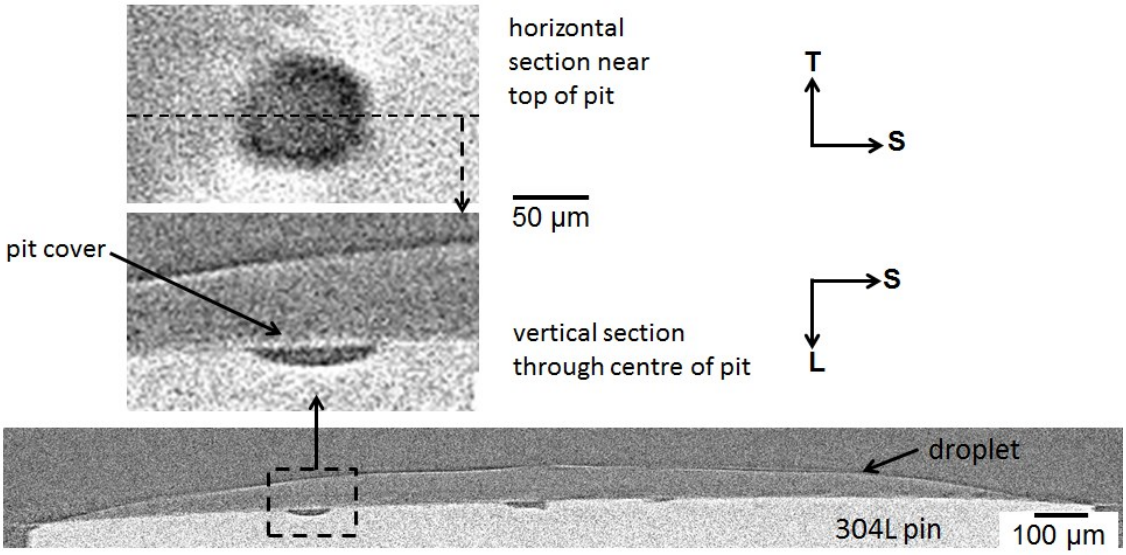

Figure 5-3 X-ray tomographic horizontal and vertical sections of a pit found on a 304L pin (2 mm diameter, ST plane) under an $MgCl_2$ droplet (CDD ~1000 µg/cm^2) after exposure at 45% RH for 31 hours at 21±1 ºC.

5.2.3 Effect of the pit position on the diameter of the shallow dish for 304L and 316L stainless steel

Pits appeared to initiate randomly within a droplet, with no clear preference towards the centre or edge of the droplet. However, close inspection showed that the diameter of the shallow dish region depends on the distance of the pit from the edge of the droplet. The technique used to measure the shallow dish diameter is described in Section 3.8.2.

5.2.3.1 Effect of the pit position on the diameter of the shallow dish for 304L stainless steel at 35% RH

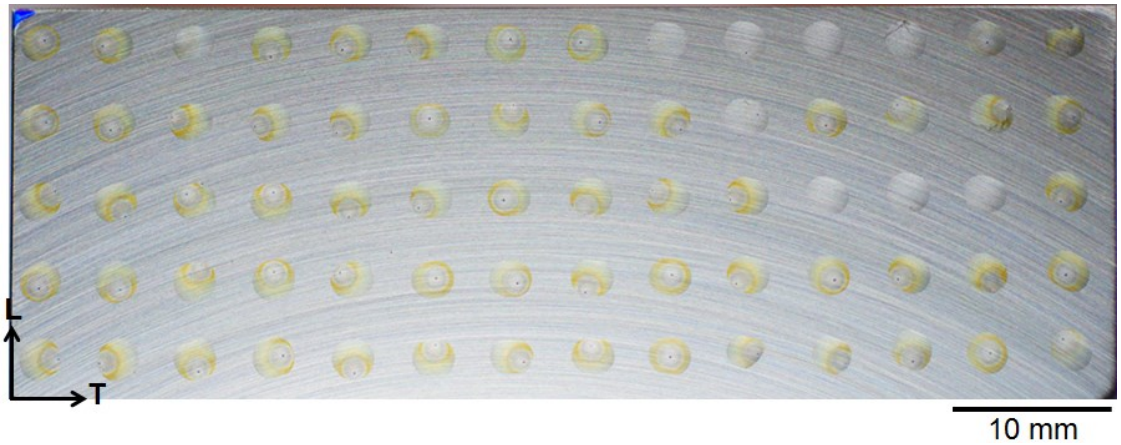

Figure 5-4 Macro photo of 304L plate surface (LT plane) deposited with arrays of $MgCl_2$ droplets (~2.5 mm equivalent diameter with ~1000 µg/cm^2 CDD at deposition), after 1 day exposure at 35% RH and 30 °C.

Figure 5-4 shows a 304L stainless steel plate after pitting at 35% RH for 1 day under droplets of $MgCl_2$ with ~1000 µg/cm^2 CDD. 66 out of 70 droplets pitted. 25 out of 66 pits were seen to be associated with micro-droplets. 19 pits showed an earing morphology and 47 pits showed satellite pitting as described in [6]. Typical examples of these morphologies are shown in Figure 5-5. In all cases attack appears to start with a shallow dish region that develops into deeper attack at the dish's edge. The satellite morphology is generally found for pits close to the droplet edge, and shows several small pits that mostly develop around the perimeter of the shallow dish region, with some small pits initiating inside the shallow dish and some far away in a few instances. The earing morphology is generally found for pits closer to the centre of the droplet, and always shows an ear-shaped attack at one side of the shallow dish with no appearance of any small pits around or close to the perimeter of the dish region.

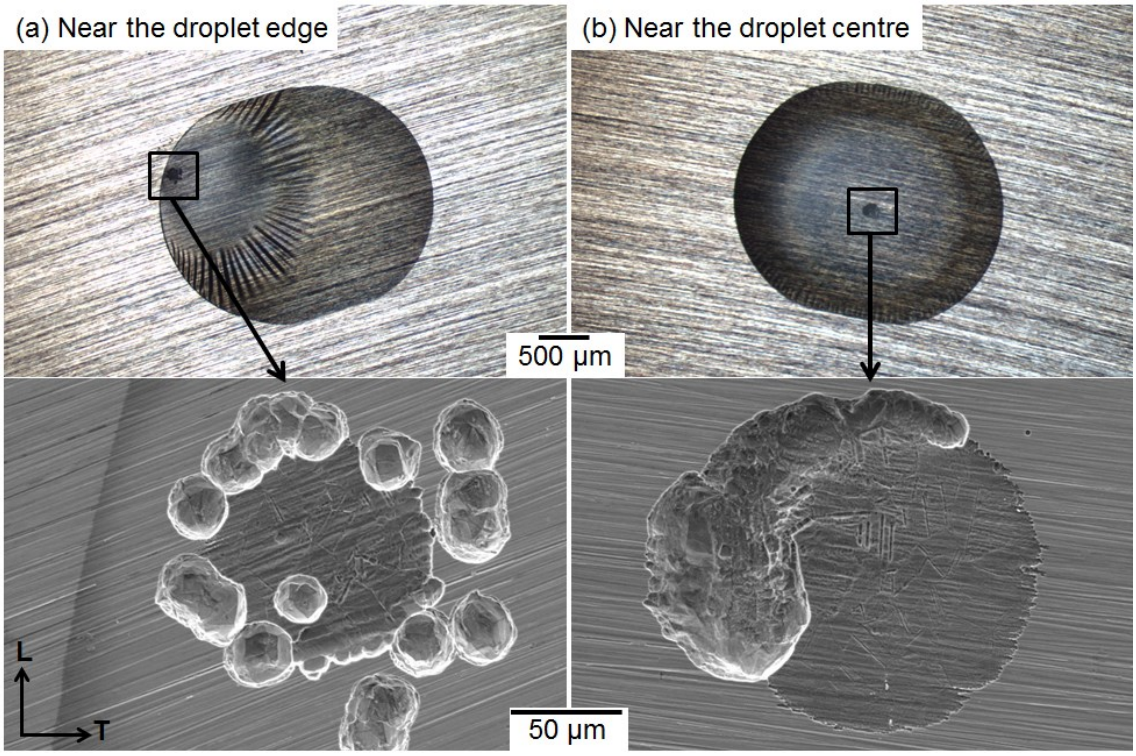

Figure 5-5 Typical pit morphologies formed on 304L stainless steel (LT plane) under $MgCl_2$ droplets (of ~2.5 mm equivalent diameter with ~1000 µg/cm^2 CDD at deposition), after 1 day exposure at 35% RH and 30 °C; (a) near the droplet edge; (b) near the droplet centre.

Propagation of satellite pits were often seen to be influenced by the local crystal structure and orientation. Figure 5-6 shows pits that have both earing attack and satellite pits, and it is the satellite pits that have crystallographic facets.

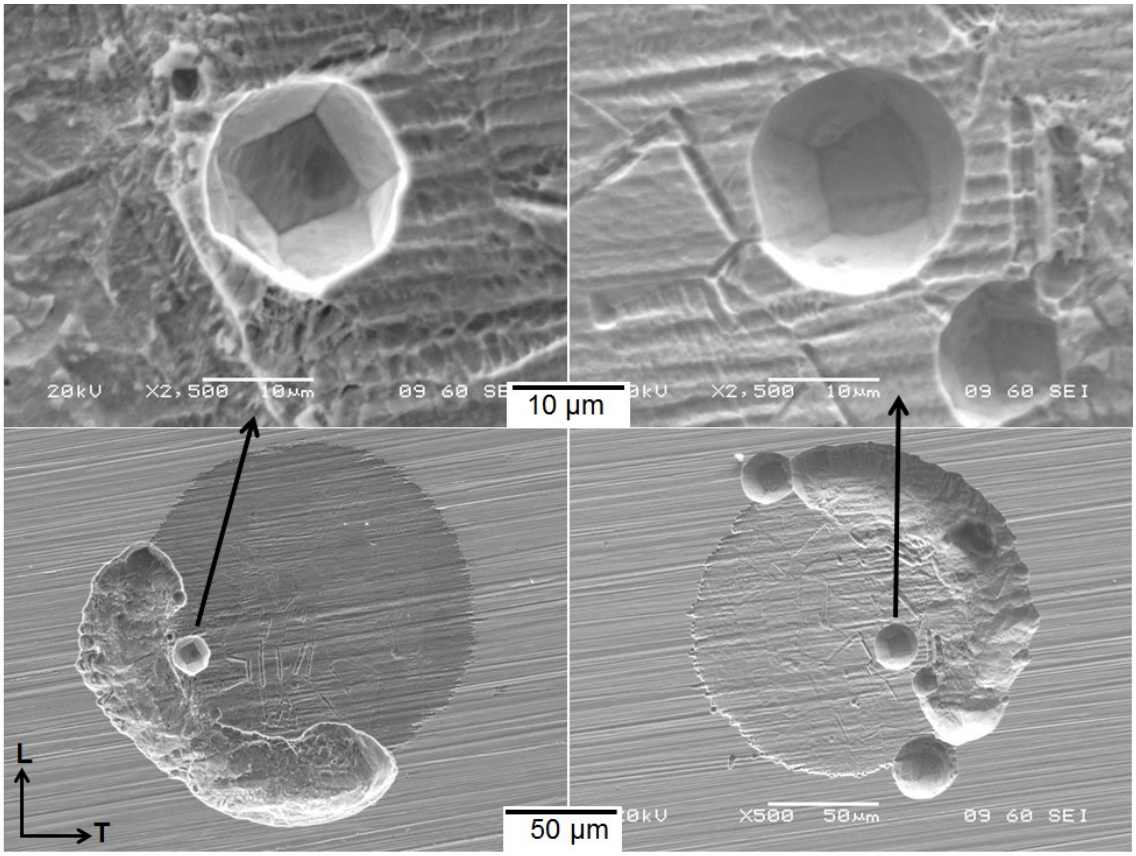

Figure 5-6 Typical pit morphologies of satellite and earing pits affected by the local crystal structure of 304L stainless steel (LT plane) under $MgCl_2$ droplets of equivalent diameter of ~2.5 mm with ~1000 µg/cm^2 CDD at deposition after 1 day exposure at 35% RH and at 30 °C.

Figure 5-7 shows an array of droplets on 304L following 1 week exposure at 35% RH at ~1000 µg/cm^2 CDD. All 70 droplets pitted. 21 of the pits were found to be associated with micro-droplets. SEM of the pits (Figure 5-8) show that the satellite pits continued to grow over one week compared to 1 day exposure (Figure 5-5). Where more than one satellite pit continued to grow, these were often similar in size. Earing morphology was also observed along with deeper attack. The continued material loss after 1 week meant that in 13 out of 70 cases, the shallow dish region was heavily attacked and was not possible to measure (Figure 5-9).

Figure 5-7 Macro photo of 304L plate surface (LT plane) with arrays of $MgCl_2$ droplets of ~2.5 mm equivalent diameter with ~1000 μg/cm^2 CDD at deposition, after 1 week exposure at 35% RH and 30 °C.

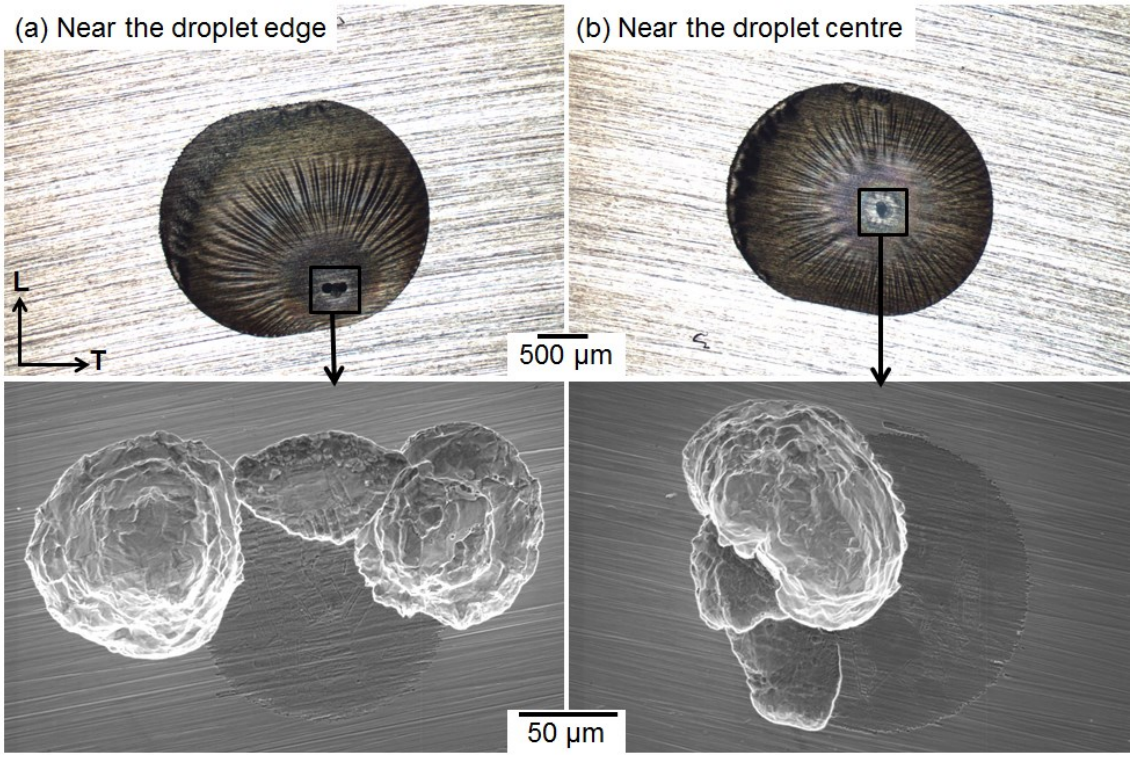

Figure 5-8 Typical pit morphologies formed on 304L stainless steel (LT plane) under $MgCl_2$ droplets (~2.5 mm equivalent diameter with ~1000 μg/cm^2 CDD at deposition), after 1 week exposure at 35% RH and 30 °C; (a) near the droplet edge; (b) near the droplet centre.

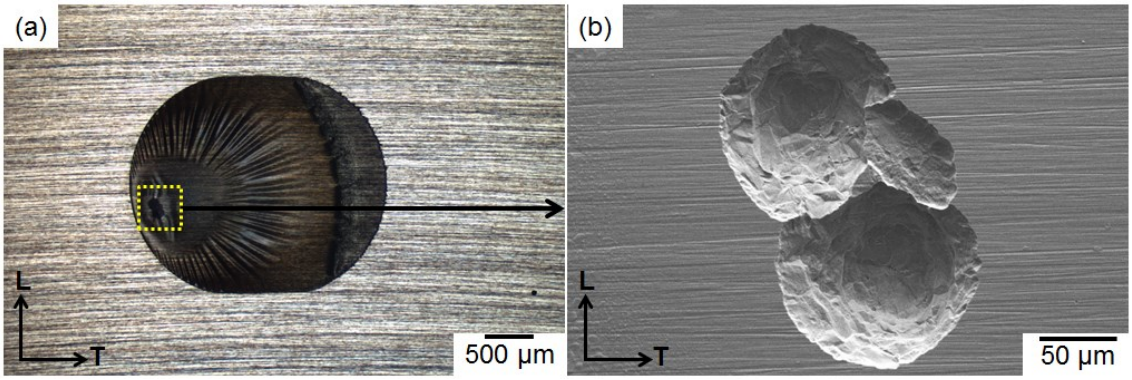

Figure 5-9 Typical pit morphology formed on 304L stainless steel (LT plane) under $MgCl_2$ droplets (~2.5 mm equivalent diameter with ~1000 µg/cm^2 CDD at deposition), after 1 week exposure at 35% RH and 30 °C; (a) droplet with a pit near the droplet edge; (b) SEM of pit with heavily attacked shallow dish region.

The position of the initiation site inside the droplet affects the morphology that develops during corrosion. Figure 5-10 shows that the occurrence of satellite pitting morphology is increased when pits initiate towards the edge of the droplets, and earing morphology is more common towards the centre of the droplets for both 1 day (Figure 5-5) and 1 week (Figure 5-8) exposure tests. The size of the shallow dish region is also affected, and is usually smaller towards the edge of the droplet and larger towards the centre for both 1 day and 1 week exposure tests. Where the shallow dish could be seen after 1 week exposure, it was of a similar size to those seen after 1 day of exposure (Figure 5-10), confirms the idea that the shallow dishes stop growing at an early stage (~1hour).

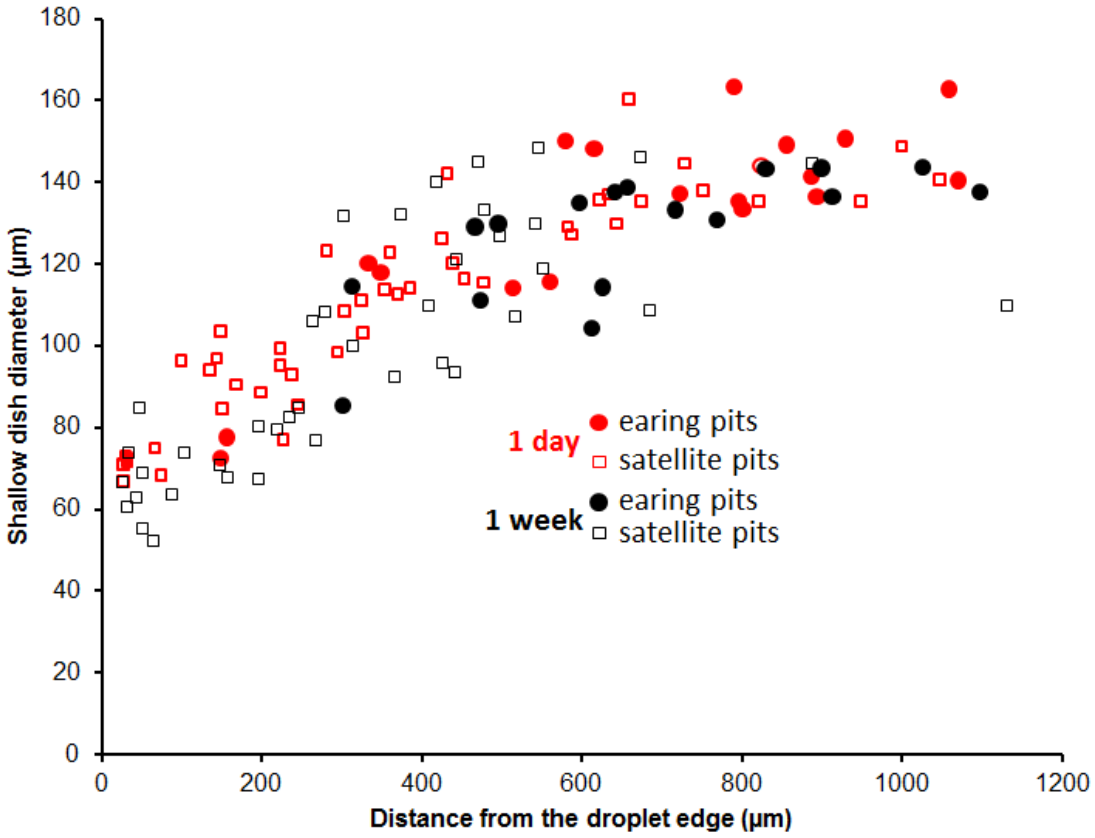

Figure 5-10 Shallow dish equivalent diameter versus the distance from the droplet edge in $MgCl_2$ droplets (~2.5 mm equivalent diameter, ~1000 µg/cm^2 CDD at deposition) on 304L (LT plane) exposed at 35% RH and 30 °C. 1 day exposure is marked with red circles and squares while 1 week exposure is marked with black circles and squares. The equivalent diameter is calculated as the diameter of a circle with the same area as the dish.

5.2.3.2 Effect of the pit position on the diameter of the shallow dish for 316L stainless steel at 35% RH

Figure 5-11 Macro photo of 316L plate surface (LT plane) after 1 week exposure at 35% RH and 30 °C under $MgCl_2$ droplets (~2.5 mm equivalent diameter, CDD of ~1000 µg/cm^2 at deposition); plate has been washed with DI water.

Figure 5-11 shows a 316L plate after exposure for droplets of $MgCl_2$ with a CDD of ~1000 µg/cm^2 at 35% RH after 1 week. 52 out of 65 droplets pitted, with 30 pits showing earing morphology (usually formed towards the centre of the droplet) and 22 pits showing satellite pitting formed towards the edge of the droplet. Typical examples of both these morphologies are shown in Figure 5-12. The satellite morphology shows an attack at one edge of the shallow dish region in addition to the formation of small pits at the perimeter of the dish region. In some cases the small pits were found at a distance close to the dish region. While the earing morphology only shows an ear-shaped attack at one edge of the shallow dish region.

As described above for 304L at the same RH, the shallow dishes have the trend of formation of smaller diameters towards the edge of the droplet and larger diameters towards the centre of the droplet. The shallow dishes were approximately of similar diameter (100±30 μm) to those seen on 304L (110±30 μm) after 1 week of exposure at 35% RH (Figure 5-13).

Among the total number of pits (52 pits), 24 of them were found to be associated with micro-droplets.

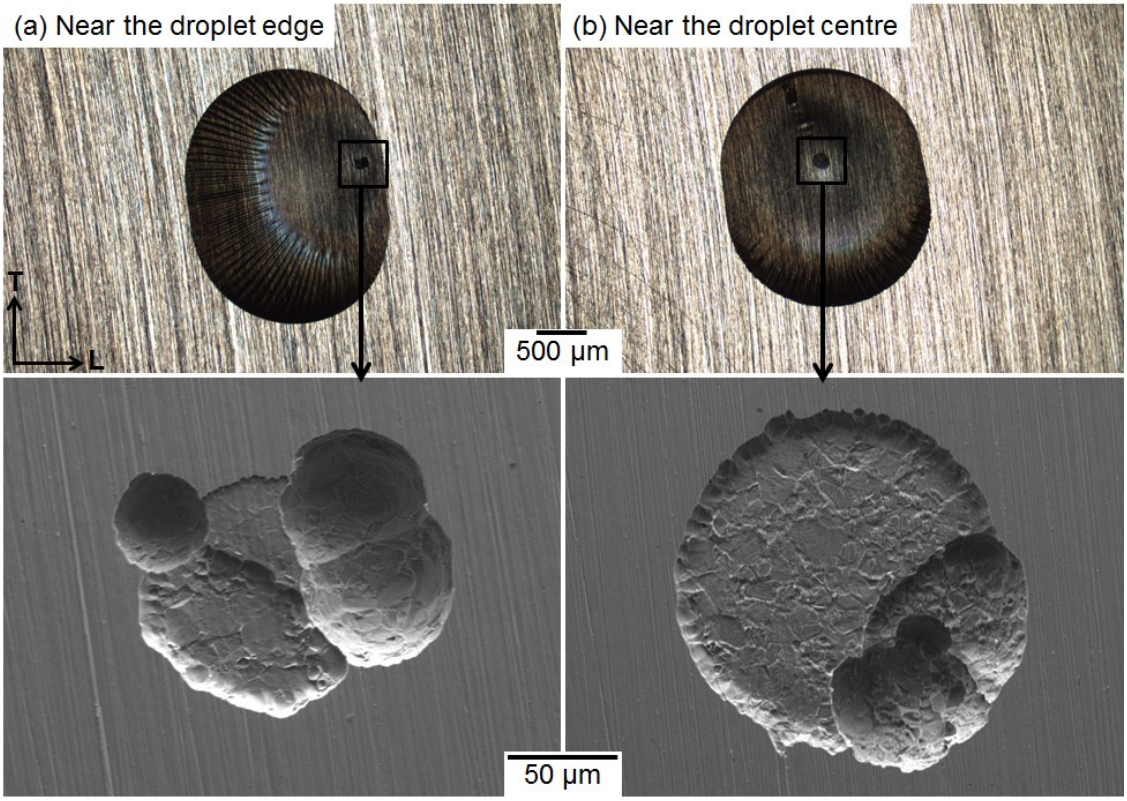

Figure 5-12 Typical pit morphology formed on 316L plate (LT plane) at 35% RH under $MgCl_2$ droplets (~2.5 mm equivalent diameter with ~1000 μg/cm^2 CDD at deposition), after 1 week exposure at 30 °C; (a) near the droplet edge; (b) near the droplet centre.

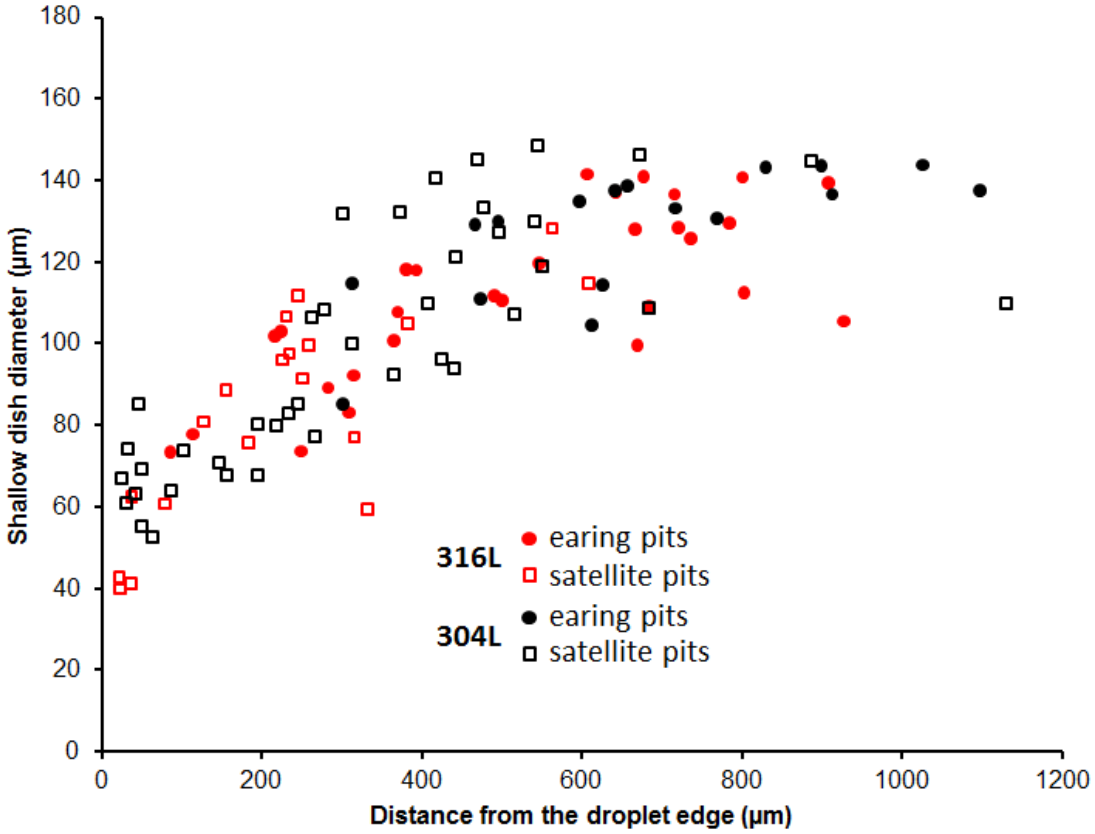

Figure 5-13 Shallow dish equivalent diameter as a function of distance from the droplet edge for $MgCl_2$ droplets (~2.5 mm equivalent diameter, ~1000 µg/cm^2 CDD at deposition) on 304L and 316L (LT plane) exposed at 30 °C and 35% RH for 1 week. The equivalent diameter is calculated as the diameter of a circle with the same area as the dish.

5.2.3.3 Effect of the pit position on the diameter of the shallow dish for 304L stainless steel at 45% RH

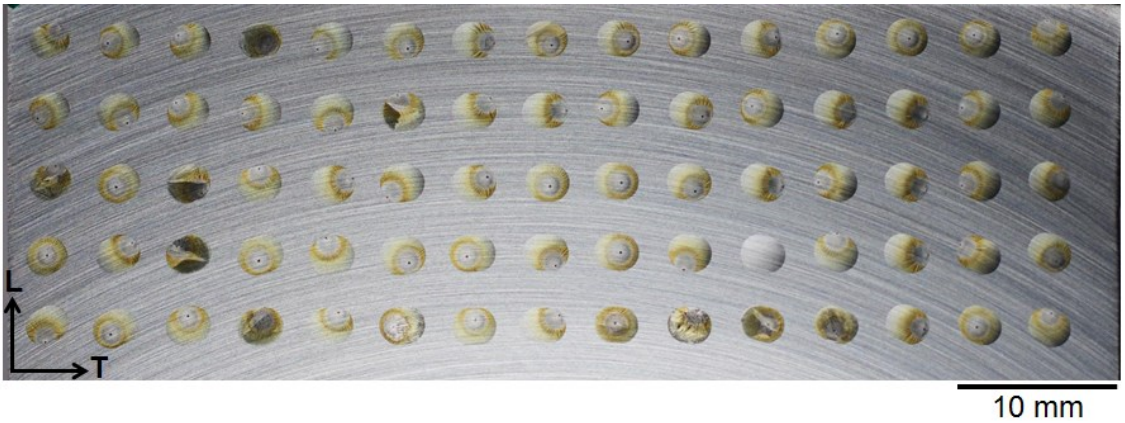

Figure 5-14 Macro photo of 304L plate surface (LT plane) with arrays of $MgCl_2$ droplets (~2.5 mm equivalent diameter, ~1000 µg/cm^2 CDD at deposition) after 1 day exposure at 45% RH and 30 °C.

Figure 5-14 shows results of pitting 304L stainless steel at 45% RH after 1 day for droplets of $MgCl_2$ with ~1000 µg/cm^2 CDD. 74 out of 75 droplets pitted. 36 out of 74 pits were found to be associated with micro-droplets. Some of the droplets appear to have crystallised, but this happened during photography after the experiment was completed. The monitored lab RH was 25% therefore it is expected $MgCl_2$ salt will crystallise because the deliquescence relative humidity (DRH) of $MgCl_2$ is 33% below this value the salt will crystallise. 39 of the pits showed earing morphology and 35 showed satellite morphology. Typical examples of these morphologies are shown in Figure 5-15. As described in the previous sections, a similar trend was observed between pit position and morphology as at 35% RH, with more ear-shaped pits occurring towards the centre of the droplets, and more satellite pits occurring towards the edge

(Figure 5-16). Shallow dish regions were also larger towards the centre of droplets.

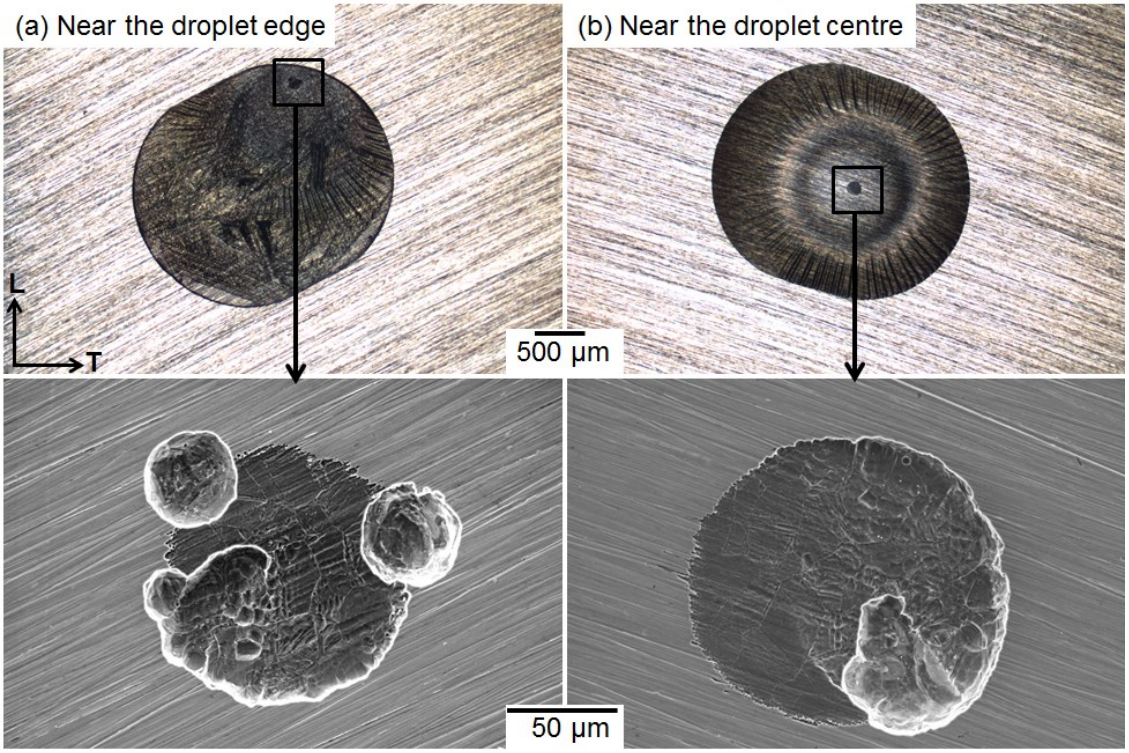

Figure 5-15 Typical pit morphologies formed on 304L stainless steel (LT plane) under $MgCl_2$ droplets (~2.5 mm equivalent diameter, ~1000 µg/cm^2 CDD at deposition), after 1 day exposure at 45% RH and at 30 °C; (a) near the droplet edge; (b) near the droplet centre.

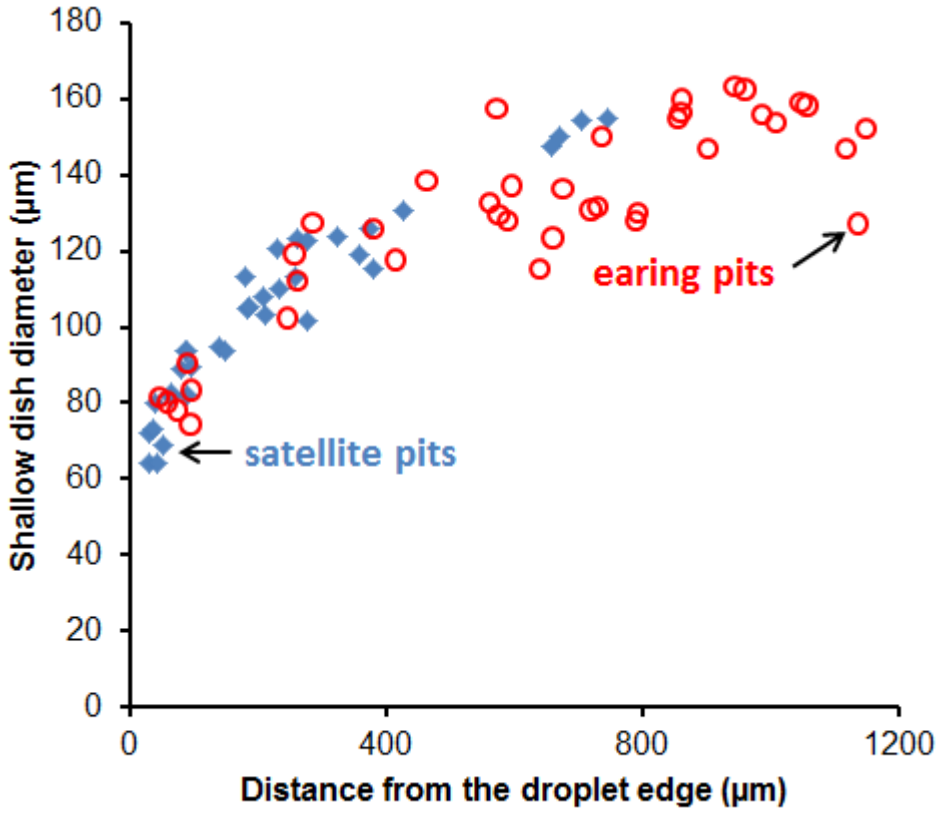

Figure 5-16 The shallow dish equivalent diameter versus the distance from the droplet edge in $MgCl_2$ droplets (~2.5 mm equivalent diameter, ~1000µg/cm^2 CDD at deposition) on 304L (LT plane) after 1 day of exposure at 45% RH at 30 °C. The equivalent diameter is calculated as the diameter of a circle with the same area as the dish.

5.2.3.4 Effect of pit position on the diameter of the shallow dish for 304L stainless steel at 48% RH

Figure 5-17 shows results of pitting 304L stainless steel at 48% RH after 1 day for droplets of $MgCl_2$ with ~1000 µg/cm^2 CDD. 64 out of 75 droplets pitted, with all droplets containing only one main pit. 25 out of 64 pits were found to be associated with micro-droplets. Pits were observed having earing morphology (Figure 5-18), satellite pits were not observed. A small hole can be seen in the centre of the shallow dish region (Figure 5-18(a)), which is possibly the cavity

that developed from the dissolving of an inclusion during the pit initiation process. Pits formed at the droplet edge were usually with one side significantly more attacked (Figure 5-19), leaving a small trace of the shallow dish. The trend in shallow dish region diameter is similar to that seen at 35% and 45% RH, with larger diameters towards the centre of the droplet (Figure 5-20).

Figure 5-17 Macro photo of 304L plate surface (LT plane),after washing with DI water, with $MgCl_2$ droplets (~2.5 mm equivalent diameter, ~1000 μg/cm^2 CDD at deposition) after 1 day exposure at 48% RH and 30 °C.

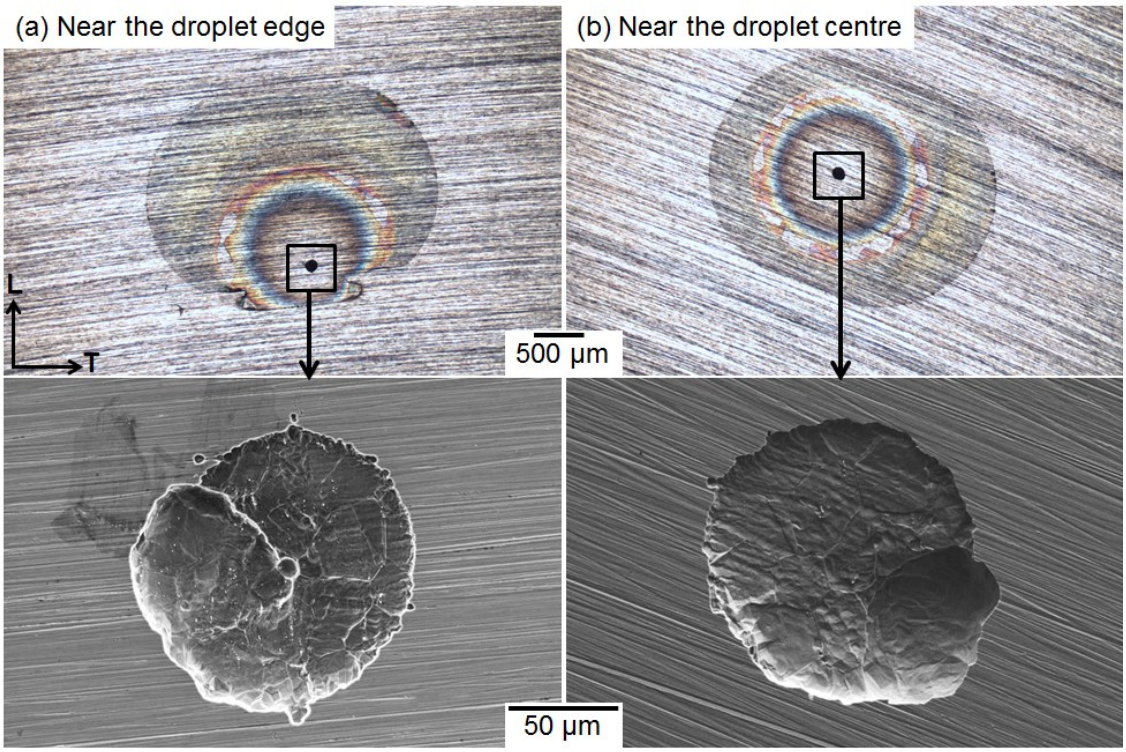

Figure 5-18 Typical pit morphology formed on 304L (LT plane) under $MgCl_2$ droplets (~2.5 mm equivalent diameter, ~1000 µg/cm^2 CDD at deposition), after 1 day exposure at 48% RH at 30 °C; (a) near the droplet edge; (b) near the droplet centre.

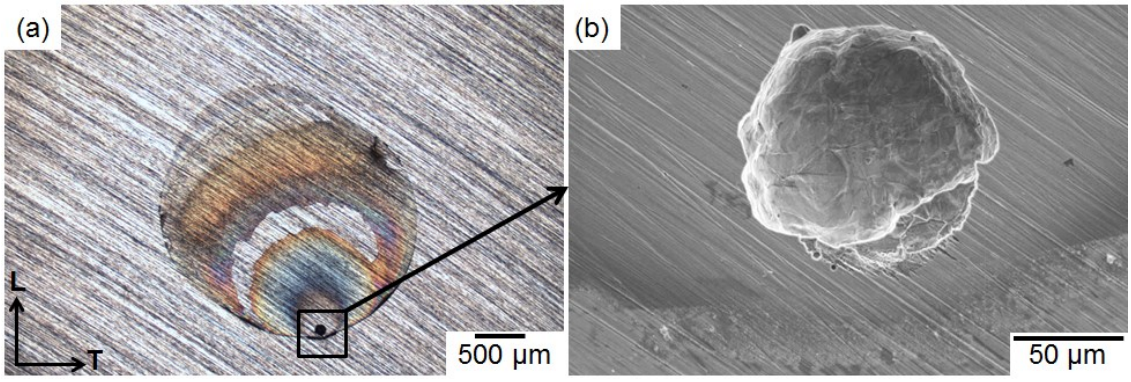

Figure 5-19 Typical pit morphology, at the droplet edge, formed on 304L (LT plane) under $MgCl_2$ droplets (~2.5 mm equivalent diameter, ~1000 µg/cm^2 CDD at deposition), after 1 day exposure at 48% RH at 30 °C; (a) optical image of the droplet after washing with DI water; (b) SEM of pit.

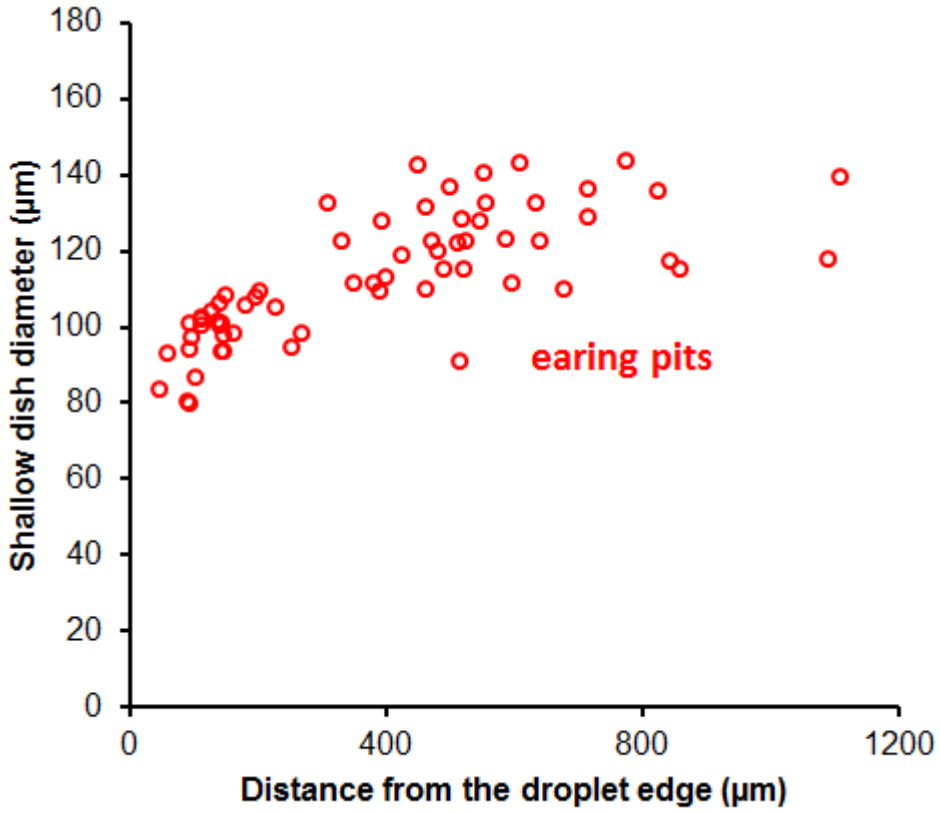

Figure 5-20 Shallow dish equivalent diameter versus the distance from the droplet edge in $MgCl_2$ droplets (~2.5 mm equivalent diameter, CDD of ~1000 µg/cm^2 at deposition) on 304L stainless steel (LT plane) after 1 day of exposure at 48% RH at 30 °C. The equivalent diameter is calculated as the diameter of a circle with the same area as the dish.

Table 5-2 summarises the results of the average shallow dish diameters as a function RH and exposure time. It can be seen that the shallow dish diameter does not change with RH and exposure time, and alloy type when comparing 304L and 316L after 1 week of exposure. For 316L at 35% RH after 1 day exposure experiment (not presented), 16 out of 20 droplets pitted. This it is not considered for making comparison to those formed on 304L at 35% RH after 1 day exposure.

Table 5-2 average diameters with standard deviations of shallow dish diameters formed on 304L and 316L (LT plane) under $MgCl_2$ droplets (~2.5 mm equivalent diameter, CDD of ~1000 µg/cm^2 at deposition) after exposure at 30 °C. The equivalent diameter is calculated as the diameter of a circle with the same area as the dish.

RH (%)	Exposure time	Alloy	No. of measured shallow dishes	Ave. shallow dish diameter (µm)
35	1 day	304L	66	120±30
35	1 week	304L	57	110±30
35	1 week	316L	52	100±30
45	1 day	304L	74	120±30
48	1 day	304L	64	110±20

5.2.4 Effect of pit position on pit diameter and depth for 316L stainless steel at 48% RH

Figure 5-21 shows results of pitting 316L stainless steel, LT plane, at 48% RH after 1 day exposure for droplets of $MgCl_2$ with ~1000 µg/cm^2 CDD. 60 out of 65 droplets pitted and in all cases, only one main pit was observed. 19 out of 60 pits were found to be associated with micro-droplets. Pits were circular in morphology with a rough interior with no obvious shallow dish (Figure 5-22). Only two droplets had pits that seemed to be growing along the rolling direction (Figure 5-23), suggesting that there might be a susceptibility to microstructural features, probably elongated inclusions, present at the alloy surface.

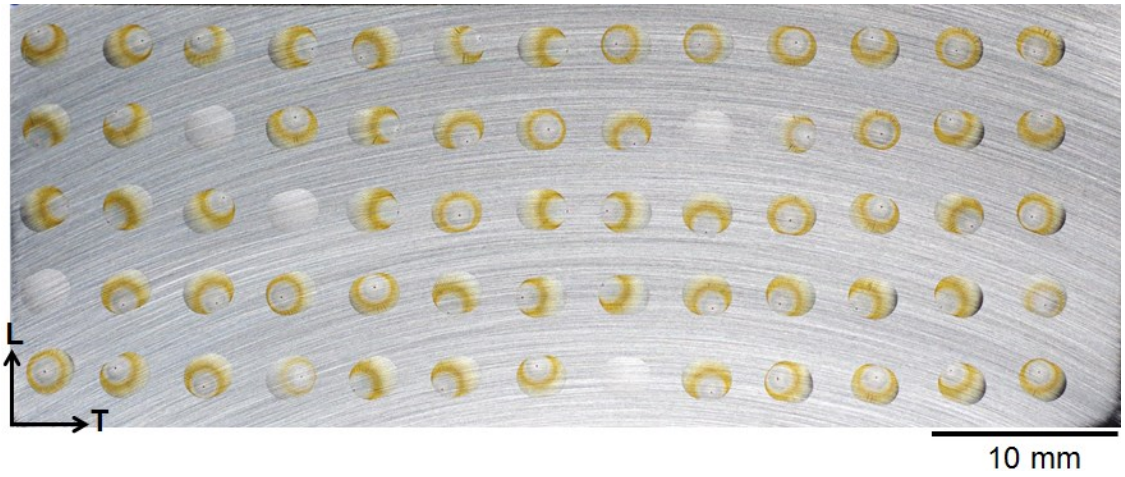

Figure 5-21 Macro photo of 316L plate surface (LT plane) with arrays of $MgCl_2$ droplets (~2.5 mm equivalent diameter, ~1000 μg/cm^2 CDD at deposition) after 1 day exposure at 48% RH and 30 °C.

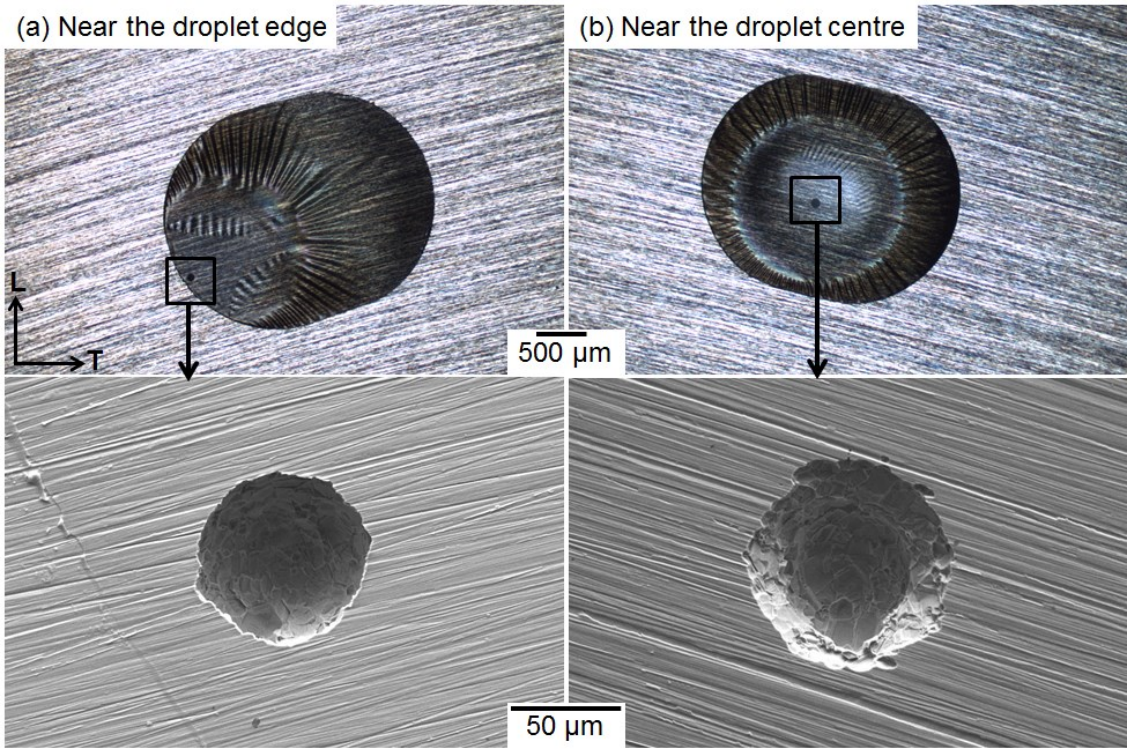

Figure 5-22 Typical pit morphology formed on 316L (LT plane) at 48% RH under $MgCl_2$ droplets (~2.5 mm equivalent diameter, ~1000 μg/cm^2 CDD at deposition) after 1 day exposure at 30 °C; (a) near the droplet edge; (b) near the droplet centre.

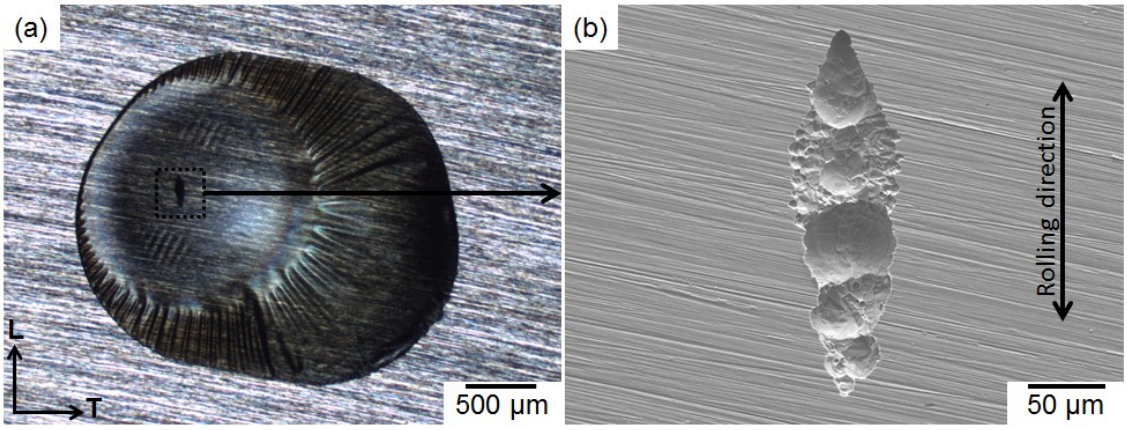

Figure 5-23 Morphology of a pit growing along the rolling direction on 316L (LT plane) surface under $MgCl_2$ droplet (~2.5 mm equivalent diameter, ~1000 µg/cm^2 CDD at deposition), after 1 day exposure at 48% RH at 30 °C; (a) optical image of droplet; (b) SEM of the pit.

Figure 5-24 shows the pit diameter and depth as a function of distance for pits formed on 316L stainless steel at 48% RH after 1 day exposure at 30 °C under $MgCl_2$ droplets of ~1000 µg/cm^2 CDD. As found under other conditions, relatively larger diameters are found towards the centre of the droplet. Pits close to the edge (<200 µm from the droplet edge) had an average pit diameter of 80±6 µm while pits >200 µm from the droplet edge had an average diameter of 90±8 µm. The equivalent pit diameter was obtained from Equation 3-2 based on the assumption that the pit mouth area is circular; the procedure was detailed in Section 3.8.2. Pit depth, with an average of 45±10 µm, was invariant with distance. The fine focus method used to measure the pits depth was described in Section 3.8.3.

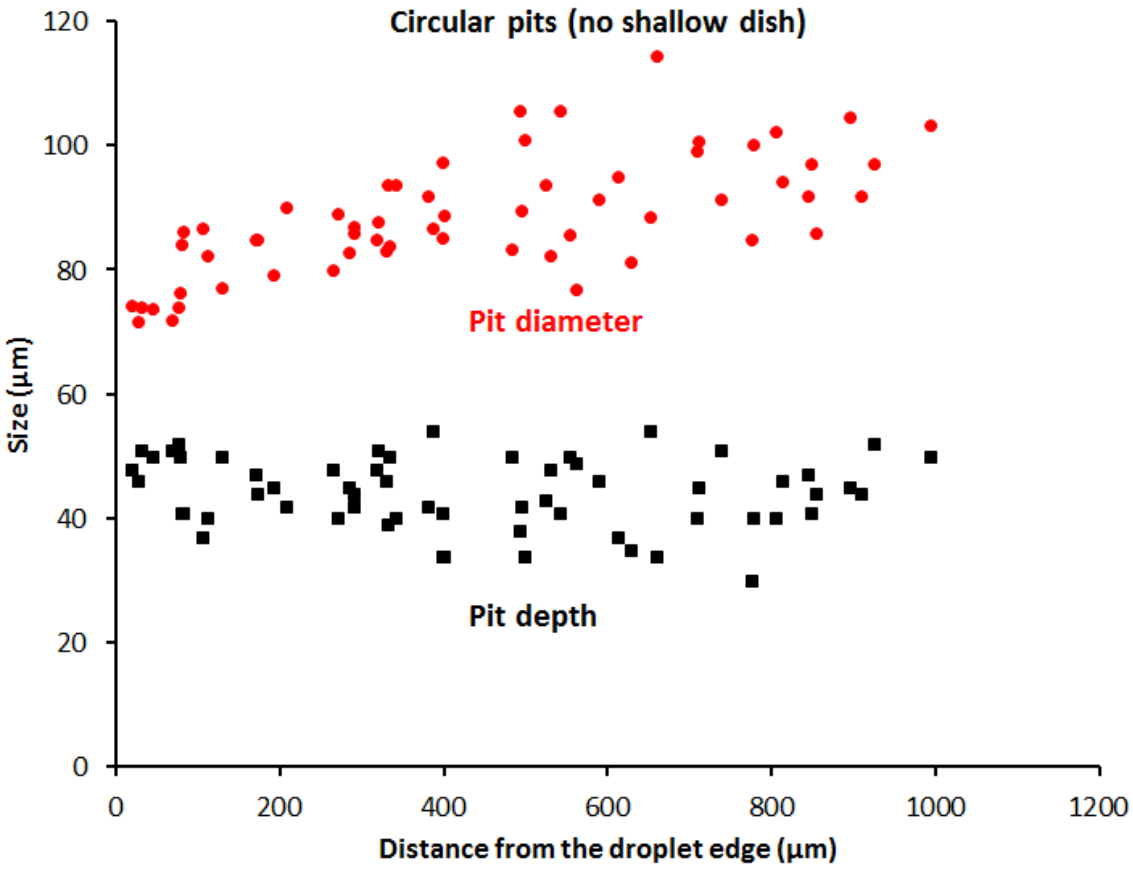

Figure 5-24 Equivalent pit diameter and depth as a function of distance for pits shown in Figure 5-21 formed on 316L stainless steel (LT plane) in $MgCl_2$ droplets (~2.5 mm equivalent diameter, ~1000 µg/cm^2 CDD at deposition) following exposure at 48% RH for 1 day at 30 °C.

5.2.5 Effect of pit position on pit diameter and depth for 304L stainless steel at 56% RH

Comparisons were made between pitting at 56% RH after 1 day (Figure 5-25) and 1 week (Figure 5-26) for droplets of $MgCl_2$ with ~1000 µg/cm^2 CDD. After 1 day, 66 out of 70 droplets pitted. 21out of 66 pits were found to be associated with micro-droplets. After 1 week, 57 out of 60 pitted. 30 out of 57 pits were found to be associated with micro-droplets. No shallow dish region was observed in any of the pits in either data set. Pits showed neither earing nor

satellite morphologies. They instead showed circular pit morphology after both 1 day (Figure 5-27) and 1 week exposure (Figure 5-28).

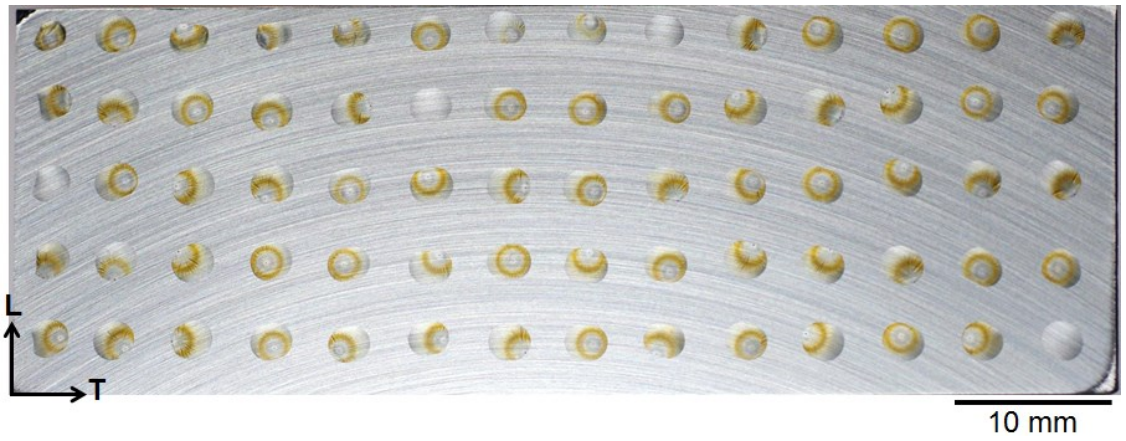

Figure 5-25 Macro photo of 304L plate surface (LT plane) deposited with arrays of $MgCl_2$ droplets (~2.5 mm equivalent diameter, ~1000 µg/cm^2 CDD at deposition), after 1 day exposure at 56% RH and 30 °C.

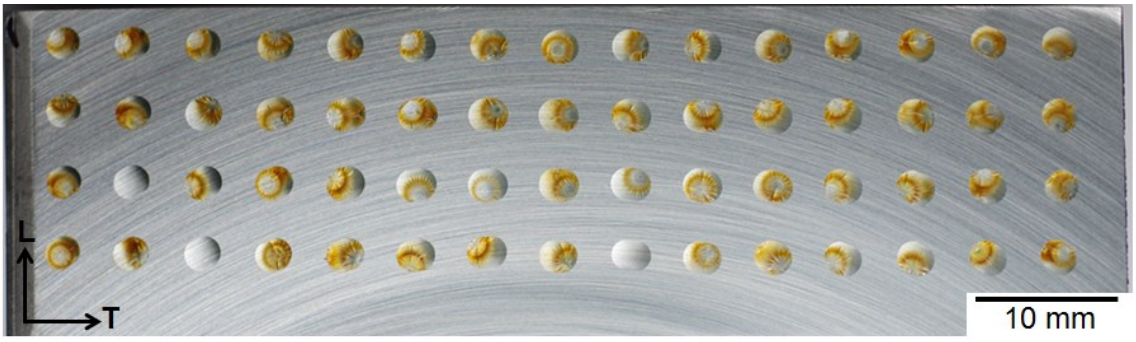

Figure 5-26 Macro photo of 304L plate surface (LT plane) deposited with arrays of $MgCl_2$ droplets (~2.5 mm equivalent diameter, ~1000 µg/cm^2 CDD at deposition), after 1 week exposure at 56% RH and 30 °C.

Figure 5-27 shows pit morphologies formed on 304L at 56% RH after 1 day exposure. The pit morphology was affected by the position of pits in the droplet. Pits near the centre of the droplet (Figure 5-27(a)) and near to the droplet edge (Figure 5-27(b)) showed a hemispherical attack with approximately the same pit

mouth diameter. Pits formed at the edge of the droplet had larger pit mouths than those grown towards the centre. 15 out of 70 pits occurred at the edge of the droplet, with 14 growing fully inside the droplet showing a deep attack into the pit towards the droplet centre (e.g. Figure 5-27(c)). Only 1 pit found to be bisected by the droplet (Figure 5-27(d)).

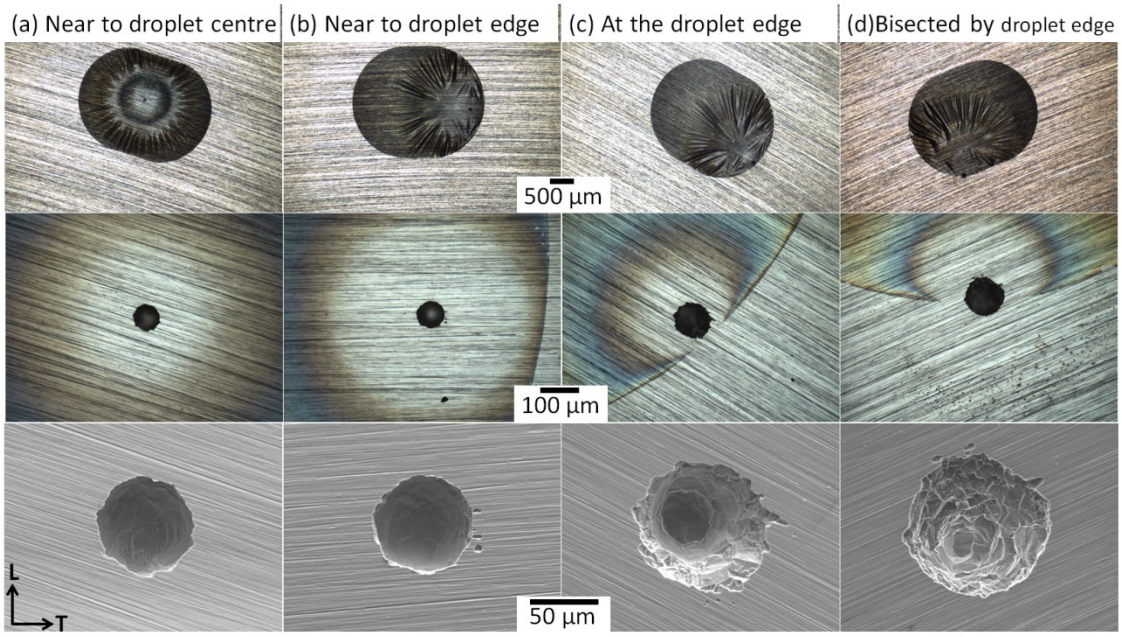

Figure 5-27 Typical pit morphologies formed on 304L (LT plane) in $MgCl_2$ droplets (~2.5 mm equivalent diameter, ~1000 µg/cm^2 CDD at deposition), after 1 day exposure at 56% RH at 30 °C; (a) near the droplet centre; (b) near the droplet edge; (c) at the droplet edge; (d) bisected by droplet edge.

After 1 week at 56% RH, the position of the pits in the droplet affects the morphology which can be categorised in 4 ways (Figure 5-28). Pits near the centre of the droplet (Figure 5-28 (a)) shows a deep, hemispherical attack into the metal. When pits occur closer to the edge (Figure 5-28 (b)) the attack appears to be less hemispherical and more layered, although the mouth of the pit is approximately the same size as that for pits found at the centre.

11 out of 60 pits occurred at the edge of the droplet, with 6 growing fully inside the droplet (Figure 5-28 (c)) and 5 pits being bisected by the droplet (Figure 5-28 (d)). Pits at the edge of the droplet have larger pit mouths than those grown towards the centre (Figure 5-29). When the pit grows fully in the droplet, the deep attack into the pit always occurs towards the droplet centre (Figure 5-28 (c)). However, when pit is bisected by the droplet edge, 3 out of 5 were seen to have deep pitting in the part of the pit that has a very thin solution layer, outside the bulk of the droplet (Figure 5-28 (d)). This was not clear for the other 2 pits.

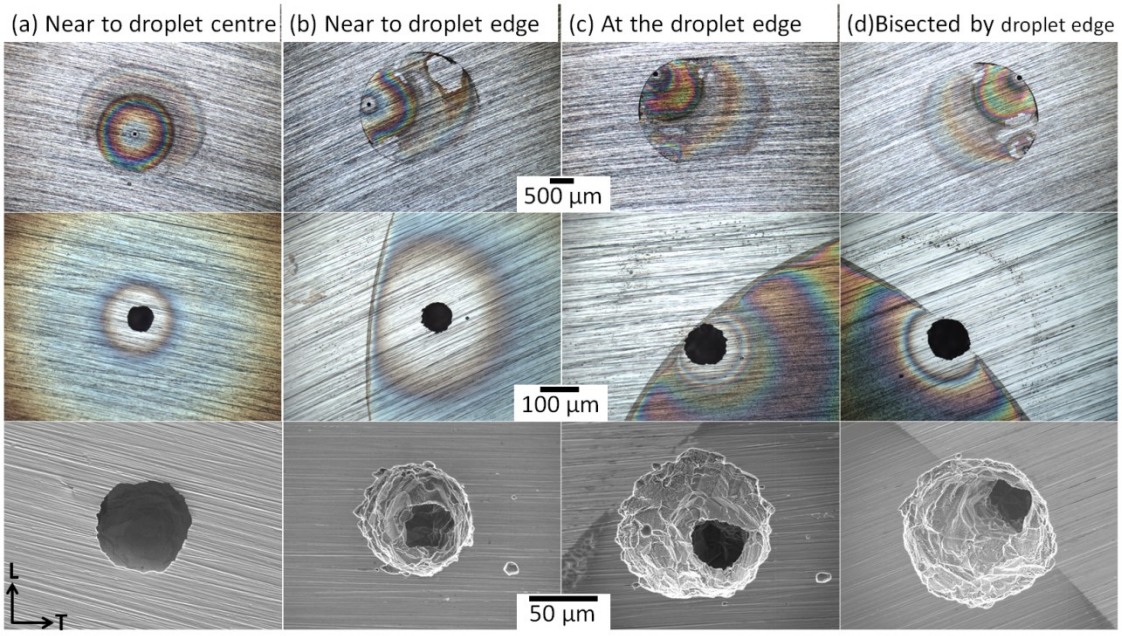

Figure 5-28 Typical pit morphologies formed on 304L (LT plane) in $MgCl_2$ droplets (~2.5 mm equivalent diameter, ~1000 µg/cm^2 CDD at deposition), after 1 week exposure at 56% RH at 30 °C; (a) near the droplet centre; (b) near the droplet edge; (c) at the droplet edge; (d) bisected by droplet edge.

The pit mouth diameter was generally larger at the edge of the droplet than towards the centre in both one day and one week experiments (Figure 5-29), with an average diameter of 89±15 μm for one day and 98±12 μm for one week. There was no significant change in pit diameter when initiation occurred further than 200 μm from the edge of the droplet in both 1 day (65±6 μm) and 1 week (68±7 μm) experiments. The procedure used to measure the pits diameter was detailed in Section 3.8.2.

Although there was very little variation in pit diameter between 1 day and 1 week experiments, there was significant variation in pit depth (Figure 5-30). Within 200 μm of the droplet edge, the average pit depth after 1 day was 50±9 μm and after 1 week was 75±11 μm. For pits >200 μm from the droplet edge, the average depth was 47±8 μm after one day and 61±9 μm after 1 week (Table 5-3). The fine focus method was used to measure the pits depth as described in Section 3.8.3.

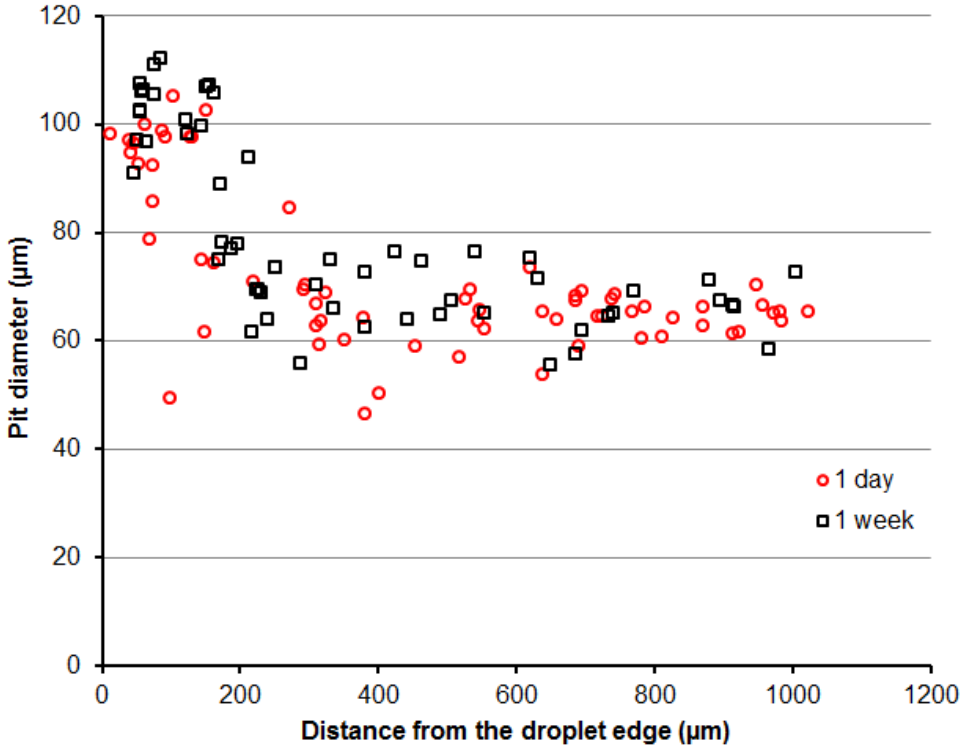

Figure 5-29 Equivalent pit diameter as a function of pit position for pits shown in Figure 5-25 and Figure 5-26, formed on 304L stainless steel (LT plane) deposited with arrays of $MgCl_2$ droplets (~2.5 mm equivalent diameter, ~1000 µg/cm^2 CDD at deposition) following exposure at 56% RH and 30 °C for 1 day (red circles) and 1 week (black squares). The equivalent diameter is calculated as the diameter of a circle with the same area as the pit mouth.

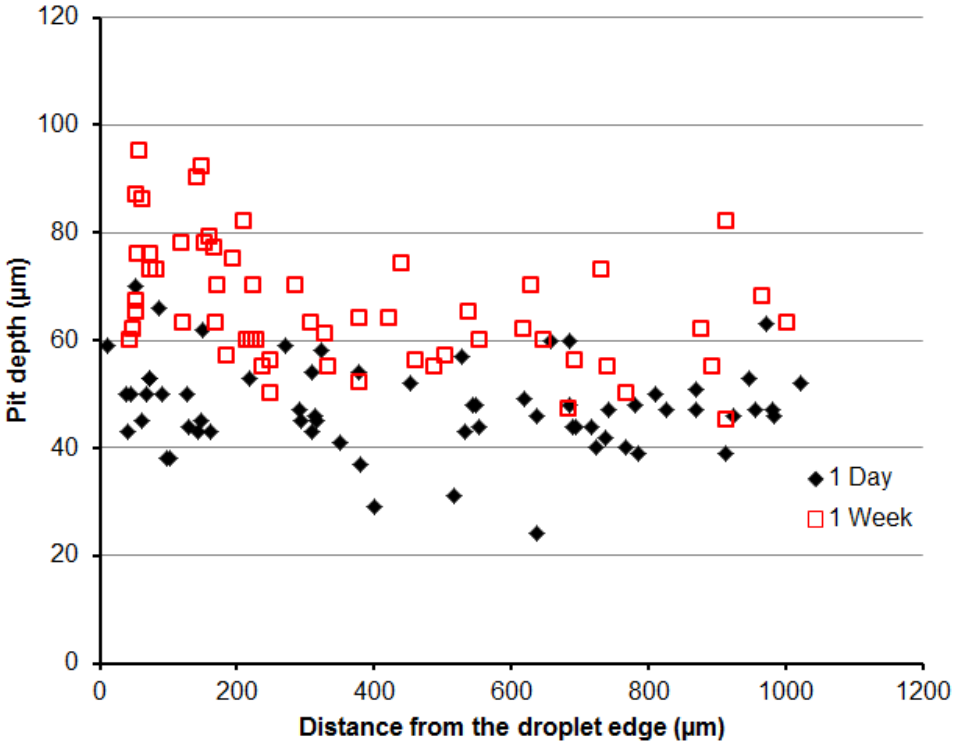

Figure 5-30 The pit depth as a function of pit position for pits shown in Figure 5-25 and Figure 5-26, formed on 304L stainless steel (LT plane) deposited with arrays of $MgCl_2$ droplets (~2.5 mm equivalent diameter, ~1000 µg/cm^2 CDD at deposition), following exposure at 56% RH and 30 °C for 1 day (black diamonds) and 1 week (red squares).

Table 5-3 The pit diameter and depth as a function of exposure time and distance from the droplet edge. Pits formed on 304L stainless steel (LT plane) under $MgCl_2$ droplets (~2.5 mm equivalent diameter, ~1000 µg/cm^2 CDD at deposition), following exposure at 30 °C.

RH (%)	Exposure time	Distance from the droplet edge (µm)	Pit diameter (µm)	Pit depth (µm)
56	1 day	<200	89±15	50±9
		>200	65±6	47±8
	1 week	<200	98±12	75±11
		>200	68±7	61±9

At 56% RH, it was often found that more than one pitting site was present under a droplet. Examples of these are shown in (Figure 5-31). For droplets containing two or more pits after 1 week exposure (lower row images in Figure 5-31) the rust deposited by the smaller pits, which tended to initiate at the edge of the droplet, overlays the rust formed by the larger pit, however the rust from the smaller pits is not affected by the rust from the larger pit, suggesting that the smaller pit(s) occurred after the main pit had stopped producing rust. Therefore it can be proposed that these pits occurred consecutively not concurrently.

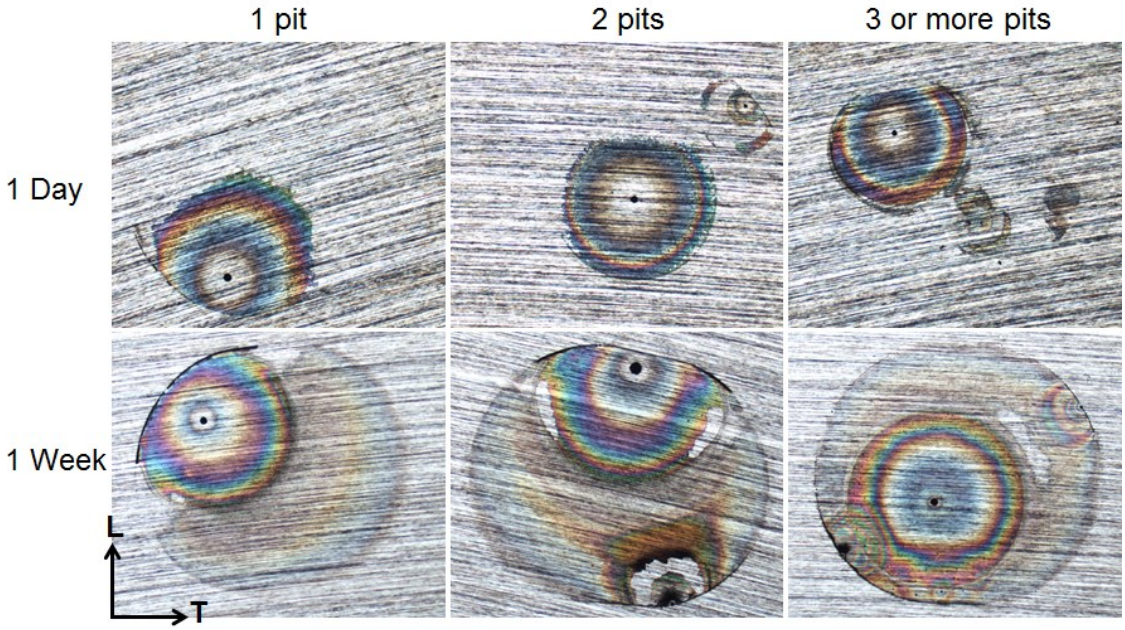

Figure 5-31 Typical examples of droplets containing 1 pit, 2 pits, and 3 or more pits at 56% RH, 30 °C of ~1000 µg/cm^2 CDD $MgCl_2$ droplets on 304L stainless steel (LT plane) after exposure for 1 day (upper optical images) and 1 week (lower optical images).

Figure 5-32 shows the number of droplets containing no pits, 1 pit, 2 pits, and 3 or more for both 1 day and 1 week exposure at 56% RH. After 1 day, 4 out of 70 (6%) droplets had no pit, 27 out of 70 (39%) droplets had only one pit, while 36 out of 70 (51%) droplets had 2 pitting sites, and 3 (4%) droplets had 3 or more. After 1 week, the number of droplets with a single pitting site was much lower, with 9 out of 60 (15%) droplets having only one pit, 20 (33%) droplets having 2 pitting sites and 28 (47%) droplets having 3 or more pitting sites, 3 out of 70 (5%) droplets had no pit.

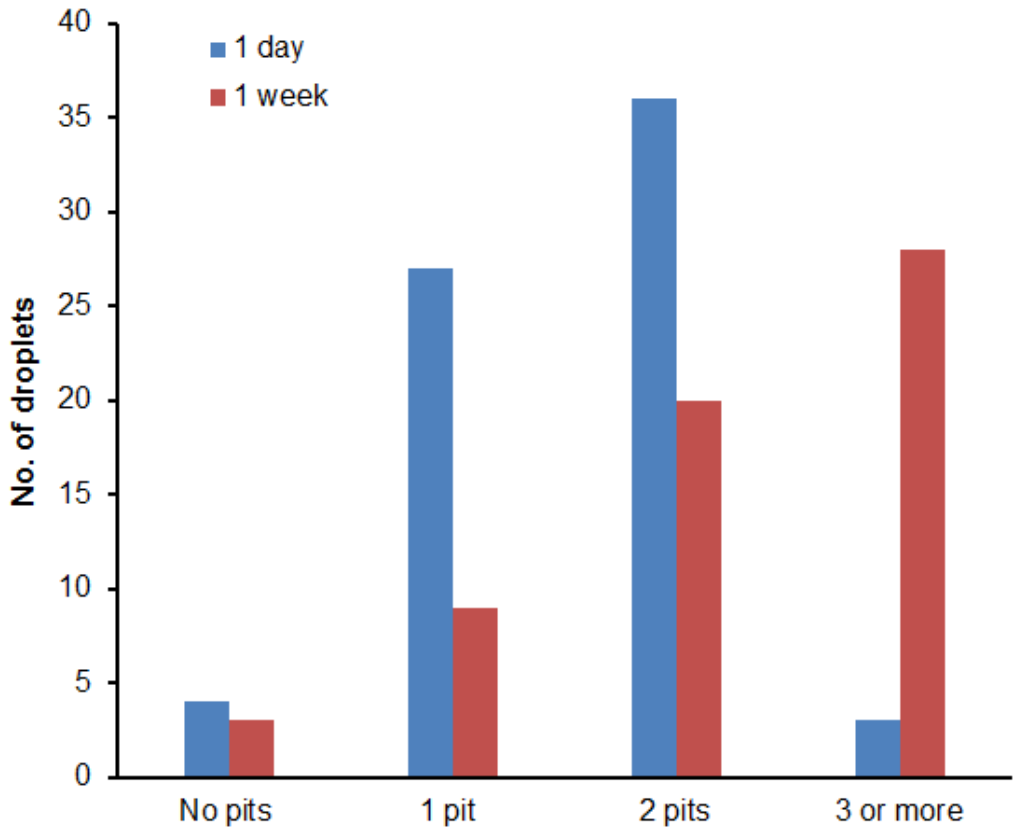

Figure 5-32 Number of pits per droplet of $MgCl_2$ droplets (~2.5 mm diameter, ~1000 µg/cm^2 CDD at deposition) for pits shown in Figure 5-25 and Figure 5-26 on 304L stainless steel plate, following exposure at 56% RH and 30 °C for 1 day (in blue) and 1 week (in brown).

5.2.6 Atmospheric pitting corrosion behaviour of 316L stainless steel at 56% RH

Pitting of 316L stainless steel at 56% RH after 1 day and 1 week exposure are shown in (Figure 5-33) and (Figure 5-34) respectively, under droplets of $MgCl_2$ with ~1000 μg/cm^2 CDD. After 1 day, only 2 out of 65 droplets pitted (1 circular pit and 1 elongated pit) while after 1 week, 9 out of 60 droplets pitted (all circular). 7 out of 9 pits were found to be associated with micro-droplets. Circular pits with a rough interior with possible grain facets morphology that correlates with the grain size of the alloy shown in Figure 3-3, without any obvious shallow dish region, were observed after both 1 day and 1 week exposure (Figure 5-35). It can be seen that there is a significant increase in pit diameter; it is 60 μm (it is only one measurement therefore it is not possible to give a range of accuracy) for 1 day but 110±10 μm for 1 week exposure. The pit depth was 75±5 μm after 1 week. Single pits per droplet were observed after 1 day of exposure while after 1 week both single pit and multiple pits (2, 3 or more) were observed. The effect of pit position on pit diameter and depth is not considered in these two data sets because of the small number of pitted droplets compared with those formed on 304L at the same RH. However, examination of individual optical micro images showed that most of the pits formed close to the droplet edge.

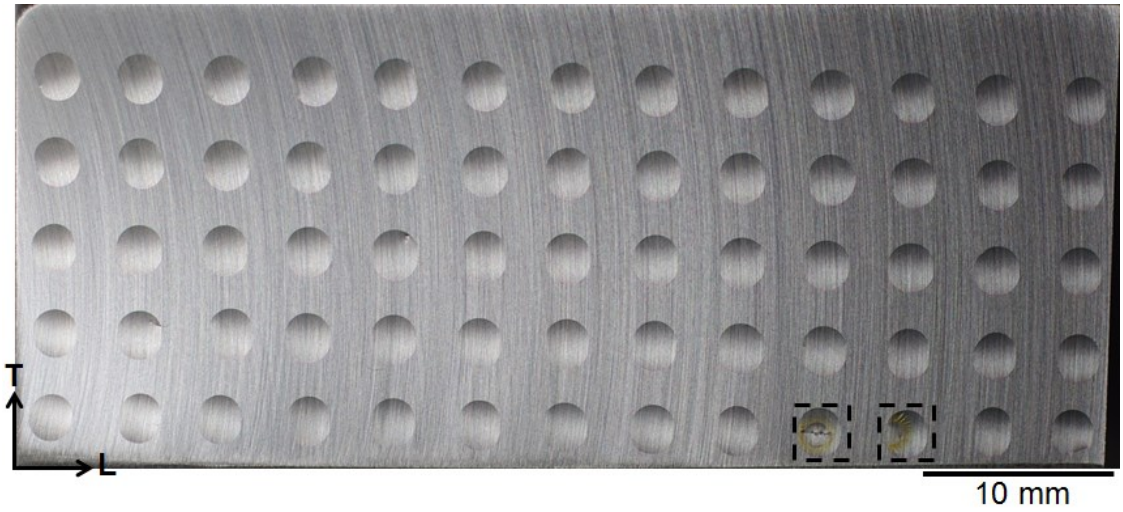

Figure 5-33 Macro photo of 316L (LT plane) with $MgCl_2$ droplets (~2.5 mm equivalent diameter, ~1000 µg/cm^2 CDD at deposition), following exposure at 56% RH for 1 day at 30 °C; pitted droplets are selected with dashed square.

Figure 5-34 Macro photo of 316L plate surface (LT plane) with $MgCl_2$ droplets (~2.5 mm equivalent diameter, ~1000 µg/cm^2 CDD at deposition), following exposure at 56% RH for 1 week at 30 °C.

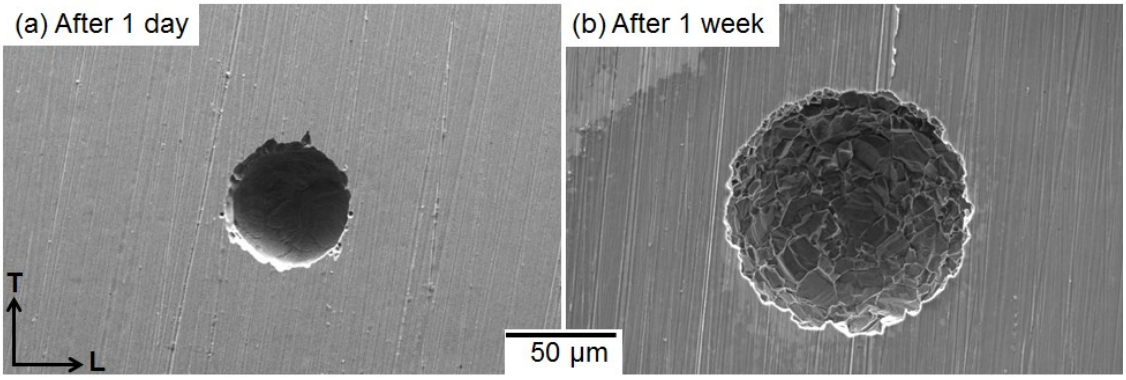

Figure 5-35 Typical pit morphologies formed on 316L stainless steel (LT plane) under $MgCl_2$ droplets (~2.5 mm equivalent diameter, ~1000 µg/cm^2 CDD at deposition), after exposure at 56% RH and 30 °C; (a) after 1 day; (b) after 1 week.

5.2.6.1 Atmospheric pitting corrosion behaviour of 304L and 316L stainless steel at 65% RH and above

304L and 316L plates were exposed to 65% RH for 1 day for droplets of $MgCl_2$ with ~1000 µg/cm^2 CDD. Figure 5-36 shows results for 304L, where 7 out of 75 droplets pitted. All droplets contained only one main pit. All pits show a circular pitting morphology and all pits were bisected by the edge of the droplet with an average pit diameter of 100±20 µm. All pits were found to be associated with micro-droplets. At this RH, no pits were found on the 316L plate. At 70% RH and above there was also no pitting for either 304L or 316L. Table 5-4 summarises the results of the tests carried out on both 304L and 316L stainless steel at the two exposure times at all RH values used in the present work.

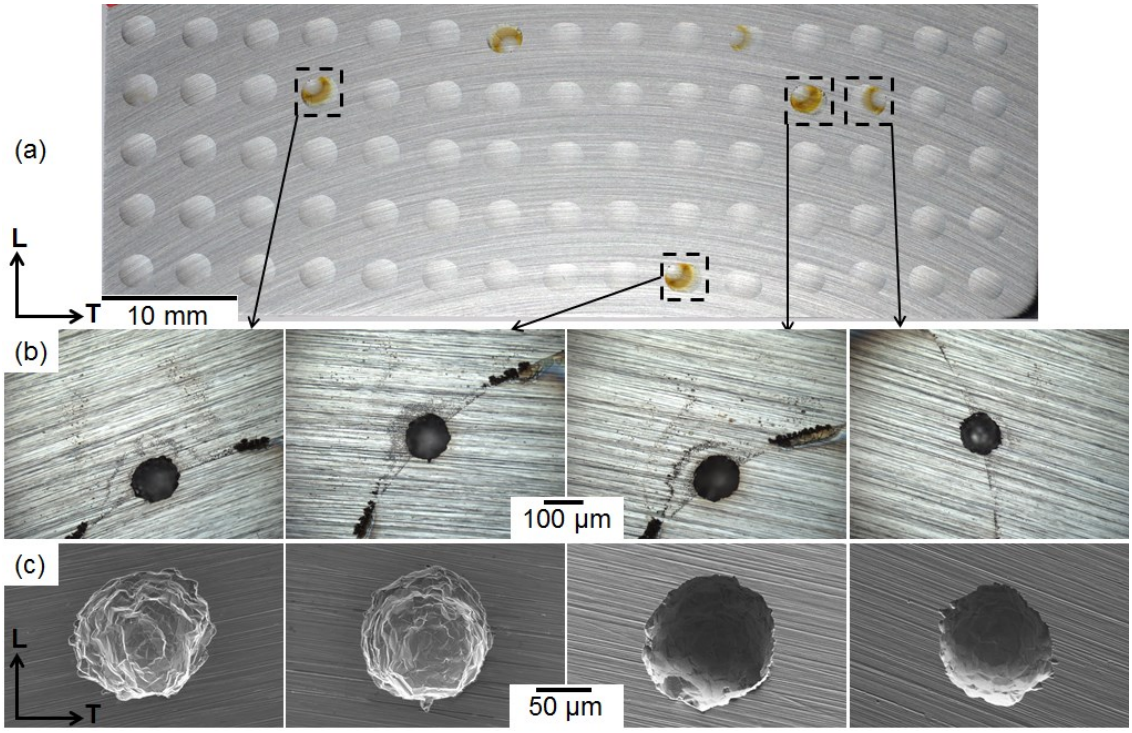

Figure 5-36 (a) macro photo of 304L plate surface (LT plane) with $MgCl_2$ droplets (~2.5 mm equivalent diameter, ~1000 µg/cm^2 CDD at deposition), after 1 day exposure at 65% RH and 30 °C; (b) optical microscope images of pits position relative to droplet edge; (c) SEM of pits.

Table 5-4 Summary of the results of the pitting behaviour at different RH and exposure time for 304L and 316L stainless steels (LT plane)under $MgCl_2$ droplets (~2.5 mm equivalent diameter, ~1000 µg/cm^2 CDD at deposition). The pit morphologies and the number of droplets pitted also the number of pits associated with micro-droplets (shown in red) at each RH and exposure time for both materials are presented.

Material \ RH(%)		35%	45%	48%	56%	65%	70%	75%
304LSS	1 day	Earing pits and Satellite pits **66/70**+ **25/66**†	Earing pits and Satellite pits **74/75** **36/74**	Earing pits only **64/75** **25/65**	Circular pits only No shallow dish **66/70** **21/66**	Circular pits only No shallow dish **7/75** **7/7**	No pits **0/75**	No pits **0/75**
	1 week	Earing pits and Satellite pits **70/70** **21/70**	Earing pits deep attack **10/10** * **5/10**	-	Circular pits only No shallow dish **57/60** **30/57**	-	No pits **0/75**	No pits **0/75**
316LSS	1 day	Earing pits and Satellite pits **16/20****** **7/16**	Earing pits and Satellite pits **3/6***** **0/3**	Circular pits only No shallow dish **60/65** **19/60**	Circular pits only No shallow dish **2/65** **1/2**	No pits **0/65**	No pits **0/65**	No pits **0/65**
	1 week	Earing pits and Satellite pits **52/65** **24/52**	Earing pits deep attack **4/10** ** **3/4**	-	Circular pits only No shallow dish **9/60** **7/9**	No pits **0/65**	No pits **0/65**	No pits **0/65**

* From Figure 6-2 (chapter 6), ** From Figure 6-4 (chapter 6), *** From Figure 6-16 (chapter 6)
**** Figure Not presented
- Test is not carried out at this condition.
+ The ratio x/y is the number of droplets with pits / total number of droplets
† The ratio x/y is the number of pits with micro-droplets / total number of pits

5.3 Discussion

5.3.1 Morphology of pits at 48% RH and below

At RH 48% and below, a shallow dish region is observed in corrosion pits in both 304L and 316L stainless steels (Figure 5-5, Figure 5-8, Figure 5-12, Figure 5-15, Figure 5-18), which has been previously reported [5, 6, 14, 21]. This is the initial stage of attack, confirmed by time-lapse images (Figure 5-1). Once the shallow dish has reached its full size, radial growth stops and other forms of attack continue. Street et al. [6] suggest that this region is caused by passive current dissolution due to the high passive current densities sustained in highly concentrated $MgCl_2$ solutions: the volume of material loss in the shallow dish region is approximately equivalent to that lost by passive current in these concentrations, which is known to be elevated by up to two orders of magnitude at high concentrations of $MgCl_2$, as shown in Mi's work [18].

Maier and Frankel [21] proposed that the dish "radial" type of attack is caused by the adsorption of sulphur species on the oxide layer. Hastuty et al. [5] have also proposed a mechanism of growth of the shallow dish region where hydrolysis caused by metal cation release drives growth radially away from the sulphur-rich initiation site. This growth continues until current density is so low the surface passivates. Recently, however, Street et al. [6] suggested that the presence of sulphur species could not be the only controlling factor based on the observation of the variation of the shallow dish diameter with distance from the edge of the droplet.

In agreement with Street's observation, the diameter of the shallow dish region is found to be affected by position of the pit inside the droplet, with diameters being generally smaller towards the edge and larger towards the centre of the droplet. This is the case for 35% RH (Figure 5-10 and Figure 5-13), 45% RH (Figure 5-16) and 48% RH (Figure 5-20), and there is no significant difference in shallow dish diameter at these different RH values (Table 5-2). As in Street's work, this was attributed to the IR drop increase towards the edge of the droplet, reducing passive current at the initiation site which results in smaller dish sizes.

In an experiment on the effect of droplet diameter on pit diameter described in Section 6.2.1, it was found that the shallow dish diameter as well as the pit diameter was increased with increasing the droplet diameter. As the area of electrolyte coverage affects the available cathodic area (with larger droplets having more cathodic area, and so more available cathodic current) this supports the idea that growth size of the shallow dish is strongly influenced by cathodic area.

At 35% and 45% RH, two pit morphologies dominated after 1 day: "satellite" pits, with several small pits surrounding the shallow dish region, and "earing" pits, with increased growth of part of the shallow dish region, which may over time extend beyond it. At 48% RH, only earing pits were seen for 304L (Figure 5-18), while for 316L almost circular pits were seen (Figure 5-22). Satellite pitting is more common at the edge of droplets suggesting that it is influenced by the thickness of the droplet above the pit, which influences both the interfacial potential (through decreased IR drop with greater droplet thickness)

and the rate of diffusion of ions away from the pit. Low diffusion allows metal ions to concentrate at initiation site, stabilising it and promoting satellite pitting. This agrees with observations that less satellite pitting occurs at higher RH, where solution droplet thicknesses are larger and diffusivity is higher [6].

Satellite pits are covered with caps (Figure 5-2) enriched in Cr, Mn, S, O and Cl. This observation is in agreement with previously reported findings [6, 7]. No significant differences are seen between the chemical composition (EDX analysis) of pit covers obtained on 304L and 316L (Table 5-1). Pit covers are also observed in tomography experiments (Figure 5-3), with a bright line just above the pit, suggesting the metallic composition of the pit cover. Similar pit covers were reported previously by Guo [7] on 304L stainless steel under $MgCl_2$ droplets (CDD ~1000 μg/cm^2) after wet-dry cycling exposure test examined in tomography at 21±1 ºC.

The earing pits seen at 35%-48% RH were formed by ear-shaped attack into the shallow dish region, as described by Maier and Frankel [21]. They attribute this to the gradual passivation of the shallow dish region, concentrating current in a smaller area. This earing attack is also seen to occur in the current work on pits with satellite morphologies but is significantly smaller (Figure 5-1). This indicates that both the satellite pitting and the earing attack start at the same time (see time-lapse in Figure 5-1), with the satellite pitting eventually dominating at lower RH values. It should be noted that Maier and Frankel did not see satellite pitting although they used an RH of 33–34%, which may be due to the different surface grinding (4000 grit instead of 800 grit). Preliminary unpublished work carried out in the current project suggests that satellite pits

may not form on mirror-polished surfaces. This would remove occluded initiation sites, allowing the earing mechanism to continue into the metal and form pits with earing morphologies.

5.3.2 Morphology of pits at 56% RH and above

For 304L exposed at 56% RH for 1 day (Figure 5-27) and 1 week exposure (Figure 5-28) and 316L exposed to the same RH and exposure times (Figure 5-35), circular pits with no shallow dish region were observed, with radial growth of the pit proportional to growth into the metal, resulting in smaller diameter pits. This is in agreement with Street et al. [6], who suggested that shallow dish regions could be caused by passive current dissolution (Figure 5-37 [18]). It can be determined that at concentrations between 0.5 and 3 M $MgCl_2$ (equivalent to 95% RH and 65% RH respectively), there is little change in passive current density, with the only major difference being a reduction in breakdown potential as concentration increases. Above 3 M $MgCl_2$, the trend in reduction of breakdown potential continues, but the passive current density begins to change dramatically, increasing by a factor of 100 times between 3 M and 5 M $MgCl_2$ (equivalent to 65% RH and 33% RH respectively). Street et al.[6] suggested that the change in morphology at 56% RH (corresponding to 3.7 M $MgCl_2$) could be a result of reducing passive current density at low concentrations, helped by decreased IR drop due to increase droplet thickness which allows breakdown potential to be achieved more easily.

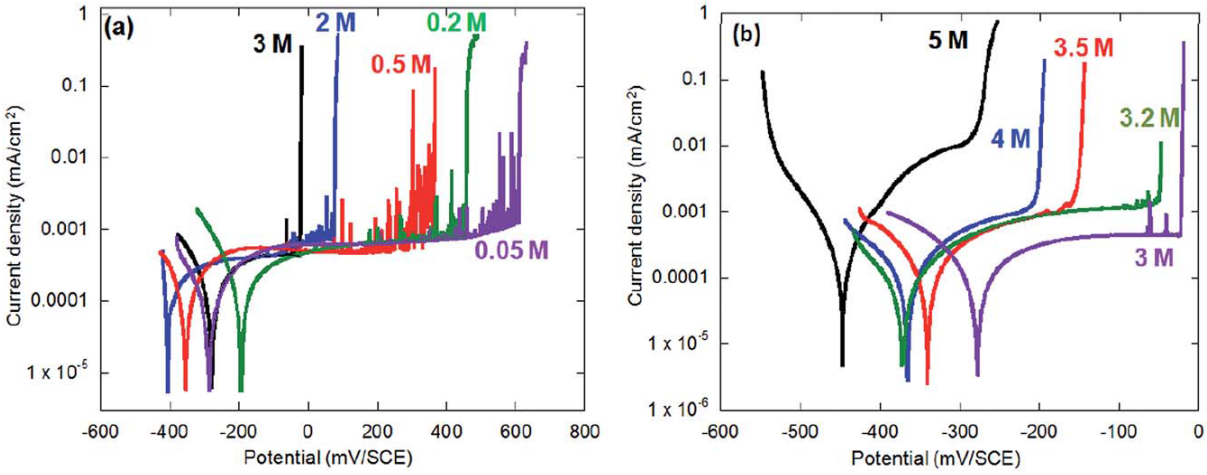

Figure 5-37 Current against potential polarisation curves for 250 µm diameter 304 stainless steel wires in $MgCl_2$ solutions with concentrations of: (a) 0.05–3 M; and (b) 3–5 M. The potential sweep rate was 0.2 mV s^{-1} [18].

The circular morphology is also seen at 65% RH (Figure 5-36) for 304L, with all the pits forming at the droplet edge (bisected by the droplet edge). A possible mechanism for this could be due to the concentrations needed for initiation to occur. Recent work by Nam et al. [9] show that $MgCl_2$ droplets on 304L require a minimum concentration to initiate, giving a range of 47%-58% RH for pit initiation at 298 K. Pitting never occurred above 60% RH in those experiments under the droplets. In the current work pitting was also seen to rely on chloride concentration. The critical humidity, however, was found to be between 65% and 70% RH for 304L. The difference between this work and that of Nam et al. is likely due to the conditions of exposure. Whereas the current work used a fixed humidity for 1 day exposure and 800 grit surface finish, Nam et al. exposed samples (with a final polish surface of 0.25 µm diamond suspension) to dynamic humidity environment, with the humidity changed at a rate of 5% RH per hour between 95% and 45% RH.

When pitting occurs in 65% RH in the present work, initiation may be occurring just outside the edge of the droplet, under monolayers of water. These very thin layers would limit diffusion away from initiation sites and allow aggressive solution pH to be generated by hydrolysis of metal cations releasing H^+ ions. Also, the initiation at the edge allows access to a strong cathodic region supplied by the droplet, driving the corrosion process. As such, these pits look "bisected" by the droplet edge, as pit growth can continue radially from the initiation site. This explains the relative rarity of these pitting events (7 out of 75) as specific conditions would need to be met for this to occur i.e. a susceptible inclusion just outside the droplet area.

5.3.3 Effect of pit position on pit depth and diameter

In the present study, for the pits found on 304L at 56% RH, it is clearly observed that the diameter and depth of pits formed at or close to the droplet edge were greater than those of pits close to the droplet centre (Figure 5-29) and (Figure 5-30). This can be attributed to the presence of a three phase boundary, where there is particularly easy access of oxygen for the cathodic reaction [23, 199-201]. Morton and Frankel [167] found that large pits only occurred at or very close to the droplet edge in droplets deposited on aluminium. They carried out experiments on aluminium under 3.5 wt.% NaCl droplets (6 µl in volume, 3-4mm diameter) with and without inhibitors and exposed at 85% RH (using saturated KCl) for 20 hours. Morton and Frankel proposed that preferential pitting generated close to the droplet edge will result in the formation of an acidic zone

that develops more pit initiation and growth for aluminium. A similar mechanism was also proposed by Li et al. [168] for aluminium.

Pits formed at the droplet edge were always surrounded by secondary droplets (this is shown in Section 6.4.4), and it is more likely that the area covered by the secondary droplets acted as a cathodic region to support the pitting attack therefore wider and deeper pits were seen. Using SKP, Morton and Frankel [167] observed that the outer edge of the secondary droplet and a wide area surrounding it acts as a cathodic region to support the pitting attack on aluminium.

While the pit depth increases between one day and one week, pit mouth diameter does not (Table 5-3). This can be attributed to pit depth being under diffusion control [123].

At lower RH values, pits had complex morphologies (satellite and earing).Therefore, it was difficult to measure pit depth and diameter. Although only circular pits were found at 48% RH for 316L (Figure 5-24), pits were found to be smaller in diameter close to the droplet edge than those formed towards the centre. This is likely to be associated to the increased IR drop under thinner solution layers found at the edge of the droplets [107].

5.3.4 The critical relative humidity for atmospheric pitting corrosion

The RH determines the concentration of the salt droplets and/or electrolyte layers since the water activity in the air and water phases is equal at equilibrium [6]. As the RH is higher, the chloride concentration becomes lower in the

droplet, leading to a decrease in the probability of occurrence of pitting corrosion [4].

For 304L, The critical relative humidity for occurrence of atmospheric pitting corrosion lies between 65% RH and 70% RH corresponding to ~3 M and 2.9 M $MgCl_2$ solution, respectively. Pits were observed up to 65% RH (Figure 5-36). Pits were not observed at 70% RH and higher (Table 5-4), while for 316L, pits were observed up to 56% RH (Figure 5-35), but were not observed at 65% RH and higher (Table 5-4). The findings for 304L are in agreement with the results of Tsutsumi et al. [4], who studied the probability of occurrence of pitting corrosion of 304 stainless steel beneath droplets of $MgCl_2$ solution and reported that the critical relative humidity for occurrence of pitting corrosion lies between 55% RH and 75% RH corresponding to 4.25 M and 2.45 M $MgCl_2$ solution respectively. Specifically, they reported that pitting corrosion progressed only when the magnesium chloride concentration exceeded 3 M (RH <65%).

For 316L, the critical relative humidity obtained in this study was in the range of 56%–65% RH at 30 °C, which is in agreement with that found recently by Padovani et al. [20]. These authors found pitting in $MgCl_2$ solution droplets up to an RH of 50% to 60% for 316L.

Passive current density is also affected by changes in RH and solution concentration (Figure 5-37). For 304L, it has been shown that in de-aerated full immersion studies [18] that passive current increases by an order of magnitude in highly concentrated solutions of $MgCl_2$ (Figure 5-37) that translate to

humidities close to deliquescence. Near saturation, passive current densities of 0.01 mA/cm^2 were observed.

5.3.5 Effect of microstructure

It is important to bear in mind that all the experiments carried out in this chapter were performed on as received 304L and 316L alloys surface (LT plane). Pits were often seen to be influenced by the local crystal structure. Pits were often seen to have a small hole in the centre of the shallow dish region e.g. (Figure 5-1) and (Figure 5-18(a)), which is possibly the cavity that developed from the dissolving of an inclusion (most commonly MnS inclusions) during the pit initiation process. This is in agreement with the observation of Tsutsumi et al. [4], Hastuty et al. [8], and Street et al. [6].

Pits can initiate and propagate along pre-existing defects, such as elongated inclusions [7, 18]. Figure 5-23 shows a pit grown on the alloy surface parallel to the rolling direction of the alloy. This is most likely to be corrosion attack along an elongated inclusion [7, 18], as mentioned previously in Section 2.10.6. However, it might also be due to a surface defect present at the alloy surface. In this chapter, among all the investigated pits, elongated pits were only observed in three cases (i.e. 3 out of 527).

Pits can also propagate along residual delta ferrite [26]. Pits with layered morphology were observed on the alloy surface of 304L (e.g. Fig.5-8 and 5-36). This was due to the preferential attack of ferrite phase, as described previously in Chapter 4.

Crystallographic facets were also observed in pits for the as received 304L stainless steel (e.g. Figure 5-6). This is most likely due to the dissolution of specific crystal plane(s) of the exposed surface. As mentioned previously, the unattacked flat walls might be belong to the {111} close-packed crystal planes of austenite, which was observed by Schwenk [125]. Possible grain facets morphology was also observed on 316L stainless steel exposed for both 1 day, and 1 week exposure (Figure 5-35). The facet size of a given grain correlates with the grain sizes of the alloy shown in Figure 3-3.

Under full immersion conditions, the effect of crystallographic orientation on the pitting corrosion has been investigated by a number of researchers [202-207]. It was found that the dissolution depth, after a given time, depends on the crystal plane of the exposed surface. Under atmospheric conditions, however, there are no specific studies of such effect.

5.4 Conclusions

1. The morphology of atmospheric corrosion pits on 304L and 316L stainless steel under $MgCl_2$ droplets is a sensitive function of RH. At RH values ≤48%, in each droplet, the first corrosion attack is in the form of a crystallographically-etched shallow dish. The diameter of these shallow dishes generally increases as the distance from droplet edge increases. At lower RH values (35% and 45%), the shallow dishes develop small satellite pits. Such pits are covered with caps enriched in Cr, Mn, S, O and Cl. At 48% RH, for 304L only earing pit morphologies were observed (no satellite pits were seen) as a result of continuous attack into the shallow region while for 316L circular pits were observed. Shallow dishes were not observed at ≥56% RH for 304L but for 316L were not observed at ≥48% RH, and instead circular, deeper and rougher pits were seen.

2. For both 35% RH and 45% RH, a greater number of pits towards the centre of the droplet, where the droplet height is higher, form an earing attack while pits nearby the droplet edge, where the droplet height is low, show satellite pits. Deeper ear-shaped attack is more likely at higher RH values since less concentrated solutions have higher ionic conductivity and diffusivity in addition to a greater droplet height leading to a lower IR drop between the cathodic and anodic regions.

3. For 304L at 56% RH, the diameter and depth of pits formed at or nearby the droplet edge was greater than that of pits close to the droplet centre.

This can be explained by the influence of three phase boundary where there is particularly easy access of oxygen for the cathodic reaction.

4. Pit size significantly increased with increasing exposure time, while the shallow dish diameter, after reaching a certain size, does not change with increasing exposure time and RH, and was in same range for both alloys.

5. For 304L, pits were observed up to ~65% RH (pits were not observed at 70% RH and higher), while for 316L, pit were observed up to ~56% RH, but were not observed at ~65% RH and higher.

6 Effect of droplet diameter and chloride deposition density on atmospheric pitting corrosion of Type 304L and 316L austenitic stainless steels

6.1 Introduction

Both the size and deposition density of salt deposits can affect the corrosion rate and pit morphologies on stainless steel samples as described in Sections 2.10.4 and 2.10.3. The salt concentration of such deposits is determined by the relative humidity to which they are exposed [6, 141]. The two most common methods of salt deposition on the metal surfaces for lab exposure experiments involve either deposition of clusters of salt particles [129, 148-152] or deposition of droplets of concentrated salt solutions by a micro-pipette [4, 5, 15, 21, 22, 134-139]. In such methods, it is not easy to establish well-defined and reproducible droplet arrays on metal surfaces. In the present study and in recent work [6], it is shown that an automatic deposition system can be used to deposit salt solution droplets of defined size and concentration on sample surfaces, allowing more systematic investigation of the influence of droplet diameter and chloride deposition density on atmospheric pitting corrosion.

Secondary spreading and micro-droplet formation have been investigated for different salt solutions and materials as described in Section 2.13. However, the formation of secondary spreading and micro-droplet formation has not been observed for $MgCl_2$ droplets on stainless steel. In this work, these have been investigated for $MgCl_2$ droplets at different RH values.

6.2 Results

6.2.1 Effect of droplet diameter on pit diameter

The effect of droplet diameter on pit diameter was investigated for both 304L and 316L austenitic stainless steels; the results for each will be described separately in this section.

Figure 6-1 shows as deposited arrays of $MgCl_2$ droplets of the same chloride deposition density (~1000 µg/cm^2) on a 304L stainless steel plate surface. Droplets were deposited with a range of volumes, 1 µl to 4 µl, giving a range of droplet diameters from 1.9 mm to 3.3 mm, respectively. Constant chloride deposition density was achieved by depositing solutions of different concentrations. This method of deposition was designed to study the effect of droplet diameter, for fixed chloride deposition density, on pit diameter and depth.

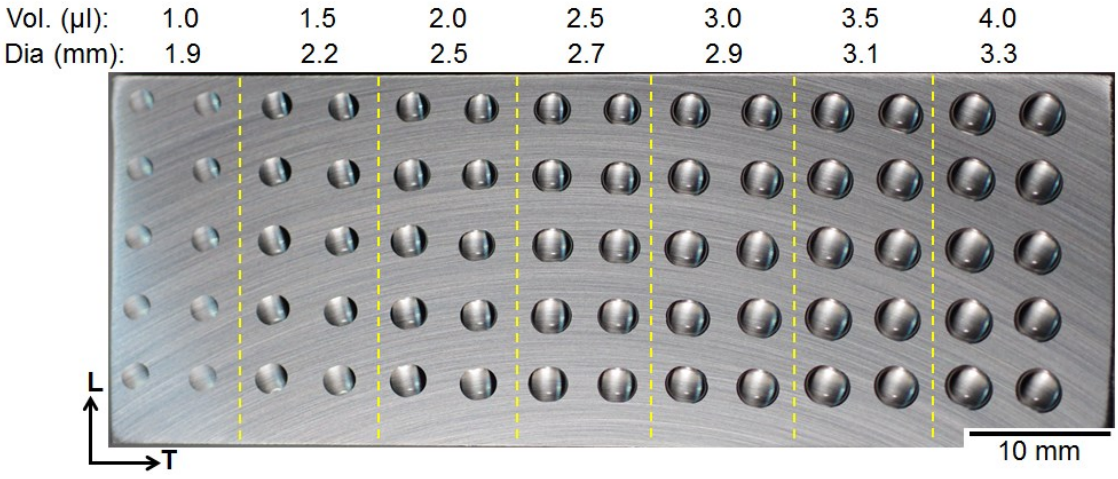

Figure 6-1 Macrograph image of a 304L stainless steel plate surface (LT plane) with as-deposited arrays of $MgCl_2$ salt solution droplets of constant CDD (~1000 µg/cm^2) with various droplet diameters ("Dia") and the correspond droplet volumes ("Vol.")

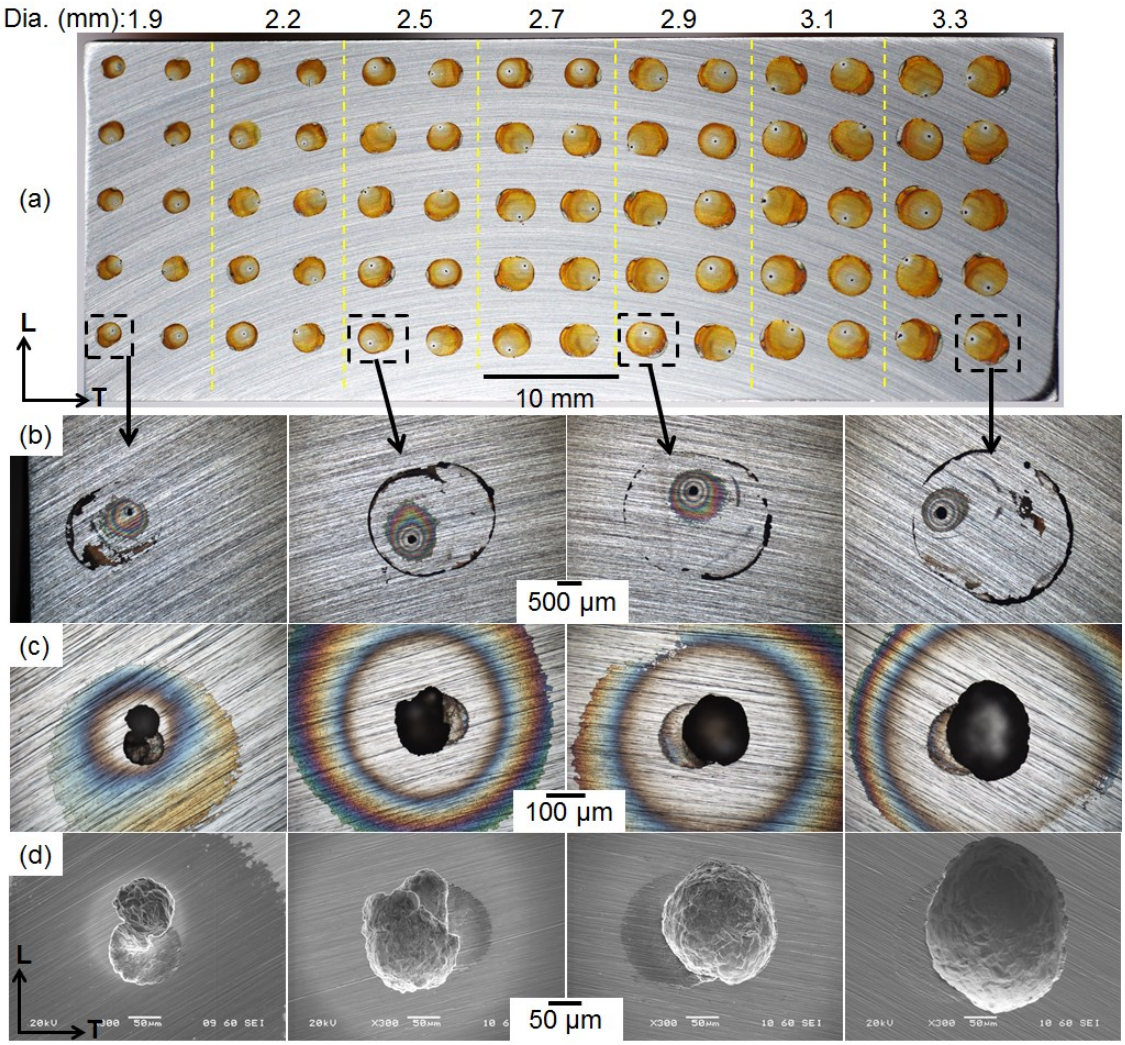

Figure 6-2 (a) a 304L stainless steel plate surface (LT plane) deposited with arrays of $MgCl_2$ droplets of fixed CDD (~1000 µg/cm^2) shown in (Figure 6-1) following exposure at 43% RH and 30 °C for 1 week; (b) typical droplets after washing with DI water; (c) micrographs of pits shown in (b); (d) SEM images of pits shown in (c).

Figure 6-2 (a) shows the macrograph of the 304L stainless steel plate surface deposited with arrays of $MgCl_2$ droplets shown in Figure 6-1 following exposure at 43% RH and 30 °C for 1 week. It can be seen from the macrograph that the droplets are still present and evidence of rust can be seen in all droplets. A single pit per droplet can be observed. Only one droplet of the ~2.2 mm

diameter set contained an elongated pit that had grown along the rolling direction of the alloy (not shown); all other pits were circular. The rust (corrosion products) was washed away with deionised (DI) water (Figure 6-2 (b)) to observe the pit morphologies shown in the lower optical micrographs (c). The SEM images show more clearly that all the pits observed had a shallow dish-shaped region with one side significantly more attacked (Figure 6-2 (d)).

In total, 38 out of 70 pits were seen to be associated with micro-droplet formation which will be discussed in section 6.3.

Figure 6-3 shows an array of droplets designed to study the influence of droplet diameter on both pit diameter and depth for deposits of constant chloride deposition density (~1000 μg/cm^2) on 316L stainless steel. In each row, droplets were deposited with a range of volumes from 1 μl to 4 μl, giving a range of initial droplet diameters from 2.0 mm to 3.1 mm respectively.

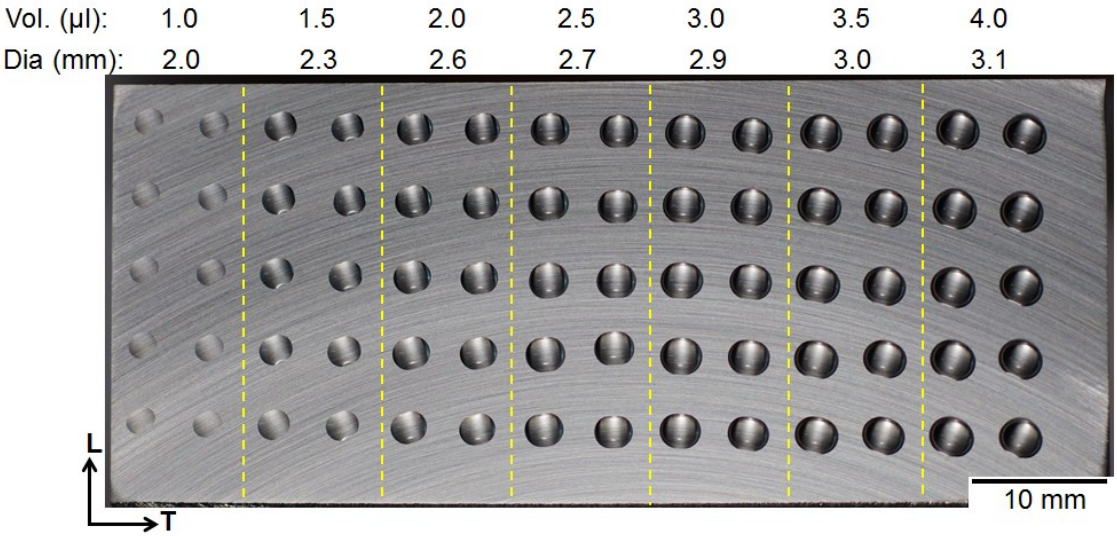

Figure 6-3 Macrograph image of a 316L stainless steel plate surface (LT plane) deposited with arrays of $MgCl_2$ droplets of same chloride deposition density (~1000 μg/cm^2) with various droplet diameters.

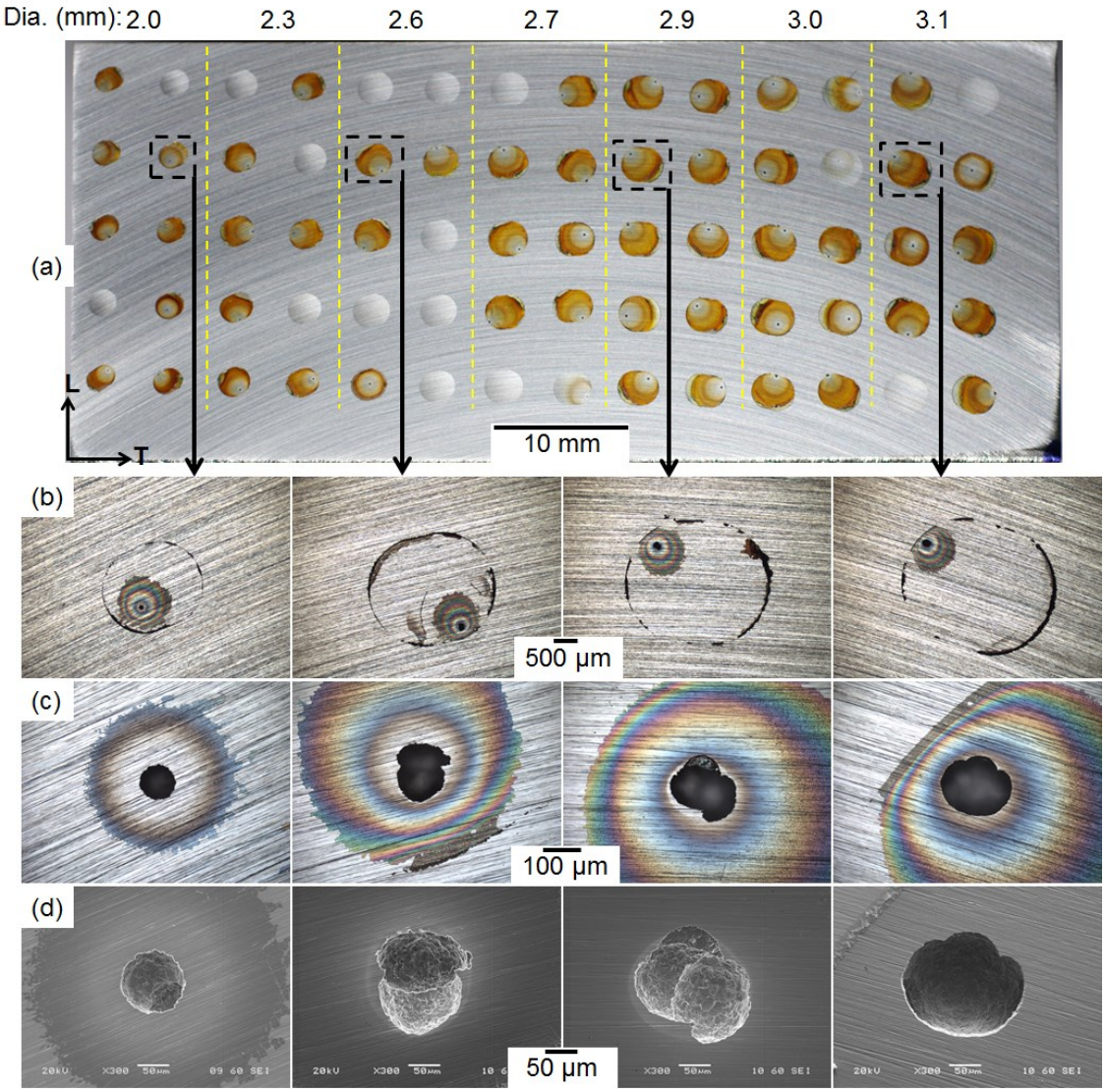

Figure 6-4 (a) a macrograph of the 316L stainless steel plate surface (LT plane) deposited with arrays of $MgCl_2$ droplets of fixed CDD (~1000 µg/cm^2) shown in Figure 6-3 following exposure at 43% RH and 30 °C for 1 week; (b) typical droplets after washing with DI water; (c) micrographs of pits shown in (b); (d) SEM images of pits shown in (c).

Figure 6-4 (a) shows the macrograph of the 316L stainless steel plate surface deposited with arrays of $MgCl_2$ droplets of fixed CDD (~1000 µg/cm^2) shown in Figure 6-3 following exposure at 43% RH and 30 °C for 1 week. It can be seen from the macrograph that droplets are still visible and evidence of rust can be

seen in all pitted droplets, which contained only one main pit. A significant number of droplets did not show any sign of corrosion, in contrast to the results for 304L stainless steel, where all droplets pitted. To reveal the pit morphologies shown in Figure 6-4 (c), the rust was washed away with deionised water (Figure 6-4 (b)). In all pits, a shallow dish-shaped region with one side significantly more attacked was observed more clearly with SEM images (Figure 6-4 (d)). In some cases no shallow dish region can be observed, this may be because the entire region has been deeply attacked after 1 week of exposure.

The number of pits associated with micro-droplets was found to be 37 out of 55 pits. This will be described in section 6.3.

Figure 6-5 shows the relationship between the equivalent pit diameter (active region only, as described in Section 3.8.2) and the deposited droplet diameter for both 304L and 316L stainless steels. It can be seen that the pit diameter increases with increasing droplet diameter approximately linearly for a fixed chloride deposition density for both 304L and 316L stainless steels. It is also evident that pits with larger diameters are formed on 304L than those that formed on 316L stainless steel. The pit depth in 304L and 316L did not vary greatly with droplet diameter, and appeared to be of a similar scale in both alloys. The variation in pit depth in 316L appeared to be greater than the variation in 304L. The fine focus method used to measure the pits depth and the uncertainty in the measurements was described in Section 3.8.3.

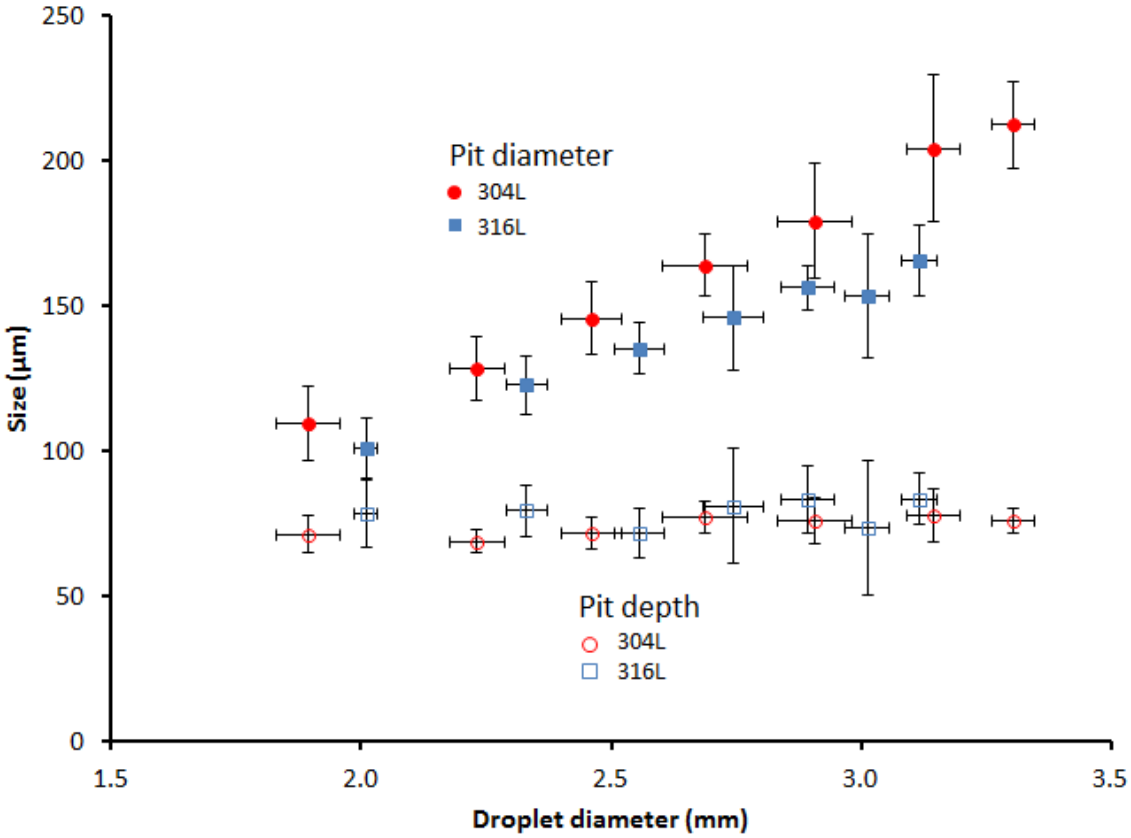

Figure 6-5 The equivalent pit diameter (active region without the shallow dish) as a function of the droplet diameter for pits shown in Figure 6-2 and Figure 6-4; the plates were deposited with arrays of $MgCl_2$ droplets of fixed CDD (~1000 µg/cm^2) and exposed at 43% RH and 30 °C for 1 week. 304L is shown in red circles and 316L is shown with blue squares, and solid symbols represent pit diameter whereas open symbols represent pit depth.

6.2.2 Effect of salt deposition density on atmospheric pitting corrosion

The effect of chloride deposition density (CDD) for fixed droplet diameter on pit diameter and depth was investigated for both 304L and 316L austenitic stainless steels. The effect of droplet diameter and exposure time on pitting behaviour was also investigated for 304L austenitic stainless steel.

Figure 6-6 shows an array of droplets on 304L stainless steel designed to study the influence of chloride deposition density on pit size for droplets of constant deposition area. In each column, droplets were deposited with a constant volume of 2 µl (giving initial deposition diameter of ~2.5 mm) and varying solution concentration, from 3.7 M to 185 µM $MgCl_2$. This gave a range of CDD values from ~10000 to 0.5 µg/cm^2, respectively, calculated upon deposition.

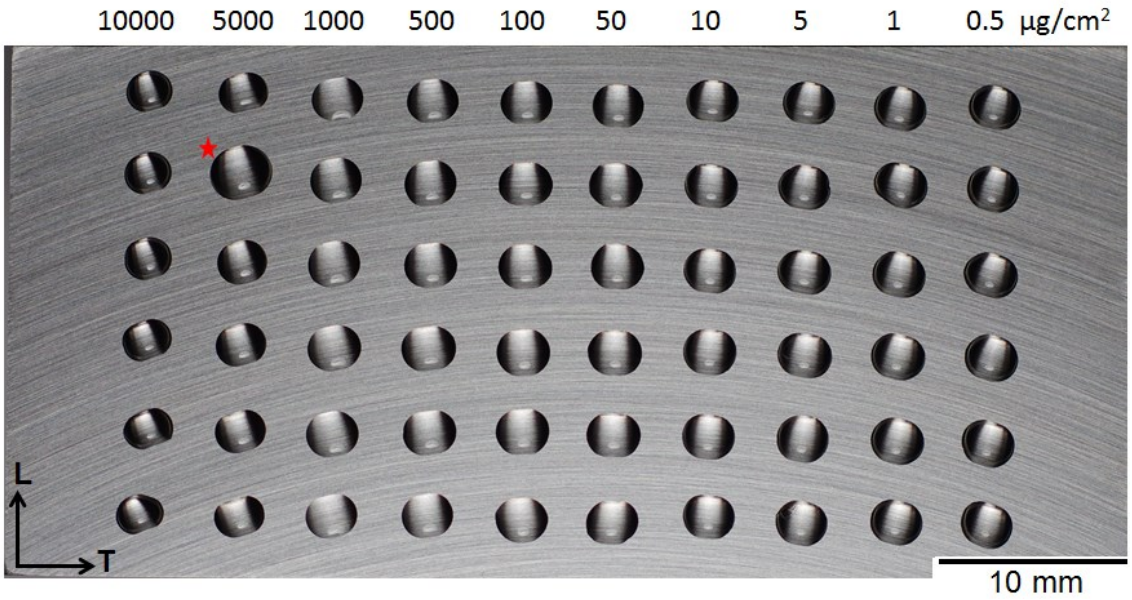

Figure 6-6 Macrograph image of a 304L stainless steel plate surface (LT plane) deposited with arrays of $MgCl_2$ droplets of fixed deposition diameter (~2.5 mm) with different CDDs ranging from ~0.5 to 10000 µg/cm^2. The droplet marked with red star had two droplets superimposed.

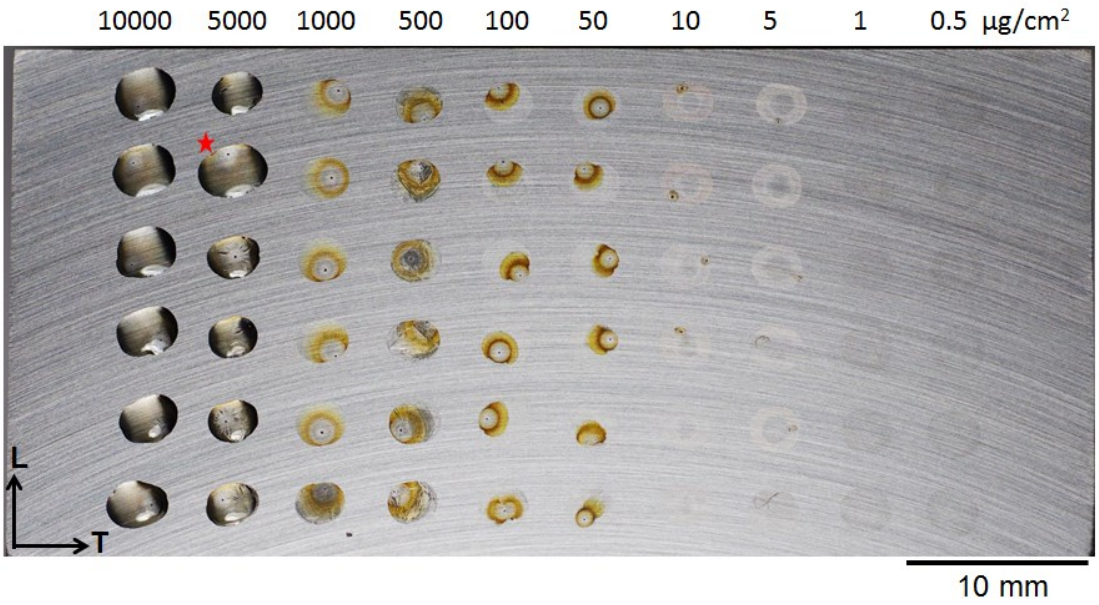

Figure 6-7 A 304L stainless steel plate surface (LT plane) deposited with arrays of $MgCl_2$ droplets of fixed deposition diameter (~2.5 mm) with different CDDs ranging from ~0.5 to 10000 µg/cm^2, as shown in Figure 6-6 following exposure at 43% RH and 30 °C for 1 day. The droplet marked with a red star had two droplets superimposed.

Following exposure at 43% RH and 30 °C for 1 day, (Figure 6-7), droplets with CDDs of 0.5 and 1 µg/cm^2 did not pit after 1 day exposure. 5 out of 6 of the droplets with a CDD of 5 µg/cm^2 pitted, and 4 out of 6 of the droplets with a CDD of 10 µg/cm^2 pitted. Both sets droplets with CDDs of 5 and 10 µg/cm^2 showed a “ring-like” shape after 1 day exposure, with the central hole being bigger in the 5 µg/cm^2 set (Figure 6-8). For CDD values ranging from 50 to10000 µg/cm^2, all droplets pitted. Droplets with a CDD of 10000 µg/cm^2 had spread significantly after 1 day of exposure.

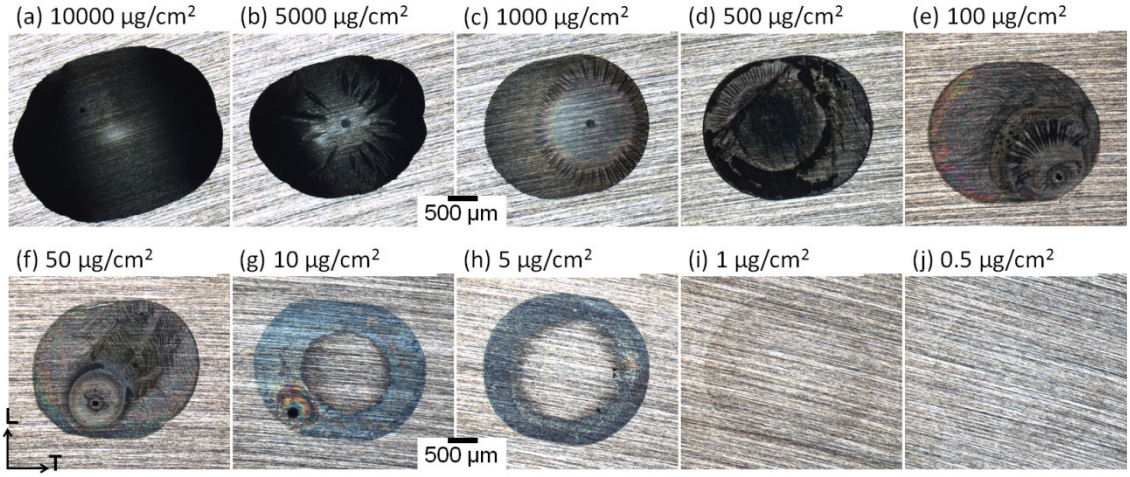

Figure 6-8 Typical examples of $MgCl_2$ droplets of fixed deposition diameter (~2.5 mm) with different CDDs ranging from ~0.5 to 10000 µg/cm^2 on the 304L stainless steel plate surface (LT plane), shown in Figure 6-7 following exposure at 43% RH and 30 °C for 1 day.

Figure 6-9 shows pit morphologies obtained at different chloride deposition levels. Pits that grew at 10000 µg/cm^2 CDD were round and deep with an average diameter of 85±10 µm. In most cases this totally consumed any shallow dish region, if indeed there was one. Pitting attack at a CDD of 5000 µg/cm^2 was deep and followed the approximate boundary of the shallow dish region. In the CDD range from 1000 to 50 µg/cm^2, an earing morphology was observed, with attack into the metal on one side of the shallow dish region.

At CDD values of 1 and 0.5 µg/cm^2, there was a faint pattern of rust but no obvious pits were observed.

At CDD of 10 and 5 µg/cm^2, pitting was seen but pits were irregular in shape and could not easily be described in terms of having a “shallow dish region”. At 5 µg/cm^2, usually a single cluster of very small (<5 µm in diameter) pits was formed.

At a CDD of 10000 µg/cm^2, one instance of a shallow dish region was seen that had been heavily attacked by the continuing corrosion but had an apparent diameter of less than 50 µm. The rest of the pits, 5 out of 6, didn't show any sign for the shallow dish and had a hemispherical pit shape. The shallow dish regions in droplets with a CDD of 5000 µg/cm^2 had an average diameter of 110±20 µm, which is much larger than for those with a CDD of 10000 µg/cm^2, and the shallow dish diameters were reduced for a CDD of 5 µg/cm^2.

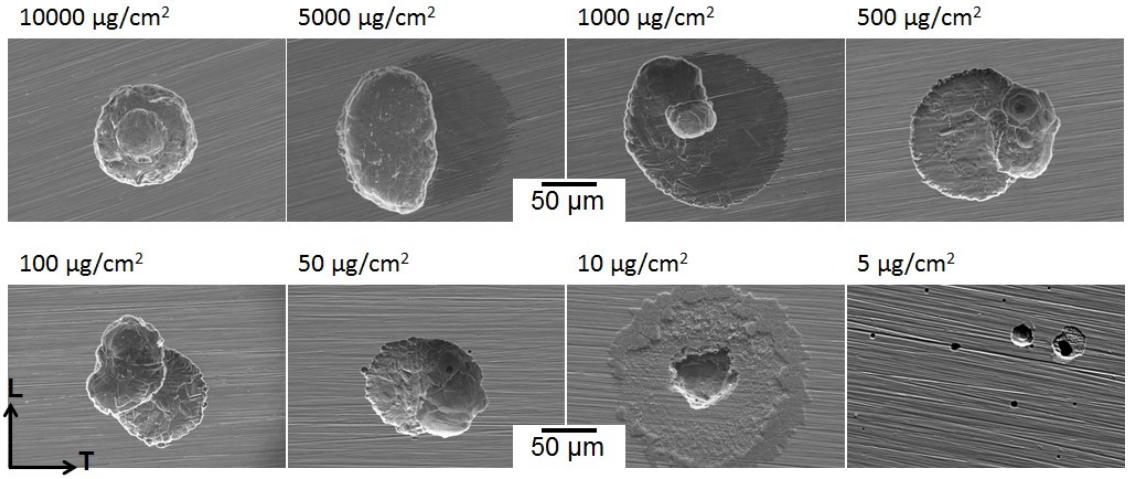

Figure 6-9 Typical pit morphologies of pits grown under $MgCl_2$ droplets of fixed deposition diameter (~2.5 mm) with different CDDs ranging from ~0.5 to 10000 µg/cm^2 on the 304L stainless steel plate surface (LT plane), as shown in Figure 6-7 following exposure at 43% RH and 30 °C for 1 day.

The total pit diameter, active region diameter (as defined in Section 3.8.2), and pit depth, for a fixed deposition area, is plotted against the initial chloride deposition density in Figure 6-10. The results show that the diameter of the active region increases with increasing CDD up to 1000 µg/cm^2.

At a CDD of 10000 µg/cm^2 there is a high amount of scatter. Similarly, the total pit diameter increases with increasing CDD up to 1000 µg/cm^2, after which the

high amount of scatter makes determining a trend difficult. The pit depth initially increases rapidly as the CDD increases from 5 to 50 μg/cm^2, but for CDD values >50 μg/cm^2, there appears to be a slight decrease in depth.

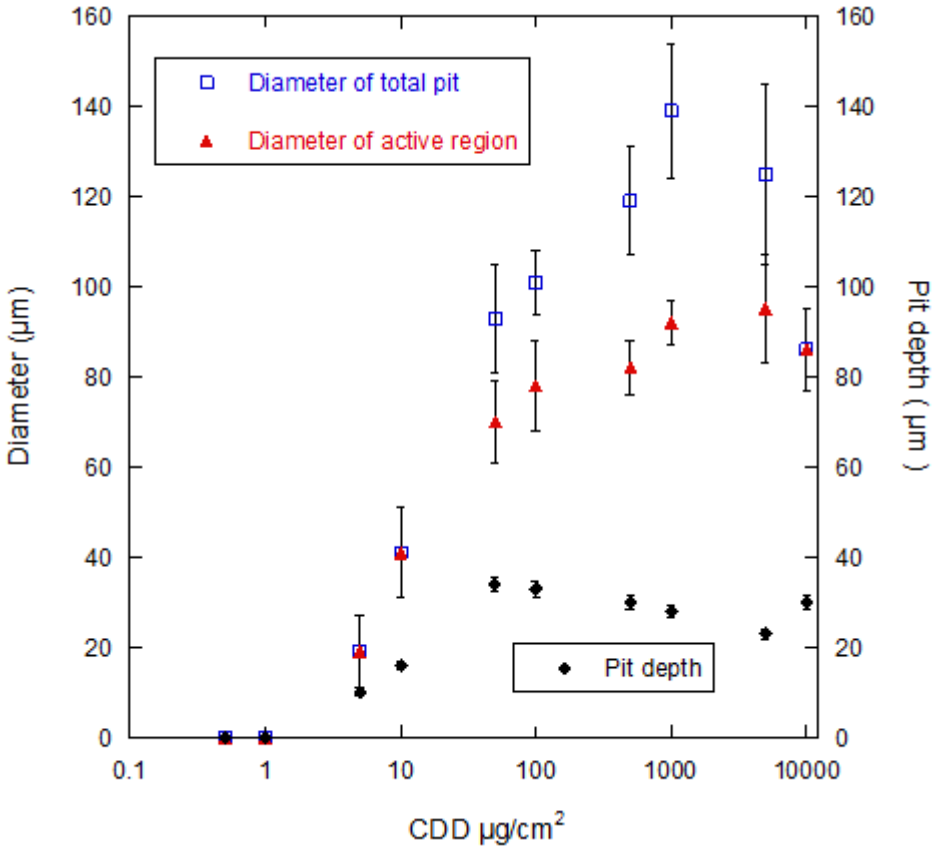

Figure 6-10 Pit size as a function of CDD for pits grown under $MgCl_2$ droplets of fixed deposition diameter (~2.5 mm) on 304L stainless steel plate (LT plane) following exposure at 43% RH and 30 °C for 1 day. The total pit diameter and active region diameter are defined in Section 3.8.2).

Figure 6-11 shows the results obtained for 304L following 1 week exposure at 45% RH under $MgCl_2$ droplets of fixed deposition diameter of ~3.3 mm. Almost all droplets pitted. A single pit per droplet was observed at CDDs of 10 and 8 µg/cm^2, while at ≤6 µg/cm^2 both single pits and multiple pits were observed. At deposition levels of ≤4 µg/cm^2, droplets showed a “ring-like” shape, with the central hole increasing with decreasing CDD. Pit morphologies are shown in Figure 6-12; it can be seen that with decreasing CDD the pits become smaller, reaching a point where it appears that clusters of small pits formed.

At deposition levels of 10 to 2 µg/cm^2, pits were generally seen with a shallow dish with attacked region while at deposition levels ≤1 µg/cm^2, pits were associated with clusters of very small pits.

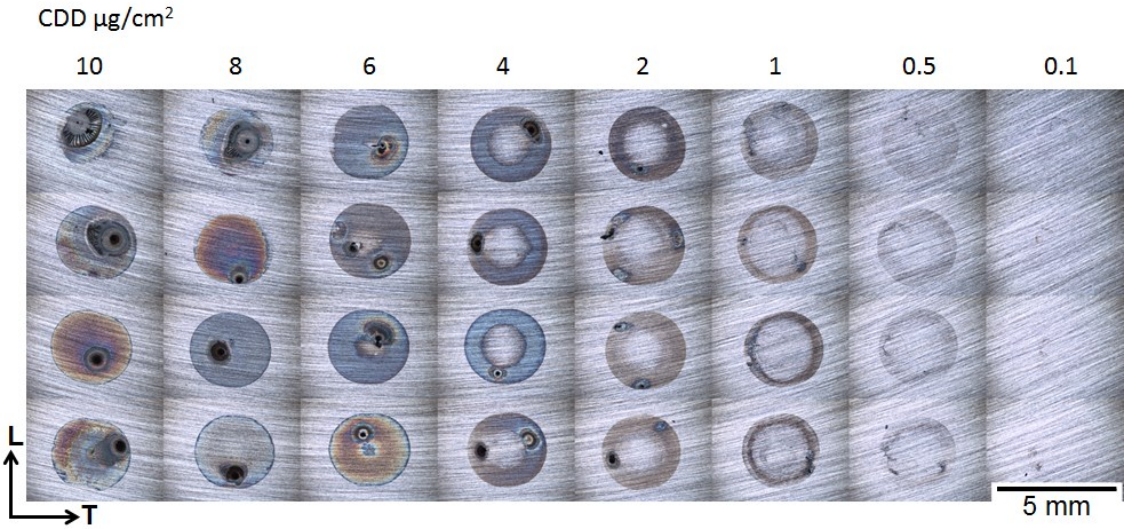

Figure 6-11 A 304L stainless steel plate surface (LT plane) deposited with arrays of $MgCl_2$ droplets of fixed deposition diameter (~3.3 mm) but with different CDDs ranging from ~10 to 0.1 µg/cm^2 following exposure at 45% RH and 30 °C for 1 week.

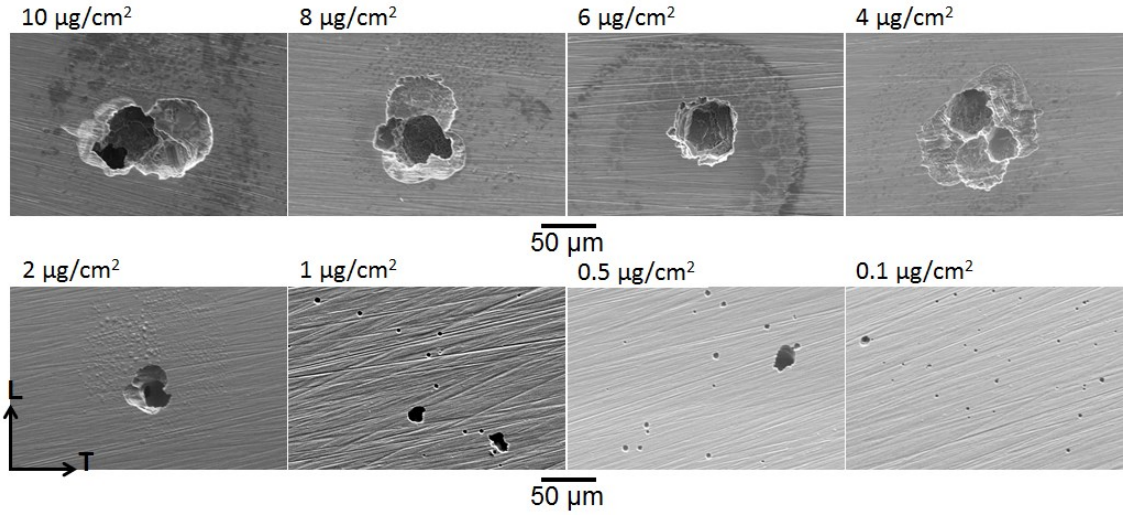

Figure 6-12 Typical morphologies of pits grown under $MgCl_2$ droplets of fixed deposition diameter (~3.3 mm) but with different CDDs ranging from ~10 to 0.1 µg/cm^2 on 304L stainless steel plate surface (LT plane) shown in Figure 6-11 following exposure at 45% RH and 30 °C for 1 week.

Figure 6-13 (upper image) shows the results obtained for 304L following 1 week exposure at 45% RH under $MgCl_2$ droplets with a fixed deposition diameter of ~2.5 mm. The electrolyte layer was found to be discontinuous. Although there was a faint pattern of rust at CDD values of 0.1 and 0.2 µg/cm^2, no obvious pits were observed. Pits were observed at CDD values of 0.5-10 µg/cm^2. Single pits per droplet were not the only case observed; pits were associated with very small pits (<5 µm in diameter) that often appear in clusters at lower deposition levels such as 0.5 µm/cm^2 (Figure 6-14). Morphologies of the largest diameter pits are shown in Figure 6-13 (lower SEM images). Figure 6-15(a) shows a typical example of a cluster of very small pits seen under an $MgCl_2$ droplet with a CDD of 0.5 µg/cm^2 at deposition on 304L stainless steel after exposure at 43% RH and 30 °C for 1 week. Figure 6-15(b) shows an SEM image at the same magnification of an area site of 130x120 µm^2 of 304L stainless steel (LT

plane) final polished with OPS, which contains seven inclusions of ≤2 μm in diameter. Two types of inclusions were observed: MnS inclusions and mixed oxide inclusions. Table 6-1 shows the chemical composition of typical examples of these two types of inclusions determined with EDX.

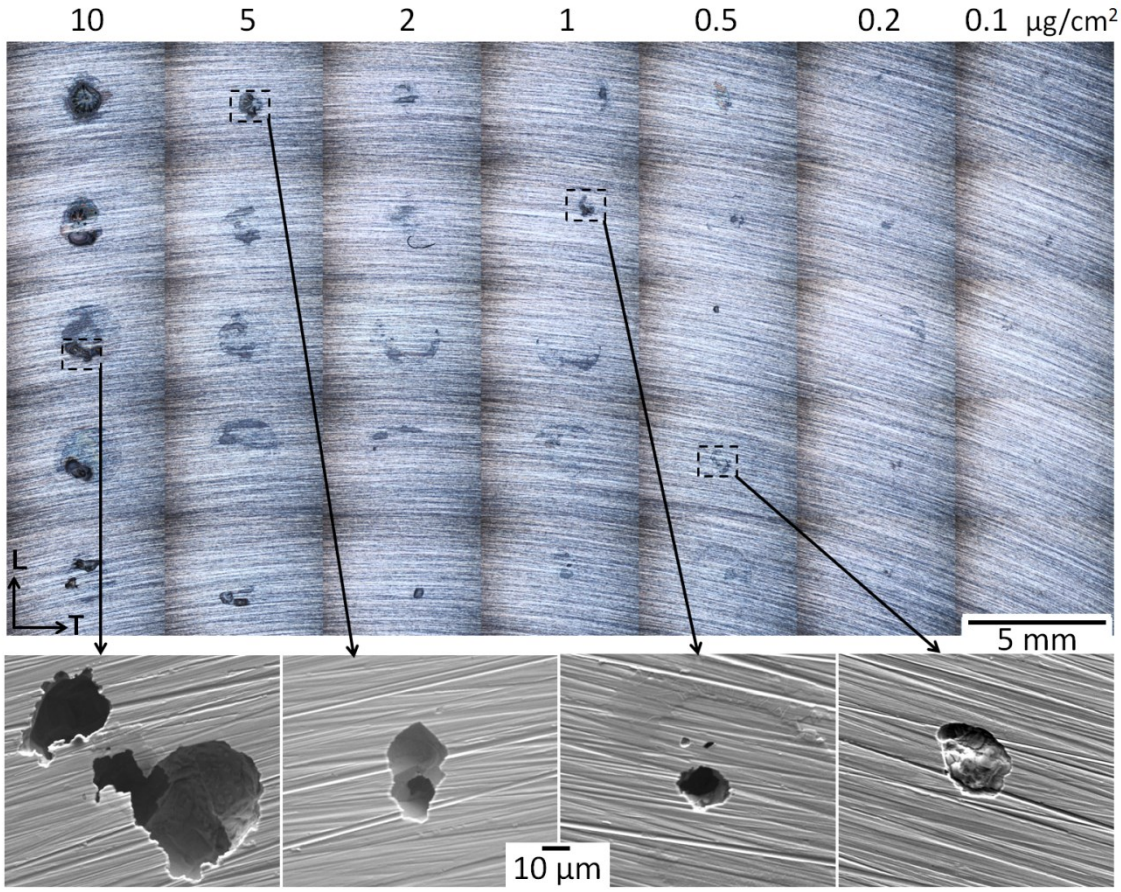

Figure 6-13 Typical morphologies of pits grown under $MgCl_2$ droplets of fixed deposition diameter (~2.5 mm) with different CDDs ranging from ~10 to 0.1 μg/cm^2 on 304L stainless steel plate surface (LT plane) following exposure at 43% RH and 30 °C for 1 week.

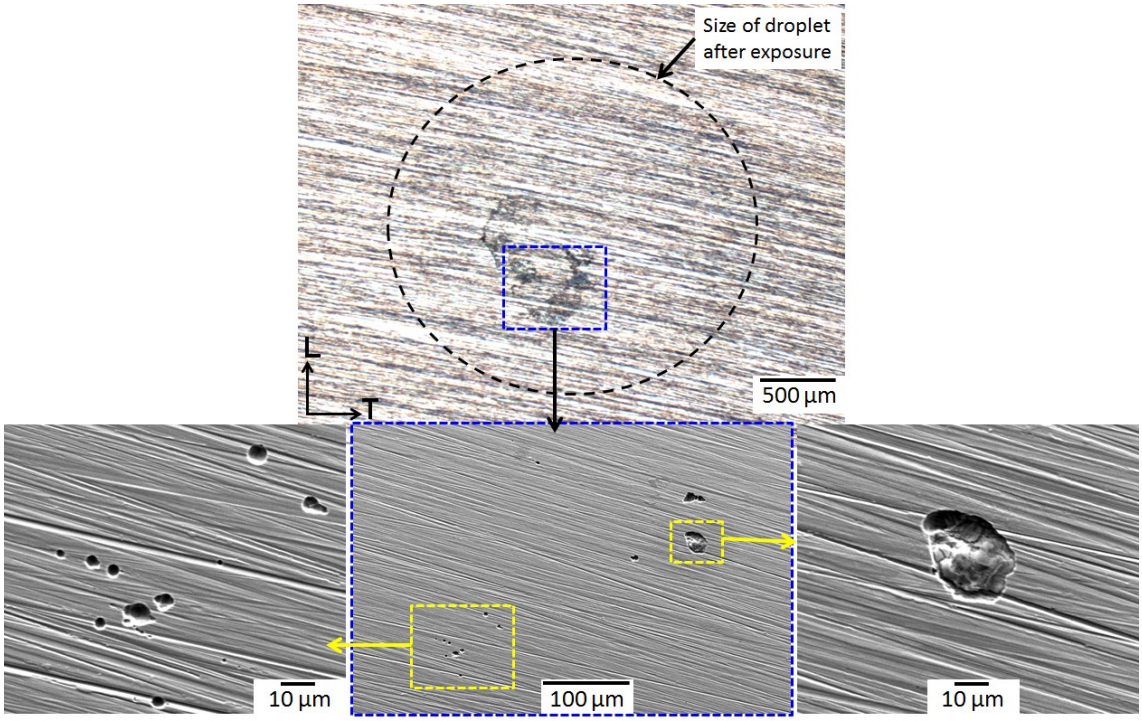

Figure 6-14 Typical example of $MgCl_2$ droplet of diameter (~2.5 mm) with a CDD of 0.5 µg/cm^2 (at deposition) on 304L stainless steel plate (LT plane), following exposure at 43% RH and 30 °C for 1 week. Multiple pits grown under the interrupted electrolyte layer.

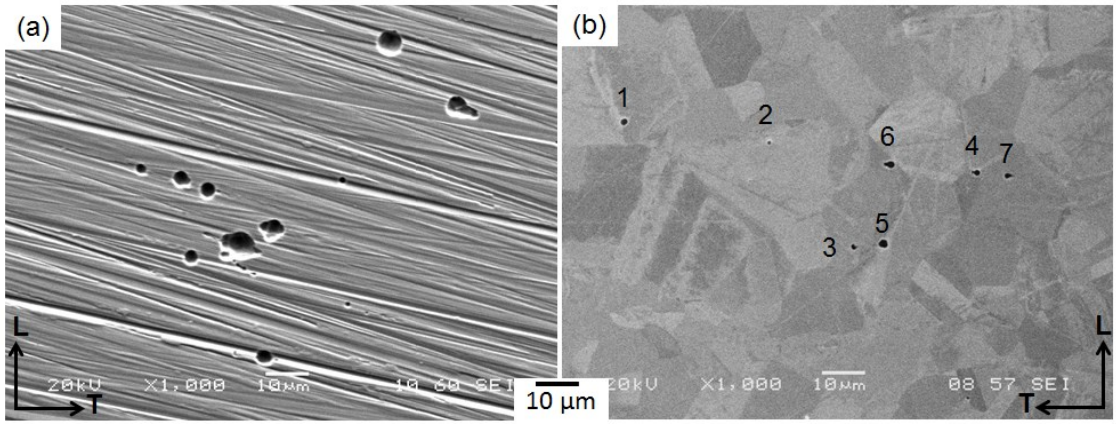

Figure 6-15 (a) Typical example of a cluster of very small pits shown in Figure 6-14, observed under an $MgCl_2$ droplet of diameter (~2.5 mm) with a CDD of 0.5 µg/cm^2 (at deposition) on 304L stainless steel plate surface (LT plane), following exposure at 43% RH and 30 °C for 1 week; (b) an SEM image at the same magnification of an area of 130x120 µm^2 of 304L stainless steel (LT plane, surface is final polished with OPS) showing the distribution of inclusions: 1-4 were MnS inclusions while 5-7 were mixed oxide inclusions.

Table 6-1 The chemical composition of typical MnS and a mixed oxide inclusion observed in 304L stainless steel (LT plane) detected with EDX.

Weight %	O	Al	Si	S	Ti	Cr	Ni	Mn	Fe
MnS inclusion	0	0	0.3	5.2	0	17	7.0	8.7	balance
mixed oxide inclusion	7.3	2.4	0.2	0.5	3.4	25	4.1	13	balance

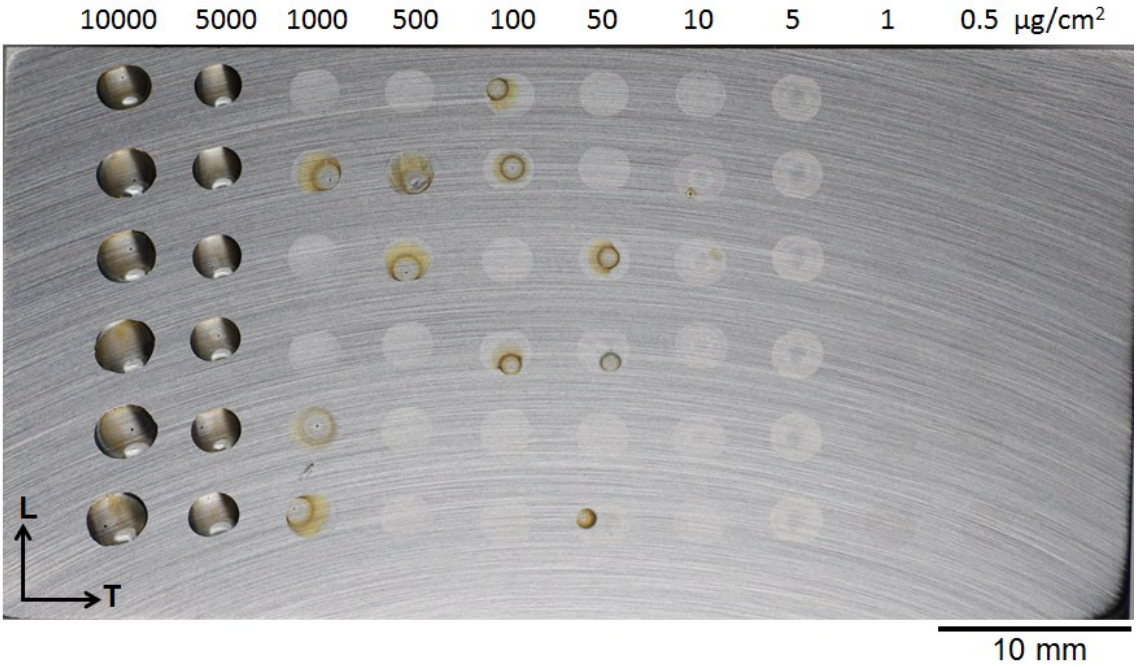

Figure 6-16 A 316L stainless steel plate surface (LT plane) deposited with arrays of $MgCl_2$ droplets of fixed deposition diameter (~2.5 mm) with different CDDs ranging from ~0.5-10000 µg/cm^2 following exposure at 43% RH and 30 °C for 1 day.

Figure 6-16 shows the results obtained for 316L following exposure at 43% RH and 30 °C for 1 day. Compared to 304L exposed to the same conditions, fewer droplets were pitted. Similar to 304L stainless steel, pits were not observed under droplets of CDD of 0.5 and 1 µg/cm^2 after 24 hours. The 5 µg/cm^2 droplets show a faint pattern of rust, but with no clear evidence of pitting. Similar to 304L stainless steel, both sets of droplets with a CDD of 5 and 10 µg/cm^2

showed a “ring-like” shape, with the central hole being bigger in the 5 μg/cm^2 set (Figure 6-17). For droplets with a CDD of 10 to 1000 μg/cm^2 not all the droplets pitted, but all of the droplets with a CDD of 5000 and 10000 μg/cm^2 did pit. Droplets under the largest CDD had spread significantly after 1 day, similar to that shown on 304L.

The pit morphologies obtained under different CDD values are shown in Figure 6-18. No shallow dish regions were observed at 10000 μg/cm^2 CDD; pits were circular in shape, with an average diameter of 110±15 μm. In the CDD range of 5000 to 500 μg/cm^2, pits with a shallow dish region were seen with an area of deeper attack into the metal surface on one side. In the CDD range of 100 to 10 μg/cm^2, pits were approximately circular with no clear trace of a shallow dish. The shallow dish diameters were reduced as CDD was reduced to 5 μg/cm^2 CDD.

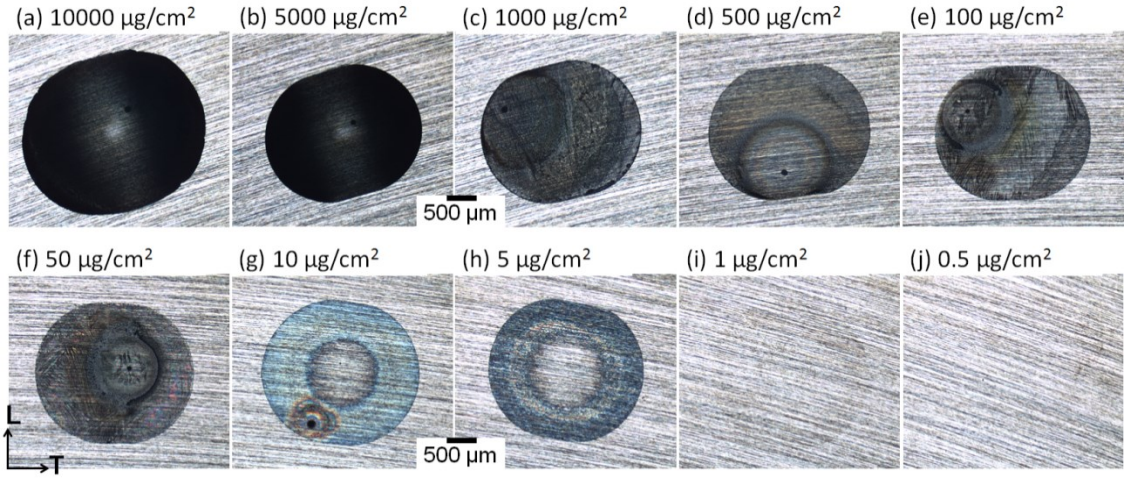

Figure 6-17 Typical examples of $MgCl_2$ droplets of fixed deposition diameter (~2.5 mm) with different CDDs ranging from ~0.5 to 10000 μg/cm^2 on the 316L stainless steel plate surface (LT plane) shown in Figure 6-16 following exposure at 43% RH and 30 °C for 1 day.

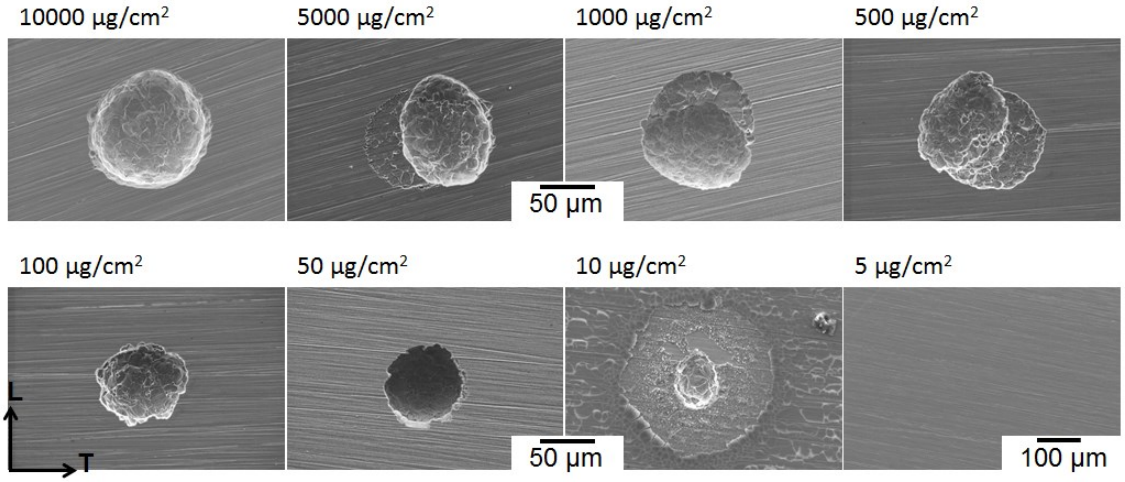

Figure 6-18 Typical morphologies of pits grown under $MgCl_2$ droplets of fixed deposition diameter (~2.5 mm) with different CDDs ranging from ~0.5 to 10000 µg/cm^2 on the 316L stainless steel plate surface (LT plane) shown in Figure 6-16 following exposure at 43% RH and 30 °C for 1 day.

Among all the pitted droplets, only one droplet of the1000 µg/cm^2 set contained an elongated pit that had grown along the rolling direction of the alloy (Figure 6-19).

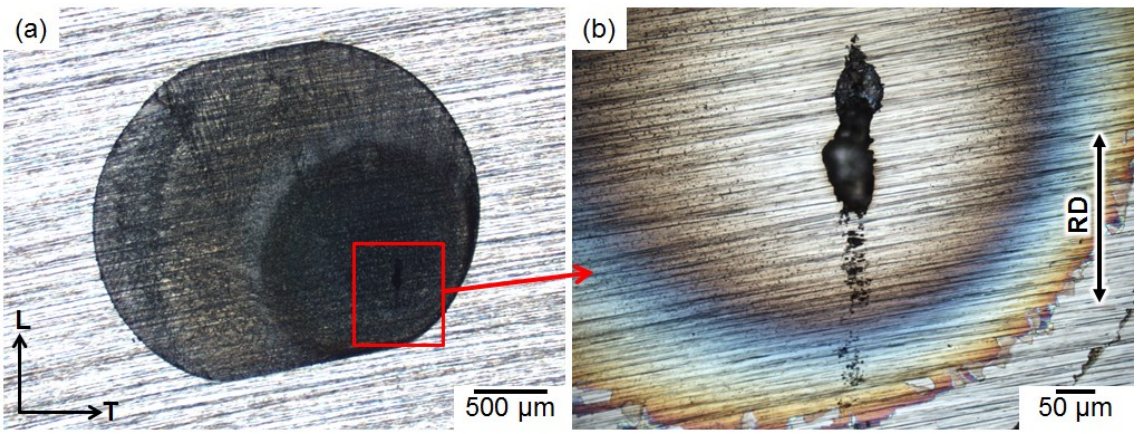

Figure 6-19 Morphology of a pit grown along the rolling direction on 316L, LT plane, under $MgCl_2$ droplet (~2.5 mm equivalent diameter, ~1000 µg/cm^2 CDD at deposition), after 1 day exposure at 43% RH and 30 °C; (a) optical image of the droplet; (b) optical image of the pit after washing with DI water.

Figure 6-20 shows the pit diameter (total pit diameter and active region diameter) and pit depth as a function of CDD for a fixed droplet area (volume). It can be seen that the total pit diameter increases with increasing CDD with the value at 5000 μm/cm^2 being within a high range of scatter which might be attributed to the thicker droplet in this set of droplets, as they did not show significant spreading (Figure 6-16 and Figure 6-17(b)). Similarly, the active region diameter increases with increasing CDD up to 500 μm/cm^2, then shows a high amount of scatter for 1000 and 5000 μm/cm^2 before increasing at 10000 μm/cm^2. For pit depth, the trend was similar to that observed for 304L: there is a rapid increase in pit depth at the beginning with increasing CDD, then no clear trend after 50 μm/cm^2.

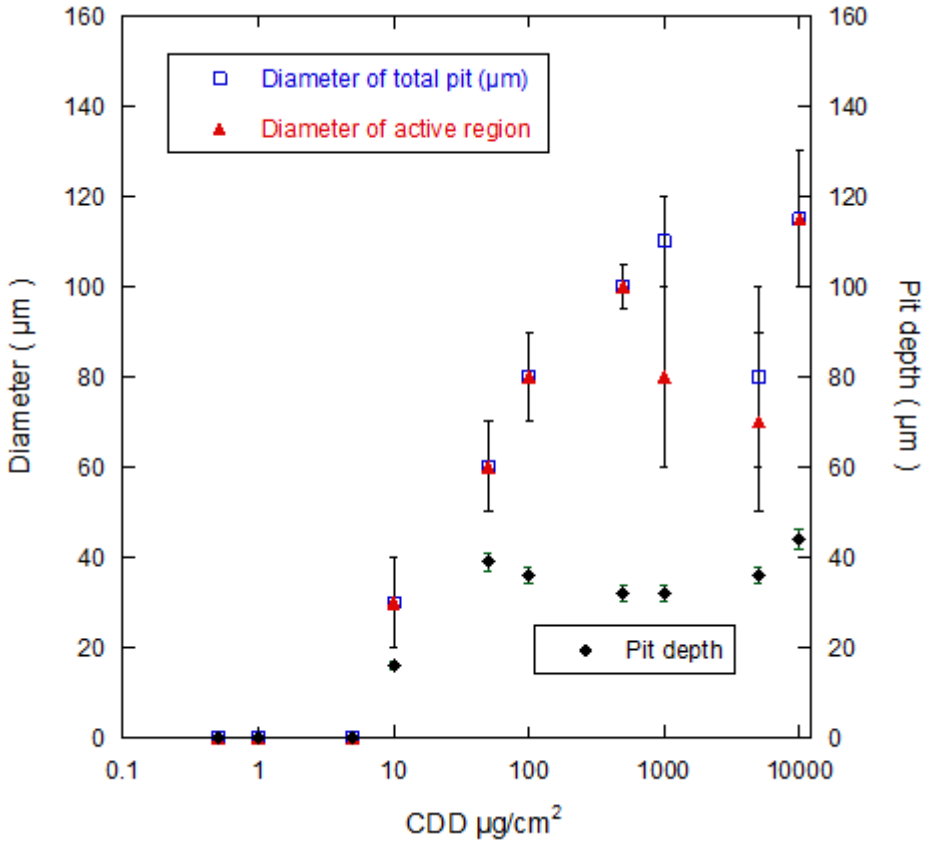

Figure 6-20 The equivalent diameters of the active region and the total pit, and the pit depth as a function of the CDD for pits formed in $MgCl_2$ deposits of fixed deposition diameter (~2.5 mm) on 316L stainless steel (LT plane) shown in Figure 6-16 following exposure at 45% RH and 30 °C for 1 day.

Table 6-2 shows that for 2.5 mm diameter droplets exposed for 1 day at 45% RH, pitting is observed down to a CDD of 10 μg/cm^2 for both 304L and 316L stainless steel, although fewer droplets pit for 316L compared with 304L. At a CDD of 5 μg/cm^2, 304L shows pitting, whereas 316L shows signs of rust staining but no obvious pits. No pits were observed at CDDs of 1 or 0.5 μg/cm^2 for either 304L or 316L under these conditions.

For ~2.5 mm diameter droplets on 304L exposed at CDD values of 1 and 0.5 µg/cm^2, no pits were observed after 1 day of exposure, but pits were observed after 1 week of exposure (Figure 6-13), indicating a lower CDD threshold after a longer exposure time. For the 1 week exposures, pitting was not observed at CD values of 0.2 and 0.1 µg/cm^2. However, larger droplets (~3.3 mm diameter) did show pitting even at a CDD value of 0.1 µg/cm^2 (Figure 6-12). The table also include the number of pits associated with micro-droplets.

Table 6-2 summary of observations of the pitting corrosion behaviour of 304L and 316L stainless steels (LT plane) under $MgCl_2$ droplets at different CDDs for fixed deposition diameters (~2.5 mm) and (~3.3 mm) at two exposure times: (a) after 1 day; (b) after 1 week at 45% RH. The ratio (x/y in black) in the table represents the number of droplets out of the total number of droplets investigated which show the indicated corrosion behaviour following exposure.

(a)

CDD µg/cm²	10000	5000	1000	500	100	50	10	5	1	0.5
304L 2.5 mm 1 day	● 6/6 0/6	● 6/6 0/6	● 6/6 1/6	● 6/6 3/6	● 6/6 3/6	● 6/6 0/6	● 4/6 0/6	● 5/6 0/6	x 6/6 0/6	x 6/6 0/6
316L 2.5 mm 1 day	● 6/6 0/6	● 6/6 1/6	● 3/6 0/6	● 2/6 0/6	● 3/6 0/6	● 3/6 0/6	● 2/6 0/6	○ 6/6 0/6	x 6/6 0/6	x 6/6 0/6

(b)

CDD µg/cm²	10	8	6	5	4	2	1	0.5	0.2	0.1
304L 2.5 mm 1 week	● 5/5 0/5	–	–	● 2/5 0/5	–	x 5/5 0/5	● 3/5 0/5	● 3/5 0/5	x 5/5 0/5	x 5/5 0/5
304L 3.3 mm 1 week	● 4/4 0/4	● 4/4 1/4	● 4/4 0/4	–	● 4/4 0/4	● 4/4 0/4	● 4/4 0/4	● 4/4 0/4	–	● 3/4 0/4

● Pit x No pit ○ Rust layer – Not measured

The ratio x/y is the number of pits associated with micro-droplets/total number of pits

6.3 Secondary spreading and micro-droplet formation

Secondary spreading and microdroplet formation is described in Section 2.13. Figure 6-21 shows the formation of micro-droplets on 304L stainless steel following exposure at 56% RH and 30 °C for 1 day. Micro-droplets were observed only when the pit initiated close or at the droplet edge. It can be seen that individual micro-droplets are hemispherical and/or circular in shape.

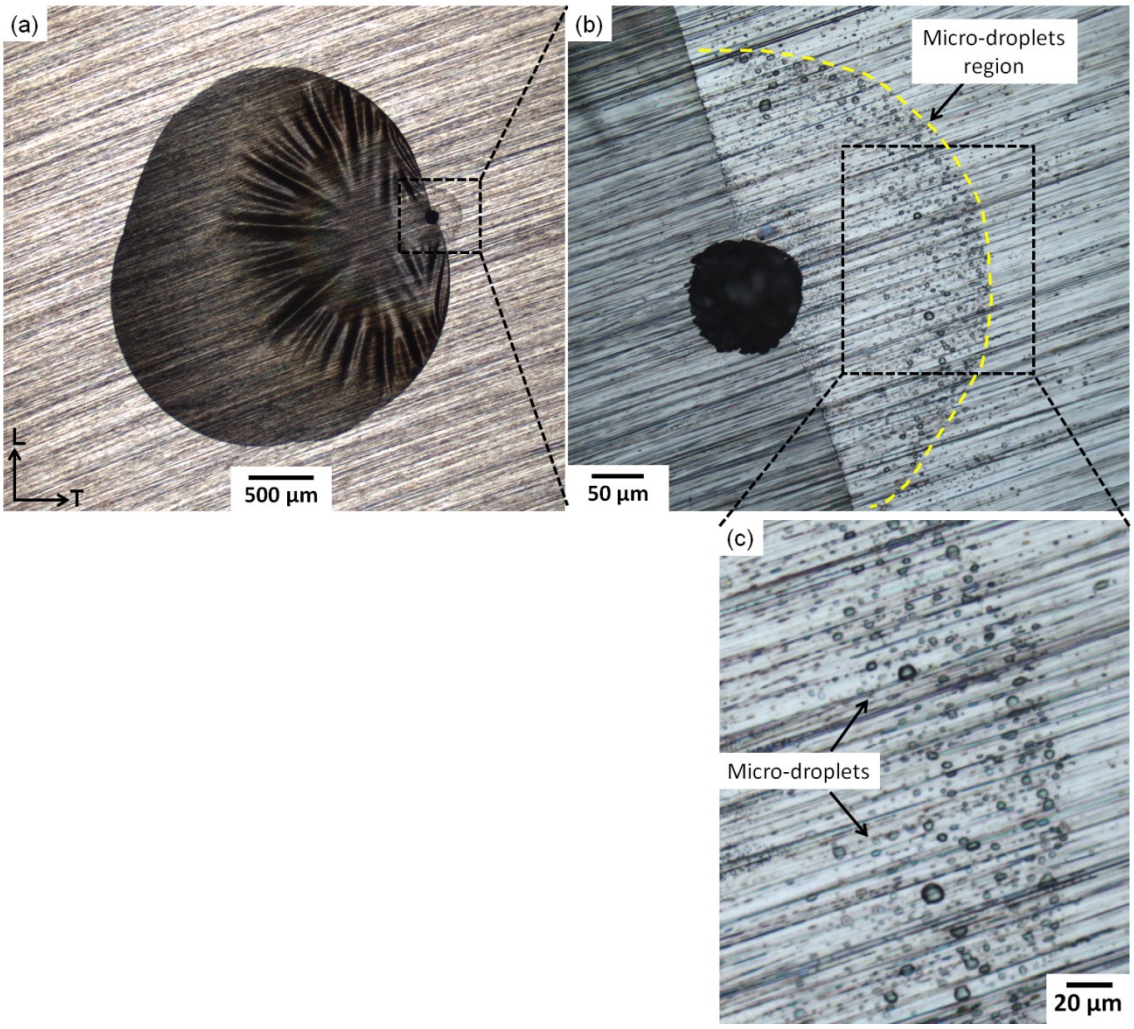

Figure 6-21 Typical example of micro-droplet formation near a pit grown under a $MgCl_2$ droplet (~2.5 mm diameter, ~1000 µg/cm^2 CDD at deposition) on 304L stainless steel (LT plane) after 1 day exposure at 56% RH and 30 °C; (a) droplet with pit at right edge; (b) magnified section of (a) showing the pit and micro-droplet region; and (c) magnified sections of (b), showing the distribution of micro-droplets.

Figure 6-22 shows the time-lapse results of atmospheric pitting corrosion of 316L stainless steel (ST plane) in ambient conditions (45±3% RH and temperature 24±2 °C) for 48 hours under a droplet of $MgCl_2$ with a CDD of ~1000 μg/cm^2. It can be seen that as the pit mouth grows with time, the size of the micro-droplet region increases. Close inspection showed that the size of micro-droplets also increased with time. The micro-droplet region grew outwards in a semicircle or oval shape near the pit following the grinding marks.

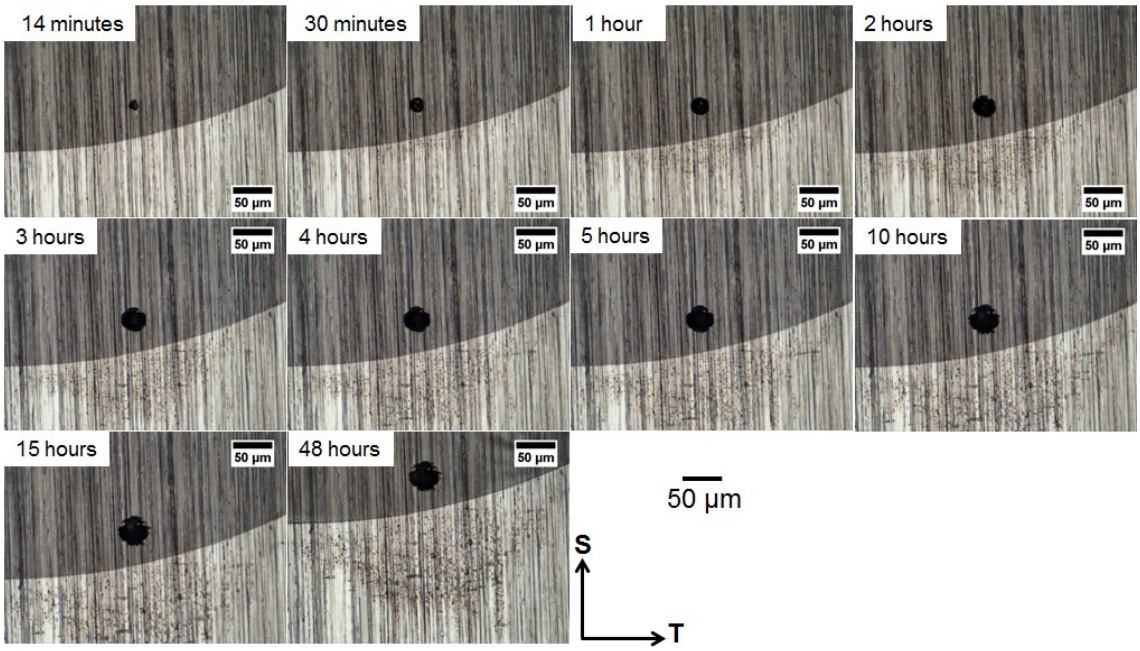

Figure 6-22 Time-lapse of a pit grown under an $MgCl_2$ droplet of ~2.5 mm diameter of CDD ~1000 μg/cm^2 at deposition on 316L stainless steel (ST plane) in ambient conditions (45±3% RH, and temperature 24±2 °C).

A corroded droplet on 304L (LT plane) after 1 day exposure at 35% RH with a pitting site developed near the droplet edge is shown in Figure 6-23 (a). Formation of micro-pits (≤8 μm in diameter) under micro-droplets in the secondary spreading area can be seen in Figure 6-23(b). The distribution of these micro-pits is shown in Figure 6-23 (c), with bigger micro-pits (≤7 μm in

diameter) formed close to the pit (which formed at the primary droplet edge) than those formed at the advancing edge of micro-droplet region (≤2 μm in diameter). Figure 6-24 shows the formation of the similar features on 316L exposed for 1 week at 35% RH.

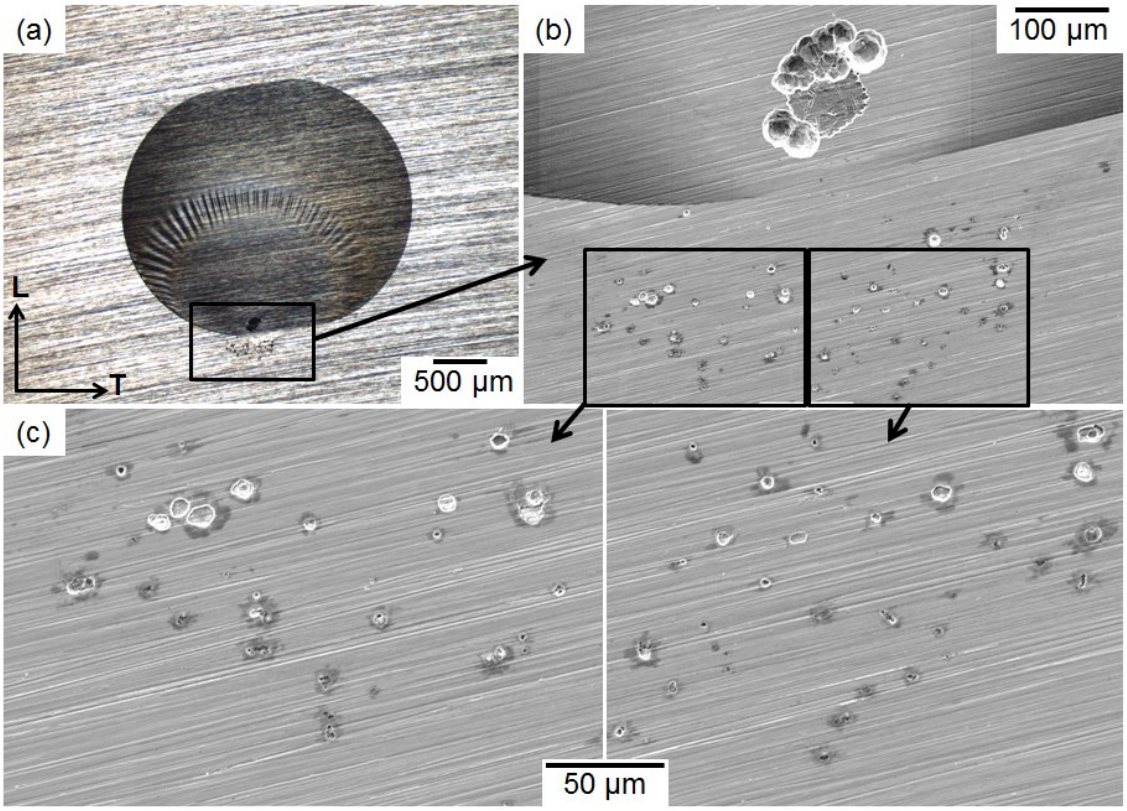

Figure 6-23 Typical example of micro-droplet formation nearby a pit grown under a $MgCl_2$ droplet (~2.5 mm diameter, ~1000 μg/cm^2 CDD at deposition) on 304L stainless steel (LT plane) after 1 day exposure at 35% RH and 30 °C; (a) droplet with a pit near the edge; (b) SEM image showing the pit and micro-pits after washing with DI water; and (c) magnified sections of (b), showing the distribution of micro-pits.

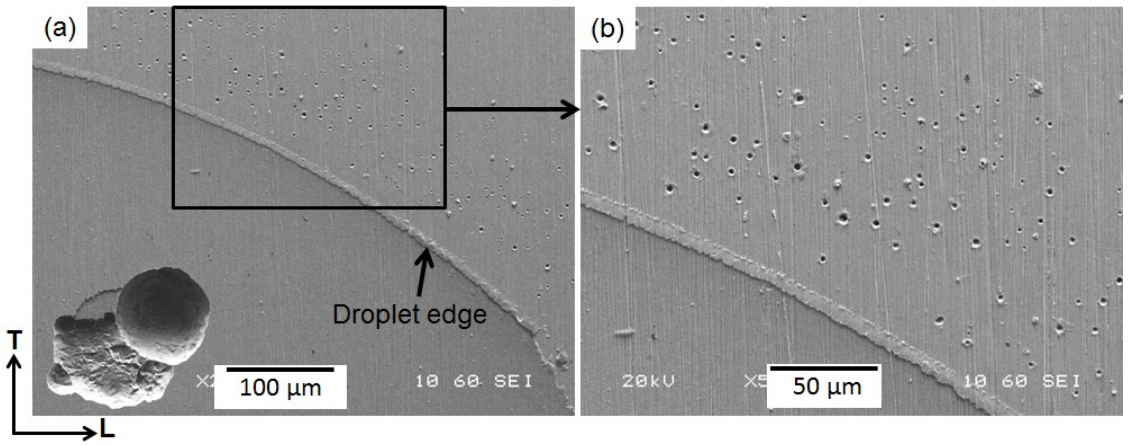

Figure 6-24 Typical example of small pits formed under micro-droplets close to the droplet edge. The pit was grown under a $MgCl_2$ droplet (~2.5 mm diameter, ~1000 µg/cm^2 CDD at deposition) on 316L stainless steel (LT plane) after 1 week exposure at 35% RH and 30 °C; the sample is washed with DI water.

A macroscopic view of a droplet on 304L stainless steel after 1 day exposure at 65% RH is shown in Figure 6-25 (a). The secondary micro-droplets are clearly seen at the bottom right edge Figure 6-25 (b). Also visible is formation of hemi-spherical shape micro-droplets in a semi-circle or oval area close to the pit. Larger micro-droplets formed close to the pit. However, Figure 6-25 (c) and (d) show no evidence of micro-pit formation under the micro-droplets.

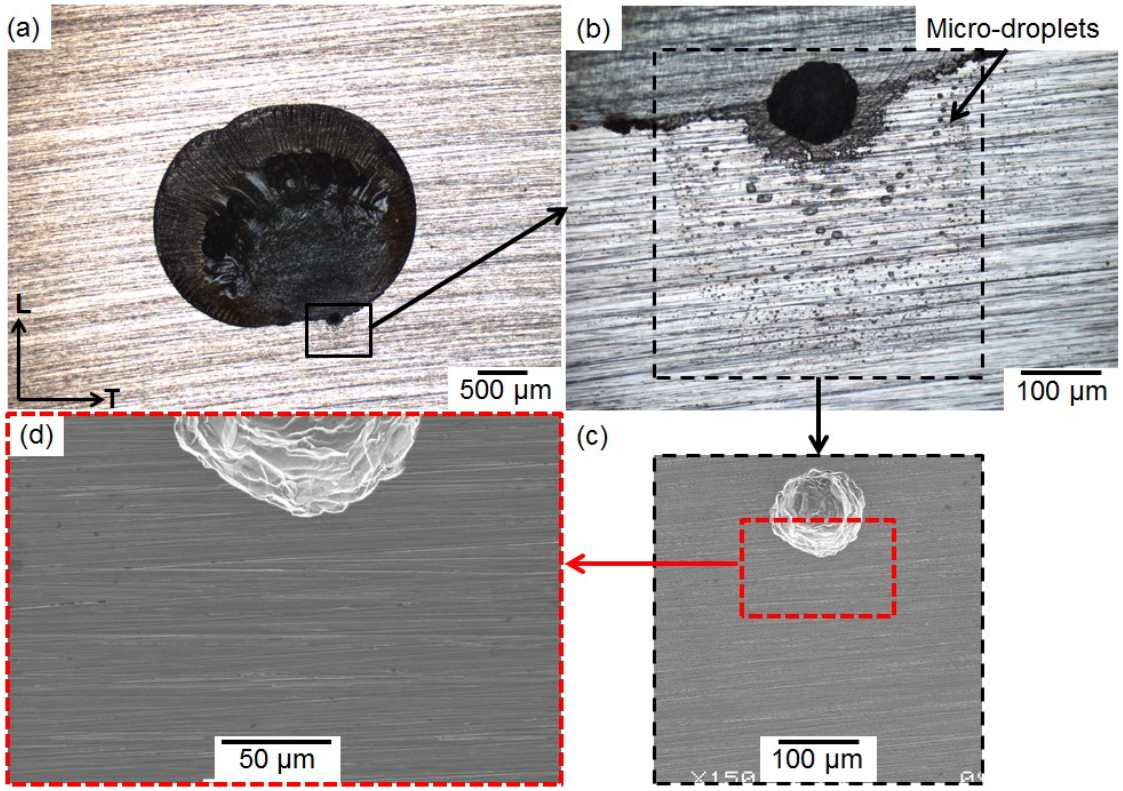

Figure 6-25 Typical example of micro-droplet formation near a pit grown under a $MgCl_2$ droplet (~2.5 mm diameter, ~1000 µg/cm^2 CDD at deposition) on 304L stainless steel (LT plane) after 1 day exposure at ~65% RH and 30 °C; (a) droplet with pit at the droplet edge; (b) magnified section of (a) showing the pit and micro-droplets distribution around the pit; (c) SEM image after washing with DI water; (d) magnified section of (c), showing no evidence of micro-pits.

6.4 Discussion

6.4.1 Effect of droplet diameter on pit diameter

In Figure 6-5, it is evident that the pit diameter increases with increasing droplet diameter for both 304L and 316L stainless steels (for a fixed chloride deposition density and relative humidity), which is in agreement with the idea that the pit growth rate increases with the available cathodic current; the larger the cathodic area the more the cathodic current [4, 22, 23, 147, 199, 208, 209]. The dominant cathodic reaction in atmospheric corrosion is generally agreed to be the oxygen reduction reaction. The increase in droplet area gives area for the cathodic reaction to take place. Pit growth in these droplets is considered to be "cathodically limited" [147], so increasing the amount of cathode will increase the overall corrosion rate.

This agrees with the previous investigation of atmospheric corrosion of 304 stainless steel foils by Mi [18, 22] who reported that the pit diameter was found to increase when the original salt deposit diameter was increased for a fixed chloride deposition density (172±25 μg/cm^2) for a range of deposits (0.5 mm to 2.8 mm) after exposure at 45% RH and 300 K for 24 hours. Mi attributed this to the idea of cathodic limitation of the pit current.

There was no significant change in pit depth with droplet area, or alloy type, for a fixed exposure time (Figure 6-5). This is consistent with the idea that metal dissolution under the salt layer at the bottom of the pit is under diffusion control. This agrees with Ghahari [107], who reported that dissolution rate at the bottom of 2D pits grown under full immersion conditions in dilute solutions is constant.

He attributed this to the presence of a salt layer, which regulates the interfacial potential, consistent with previous work, e.g. [121, 122, 210, 211]. Recently, the presence of salt layer at the bottom of the pit was confirmed by using X-ray diffraction measurements [123].

In Figure 6-5, it is also evident that slightly wider pits form on 304L compared with those that form on 316L. The sides of the pit are not considered to have a salt layer, as they are closer to the mouth of the pit where the solution is more dilute as metal ions can escape into the bulk solution. As such, the pit sides are under activation control and can experience much more materials loss. The decrease in active dissolution rate for 316L compared with 304L [212] would result in a lower current density on the pit walls and therefor a smaller pit mouth [213].

6.4.2 Effect of chloride deposition density on pit growth

Figure 6-10 and Figure 6-20 for 304L and 316L, respectively, show that, in general, for the same initial deposition area and constant relative humidity, the pit diameter increases with increasing the chloride deposition density (amount of salt deposition). This finding is consistent with Mi's [18] observation of pit diameter increasing with increasing chloride deposition density. Mi investigated the effect of chloride deposition density on pit size (volume) under constant relative humidity and temperature in both lab based tests and in X-ray microtomography experiments under droplets of $MgCl_2$ solution on 304

stainless steel foil and stainless steel pins exposed to lab temperature and 45% RH for 24 hours.

The estimated electrolyte height obtained from Mi's X-ray microtomography experiments (Figure 2-21) shows that the electrolyte layer height increases with increasing salt deposition density at controlled RH and controlled droplet area and temperature. The droplets morphologies observed in (Figure 6-8) and (Figure 6-17) suggests that this is the case in the present study as well. Since the droplets are deposited with same initial deposited area, changes in the amount of salt deposition will result in changes of the droplet height for measurements at fixed temperature and relative humidity exposure environments, because the droplet concentration is controlled by the relative humidity.

There are two possible influences that can result from the droplet height: the droplet height can have a straightforward influence on the diffusion pathway length of oxygen (the cathodic reactant) from the atmosphere [21]; as the diffusion path increases, the oxygen reduction reaction rate will decrease, predicting the formation of smaller pits. A thicker electrolyte, on the other hand, can lead to a lower approach resistance between the pit and the cathodic area, resulting in a higher pit current density, and anticipating that larger pits would form [5, 18, 22, 147]. The observation of larger pits with higher CDD values indicates that the ohmic effect dominates.

The pit depth as a function of CDD for 1 day exposure (Figure 6-10 and Figure 6-20) shows approximately the same trend and depth range in both 304L and

316L stainless steel. As described above, the growth of pits is controlled by the diffusion of metal ions from the bottom of the pit, which will not be greatly affected by the droplet height.

6.4.3 Threshold CDD for pitting

Pits propagate at CDDs of 10 μg/cm^2 and above with diameters >30 μm, and increase in diameter with increasing CDD, as described above. However, at lower deposition levels (<10 μg/cm^2), much smaller pits are formed (<30 μm). At lower CDD values, ring-like droplet morphologies where observed e.g. for 1 day exposure of constant droplet diameter of ~2.5 mm for both 304L (Figure 6-8) and 316L (Figure 6-17), at 10 and 5 μg/cm^2, with the central hole being larger in the 5 μg/cm^2 deposition level. Ring-like droplet shapes were also observed after 1 week exposure with a larger fixed deposition diameter of ~3.3 mm (Figure 6-11) at deposition levels starting from 4 μg/cm^2 and lower, with the central hole increasing with decreasing deposition level. A similar ring-like droplet morphology is previously seen by Albores-Silva et al. [19] and Padovani et al.[20] under $MgCl_2$ solution of 10 μg/cm^2 up to 50 μg/cm^2 on 316L stainless steel (Figure 2-22). They described the appearance as "*multiple droplets with anodic and cathodic domains*". These authors attributed the discontinuity of the film to the shrinkage of the droplet while it is reaching equilibrium with the environment. The reason for the observed ring-like droplet morphology at relatively higher deposition levels (up to 50 μg/cm^2) in the Albores-Silva study compared to that obtained in the present study may be related to the fact that in

their study, relatively larger droplets of $MgCl_2$ of 5.5 to 6.5 mm in diameter (estimated measure after exposure) were used.

A possible reason for the formation of ring-like droplet morphology might be that the easy oxygen access at the thinner parts of the droplets, i.e. at the edge, creates a preference for cathodic reactions to occur there. This chemical change around the perimeter of the droplet, by increasing OH^- concentration, may change the interfacial energy between the passive film and the solution and allow a reduced contact angle to occur at very low CDDs. Products with low solubility, such as $Mg(OH)_2$ or $MgCO_3$ (where Mg ions react with atmospheric CO_2), may also form around the edge of the droplet due to the change in pH, pinning the perimeter of the droplet as solution volume reduces.

It was also observed that at lower deposition levels (<10 $\mu g/cm^2$) e.g. 5 $\mu g/cm^2$ (Figure 6-9), ≤1 $\mu g/cm^2$ (Figure 6-12), and 0.5 $\mu g/cm^2$ (Figure 6-14) pits were found to be associated with small clusters of very small pits. Figure 6-15(b) shows typical inclusions size of ≤2 μm in diameter, the smallest pits at the lowest CDD is about the same as the inclusions, consistent with inclusion dissolution, and at slightly higher CDDs the pits are slightly larger, so the pits have grown a bit. This was attributed to the fact that once a pit initiated and start to grow an acidic region will develop around it [88, 97, 99]. It is possible that the acidic region will dissolve nearby inclusions.

The presence of enough volume of electrolyte solution, which enables the transport of ionic species, can play an important role in pitting corrosion [4, 5, 18-20, 22, 214]. Tomashov [214] described the effect of water film thickness on

the atmospheric corrosion rate, and reported that this can have a maximum influence at certain film thickness.

For atmospheric pitting corrosion to occur, it has been reported that there is a lower threshold of chloride deposition density of 10-25 μg/cm^2 [19, 20, 163, 215] . However, in the present work pits were observed at lower CDDs (Table 6-2) and the CDD threshold was seen to be affected by the initial deposition area (droplet diameter) and exposure time. This might be because, in the present study, higher resolution SEM characterisation identifies small sites of corrosion attack, on the order of 10 μm and below. The main difference between CDD thresholds identified in the current work compared with previous work might come from what is defined “a pit”. For example, Albores-Silva et al. [19] reported that they observed pitting at 10 μg/cm^2 droplets at 30 °C and 50 °C after 12 weeks of exposure at ~30% RH under $MgCl_2$ droplets on 316L stainless steel. However, no images of pits are shown and the minimum pit size recorded is not stated. Later, based on the same results of Albores-Silva, Padovani et al. [20] reported that, pit depths were in the range of 10-20 μm for lower chloride deposition densities, while for higher deposition densities they reported that the pit depth was in the range of 20-70 μm. However, Padovani reported the maximum pit diameter to be ~90 μm for the pits observed at 10 and 25 μg/cm^2.

In the present work, looking at Figure 6-10 and Figure 6-20, we get a threshold of 10 μg/cm^2 if we define a pit as being >30 μm in diameter and >10 μm deep.

6.4.4 Secondary spreading and micro-droplet formation

The formation of micro-droplets and their growth which led to the formation of secondary spreading region have described in Section 2.13. In the present work, significant secondary spreading and micro-droplet formation was observed, where the preferential pitting initiated close to droplet edge on both 304L and 316L stainless steels under droplets of $MgCl_2$ at different fixed RH values at 30 °C. Researchers who carried out experiments under the same conditions presented in this work ($MgCl_2$ salt solution, 45% RH and ~30 °C) on 304L stainless steel plate [7] and 304L stainless steel foil [18, 22] have not seen microdroplets; this could be due to the lower magnification images used in their studies or the pit location within the droplet since in the present work micro-droplets were only observed when the pit initiated at or close to the droplet edge.

Previous researchers have investigated secondary spreading and micro-droplets formation using droplets and/or deliquescence of salt particles over a range of salts (e.g. NaCl, KCl, and $MgCl_{2,...}$etc.) on different materials such as carbon steel, stainless steel, aluminium, copper and zinc. However, secondary spreading was not observed on stainless steel under any of the examined salt solutions including $MgCl_2$ [136, 151, 156, 165, 166]. Tsuru et al. [136] and Zhang et al. [151] attributed the prevention of formation and expansion of the secondary spreading zone and the micro-droplets to the precipitation of magnesium hydroxide $Mg(OH)_2$, which is relatively insoluble, towards the periphery of the main droplet: this diminishes the concentration of OH^- and increases the ionic strength at the edge of the main droplet (Figure 6-26).

Bian et al. [166] reported that no obvious micro-droplet formation was seen on the stainless steel surface under KCl droplets. They attributed this to the very weak corrosion activity on the surface of stainless steel.

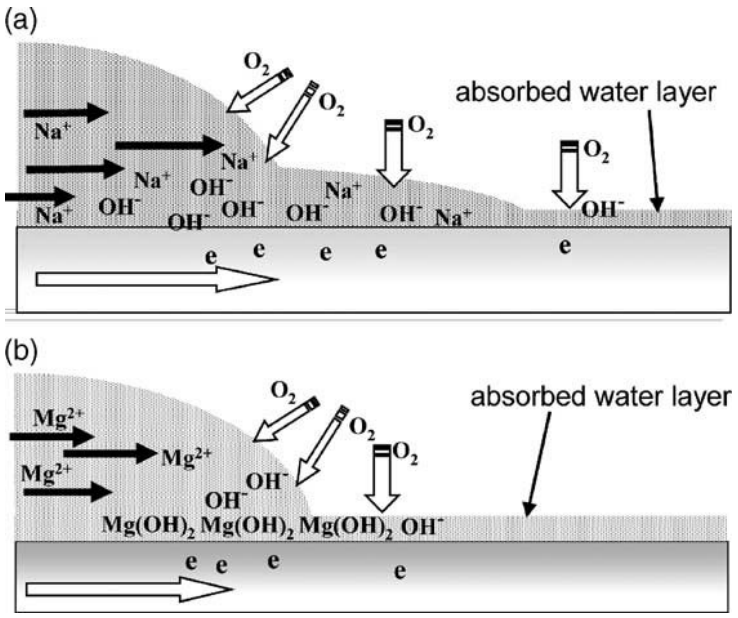

Figure 6-26 Illustration of mechanism of the secondary spreading area expansion for: (a) NaCl; and (b) $MgCl_2$ salt solutions [136].

In the present work, the location of the micro-droplet region is found to be around pits initiated at or close to the droplet edge (≤ 250 μm from the droplet adge). However, not all the pits formed in this range showed the formation of micro-droplet. It was almost but not always. The reason for why some pits in this range did not show micro-droplet formation is still unknown. Some previous researchers also reported that secondary micro-droplets formed around the pit initiated close to the droplet edge on carbon steel [166] and aluminium [167, 168].

In this study it is also observed that the micro-droplets region grew outwards in a semi-circle or oval shape; this agrees with the shape previously reported by

some researchers [165, 166]. Bian et al. [166] attributed the oval shape to the superficial grinding marks on carbon steel. Similarly, Zhang et al. [165] reported that the boundary of the elliptic area covered with micro-droplets spread faster in parallel orientation with respect to the polishing direction on carbon steel. This effect is confirmed by the time-lapse carried out in the present work (Figure 6-22).

Figure 6-22 shows that the size of the micro-droplet region and the size of individual droplets increase with increasing pit size over time. This indicates that the spreading process of micro-droplets is linked with the diffusion of cations (e.g. Mg^{+2}) in the primary droplet towards the spreading region. This finding is consistent with the findings of previous authors who investigated the secondary spreading with time [136, 156, 164, 166-168].

The hemispherical morphology of individual micro-droplets is similar to those previously reported to form under NaCl and other salts on carbon steel [136, 156, 166], aluminium [164, 166, 167], zinc [216], magnesium alloys [217], and copper [136, 156, 218].

Figure 6-23 shows the formation of many micro-pits under micro-droplet region which formed close to the pit initiated near to the main droplet edge. This observation was not reported previously for atmospheric pitting corrosion of stainless steel under $MgCl_2$ droplets or other salts. For the study of the aluminium alloy AA7075-T6 under NaCl droplets, Morton and Frankel [167] proposed a mechanism for the formation and growth of these secondary droplets (Figure 6-27). They proposed that the anode (preferential pitting site)

close to the main droplet edge can form an acidic zone that develops further pit initiation and growth. The growth of the secondary droplet is driven by the generation of ions from the anodic region at the edge of the droplet, which can absorb water from the atmosphere. Morton and Frankel also reported that the surface area under these micro-droplets undergoes serious corrosion attack, generating many small pits throughout the wetted surface area. The mechanism proposed by Morton and Frankel is similar to the mechanism considered for the formation of secondary droplets with filiform corrosion reported by Li et al. [168] for Al–Mg–Si alloy under droplets of $MgCl_2$ solution. Thus, in the present work, the formation of micro-pits under micro-droplets is attributed to the formation of an acidic zone that develops further pit initiation and growth. Such micro-pits were not observed under micro-droplets at high RH values (>56% RH) but they were observed at 56% RH and below for both 304L and 316L stainless steels. This might be due to the less concentrated (more dilute) conditions at high RH values and aggressive conditions at low RH.

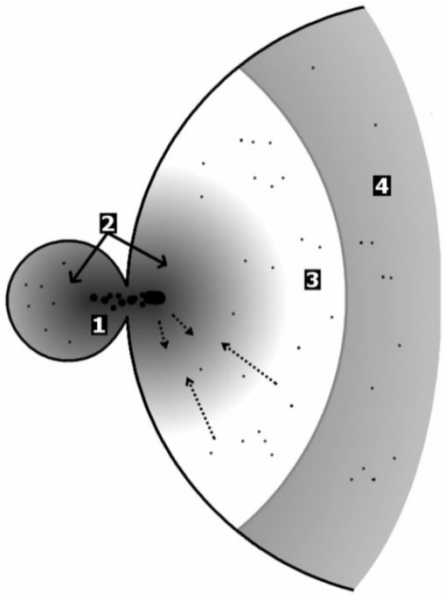

Figure 6-27 A Schematic representation of secondary droplet phenomenon of AA7075-T6 under NaCl droplet salt solution. Region 1 represents the pit initiation site (anode) within the main droplet associated with many small pits where the secondary spreading takes place. Region 3 represents the main supporting cathodic area surrounding the anode. Region 2 is covered with corrosion products. The dotted arrows represent the ion transport between these two regions. Region 4 represents the main part of the droplet [167].

Based on the previous mechanisms proposed for the formation of micro-droplets and secondary spreading area by Tsuru et al. [136] for $MgCl_2$ and NaCl (Figure 6-26), Zhang [156] for NaCl (Figure 2-28) , and Morton and Frankel [167] for a pit at the edge of the droplet under NaCl salt solution on aluminium (Figure 6-27), a mechanism can be proposed for the formation of such features under $MgCl_2$ salt solution for a pit initiated at or close to the edge of the original droplet on stainless steel as follows:

It is assumed that a very thin water layer will form around the original droplet because of the presence of highly humid environment. Once a pit initiates next to or at the edge of the droplet, an acidic zone will develop and act as a local

anode. When preferential sites act as cathodes on the monolayer, this will form water clusters as the concentration of ions increases. The oxygen reduction reactions that occur on the water clusters would create a charge imbalance, driving cations (e.g. Mg^{+2}) towards them and forming microdroplets. Over time, coalescence of micro-droplets will lead to the formation of an electrolyte layer which is known to be the secondary spreading region. Figure 6-28 shows a demonstration of this mechanism for the case of pit initiated at/close to the main droplet edge of $MgCl_2$ on stainless steel.

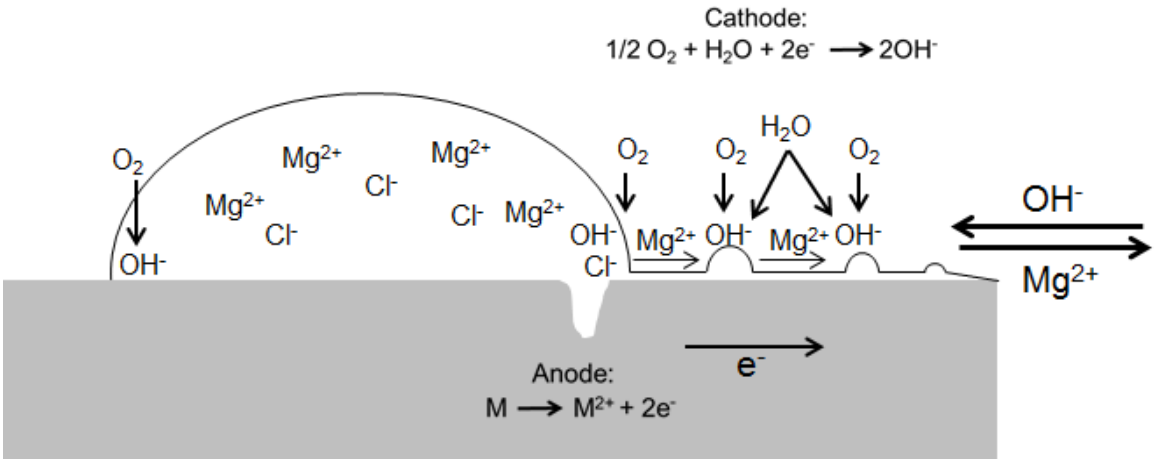

Figure 6-28 Schematic representation of secondary spreading and micro-droplet formation on stainless steel for a pit at or close to the droplet edge under $MgCl_2$ salt solution. Incorporating the mechanisms proposed by Morton and Frankel [167], Zhang et al. [156] and Tsuru et al. [136].

The observed mechanism of the formation of micro-droplets and secondary spreading area under $MgCl_2$ on stainless steel is consistent with the previous mechanisms proposed for the formation of micro-droplets and secondary spreading area in terms of cations being drawn towards OH^- at the edge of droplets. However, the formation of insoluble Mg species that prevent the

migration of cations is unlikely, as this mechanism appeared to work on when using $MgCl_2$ droplets.

The explanation given by Morton and Frankel [167] for the formation of multiple pits under the secondary spreading region in Al alloy may be the correct explanation for the formation of multiple pits under the secondary spreading region in austenitic stainless steels investigated in this study. They states that the local acidic region that is resulted from the cation hydrolysis promotes further pit initiation and growth (Figure 2-29 and Figure 6-27). It has been reported that separate corrosion cells can form in single micro-droplet(s) and cause corrosion [19]. Albores-Silva et al. [19], reported that when the continuity of the salt film is interrupted, this would lead to the formation of multiple droplets with anodic and cathodic domains and this can transfer the corrosion under a large corrosion cell into multiple small ones.

Microdroplets are formed by the migration of ions across monolayers of water on the surface outside the border of the main droplet, According to both Zhang et al. [151] (Figure 2-28) and Tsuru et al. [136] (Figure 6-26). This circuit will have a very high IR drop due to the thinness of the ionic pathway. As the microdroplets grown, it becomes easier for cathodic regions to complete a circuit with anodes that develop locally rather than crossing the monolayer towards the main droplet. As such, dissolution can occur under microdroplets. In this work, pitting under microdroplets is not seen in high RH conditions, such as observed at 65% RH. This could be because at this RH there are more monolayers [219] to allow a stronger ionic connection between the microdroplet

and the anode in the main droplet. At 35% RH, however, the ionic pathway can be reduced to a single monolayer, making it charge transfer difficult.

6.4.5 Effect of microstructure

As described in chapter 4, secondary crystallographic phases such as delta ferrite can effect on pit initiation and/or propagation. Pits with layered attack morphology were observed on 304L stainless steel (e.g. Figure 6-2 and Figure 6-25). This was attributed to the preferential attack (propagation) along ferrite bands. Pits with rough interior were observed on 316L with no layered attack. This might be because of the presence of centreline segregation (ferrite bands) in the middle of the plate.

On the other hand, it is well agreed that inclusions such as MnS [1, 51, 88-90] and mixed oxide inclusions [50, 91-93] can play a vital role in pitting corrosion in stainless steels. For 304L stainless steel (LT plane), in the present study, pits were often found to be associated with small clusters of very small pits especially at lower deposition levels (<10 $\mu g/cm^2$) e.g. 5 $\mu g/cm^2$ (Figure 6-9), ≤1 $\mu g/cm^2$ (Figure 6-12), and 0.5 $\mu g/cm^2$ (Figure 6-14)).The typical inclusions size, on LT plane, was of ≤2 μm in diameter (Figure 6-15(b)). At the lowest CDD, the smallest pits are about the same as the inclusions. At slightly higher CDDs the pits were slightly larger, so the pits have grown a bit (consistent with inclusion dissolution (see Figure 2-10 [88], Figure 2-12 [97], and Figure 2-15 [4])). It is widely accepted that once a pit initiated and start to grow an acidic region will develop around it [88, 97, 99]. It is well agreed that the acidic region will dissolve nearby inclusions. Therefore, the formation of small pits was attributed to the inclusion dissolution.

Among all the droplets investigated in this section (328 droplets), only one droplet had an elongated pit that seemed to be growing along the rolling direction (Figure 6-19), which was attributed to the susceptibility to the microstructural features, most commonly elongated inclusions, present at the alloy surface.

6.5 Conclusions

1. For atmospheric pitting corrosion of both 304L and 316L stainless steels at constant chloride deposition density (CDD), the pit diameter increases with increasing droplet diameter. This is attributed to an increase in effective cathode area, which causes an increase in potential. However, there is no significant change in pit depth with droplet diameter, which is consistent with the view that this is under diffusion control. For the same chloride deposition density, slightly wider pits formed on 304L than on 316L, but there is no significant difference in pit depth.

2. For both 304L and 316L stainless steels, for a fixed droplet area at 45% RH, the active pit diameter (as distinct from the initial shallow dish area) for a 1-day corrosion test shows a relatively small increase with CDD values ranging from 50-10000 $\mu g/cm^2$.

3. At a CDD of 10 μg/cm^2 and below, the active pit diameter is far smaller owing to a limited solution volume. A discontinuous droplet layer is observed at such low CDDs. As the CDD is decreased, pits become smaller, reaching a point where it appears that an inclusion has dissolved, but the corrosion does not spread. For 304L, this “threshold” is lower for longer times and larger droplets, and the threshold is higher for 316L compared with 304L.

4. Micro-droplets were observed on 304L and 316L stainless steel under $MgCl_2$ salt droplets when preferential pitting occurred, almost but not always, at or close to the droplet edge (≤ 250 μm). As the pit mouth grew with time, the covering region and size of micro-droplets increased. Micro-droplets can lead to the formation of micro-pits in the spreading area (micro-pits were observed at 56% RH and below but not observed at 65% RH and above). This is attributed to the formation of an acidic zone that develops further pit initiation and growth. No secondary spreading was observed in droplets that did not pit.

7 General Discussion

7.1 Effect of microstructure

Work on different plate orientations has confirmed that atmospheric localised corrosion of stainless steel will take place preferentially along delta ferrite bands parallel to the surface of the plate. This is probably due to the difference in the chemical composition of the ferrite phase with respect to the austenite phase (the matrix). Such effects have been observed in atmospheric corrosion of duplex stainless steels. The alloy plate used in the present work is typical of that used in radioactive waste containers, which have a minimum wall thickness of 2.3 mm [20]. A key concern for these containers is the development of atmospherically-induced stress corrosion cracking (AISCC) over long term exposures. The fissures formed when ferrite undergoes preferential corrosion are very narrow (typically <1 μm), so if stress were to be applied perpendicular to the fissures, then cracking could be a significant risk owing to the high stress intensity. However, this risk is low because in such containers the residual stresses will be parallel to the plate surface [26]. Furthermore, when pitting corrosion develops on the plate surface, the pits spread laterally parallel to the surface, which could decrease the risk of AISCC.

The development of intermetallic phases e.g. MnS and mixed oxides inclusions which are also aligned along the rolling direction can leads to the formation of elongated pits. The use of a clean grade of Type 304 stainless steel alloys, which are processed with the intent of having fewer and smaller inclusions [50], is recommended.

Solution annealing of samples has shown that residual delta ferrite can be eliminated or reduced from the alloy. As a result the pit morphology has changed from irregular to equiaxed etched pits. Knowledge of the ferrite content is important to accurately predict corrosion propagation on the ILW containers and to better develop new containers that avoid the existence of these phases, for example by better processing (e.g. more thorough solution treatment). Such extra processing steps, however, may raise the cost of the containers, and so should be judged against their expected service lifetime.

It has been observed that plate thickness might have a role in influencing the pit morphology. On LT plane of 304L stainless steel (3 mm plate) always a layered attack morphology is observed while on 316L stainless steel (6 mm plate) on the same plane e.g. Figure 5-35 no layered attack was observed and instead the pit interior was rough and correlated with the grain size of the alloy. It is speculated that this is due to the presence of less centreline segregation at the edge of the 316L stainless steel plate compared to 304L. This could be an important consideration when selecting materials for nuclear waste storages as thinner plates are more susceptible to this defect.

7.2 Chloride deposition density (CDD) threshold for pitting

A chloride deposition density of 10 μg/cm^2 has been identified as a “safe” value to prevent the formation of pits that could develop into AISCC over long time-periods [15, 19, 20, 163, 215].

In the present work, pits have been observed at CDDs as low as 0.1 μg/cm^2. However, these are small, formed in clusters and were similar in size to

inclusions, likely to represent dissolution of inclusions. It is unlikely that such small pits will develop into AISCC.

It has been possible to say that in general the pit diameter increases with increasing chloride deposition density (Figure 6-10 and Figure 6-20). Note that there is a substantial increase in pit size above 10 μg/cm^2 for experiments which lasted for 1 day.

Padovani et al. [20] reported that, pit depths were in the range of 10-20 μm on 316L after 12 weeks for “lower” chloride deposition densities (unspecified, but assumed to be approximately 10-100 μg/cm^2 CDD) , while for higher deposition densities they reported that the pit depth was in the range of 20-70 μm. These results match with those found here after only 1 day exposure. Although the exposure conditions were somewhat different (~33% RH for Padovani, ~43% RH for the tests discussed here), suggesting that pit depth does not develop substantially after the first 24 hour of growth. However, Padovani reported the maximum pit diameter to be ~90 μm for the pits observed at 10 and 25 μg/cm^2, contrasting to values of ~30 μm found in this work. This suggests that the pits are still developing laterally, if not increasing in depth.

Padovani et al. [20] suggested that the reasons for the existence of thresholds for the chloride deposition density required to assist pitting corrosion are linked to the nature of the electrolyte (uniform or discontinuous) formed at different deposition densities. In the present work, ring-like droplet morphologies were observed at lower CDD values (Figure 6-8 and Figure 6-17). Padovani and Albores-Silva, also show this ring like formation at low CDDs. These

observations are consistent with the idea that the 10 μg/cm^2 threshold is the point at which the electrolyte becomes discontinuous. A discontinuous electrolyte cannot provide enough cathode areas to support pit propagation that could lead to AISCC.

Obtaining safe conditions for above-ground storages of intermediate level nuclear waste is one of the objectives of the current study. Although in the present study the threshold of chloride deposition density was even lower compared to that obtained in literature 10-25 μg/cm^2 [19, 20, 163, 215], the results supports the recommendation that chloride deposition density on the surface of containers should be monitored to ensure that only low concentrations are present, controlled by the use of air filters in storage areas.

7.3 Influence of relative humidity and chloride deposition density on pit morphology

It has been determined that susceptibility to atmospheric pitting corrosion is influenced by relative humidity and the initial chloride deposition density.

This work has confirmed that the pit morphology is a function of RH. At lower RH values, satellite and earing pits (both had shallow dish region) were observed while at higher RH values only circular pits were observed (with no shallow dish region). The formation of shallow dish has been attributed to the passive current dissolution. It has been demonstrated that the diameter of the shallow dishes is a function of the distance from the edge of the droplet and it is not a function of RH or time. Preliminary evidence suggests that growth size of

the shallow dish is most strongly influenced by cathodic area. It has also been observed that a greater number of earing pits formed toward the centre of the droplet while satellite pits formed toward the droplet edge. This morphology difference has been attributed to the changes in the IR drop, and differences in solution diffusivity and conductivity, which are linked with RH. It has been determined that the critical RH for the occurrence of atmospheric pitting corrosion is in the range of 65%–70% RH for 304L stainless steel while that for 316L is in the range of 56%–65% RH at 30 °C.

It has been possible to say that in general the pit diameter increases with increasing chloride deposition density. This might be related with a lower ohmic drop between the pit and the droplet layer. It has also been observed that localised pitting corrosion can take place on stainless steels with extremely low levels of chloride depositions on a metal surface during exposure at 45% RH at 30 °C. Definite of CDD threshold has been determined for both 304L and 316L stainless steels. It has been shown that this threshold is higher for 316L compared with 304L. And for 304L the threshold is lower for longer times and larger droplets. It is important to be aware about this effect for storage conditions of intermediate level nuclear waste and keep the chloride deposition levels limited.

7.4 Effect of droplet diameter

By investigating large arrays of droplets it has been observed that the pit diameter increases with increasing droplet diameter during atmospheric exposure of both 304L and 316L stainless steels beneath $MgCl_2$ droplets at

45% RH and 30 °C. This has been attributed to an increase in the effective cathode area, which can cause an increase in potential. However, it has been observed that there is no significant change in pit depth, which indicates that this is under diffusion control. It has also been observed that slightly wider pits formed on 304L than on 316L; however, no significant difference in pit depth was seen. These effects have been observed under full immersion electrochemistry [123], but not previously verified under atmospheric conditions.

7.5 Effect of pit location within the droplet

Although previous work has made comments regarding the position of pits within a droplet [6, 23, 82, 199, 220], this work has measured the effect of the pit location within a droplet on its morphology. It has been demonstrated that pits that form close and/or at the droplet edge have a bigger size. This has been attributed to three effects: (1) the effect of a three phase boundary, where there is particularly easy access of oxygen for the cathodic reaction, (2) the formation of an acidic zone that develop more pit initiation and growth, and (3) the formation of secondary spread zone which increases the covered wetted area and acts as a cathodic region to support the pitting attack. Experiments on stainless steel samples have shown that secondary spreading processes take place when pits form close and/or at the droplet edge, a process which has previously been unreported under $MgCl_2$ droplets. This occurs very rapidly and significantly at the early stages of atmospheric exposure of stainless steel beneath $MgCl_2$ droplets. Consequently this increases the size of the potential cathodic region.

7.6 Deposition technique

The results show that automated robotic droplet deposition is a successful method to obtain consistent results on the pit growth under atmospheric conditions. Salt droplets can be deposited in arrays with controlled volumes and concentrations. In this work large arrays of droplets were used (up to 75) in order to obtain statistically significant results. The technique can be further modified to deposit mixed salts in combinatorial arrays. Realistic deposits in stores contain many different chemical species, so it will permit exploration of different ratios of inhibiting species e.g. sulphates and nitrates.

8 Future work

8.1 Study the effect of crystallographic orientation (texture)

In the current work, the results showed that the faceted pits (flat walled pits) can form under atmospheric conditions. According to Schwenk's work [125], it is possible that pit bounding planes are belong to {111} crystal planes of austenite which have the lowest dissolution rate. However, preferential attacked planes were not known. The effect of crystallographic orientation on the pitting corrosion has been investigated under full immersion conditions [202-207]. However, there are no specific studies of this effect under atmospheric conditions. The results of this study suggest that crystallographic orientation plays an important role in localized corrosion. Thus this effect needs further study.

8.2 Study the effect of sample position on the morphology of corrosion pits

Containers have vertical sides and upward facing and downward facing horizontal surfaces [163, 221]. It is known that pit morphology is influenced by surface orientation under full immersion conditions [75, 222]. The effect of sample position (Figure 8-1) on the shape and the kinetics of pit growth in austenitic stainless steel (18Cr-l2Ni-2Mo-Ti) have been investigated under potentiostatic conditions by Mankowski and Szklarska-Smialowska [222]. They reported that pits grew faster into the metal in the case of covered pits facing downwards (type 1) than that facing upwards (type 2), However, an intermediate rate were reported in the case of pits growing on a vertical mode

(type 3). Figure 8-1 shows the assumed distribution of salt layer (dotted areas) in pits growing in three different modes. Donohoe et al. (Figure 8-2(a)) showed a pit on a section of the internal surface of an 18Cr-8Ni-1Ti stainless steel tank used in a nuclear waste cooling water system. When looking at the cross-section of this pit (Figure 8-2(b)) it was observed that the pit propagated vertically up the tank wall without penetrating the other side of the metal. This was attributed to variation in alloy composition in the centre of the steel plate.

However, under atmospheric conditions such effect has not been investigated. SEM, FIB and synchrotron X-ray micro-tomography can be correlated together to study this effect. It is expected that dissolution will follow structural features (microstructural orientation).

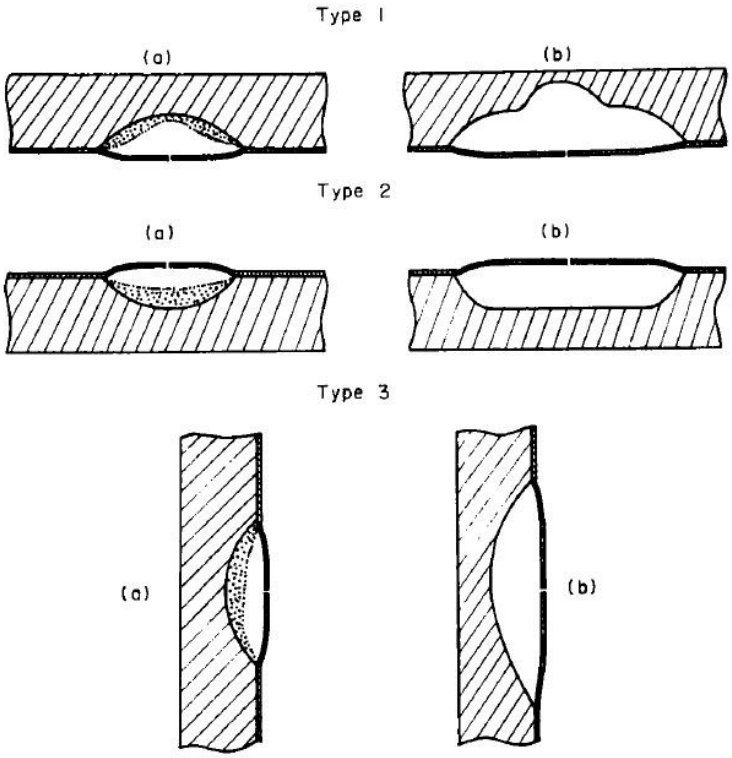

Figure 8-1 distribution of salt layer (dotted areas) in pits growing in three different modes; downward mode (Type 1); upward mode (Type 2); and vertical mode (type 3)[222].

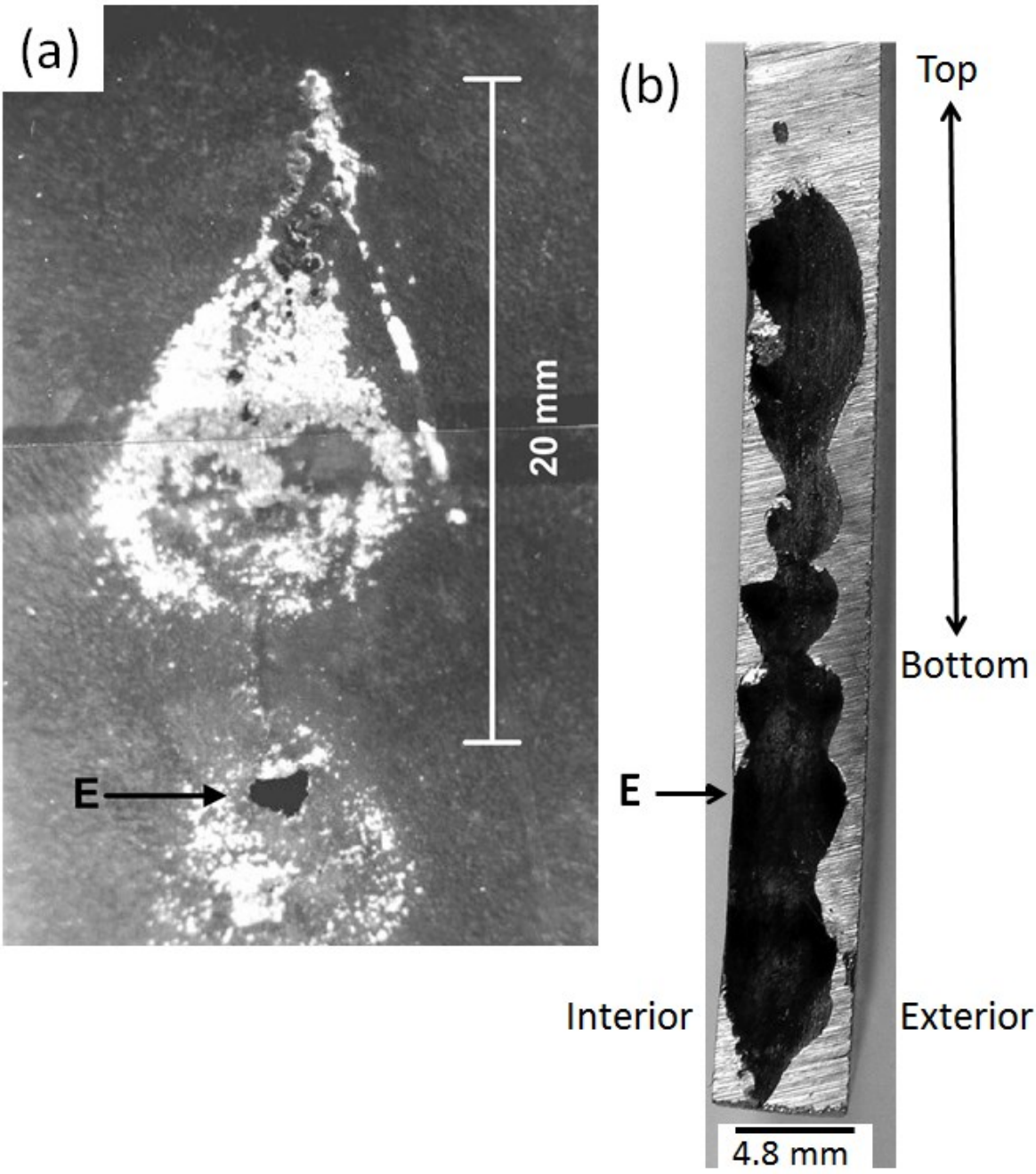

Figure 8-2 Localized corrosion of 18Cr-8Ni-1Ti stainless steel tank used in a nuclear waste cooling water system; (a) a pit on a section of the internal surface ; (b) a cross-sectional view of pit shown in (a). The symbol “E” in both figures represents the approximate position of the pit mouth ("exit hole"). The plate thickness was nominally ~4.8 mm. This figure adapted from [75].

8.3 Effect of deposit chemistry on atmospheric pitting corrosion of stainless steel

In real atmospheric conditions aerosols contain a mixture of salts, including, Ca^{2+}, Cl^{-}, Mg^{2+}, SO_4^{2-}, K^{+}, PO_4^{3-}, NH_4^{+}, NO_3^{-}, Na^{+} [223]. Surveys within nuclear waste stores have shown sulphate (SO_4^{2-}) and nitrate (NO_3^{-}) [163]. These are known to be corrosion inhibitors [224, 225]. Many studies to date on atmospheric corrosion of stainless steels have examined the influence of pure $MgCl_2$ [4, 5, 15, 21, 139, 146], pure NaCl [15, 23, 129, 146, 147], $CaCl_2$ [16] and artificial sea water [4, 5], whereas, only few of them investigate the effect of other mixed salts [7]. In the present work, all the experiments have been performed under $MgCl_2$ salt solution droplets. Atmospheric pitting corrosion test could be planned on the same materials under mixed salt solution droplets at different ratios using automated solution deposition system as it allows both precise mixing of different salt systems, and reproducible deposition procedures.

8.4 Investigating wet-dry cycling exposure

Both lab based experiments and synchrotron X-ray micro-tomography tests in the current work were performed under constant relative humidity while in real atmospheric conditions fluctuation in relative humidity (wet-dry cycling) is more realistic.

Although some previous studies have investigated the effect of wet-dry cycling for different materials [7-14], there is need for more detailed work to study this

effect under atmospheric corrosion conditions on stainless steels in particular for safe ILW storage conditions.

9 Appendices

9.1 Appendix 1: mill certificates of materials used

Figure 9-1 and Figure 9-2 give the mill certificates provided by the manufacturers of the stainless steel plates used in the work presented in this thesis.

9.2 Appendix 2, data logger diagrams

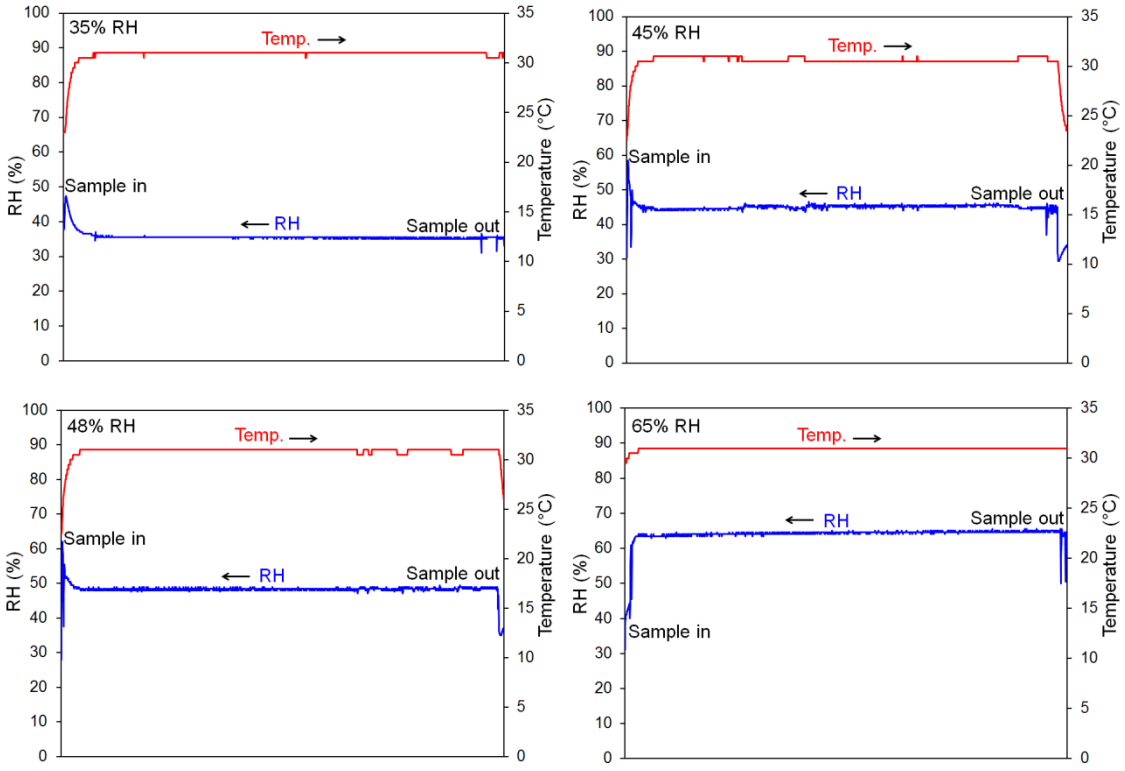

Figure 9-3 Monitored RH and temperature of controlled chamber for 1 day of exposure.

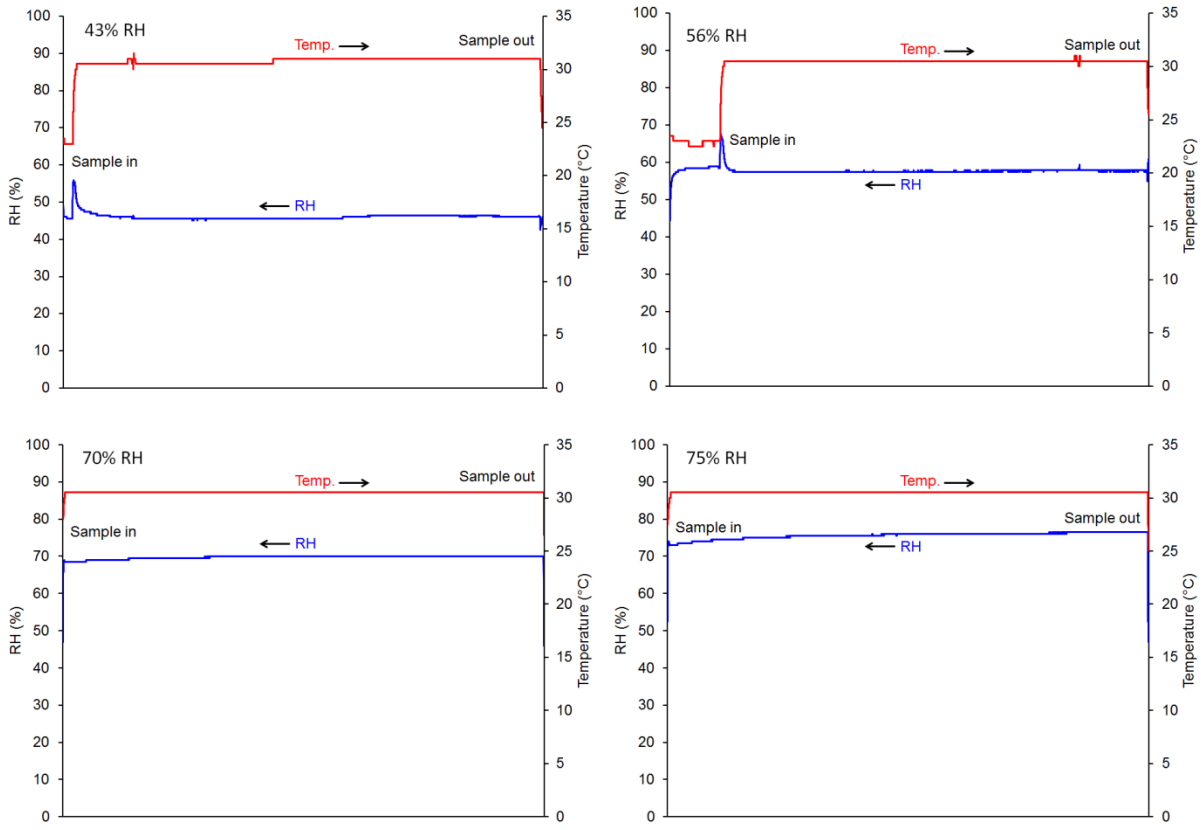

Figure 9-4 Monitored RH and temperature of saturate salts, given in table 1-3, for 1 week of exposure.

10 References

1. Frankel, G.S., *Pitting Corrosion of Metals: A Review of the Critical Factors.* Journal of the Electrochemical Society, 1998. **145**(6): p. 2186-2198.
2. Frankel, G.S. and N. Sridhar, *Understanding localized corrosion.* Materials Today, 2008. **11**(10): p. 38-44.
3. Newman, R.C., *2001 W.R. Whitney Award Lecture: Understanding the Corrosion of Stainless Steel.* Corrosion, 2001. **57**(12): p. 1030-1041.
4. Tsutsumi, Y., A. Nishikata, and T. Tsuru, *Pitting corrosion mechanism of Type 304 stainless steel under a droplet of chloride solutions.* Corrosion Science, 2007. **49**(3): p. 1394-1407.
5. Hastuty, S., A. Nishikata, and T. Tsuru, *Pitting corrosion of Type 430 stainless steel under chloride solution droplet.* Corrosion Science, 2010. **52**(6): p. 2035-2043.
6. Street, S.R., N. Mi, A. Cook, H.B. Mohammed-Ali, L.Y. Guo, T. Rayment, and A.J. Davenport, *Atmospheric pitting corrosion of 304L stainless steel: the role of highly concentrated chloride solutions.* Faraday Discussions, 2015. **180**: p. 251-265.
7. Guo, L., Atmospheric Localised Corrosion of Stainless Steel, [PhD thesis]. Birmingham (UK):University of Birmingham; 2015.
8. Hastuty, S., Y. Tsutsumi, A. Nishikata, and T. Tsuru,, *Pitting corrosion of type 430 stainless steel in the process of drying of chloride solution layer.* Isij International, 2012. **52**(5): p. 863-867.
9. Van Nam, T., E. Tada, and A. Nishikata, *Pit Initiation and Repassivation of Stainless Steels Exposed to Cyclic Relative Humidity Changes.* Journal of The Electrochemical Society, 2015. **162**(9): p. C419-C425.
10. Chen, A., F. Cao, X. Liao, W. Liu, L. Zheng, J. Zhang, and C. Cao, *Study of pitting corrosion on mild steel during wet–dry cycles by electrochemical noise analysis based on chaos theory.* Corrosion Science, 2013. **66**(0): p. 183-195.
11. Yadav, A.P., A. Nishikata, and T. Tsuru, *Electrochemical impedance study on galvanized steel corrosion under cyclic wet–dry conditions—influence of time of wetness.* Corrosion Science, 2004. **46**(1): p. 169-181.
12. Nishikata, A., Y. Yamashita, H. Katayama, T. Tsuru, a. Usami, K. Tanabe, and H. Mabuchi, *An electrochemical impedance study on atmospheric corrosion of steels in a cyclic wet-dry condition.* Corrosion Science, 1995. **37**(12): p. 2059-2069.
13. Cruz, R.P.V., A. Nishikata, and T. Tsuru, *AC impedance monitoring of pitting corrosion of stainless steel under a wet-dry cyclic condition in chloride-containing environment.* Corrosion Science, 1996. **38**(8): p. 1397-1406.
14. Cruz, R.P.V., A. Nishikata, and T. Tsuru, *Pitting corrosion mechanism of stainless steels under wet-dry exposure in chloride-containing environments.* Corrosion Science, 1998. **40**(1): p. 125-139.

15. Prosek, T., A. Iversen, C. Taxén, and D. Thierry, *Low-Temperature Stress Corrosion Cracking of Stainless Steels in the Atmosphere in the Presence of Chloride Deposits.* Corrosion, 2009. **65**(2): p. 105-117.
16. Prosek, T., A. Le Gac, D. Thierry, S. Le Manchet, C. Lojewski, A. Fanica, E. Johansson, C. Canderyd, F. Dupoiron, T. Snauwaert, F. Maas, and B. Droesbeke, *Low-Temperature Stress Corrosion Cracking of Austenitic and Duplex Stainless Steels Under Chloride Deposits.* Corrosion, 2014. **70**(10): p. 1052-1063.
17. Prosek T., *Material classification for climbing anchors - Phase 2: Development of an anchor classification and related test procedure for the evaluation of stress corrosion cracking (SCC) and corrosion resistances of climbing anchors*. 2014, Institut de la Corrosion (French Corrosion Institute): Brest (France). p. 1-27.
18. Mi N., Synchrotron X-ray Studies of Atmospheric Pitting Corrosion of Stainless Steel, [PhD thesis]. Birmingham (UK):University of Birmingham; 2013.
19. Albores-Silva, O.E., E.A. Charles, and C. Padovani, *Effect of chloride deposition on stress corrosion cracking of 316L stainless steel used for intermediate level radioactive waste containers.* Corrosion Engineering, Science and Technology, 2011. **46**(2): p. 124-128.
20. Padovani, C., O.E. Albores-Silva, and E.A. Charles, *Corrosion Control of Stainless Steels in Indoor Atmospheres—Laboratory Measurements Under MgCl2 Deposits at Constant Relative Humidity (Part 1).* Corrosion, 2015. **71**(3): p. 292-304.
21. Maier, B. and G.S. Frankel, *Pitting corrosion of bare stainless steel 304 under chloride solution droplets.* Journal of the Electrochemical Society, 2010. **157**(10): p. C302-C312.
22. Mi, N., M. Ghahari, T. Rayment, and A.J. Davenport, *Use of inkjet printing to deposit magnesium chloride salt patterns for investigation of atmospheric corrosion of 304 stainless steel.* Corrosion Science, 2011. **53**(10): p. 3114-3121.
23. Wang, Y., W. Wang, Y. Liu, L. Zhong, and J. Wang, *Study of localized corrosion of 304 stainless steel under chloride solution droplets using the wire beam electrode.* Corrosion Science, 2011. **53**(9): p. 2963-2968.
24. Örnek C., A. H. Ahmed, and D. L. Engelberg, *Effect of Microstructure on Atmospheric Induced Corrosion of Heat treated Grade 2205 and 2507 Duplex Stainless Steels*, in *Eurocorr 2012*. 2012: Istanbul -Turkey.
25. Örnek C; D. L. Engelberg, S.B.L., T. L. Ladwein, *Effect of "475°c embrittlement" on the corrosion behaviour of grade 2205 duplex stainless steel investigated using local prob ing techniques.* Corrosion Management 2013: p. 9-11.
26. Davenport, A.J., L. Guo, N. Mi, H. Mohammed-Ali, M. Ghahari, S.R. Street, N.J. Laycock, T. Rayment, C. Reinhard, C. Padovani, and D. Krouse, *Mechanistic studies of atmospheric pitting corrosion of stainless steel for ILW containers.* Corrosion Engineering, Science and Technology, 2014. **49**(6): p. 514-520.
27. Örnek, C. and D.L. Engelberg, *SKPFM measured Volta potential correlated with strain localisation in microstructure to understand*

corrosion susceptibility of cold-rolled grade 2205 duplex stainless steel. Corrosion Science, 2015. **99**: p. 164-171.
28. Örnek, C. and D.L. Engelberg, *Correlative EBSD and SKPFM characterisation of microstructure development to assist determination of corrosion propensity in grade 2205 duplex stainless steel.* Journal of Materials Science, 2015: p. 1-18.
29. Örnek, C., X. Zhong, and D.L. Engelberg, *Low-Temperature Environmentally Assisted Cracking of Grade 2205 Duplex Stainless Steel Beneath a MgCl2:FeCl3 Salt Droplet.* Corrosion, 2016. **72**(3): p. 384-399.
30. Laycock, N.J. and R.C. Newman, *Temperature dependence of pitting potentials for austenitic stainless steels above their critical pitting temperature.* Corrosion Science, 1998. **40**(6): p. 887-902.
31. Leckie, H.P. and H.H. Uhlig, *ENVIRONMENTAL FACTORS AFFECTING CRITICAL POTENTIAL FOR PITTING IN 18-8 STAINLESS STEEL.* Journal of the Electrochemical Society, 1966. **113**(12): p. 1262-&.
32. Asami, K. and K. Hashimoto, *Importance of initial surface film in the degradation of stainless steels by atmospheric exposure.* Corrosion Science, 2003. **45**(10): p. 2263-2283.
33. Sugimoto, K. and Y. Sawada, *The role of molybdenum additions to austenitic stainless steels in the inhibition of pitting in acid chloride solutions.* Corrosion Science, 1977. **17**(5): p. 425-445.
34. Schweitzer P.A., *Fundamentals of Metallic Corrosion: Atmospheric and Media Corrosion of Metals*. Second ed. 2007, USA: CRC Press.
35. Kyriakongonas A. P., 3D Numerical Modeling of Austenitic Stainless Steel 316L Multi-pass Butt Welding and Comparison with Experimental Results [Master of Scince]. National Technical University of Athens; 2009.
36. Akgün, O.V., M. Ürgen, and A.F. Çakir, *The effect of heat treatment on corrosion behavior of laser surface melted 304L stainless steel.* Materials Science and Engineering: A, 1995. **203**(1–2): p. 324-331.
37. Fu J. W., Y. S. Yang, J. J. Guo, J. C. Ma, and W. H. Tong, *Microstructure evolution in AISI 304 stainless steel during near rapid directional solidification.* Materials Science and Technology, 2009. **25**(8): p. 1013-1016.
38. Fu, J.W., Y.S. Yang, J.J. Guo, J.C. Ma, and W.H. Tong, *Formation of a two-phase microstructure in Fe–Cr–Ni alloy during directional solidification.* Journal of Crystal Growth, 2008. **311**(1): p. 132-136.
39. Lippold J.C. and Savage W.F., *Solidification of austenitic stainless steel weldments, part 1 - a proposed mechanism.* Welding Journal, 1979. **58**(12): p. 362s-374s.
40. Cieslak, M.J., Ritter, A. M., Savage, W. F., *Solidification cracking and analytical electron microscopy of austenitic stainless steel weld metals.* Welding Journal, 1982. **61**(1): p. 1-s to 8-s.
41. Elmer, J.W., S.M. Allen, and T.W. Eagar, *Microstructural development during solidification of stainless steel alloys.* Metallurgical Transactions A, 1989. **20**(10): p. 2117-2131.

42. Rho, B.S., H.U. Hong, and S.W. Nam, *The effect of δ-ferrite on fatigue cracks in 304L steels.* International Journal of Fatigue, 2000. **22**(8): p. 683-690.
43. Manning, P.E., C.E. Lyman, and D.J. Duquette, *A STEM Examination of the Localized Corrosion Behavior of a Duplex Stainless Steel.* Corrosion, 1980. **36**(5): p. 246-251.
44. Mangonon, P. and G. Thomas, *The martensite phases in 304 stainless steel.* Metallurgical Transactions, 1970. **1**(6): p. 1577-1586.
45. Tavares, S.S.M., D. Fruchart, and S. Miraglia, *A magnetic study of the reversion of martensite α' in a 304 stainless steel.* Journal of Alloys and Compounds, 2000. **307**(1–2): p. 311-317.
46. Seetharaman, V. and R. Krishnan, *Influence of the martensitic transformation on the deformation behaviour of an AISI 316 stainless steel at low temperatures.* Journal of Materials Science, 1981. **16**(2): p. 523-530.
47. Childress, J., S.H. Liou, and C.L. Chien, *Ferromagnetism in metastable 304 stainless steel with bcc structure.* Journal of Applied Physics, 1988. **64**(10): p. 6059-6061.
48. Shteinberg, M.M., Y.N. Goikhenberg, M.A. Smirnov, and D.A. Mirzaev, *Strengthening of stainless steels by deformation, the martensitic transformation, and aging.* Metal Science and Heat Treatment, 1972. **14**(7): p. 586-588.
49. Altenberger, I., B. Scholtes, U. Martin, and H. Oettel, *Cyclic deformation and near surface microstructures of shot peened or deep rolled austenitic stainless steel AISI 304.* Materials Science and Engineering: A, 1999. **264**(1–2): p. 1-16.
50. Jun, J., K. Holguin, and G.S. Frankel, *Pitting Corrosion of Very Clean Type 304 Stainless Steel.* Corrosion, 2014. **70**(2): p. 146-155.
51. Stewart, J. and D.E. Williams, *The initiation of pitting corrosion on austenitic stainless steel: on the role and importance of sulphide inclusions.* Corrosion Science, 1992. **33**(3): p. 457-474.
52. Llewellyn, D.T. and R.C. Hudd, *Steels - Metallurgy and Applications (3rd Edition)*. 1998, Elsevier: Butterworth-Heinemann: Oxford.
53. DENG;, X., M. JIANG;, and X. WANG;, *Mechanisms of inclusion evolution and intra-granular acicular ferrite formation in steels containing rare earth elements.* Acta Metall Sin(English), 2012. **25**(3): p. 241-248.
54. Holappa, L., M. Hämäläinen, M. Liukkonen, and M. Lind, *Thermodynamic examination of inclusion modification and precipitation from calcium treatment to solidified steel.* Ironmaking & Steelmaking, 2003. **30**(2): p. 111-115.
55. Lind, M., MECHANISM AND KINETICS OF TRANSFORMATION OF ALUMINA INCLUSIONS IN STEEL BY CALCIUM TREATMENT, [Doctoral Thesis]. Helsinki University of Technology; 2006.
56. Yang, J., X.-h. Wang, M. Jiang, and W.-j. Wang, *Effect of Calcium Treatment on Non-Metallic Inclusions in Ultra-Low Oxygen Steel Refined by High Basicity High Al2O3 Slag.* Journal of Iron and Steel Research, International, 2011. **18**(7): p. 8-14.

57. Oikawa, K., H. Ohtani, K. Ishida, and T. Nishizawa, *The Control of the Morphology of MnS Inclusions in Steel during Solidification.* ISIJ International, 1995. **35**(4): p. 402-408.
58. Schaeffler, A.L., *Constitution diagram for stainless steel weld metal.* Metal Progress, 1949. **56**(11): p. 680-680B.
59. DeLong W.T., G.A. Ostrom, and E.R. Szumachowski, *Measurement and calculation of ferrite in stainless-steel weld metal.* Welding Journal, 1956. **35**(11): p. 526.
60. McCowan C.N., T.A. Siewert, and D.L. Olson, *Stainless steel weld metal: prediction of ferrite content.* WRC Bulletin, 1989. **342**.
61. Lake, F.B., *Effect of copper on stainless steel weld metal ferrite content.* Paper presented at the 1990 AWS Annual Meeting Anaheim CA.
62. Dong-Cherng Wen, *Influence of Hot Rolling and Post-Tempering on the Mechanical Properties of Duplex Stainless Steel Containing Martensite and Ferrite.* MATERIALS TRANSACTIONS, 2006. **47**(11): p. 2779-2785
63. Lake F., *A new constitution diagram for predicting ferrite content of stainless steel weld metals.* Materials & Design, 1993. **14**(6): p. 345-348.
64. Elmer, J.W. and T.W. Eagar, *Measuring the residual ferrite content of rapidly solidified stainless steel alloys.* Welding Journal, 1990: p. 141-s-150-s.
65. Cullity, B.D., *Elements of X-ray Diffraction*. 2nd ed. 1978, USA: Addison–Wesley Publishing Company.
66. Bermejo, M.A.V., *Predictive and measurement methods for delta ferrite determination in stainless steels.* Welding journal, 2012. **91**: p. 113.
67. Kim, S.H., H.K. Moon, T. Kang, and C.S. Lee, *Dissolution kinetics of delta ferrite in AISI 304 stainless steel produced by strip casting process.* Materials Science and Engineering: A, 2003. **356**(1–2): p. 390-398.
68. Kožuh, S., M. Goic, and L. Kosec, *The effect of annealing on properties of AISI 316L base and weld metals.* RMZ-Materials and Geoenvironment, 2007. **54**(3): p. 331-344.
69. Toor, I.-u.-H., *Effect of Mn Content and Solution Annealing Temperature on the Corrosion Resistance of Stainless Steel Alloys.* Journal of Chemistry, 2014. **2014**: p. 8.
70. Kim S. Y., H.S. Kwon, and H. Kim, *Effect of Delta ferrite on corrosion resistance of type 316L stainless steel in acidic chloride solution by micro-droplet cell.* Solid State Phenomena, 2007. **124-126**: p. 1533-1536.
71. Hull, F.C., WELDING JOURNAL, 1967. **46**: p. 399.
72. Matsuda, F., H. Nakagawa, T. Uehara, S. Katayama, and Y. Arata, *A New Explanation for Role of Delta-Ferrite Improving Weld Solidification Crack Susceptibility in Austenitic Stainless Steel(Materials, Metallurgy, Weldability).* Transactions of JWRI, 1979. **8**(1): p. 105-112.
73. BROOKS J. A., A. W. THOMPSON, and J.C. WILLIAMS, *A Fundamental Study of the Beneficial Effects of Delta Ferrite in Reducing Weld Cracking.* WELDING JOURNAL, 1984: p. 71s-83s.
74. Manning, P.E., D.J. Duquette, and W.F. Savage, , *Technical Note: The Effect of Retained Ferrite on Localized Corrosion in Duplex 304L Stainless Steel*. 1980, Welding Research Supplement. p. 260-s-262-s.

75. Donohoe, C.J., G.O.H. Whillock, and P.J. Apps, *Localized Corrosion of Stainless Steel in a Nuclear Waste Cooling Water System—Part 2: Plant Inspection Findings.* Corrosion, 2012. **68**(9): p. 844-852.
76. Eghbali, F., M. Moayed, A. Davoodi, and N. Ebrahimi, *Critical pitting temperature (CPT) assessment of 2205 duplex stainless steel in 0.1 M NaCl at various molybdate concentrations.* Corrosion Science, 2011. **53**(1): p. 513-522.
77. Tomashov, N.D., G.P. Chernova, and O.N. Marcova, *Effect of Supplementary Alloying Elements On Pitting Corrosion Susceptibility Of 18Cr-14Ni Stainless Steel.* Corrosion, 1964. **20**(5): p. 166t-173t.
78. Ebrahimi, N., M.H. Moayed, and A. Davoodi, *Critical pitting temperature dependence of 2205 duplex stainless steel on dichromate ion concentration in chloride medium.* Corrosion Science, 2011. **53**(4): p. 1278-1287.
79. Deng, B., Y. Jiang, J. Gong, C. Zhong, J. Gao, and J. Li, *Critical pitting and repassivation temperatures for duplex stainless steel in chloride solutions.* Electrochimica Acta, 2008. **53**(16): p. 5220-5225.
80. Garfias-Mesias, L.F., J.M. Sykes, and C.D.S. Tuck, *The effect of phase compositions on the pitting corrosion of 25 Cr duplex stainless steel in chloride solutions.* Corrosion Science, 1996. **38**(8): p. 1319-1330.
81. Luppo, M.i., A. Hazarabedian, and J. Ovejero-García, *Effects of delta ferrite on hydrogen embrittlement of austenitic stainless steel welds.* Corrosion Science, 1999. **41**(1): p. 87-103.
82. Örnek C., Xiangli Zhong, and D. Engelberg, *Low-temperature Environment Assisted Cracking of Grade 2205 Duplex Stainless Steel beneath a MgCl2:FeCl3 Salt Droplet.* Corrosion, 2015. **in press**.
83. Lo, I.H., Y. Fu, C.-J. Lin, and W.-T. Tsai, *Effect of electrolyte composition on the active-to-passive transition behavior of 2205 duplex stainless steel in H2SO4/HCl solutions.* Corrosion Science, 2006. **48**(3): p. 696-708.
84. Yau, Y.H. and M.A. Streicher, *The Effect of Chromium Content (0 to 35%) in Fe-Cr Alloys on Corrosion Rates and Mechanisms in 1.0 N Sulfuric Acid.* Corrosion, 1991. **47**(5): p. 352-359.
85. Llewellyn, D.T., *Steels: Metallurgy and Applications*. First ed. (1992), UK: Butterworth-Heinemann.
86. Trethewey K.R. and J. Chamberlain, *Corrosion for science and engineering*. 2nd ed. 1995: Longman Scientific & Technical.
87. Sharland, S.M., *A review of the theoretical modelling of crevice and pitting corrosion.* Corrosion Science, 1987. **27**(3): p. 289-323.
88. Wranglen, G., *Pitting and sulphide inclusions in steel.* Corrosion Science, 1974. **14**(5): p. 331-349.
89. Eklund, G.S., *Initiation of Pitting at Sulfide Inclusions in Stainless Steel.* Journal of the Electrochemical Society, 1974. **121**(4): p. 467-473.
90. Baker, M.A. and J.E. Castle, *The initiation of pitting corrosion at MnS inclusions.* Corrosion Science, 1993. **34**(4): p. 667-682.
91. Ke, R. and R. Alkire, *Surface Analysis of Corrosion Pits Initiated at MnS Inclusions in 304 Stainless Steel.* Journal of the Electrochemical Society, 1992. **139**(6): p. 1573-1580.

92. Ke, R. and R. Alkire, *Initiation of Corrosion Pits at Inclusions on 304 Stainless Steel.* Journal of The Electrochemical Society, 1995. **142**(12): p. 4056-4062.
93. Wijesinghe, T.L.S.L. and D.J. Blackwood, *Real time pit initiation studies on stainless steels: The effect of sulphide inclusions.* Corrosion Science, 2007. **49**(4): p. 1755-1764.
94. Smialowski, M., Z. Szklarska-Smialowska, M. Rychcik, and A. Szummer, *Effect of sulphide inclusions in a commercial stainless steel on the nucleation of corrosion pits.* Corrosion Science, 1969. **9**(2): p. 123-125.
95. Zheng, S.J., Y.J. Wang, B. Zhang, Y.L. Zhu, C. Liu, P. Hu, and X.L. Ma, *Identification of MnCr2O4 nano-octahedron in catalysing pitting corrosion of austenitic stainless steels.* Acta Materialia, 2010. **58**(15): p. 5070-5085.
96. Sedriks, A.J., *Plenary Lecture—1986: Effects of Alloy Composition and Microstructure on the Passivity of Stainless Steels.* Corrosion, 1986. **42**(7): p. 376-389.
97. Castle, J.E. and R. Ke, *Studies by auger spectroscopy of pit initiation at the site of inclusions in stainless steel.* Corrosion Science, 1990. **30**(4–5): p. 409-428.
98. Lott, S.E. and R.C. Alkire, *The Role of Inclusions on Initiation of Crevice Corrosion of Stainless Steel: I . Experimental Studies.* Journal of The Electrochemical Society, 1989. **136**(4): p. 973-979.
99. Webb, E.G. and R.C. Alkire, *Pit Initiation at Single Sulfide Inclusions in Stainless Steel: I. Electrochemical Microcell Measurements.* Journal of the Electrochemical Society, 2002. **149**(6): p. B272-B279.
100. Webb, E.G. and R.C. Alkire, *Pit Initiation at Single Sulfide Inclusions in Stainless Steel: II. Detection of Local pH, Sulfide, and Thiosulfate.* Journal of the Electrochemical Society, 2002. **149**(6): p. B280-B285.
101. Webb, E.G. and R.C. Alkire, *Pit Initiation at Single Sulfide Inclusions in Stainless Steel: III. Mathematical Model.* Journal of the Electrochemical Society, 2002. **149**(6): p. B286-B295.
102. Laycock, N.J., *Effects of Temperature and Thiosulfate on Chloride Pitting of Austenitic Stainless Steels.* Corrosion, 1999. **55**(6): p. 590-595.
103. Newman, R.C., W.P. Wong, H. Ezuber, and A. Garner, *Pitting of Stainless Steels by Thiosulfate Ions.* Corrosion, 1989. **45**(4): p. 282-287.
104. Marcus, P., A. Teissier, and J. Oudar, *The influence of sulphur on the dissolution and the passivation of a nickel-iron alloy—I. electrochemical and radiotracer measurements.* Corrosion Science, 1984. **24**(4): p. 259-268.
105. Marco, J.F., J.R. Gancedo, W. Meisel, P. Griesbach, and P. Gütlich, *Technical Note: Study of the Cl−-Induced Breakdown of the Passive Layer on Steel.* Corrosion, 1991. **47**(7): p. 498-500.
106. Webb, E.G., T. Suter, and R.C. Alkire, *Microelectrochemical Measurements of the Dissolution of Single MnS Inclusions, and the Prediction of the Critical Conditions for Pit Initiation on Stainless Steel.* Journal of the Electrochemical Society, 2001. **148**(5): p. B186-B195.

107. Ghahari S.M., In Situ Synchrotron X-Ray Characterisation and Modelling of Pitting Corrosion of Stainless Steel, [PhD thesis]. University of Birmingham; 2012.
108. Manning, P.E., D.J. Duquette, and W.F. Savage, *The Role of Sulfide Inclusion Morphology in Pit Initiation of Several Type 300 Series Stainless Steels.* Corrosion, 1980. **36**(6): p. 313-319.
109. Suter, T. and H. Böhni, *A new microelectrochemical method to study pit initiation on stainless steels.* Electrochimica Acta, 1997. **42**(20–22): p. 3275-3280.
110. Szklarska-Smialowska Z., *Pitting Corrosion of Metals*. 1986, Houston, Texas: National Association of Corrosion Engineers.
111. Noh, J.S., N.J. Laycock, W. Gao, and D.B. Wells, *Effects of nitric acid passivation on the pitting resistance of 316 stainless steel.* Corrosion Science, 2000. **42**(12): p. 2069-2084.
112. Muto, I., S. Kurokawa, and N. Hara, *Microelectrochemistry on CrS and MnS Inclusions and Its Relation with Pitting Potentials of Stainless Steels.* ECS Transactions, 2009. **16**(52): p. 269-279.
113. Muto, I., D. Ito, and N. Hara, *Microelectrochemical Investigation on Pit Initiation at Sulfide and Oxide Inclusions in Type 304 Stainless Steel.* Journal of The Electrochemical Society, 2009. **156**(2): p. C55-C61.
114. Burstein, G.T., P.C. Pistorius, and S.P. Mattin, *The nucleation and growth of corrosion pits on stainless steel.* Corrosion Science, 1993. **35**(1–4): p. 57-62.
115. Pistorius, P.C. and G.T. Burstein, *Metastable Pitting Corrosion of Stainless Steel and the Transition to Stability.* Philosophical Transactions: Physical Sciences and Engineering, 1992. **341**(1662): p. 531-559.
116. Newman, R.C. and E.M. Franz, *Growth and Repassivation of Single Corrosion Pits in Stainless Steel.* Corrosion, 1984. **40**(7): p. 325-330.
117. Suleiman, M.I. and R.C. Newman, *The use of very weak galvanostatic polarization to study localized corrosion stability in stainless steel.* Corrosion Science, 1994. **36**(9): p. 1657-1665.
118. Galvele, J.R., *Transport Processes and the Mechanism of Pitting of Metals.* Journal of the Electrochemical Society, 1976. **123**(4): p. 464-474.
119. Davenport, A.J., Second year corrosion lecture notes. 2015, University of Birmingham: Birmingham.
120. Novakovski, V.M. and A.N. Sorokina, *Model study of chloride pitting in 18-8 stainless steel.* Corrosion Science, 1966. **6**(5): p. 227-233.
121. Isaacs, H.S., *The Behavior of Resistive Layers in the Localized Corrosion of Stainless Steel.* Journal of The Electrochemical Society, 1973. **120**(11): p. 1456-1462.
122. Tester, J.W. and H.S. Isaacs, *Diffusional Effects in Simulated Localized Corrosion.* Journal of The Electrochemical Society, 1975. **122**(11): p. 1438-1445.
123. Ghahari, M., D. Krouse, N. Laycock, T. Rayment, C. Padovani, M. Stampanoni, F. Marone, R. Mokso, and A.J. Davenport, *Synchrotron X-ray radiography studies of pitting corrosion of stainless steel: Extraction of pit propagation parameters.* Corrosion Science, 2015. **100**: p. 23-35.

124. ASTM G46-94, *Standard Guide for Examination and Evaluation of Pitting Corrosion*. 2005, ASTM International: West Conshohocken, PA, United States.
125. Schwenk W., *Theory Of Stainless Steel Pitting.* Corrosion, 1964. **20**(4): p. 129t-137t.
126. Janik-Czachor M. and Z. Szklarska-Smialowska, *Pitting corrosion of single crystals of the Fe-16 Cr alloy in solutions containing Cl− ions.* Corrosion Science, 1968. **8**(4): p. 215-220.
127. Pickering, H.W. and R.P. Frankenthal, *On the Mechanism of Localized Corrosion of Iron and Stainless Steel: I . Electrochemical Studies.* Journal of The Electrochemical Society, 1972. **119**(10): p. 1297-1304.
128. Frankenthal, R.P. and H.W. Pickering, *On the Mechanism of Localized Corrosion of Iron and Stainless Steel: II . Morphological Studies.* Journal of The Electrochemical Society, 1972. **119**(10): p. 1304-1310.
129. Li, S.X. and L.H. Hihara, *Atmospheric corrosion initiation on steel from predeposited NaCl salt particles in high humidity atmospheres.* Corrosion Engineering, Science and Technology, 2010. **45**(1): p. 49-56.
130. Albores-Silva, O.E., E.A. Charles, and C. Padovani, *Effect of chloride deposition on stress corrosion cracking of 316L stainless steel used for intermediate level radioactive waste containers.* Corrosion Engineering Science and Technology, 2011. **46**(2): p. 124-128.
131. Cole, I.S., N.S. Azmat, A. Kanta, and M. Venkatraman, *What really controls the atmospheric corrosion of zinc? Effect of marine aerosols on atmospheric corrosion of zinc.* International Materials Reviews, 2009. **54**(3): p. 117-133.
132. Cole, I.S., W.D. Ganther, D.A. Paterson, G.A. King, S.A. Furman, and D. Lau, *Holistic model for atmospheric corrosion: Part 2 - Experimental measurement of deposition of marine salts in a number of long range studies.* Corrosion Engineering, Science and Technology, 2003. **38**(4): p. 259-266.
133. Mendoza, A.R. and F. Corvo, *Outdoor and indoor atmospheric corrosion of carbon steel.* Corrosion Science, 1999. **41**(1): p. 75-86.
134. Schindelholz, E., B.E. Risteen, and R.G. Kelly, *Effect of Relative Humidity on Corrosion of Steel under Sea Salt Aerosol Proxies: I. NaCl.* Journal of The Electrochemical Society, 2014. **161**(10): p. C450-C459.
135. Schindelholz, E., B.E. Risteen, and R.G. Kelly, *Effect of Relative Humidity on Corrosion of Steel under Sea Salt Aerosol Proxies: II. MgCl2, Artificial Seawater.* Journal of The Electrochemical Society, 2014. **161**(10): p. C460-C470.
136. Tsuru, T., K.-I. Tamiya, and A. Nishikata, *Formation and growth of micro-droplets during the initial stage of atmospheric corrosion.* Electrochimica Acta, 2004. **49**(17–18): p. 2709-2715.
137. Dubuisson, E., P. Lavie, F. Dalard, J.-P. Caire, and S. Szunerits, *Study of the atmospheric corrosion of galvanised steel in a micrometric electrolytic droplet.* Electrochemistry Communications, 2006. **8**(6): p. 911-915.

138. Dubuisson, E., P. Lavie, F. Dalard, J.-P. Caire, and S. Szunerits, *Corrosion of galvanised steel under an electrolytic drop.* Corrosion Science, 2007. **49**(2): p. 910-919.
139. Padovani, C., O. Albores-Silva, and A. Charles, *Corrosion control of stainless steels in indoor atmospheres – laboratory measurements under MgCl2 deposits at constant relative humidity (Part 1).* Corrosion, 2014.
140. Schindelholz E. and R.G. Kelly, *Application of Inkjet Printing for Depositing Salt Prior to Atmospheric Corrosion Testing.* Electrochemical and Solid State Letters 2010. **13**(10): p. C29-C31.
141. Tsutsumi, Y., A. Nishikata, and T. Tsuru, *Initial Stage of Pitting Corrosion of Type 304 Stainless Steel under Thin Electrolyte Layers Containing Chloride Ions.* Journal of The Electrochemical Society, 2005. **152**(9): p. B358-B363.
142. Nishikata A, A.H. Nakamura, T.V. Nam, and Tada. E., *Relative Humidity for Onsets of Pitting Corrosion and Repassivation of Stainless Steels under Wet-dry Cyclic Conditions Containing Chloride*, in *EUROCORR 2014*. 2014: Pisa, Italy.
143. Matsumi M., A. Nishikata, and T. Tsuru., *in Preceedings of the Japan Conference on Material and Environments 46.* Fukuoka, 1999: p. 13.
144. Tsutsumi, Y., A. Nishikata, and T. Tsuru, *Monitoring of Rusting of Stainless Steels in Marine Atmospheres Using Electrochemical Impedance Technique.* Journal of The Electrochemical Society, 2006. **153**(7): p. B278-B282.
145. Cook, A.B., S.B. Lyon, N.P.C. Stevens, M. Gunther, G. McFiggans, R.C. Newman, and D.L. Engelberg, *Assessing the risk of under-deposit chloride-induced stress corrosion cracking in austenitic stainless steel nuclear waste containers.* Corrosion Engineering, Science and Technology, 2014. **49**(6): p. 529-534.
146. Tada, E. and G.S. Frankel, *Effects of Particulate Silica Coatings on Localized Corrosion Behavior of AISI 304SS under Atmospheric Corrosion Conditions.* Journal of the Electrochemical Society, 2007. **154**(6): p. C318-C325.
147. Chen, Z.Y. and R.G. Kelly, *Computational Modeling of Bounding Conditions for Pit Size on Stainless Steel in Atmospheric Environments.* Journal of the Electrochemical Society, 2010. **157**(2): p. C69-C78.
148. Neufeld, A.K., I.S. Cole, A.M. Bond, and S.A. Furman, *The initiation mechanism of corrosion of zinc by sodium chloride particle deposition.* Corrosion Science, 2002. **44**(3): p. 555-572.
149. Cole I.S. Lau D.; Paterson D.A., *Holistic model for atmospheric corrosion Part 6 – From wet aerosol to salt deposit.* Corrosion Engineering, Science and Technology, 2004. **39**(3): p. 209-218.
150. Chen, Z.Y., D. Persson, F. Samie, S. Zakipour, and C. Leygraf, *Effect of Carbon Dioxide on Sodium Chloride-Induced Atmospheric Corrosion of Copper.* Journal of The Electrochemical Society, 2005. **152**(12): p. B502-B511.
151. Zhang, J., J. Wang, and Y. Wang, *Electrochemical investigations of micro-droplets formed on metals during the deliquescence of salt*

particles in atmosphere. Electrochemistry Communications, 2005. **7**(4): p. 443-448.
152. Lobnig, R., J.D. Sinclair, M. Unger, and M. Stratmann, *Mechanism of Atmospheric Corrosion of Copper in the Presence of Ammonium Sulfate Particles: Effect of Surface Particle Concentration.* Journal of The Electrochemical Society, 2003. **150**(6): p. A835-A849.
153. Katayama, H., K. Noda, H. Masuda, M. Nagasawa, M. Itagaki, and K. Watanabe, *Corrosion simulation of carbon steels in atmospheric environment.* Corrosion Science, 2005. **47**(10): p. 2599-2606.
154. Chen, Z.Y., S. Zakipour, D. Persson, and C. Leygraf, *Effect of Sodium Chloride Particles on the Atmospheric Corrosion of Pure Copper.* Corrosion, 2004. **60**(5): p. 479-491.
155. Maier, B. and G.S. Frankel, *Pitting Corrosion of Silica-Coated Type 304 Stainless Steel Under Thin Electrolyte Layers.* Corrosion, 2011. **67**(3): p. 035004-1-035004-10.
156. Zhang, J., J. Wang, and Y. Wang, *Micro-Droplets Formation during the Deliquescence of Salt Particles in Atmosphere.* Corrosion, 2005. **61**(12): p. 1167-1172.
157. Stratmann, M. and H. Streckel, *On the atmospheric corrosion of metals which are covered with thin electrolyte layers—I. Verification of the experimental technique.* Corrosion Science, 1990. **30**(6–7): p. 681-696.
158. Stratmann, M. and H. Streckel, *On the atmospheric corrosion of metals which are covered with thin electrolyte layers—II. Experimental results.* Corrosion Science, 1990. **30**(6–7): p. 697-714.
159. Stratmann, M., H. Streckel, K.T. Kim, and S. Crockett, *On the atmospheric corrosion of metals which are covered with thin electrolyte layers-iii. the measurement of polarisation curves on metal surfaces which are covered by thin electrolyte layers.* Corrosion Science, 1990. **30**(6–7): p. 715-734.
160. Nishikata, A., Y. Ichihara, and T. Tsuru, *An application of electrochemical impedance spectroscopy to atmospheric corrosion study.* Corrosion Science, 1995. **37**(6): p. 897-911.
161. Nishikata, A., Y. Ichihara, and T. Tsuru, *Electrochemical impedance spectroscopy of metals covered with a thin electrolyte layer.* Electrochimica Acta, 1996. **41**(7–8): p. 1057-1062.
162. Winsley R.J., S.N.R., Reddy B., Rance A.P., Fennell PAH. 4 Meter Box Monitoring Programme - Final Report for the Period 2007-2010. Serco Report SERCO/TCS/006028.01/Issue 1. 2011 report to RWMD and SERCO/TCS/006028.01/Issue001/FinalReport.
163. Padovani, C., R.J. Winsley, N.R. Smart, P.A.H. Fennell, C. Harris, and K. Christie, *Corrosion Control of Stainless Steels in Indoor Atmospheres—Practical Experience (Part 2).* Corrosion, 2015. **71**(5): p. 646-666.
164. du Plessis, A., Studies on Atmospheric Corrosion Processes in AA2024, [Ph.D. thesis]. Birmingham, UK:University of Birmingham; 2015.
165. ZHANG J.-b.; WANG J.; WANG Yan-hua, *Phenomenon of Micro-droplets Formation on Metals during the Deliquescence of Salt Particles in Atmosphere.* Acta Phys. Chim. Sin., 2005. **21**(09): p. 993-996.

166. Bian, L., Y. Weng, and X. Li, *Observation of micro-droplets on metal surface in early atmospheric corrosion.* Electrochemistry Communications, 2005. **7**(10): p. 1033-1038.
167. Morton, S.C. and G.S. Frankel, *Atmospheric pitting corrosion of AA7075-T6 under evaporating droplets with and without inhibitors.* Materials and Corrosion, 2014. **65**(4): p. 351-361.
168. Li, J.F., B. Maier, and G.S. Frankel, *Corrosion of an Al–Mg–Si alloy under MgCl2 solution droplets.* Corrosion Science, 2011. **53**(6): p. 2142-2151.
169. Wang, J., L. Liang, and J. Jiang, *The role of electrochemical polarization in micro-droplets formation.* Electrochemistry Communications, 2008. **10**(11): p. 1788-1791.
170. *DiamondLightSource. How Diamond Works [cited 2015/ 12/018]. Available from: http://www.diamond.ac.uk/Home/About/How-Diamond-Works.html.*
171. Salvo, L., M. Suéry, A. Marmottant, N. Limodin, and D. Bernard, *3D imaging in material science: Application of X-ray tomography.* Comptes Rendus Physique, 2010. **11**(9–10): p. 641-649.
172. Stock, S.R., *X-ray microtomography of materials.* International Materials Reviews, 1999. **44**(4): p. 141-164.
173. Banhart J., *Advanced Tomographic Methods in Materials Research and Engineering*. 2008, New York: Oxford University Press Inc.
174. *http://www.chemicalghosts.org/research/synchrotron-science/*. 2015 [cited 2015 01/12].
175. Ghahari, S.M., A.J. Davenport, T. Rayment, T. Suter, J.-P. Tinnes, C. Padovani, J.A. Hammons, M. Stampanoni, F. Marone, and R. Mokso, *In situ synchrotron X-ray micro-tomography study of pitting corrosion in stainless steel.* Corrosion Science, 2011. **53**(9): p. 2684-2687.
176. Marrow, T.J., L. Babout, A.P. Jivkov, P. Wood, D. Engelberg, N. Stevens, P.J. Withers, and R.C. Newman, *Three dimensional observations and modelling of intergranular stress corrosion cracking in austenitic stainless steel.* Journal of Nuclear Materials, 2006. **352**(1–3): p. 62-74.
177. Burnett, T.L., S.A. McDonald, A. Gholinia, R. Geurts, M. Janus, T. Slater, S.J. Haigh, C. Ornek, F. Almuaili, D.L. Engelberg, G.E. Thompson, and P.J. Withers, *Correlative Tomography.* Sci. Rep., 2014. **4**.
178. Connolly, B.J., D.A. Horner, S.J. Fox, A.J. Davenport, C. Padovani, S. Zhou, A. Turnbull, M. Preuss, N.P. Stevens, T.J. Marrow, J.Y. Buffiere, E. Boller, A. Groso, and M. Stampanoni, *X-ray microtomography studies of localised corrosion and transitions to stress corrosion cracking.* Materials Science and Technology, 2006. **22**(9): p. 1076-1085.
179. Knight, S.P., M. Salagaras, A.M. Wythe, F. De Carlo, A.J. Davenport, and A.R. Trueman, *In situ X-ray tomography of intergranular corrosion of 2024 and 7050 aluminium alloys.* Corrosion Science, 2010. **52**(12): p. 3855-3860.
180. Knight, S.P., M. Salagaras, and A.R. Trueman, *The study of intergranular corrosion in aircraft aluminium alloys using X-ray tomography.* Corrosion Science, 2011. **53**(2): p. 727-734.

181. Davenport, A.J., C. Padovani, B.J. Connolly, N.P.C. Stevens, T.A.W. Beale, A. Groso, and M. Stampanoni, *Synchrotron X-Ray Microtomography Study of the Role of Y in Corrosion of Magnesium Alloy WE43.* Electrochemical and Solid-State Letters, 2007. **10**(2): p. C5-C8.
182. Xu, W., Synchrotron x-ray and electrochemical studies of pitting corrosion of iron, [Ph.D.]. University of Birmingham, UK: 2014.
183. Nagy, Z. and H. You, *RADIOLYTIC EFFECTS ON THE IN-SITU INVESTIGATION OF BURIED INTERFACES WITH SYNCHROTRON X-RAY TECHNIQUES.* Journal of Electroanalytical Chemistry, 1995. **381**(1-2): p. 275-279.
184. *MIG WELD GmbH International. Schaeffler diagramm* [cited 2016 07 23]; Available from: http://www.migweld.de/english/service/welding-stainless-steels/schaeffler-diagram-without-filler-metal/.
185. Schindelin J, A.-C.I., Frise E, Kaynig V, Longair M, Pietzsch T, et al. Fiji: an open-source platform for biological-image analysis. Nature Methods. 2012;9(7):676-82.
186. ASTM E104-02, *Standard Practice for Maintaining Constant Relative Humidity by Means of Aqueous Solutions*. 2007, ASTM International: West Conshohocken, PA, United States.
187. Vacher H.C. and C.J. Bechtoldt, *Delta Ferrite-Austenite Reactions and the Formation of Carbide, Sigma, and Chi Phases in 18 Chromium-8 Nickel-3.5 Molybdenum Steels.* Journal of Research of the National Bureau of Standards, 1954. **35**(2): p. 67-76.
188. Ahmed, I.I., J.Q. da Fonseca, and A.H. Sherry, *Effect of strain paths and residual delta ferrite on the failure of cold rolled austenitic stainless steels, type 304L.* The Journal of Strain Analysis for Engineering Design, 2013. **48**(7): p. 410-419.
189. Mesu J.G., B., A. M., De Groot, F. M. F.,Weckhuysen, B. M. , Observing the influence of X-rays on aqueous copper solutions by in situ combined video/XAFS/UV-Vis spectroscopy. 13th International Conference on X-Ray Absorption Fine Structure (XAFS13); 2007; Stanford, CA: American Institute of Physics.
190. Chiba, A., I. Muto, Y. Sugawara, and N. Hara, *A Microelectrochemical System for In Situ High-Resolution Optical Microscopy: Morphological Characteristics of Pitting at MnS Inclusion in Stainless Steel.* Journal of The Electrochemical Society, 2012. **159**(8): p. C341-C350.
191. Saluja R. and K.M. Moeed, *METALLURGICAL BEHAVIOUR OF AISI 304 STEEL BUTT WELDS UNDER SEGREGATION.* INTERNATIONAL JOURNAL OF MECHANICAL ENGINEERING AND TECHNOLOGY, 2014. **5**(2): p. 36-43.
192. Mumtaz, K., S. Takahashi, J. Echigoya, Y. Kamada, L.F. Zhang, H. Kikuchi, K. Ara, and M. Sato, *Magnetic measurements of martensitic transformation in austenitic stainless steel after room temperature rolling.* Journal of Materials Science, 2004. **39**(1): p. 85-97.
193. Nakada, N., H. Ito, Y. Matsuoka, T. Tsuchiyama, and S. Takaki, *Deformation-induced martensitic transformation behavior in cold-rolled and cold-drawn type 316 stainless steels.* Acta Materialia, 2010. **58**(3): p. 895-903.

194. Naraghi, R., Martensitic Transformation in Austenitic Stainless Steels, [Masters thesis]. Sweden:Royal Institute of Technology; Masters Degree, 2009.
195. Zhang, M.X., P.M. Kelly, L.K. Bekessy, and J.D. Gates, *Determination of retained austenite using an X-ray texture goniometer.* Materials Characterization, 2000. **45**(1): p. 39-49.
196. Lothongkum, G., P. Wongpanya, S. Morito, T. Furuhara, and T. Maki, *Effect of nitrogen on corrosion behavior of 28Cr–7Ni duplex and microduplex stainless steels in air-saturated 3.5 wt% NaCl solution.* Corrosion Science, 2006. **48**(1): p. 137-153.
197. Batista S.R.F. and S.E. Kuri;, *Aspect of selective and pitting corrosion in cast duplex stainless steel.* Anti-Corrosion Methods and Materials, 2004. **51**(3): p. 205–208.
198. Azmat, N.S., K.D. Ralston, T.H. Muster, B.C. Muddle, and I.S. Cole, *A High-Throughput Test Methodology for Atmospheric Corrosion Studies.* Electrochemical and Solid-State Letters, 2011. **14**(6): p. C9-C11.
199. Wang, Y.H., Y.Y. Liu, W. Wang, L. Zhong, and J. Wang, *Influences of the three-phase boundary on the electrochemical corrosion characteristics of carbon steel under droplets.* Materials and Corrosion, 2013. **64**(4): p. 309-313.
200. Jiang, J., J. Wang, Y.-h. Lu, and J.-z. Hu, *Effect of length of gas/liquid/solid three-phase boundary zone on cathodic and corrosion behavior of metals.* Electrochimica Acta, 2009. **54**(5): p. 1426-1435.
201. Nishikata, A., Y. Ichihara, Y. Hayashi, and T. Tsuru, *Influence of Electrolyte Layer Thickness and pH on the Initial Stage of the Atmospheric Corrosion of Iron.* Journal of the Electrochemical Society, 1997. **144**(4): p. 1244-1252.
202. Horton D. J., A. W. Zhu, J.R. Scully, and M. Neurock, *Crystallographic controlled dissolution and surface faceting in disordered face-centered cubic FePd.* MRS Communications 2014. **4**: p. 113-119.
203. Krishnan S., J. Dumbre, S. Bhatt, Esther T. Akinlabi, and R. Ramalingam, *Effect of Crystallographic Orientation on the Pitting Corrosion Resistance of Laser Surface Melted AISI 304L Austenitic Stainless Steel.* International Journal of Mechanical, Aerospace, Industrial and Mechatronics Engineering, 2013. **7**(4): p. 239-242.
204. Ravi Kumar, B., R. Singh, B. Mahato, P.K. De, N.R. Bandyopadhyay, and D.K. Bhattacharya, *Effect of texture on corrosion behavior of AISI 304L stainless steel.* Materials Characterization, 2005. **54**(2): p. 141-147.
205. Shahryari, A., J.A. Szpunar, and S. Omanovic, *The influence of crystallographic orientation distribution on 316LVM stainless steel pitting behavior.* Corrosion Science, 2009. **51**(3): p. 677-682.
206. Kumar, B.R., A.K. Singh, S. Das, and D.K. Bhattacharya, *Cold rolling texture in AISI 304 stainless steel.* Materials Science and Engineering: A, 2004. **364**(1–2): p. 132-139.
207. Buck, W.R. and H. Leidheiser, *The Corrosion of Single Crystals and Recrystallized Single Crystals of Iron and Steel in Citric Acid.* Journal of The Electrochemical Society, 1957. **104**(8): p. 474-481.

208. Cui, F.S., F.J. Presuel-Moreno, and R.G. Kelly, *Computational modeling of cathodic limitations on localized corrosion of wetted SS 316L at room temperature.* Corrosion Science, 2005. **47**(12): p. 2987-3005.
209. Chen, Z.Y. and R.G. Kelly, *An analytical modeling method for calculating the maximum cathode current deliverable by a circular cathode under atmospheric exposure*, in *Simulation of Electrochemical Processes II*, V.G. DeGiorgi, C.A. Brebbia, and R.A. Adey, Editors. 2007. p. 33-41.
210. Ernst, P. and R.C. Newman, *Pit growth studies in stainless steel foils. I. Introduction and pit growth kinetics.* Corrosion Science, 2002. **44**(5): p. 927-941.
211. Hunkeler, F., A. Krolikowski, and H. Böhni, *A study of the solid salt film on nickel and stainless steel.* Electrochimica Acta, 1987. **32**(4): p. 615-620.
212. Newman, R.C., *The dissolution and passivation kinetics of stainless alloys containing molybdenum—1. Coulometric studies of Fe・Cr and Fe・Cr・Mo alloys.* Corrosion Science, 1985. **25**(5): p. 331-339.
213. Street, S.R., *Personal Communication*. 2015.
214. TOMASHOV N. D., *Development of the Electrochemical Theory of Metallic Corrosion.* Corrosion, 1964. **20**(1): p. 7t-14t.
215. Padovani, C., *Overview of UK research on the durability of container materials for radioactive wastes.* Corrosion Engineering, Science and Technology, 2014. **49**(6): p. 402-409.
216. Muster, T.H., A. Bradbury, A. Trinchi, I.S. Cole, T. Markley, D. Lau, S. Dligatch, A. Bendavid, and P. Martin, *The atmospheric corrosion of zinc: The effects of salt concentration, droplet size and droplet shape.* Electrochimica Acta, 2011. **56**(4): p. 1866-1873.
217. Chen, J., J. Wang, E. Han, and W. Ke, *In situ observation of formation and spreading of micro-droplets on magnesium and its alloy under cyclic wet–dry conditions.* Corrosion Science, 2007. **49**(3): p. 1625-1634.
218. Chen, Z.Y., D. Persson, A. Nazarov, S. Zakipour, D. Thierry, and C. Leygraf *In Situ Studies of the Effect of CO2 on the Initial NaCl-Induced Atmospheric Corrosion of Copper.* Journal of The Electrochemical Society, 2005. **152**(9): p. B342-B351.
219. Jung, R.-H., H. Tsuchiya, and S. Fujimoto, *XPS characterization of passive films formed on Type 304 stainless steel in humid atmosphere.* Corrosion Science, 2012. **58**(0): p. 62-68.
220. Frankel, G., G. Thornton, S. Street, T. Rayment, D. Williams, A. Cook, A. Davenport, S. Gibbon, D. Engelberg, C. Ornek, A. Mol, P. Marcus, D. Shoesmith, C. Wren, K. Yliniemi, G. Williams, S. Lyon, R. Lindsay, T. Hughes, J. Lutzenkirchen, S.T. Cheng, J. Scully, S.F. Lee, R. Newman, C. Taylor, R. Springell, J. Mauzeroll, S. Virtanen, S. Heurtault, and J. Sullivan, *Localised corrosion: general discussion.* Faraday Discussions, 2015. **180**: p. 381-414.
221. Smart, N.R., R.J. Winsley, P.A.H. Fennell, B. Reddy, A.P. Rance, and C. Padovani, *Waste container durability: monitoring of a stainless steel 4 metre box over 12 years.* Mineralogical Magazine, 2012. **76**(8): p. 2891-2899.

222. Mankowski, J. and Z. Szklarska-Smialowska, *The effect of specimen position on the shape of corrosion pits in an austenitic stainless steel.* Corrosion Science, 1977. **17**(9): p. 725-735.
223. Harris, C., *A Survey of Current Environmental Conditions Within ILW Interim Stores and Potential GDF Analogues*. 2015, Amec, 17391/TR/0007.
224. Brossia, C.S. and R.G. Kelly, *Influence of Alloy Sulfur Content and Bulk Electrolyte Composition on Crevice Corrosion Initiation of Austenitic Stainless Steel.* Corrosion, 1998. **54**(2): p. 145-154.
225. UHLIG, H.H. and J.R. GILMAN, *Pitting of 18-8 Stainless Steel in Ferric Chloride Inhibited by Nitrates.* Corrosion, 1964. **20**(9): p. 289t-292t.